

Predictive Dynamic Simulation of Child Gait Using Direct Collocation Optimal Control

by

Mahdokht Ezati

A thesis
presented to the University of Waterloo
in fulfillment of the
thesis requirement for the degree of
Doctor of Philosophy
in
Systems Design Engineering

Waterloo, Ontario, Canada, 2021

© Mahdokht Ezati 2021

Examining Committee Membership

The following served on the Examining Committee for this thesis. The decision of the Examining Committee is by majority vote.

External Examiner: Dr. Maxime Raison
Professor, Dept. of Mechanical Engineering,
Polytechnique Montréal

Supervisor: Dr. John McPhee
Professor, Dept. of Systems Design Engineering,
University of Waterloo

Internal Member: Dr. Eihab Abdel-Rahman
Professor, Dept. of Systems Design Engineering,
University of Waterloo

Dr. Nasser Lashgarian Azad
Associate Professor, Dept. of Systems Design Engineering,
University of Waterloo

Internal-External Member: Dr. Dana Kulić
Professor, Dept. of Mechanical and Aerospace Engineering,
Monash University

Author's Declaration

This thesis consists of material all of which I authored or co-authored: see Statement of Contributions included in the thesis. This is a true copy of the thesis, including any required final revisions, as accepted by my examiners.

I understand that my thesis may be made electronically available to the public.

Statement of Contributions

This thesis contains some material that was taken from multi-author papers including:

Conference Papers

- M. Ezati, B. Ghannadi, N. Mehrabi, and J. McPhee, 2017, “Optimal vertical jump of a human,” 4th International Conference On Control Dynamic Systems, And Robotics (CDSR), volume 233, pages 1-8, Toronto, Ontario, Canada. doi: 10.11159/cdsr17.103.
Contributions of B. Ghannadi: technical help with MapleSim software
Contributions of N. Mehrabi: technical help with GPOPS-II toolbox
- M. Ezati, P. Brown, and J. McPhee, 2018, “Forward dynamic simulation of the human vertical jump including an ellipsoidal volumetric foot-ground contact model,” World Congress of Biomechanics, Dublin, Ireland.
Contributions of P. Brown: technical help with the contact model
Contributions of B. Ghannadi: technical help with Maple software
- M. Ezati and J. McPhee, 2018, “Predictive simulation of human vertical jump using direct collocation method,” Canadian Society of Biomechanics, Halifax, Nova Scotia, Canada.
- M. Ezati, B. Ghannadi and J. McPhee, 2019, “Parameter identification for a symbolic ellipsoidal volumetric foot-ground contact model using direct collocation method,” ECCOMAS Thematic Conference on Multibody Dynamics, Duisburg, Germany.
Contributions of B. Ghannadi: technical help with Maple software
- M. Ezati, B. Ghannadi and J. McPhee, 2019, “Simulation of a symbolic human gait model with an ellipsoidal foot-ground contact model using direct collocation optimization,” XVII International Symposium on Computer Simulation in Biomechanics, Canmore, Alberta, Canada.
Contributions of B. Ghannadi: technical help with Maple software
- M. Ezati, B. Ghannadi and J. McPhee, 2021, “A muscle-torque-generator model fit for child gait dynamic simulation,” The 6th Joint International Conference on Multibody System Dynamics and The 10th Asian Conference on Multibody System Dynamics, New Delhi, India. (Accepted, not presented yet)
Contributions of B. Ghannadi: technical help with Maple software

Journal Papers

- M. Ezati, B. Ghannadi, and J. McPhee, A review of simulation methods for human movement dynamics with emphasis on gait. *Multibody Syst Dyn* 47, 265–292 (2019). <https://doi.org/10.1007/s11044-019-09685-1>

Contributions of B. Ghannadi: technical review of the paper

- M. Ezati, P. Brown, B. Ghannadi, and J. McPhee, Comparison of direct collocation optimal control to trajectory optimization for parameter identification of an ellipsoidal foot–ground contact model. *Multibody Syst Dyn* 49, 71–93 (2020). <https://doi.org/10.1007/s11044-020-09731-3>

Contributions of P. Brown: technical help with the contact model

Contributions of B. Ghannadi: technical help with Maple software

Abstract

Despite many studies in human gait analysis, human gait predictive simulation is still challenging researchers to increase the accuracy and computational efficiency for evaluative studies, including the design of wearable robotic systems, athletic training, rehabilitation, orthosis design, and orthosis tuning. Moreover, the majority of recent predictive gait simulations focused on adult and older people. In contrast, clinical centers working on child rehabilitation and treatments of child gait disorders prefer to rely more on findings from pediatric gait predictive simulations than from adult gait predictive simulations.

This thesis developed a 2-dimensional (2D) 11-degree-of-freedom (11-DOF) child model actuated by muscle torque generators and in contact with the ground through a 3-dimensional (3D) ellipsoidal volumetric foot-ground contact model. We took advantage of muscle torque generators to propose simplified but accurate and computationally-efficient musculoskeletal and neuromusculoskeletal models for children. These models predict physiologically-realistic torques, motions, ground reaction forces, muscle excitations, and metabolic energy consumption for natural, slow and fast gaits using direct collocation optimal control.

First, we highlighted the features of current skeletal, musculoskeletal, and neuromusculoskeletal human gait models. We found that symbolic programming, a fast optimal control method, an accurate volumetric foot-ground contact model, and a two-segment foot model are required to develop a computationally-efficient and accurate predictive simulation of gait. Then, to investigate the importance of these requirements, we studied a more straightforward task (vertical jump) than gait. We showed that a toe-included human model with 3D ellipsoidal volumetric foot-ground contact model would simulate this lower-extremity task more accurately than a toeless human model with a kinematically-constrained foot-ground contact model. According to the findings from the vertical jump model, we decided to develop a 2D human model for our child gait, including metatarsal joints with a 3D ellipsoidal volumetric contact model, and we identified the contact parameters using three approaches: (1) GlobalSearch trajectory optimization, (2) Direct collocation optimal control, and (3) Direct collocation optimal control along with mass-&-joint-property identification. We showed that the third approach is more accurate than the other two approaches and concluded that the contact parameters should be identified along with the mass and joint properties to have a more realistic gait simulation. For all child gait simulations in the remainder of the thesis, we decided to use direct collocation optimal control in which the contact parameters and mass and joint properties are set to the identified values.

To develop the muscle model, we adapted a recently-developed muscle-torque-generator (MTG) model to our child model, and identified the MTG parameters using experimental

child gait data. We used the identified muscle torque generators to generate simplified but accurate musculoskeletal and neuromusculoskeletal models that best fit child gait. The control inputs of the musculoskeletal and neuromusculoskeletal models are MTG activations and muscle excitations, respectively. Our proposed neuromusculoskeletal model enabled us to predict muscle excitations comparable with EMG data, and estimate the metabolic energy rate, metatarsal angles, and metatarsal torques consistent with the literature. We also developed 16 optimizations (8 optimizations for each musculoskeletal and neuromusculoskeletal model), ranging from fully-data-tracking to fully-predictive optimizations, to simulate a child natural-speed (1.26 m/s) gait and compare the models in terms of prediction accuracy and computational time. We illustrated that the neuromusculoskeletal model was more computationally-efficient than the musculoskeletal model, since the control inputs of the neuromusculoskeletal model are muscle excitations with a reasonable initial guess (i.e., EMG data were used as the initial guess for the muscle excitations). We also showed that the fully-predictive neuromusculoskeletal model could predict more accurate results with less computational time than the fully-predictive musculoskeletal model. Furthermore, the muscle excitations predicted by the fully-predictive neuromusculoskeletal model were more accurate than those predicted by the data-tracking gait models.

Finally, we used our proposed musculoskeletal and neuromusculoskeletal models to generate semi-predictive simulations of four different-speed gaits for children: very slow walking at 0.9 m/s, slow walking at 1.09 m/s, fast walking at 1.29 m/s, and very fast walking at 1.58 m/s. In the different-speed gait simulations, we did not track the experimental data of the slow or fast gaits since we wanted to evaluate whether our proposed musculoskeletal and neuromusculoskeletal models are able to minimize the reliance of simulations on experiments and predict dynamically-consistent and physically-realistic slow and fast gaits, without tracking the experimental data of the corresponding slow and fast gaits. We showed that the neuromusculoskeletal model was more computationally-efficient and accurate than the musculoskeletal model in simulating slow and fast gaits. We also plotted the cost of transport (COT) values with respect to the gait speeds; The plot follows the expected ‘U’-shaped curve, where the minimum (the most efficient COT) occurs at the natural speed (preferred speed), in agreement with experimental observations.

Acknowledgements

I would like to express my sincere gratitude to my benevolent supervisor, Professor John McPhee, who graciously helped me carry out this project.

I must express my heartfelt gratitude to Dr. Borna Ghannadi, my husband, for his continued support, encouragement, and help in sharing the information about different aspects of this project.

I would like to thank Marco Rabuffetti and Maurizio Ferrarin from Polo Tecnologico, IRCCS S. Maria Nascente, Fondazione Don C. Gnocchi, Italy for providing us with their gait experimental data.

I am extremely grateful for the professional help of Dr. Matthew Millard from Heidelberg University, Germany, and Dr. Antoine Falisse from Stanford University, California.

I sincerely appreciate the way my colleagues (Mr. Peter Brown, Miss Merwa Al-Rasheed, Dr. Reza Sharif Razavian, Dr. Naser Mehrabi, Mr. Brock Laschowski, and Mr. Ali Nasr) supported this project.

I would like to thank the Natural Sciences and Engineering Research Council of Canada (NSERC) and the Canada Research Chairs (CRC) program for funding my research.

Dedication

This is dedicated to **Borna**, my encouraging husband, **Susan** and **Nasser**, my sympathetic parents, and **Nastaran**, my lovely sister.

Table of Contents

List of Tables	xiv
List of Figures	xvii
1 Introduction	1
1.1 Motivations	1
1.2 Adaptations and Contributions	3
1.3 Thesis Outline	5
2 Literature Review	7
2.1 Basic Concepts	9
2.1.1 Terminologies	9
2.1.2 Problem Formulation	9
2.1.3 Human Models	11
2.1.4 Simulation Solvers	11
2.1.5 Human Task Analysis Classification	12
2.2 Skeletal Models	13
2.2.1 Inverse Approaches	14
2.2.2 Forward Approaches	14
2.2.3 Mixed Approaches	15
2.3 Musculoskeletal/Neuromusculoskeletal Models	17

2.3.1	Muscle Redundancy Problem	17
2.3.2	Optimal Control Methods	22
2.3.3	Forward Approaches	23
2.3.4	Inverse Approaches	24
2.3.5	Mixed Approaches	25
2.3.6	Implicit Approaches	29
2.4	Summary	31
3	Human Vertical Jump Simulation	35
3.1	Kinematically-Constrained Contact	36
3.1.1	Model Properties	36
3.1.2	Dynamic Modeling	37
3.2	3D Ellipsoidal Volumetric Foot-Ground Contact	38
3.2.1	Model Properties	39
3.2.2	Dynamic Modeling	40
3.3	Predictive Vertical Jump Simulation	40
3.4	Results and Discussion	45
3.4.1	Joint Angles	45
3.4.2	Joint Torques	46
3.4.3	Foot-Ground Contact Forces	47
3.4.4	Foot Position and Orientation	49
3.5	Conclusion	51
4	Foot-Ground Contact Model Development For Child Gait	53
4.1	Model Description	54
4.1.1	Human Model	54
4.1.2	Foot-Ground Contact Model	56
4.1.3	Dynamics Modeling	62

4.2	Experimental Data	62
4.2.1	HAT and Right Leg Without Metatarsal Joint	63
4.2.2	Right Metatarsal Joint	64
4.2.3	Left leg	66
4.3	Foot-Ground Contact Parameter Identification	66
4.3.1	Trajectory Optimization	67
4.3.2	Optimal Control	70
4.3.3	Results and Discussion	74
4.4	Contact, Segment, and Joint Parameter Identification Using Optimal Control	81
4.4.1	Modifications	84
4.4.2	Results and Discussion	86
4.5	Conclusion	89
5	Muscle-Torque-Generator Model Development For Child Gait	91
5.1	Muscle-Torque-Generator Model	92
5.1.1	Muscle-Torque-Generator Parameter Identification	94
5.1.2	Results and Discussion	98
5.2	Musculoskeletal Model	99
5.2.1	Natural Child Gait Simulation	102
5.2.2	Results and Discussion	105
5.3	Neuromusculoskeletal Model	107
5.3.1	Experimental EMG Data	109
5.3.2	Muscle Activation Dynamics	110
5.3.3	Calculation of Metabolic Energy Consumption Rate	111
5.3.4	Natural Child Gait Simulation	115
5.3.5	Results and Discussion	118
5.4	Conclusion	123

6	Natural-Speed Gait Prediction Using the Musculoskeletal and Neuro-musculoskeletal Child Models: Investigation of Different Cost Functions	125
6.1	Optimization Methodology	126
6.2	Results and Discussion	131
6.2.1	Weighting Factor Examination	131
6.2.2	Computational Time Examination	132
6.2.3	Prediction Accuracy Examination	133
6.2.4	Fully-Predictive Gait Simulation Using The Neuromusculoskeletal Model	139
6.3	Conclusion	142
7	Slow-Speed and Fast-Speed Gait Prediction Using the Musculoskeletal and Neuromusculoskeletal Child Models: A Semi-Predictive Approach	144
7.1	Semi-Predictive Optimization Methodology	145
7.2	Results and Discussion	147
7.3	Conclusion	157
8	Conclusion	158
8.1	Summary	158
8.2	Recommendations for Future Work	161
	References	162

List of Tables

2.1	Recent methods to analyze SK models	32
2.2	Recent methods to analyze MSK models	32
2.3	Recent methods to analyze NMSK models	33
3.1	Body segment properties	37
3.2	The variables in the toeless model	37
3.3	The variables in the toe-included model	38
3.4	Ellipsoidal contact model parameters	39
3.5	Maximum possible ranges of human joint angles, angular velocities and torques	41
3.6	Guess points	42
3.7	Event constraints	43
3.8	Path constraints	44
3.9	Cost functions	44
3.10	The values of weights in each model	45
3.11	Solver properties	45
4.1	Anthropometric data of all segments except for the feet	55
4.2	Joint stiffness and damping coefficient	56
4.3	Anthropometric data of the feet	56
4.4	Contact models	58
4.5	Volumetric contact model parameters	61

4.6	Known postures for the metatarsal trajectory	65
4.7	Bounds for contact parameters of the ellipsoids on the left leg	70
4.8	Weighting factor values	75
4.9	Root-mean-square errors for the trajectory optimization and optimal control	75
4.10	The optimized geometry parameters for the left foot from trajectory optimization	75
4.11	The optimized geometry parameters for the left foot from optimal control .	79
4.12	The optimized contact parameters from trajectory optimization	79
4.13	The optimized contact parameters from optimal control	79
4.14	Bounds on body and joint parameters	84
4.15	The body properties tuned through the new approach	86
4.16	The joint properties tuned through the new approach	87
4.17	The optimized geometry parameters for the left foot from the new approach	88
4.18	The optimized contact parameters from the new approach	88
5.1	Bounds on the fitting parameters	97
5.2	The identified MTG fitting parameters	98
5.3	Weighting factor values for the gait simulation using the MSK model . . .	106
5.4	Root-mean-square errors for the gait simulation using the MSK model . . .	106
5.5	Agonist-antagonist pairs of muscles actuating joints	110
5.6	The optimal fiber lengths of the muscles scaled for the child model	112
5.7	The physiological cross-sectional area of the muscles scaled for the child model	112
5.8	The f_{fast} values considered for the child muscles	113
5.9	Weighting factor values for the gait simulation using the NMSK model . .	119
5.10	The parameters identified by the NMSK model	119
5.11	Root-mean-square errors for the gait simulation using the NMSK model . .	120
6.1	The configurations of the multi-objective cost functions for the MSK-model and NMSK-model optimizations	130

6.2	The weighting factors for the cost terms of the MSK-model and NMSK-model optimizations	131
6.3	Computational times of the MSK-model and NMSK-model optimizations with the different cost functions	132
7.1	Weighting factors for the slow-gait and fast-gait simulations	148
7.2	Computational times of the slow-gait and fast-gait simulations	148

List of Figures

2.1	Dynamic formulation workflow	10
2.2	The flowchart of human task analysis classification	13
2.3	The workflow of forward and inverse approaches for SK models	13
2.4	Different methods in optimal control theory	23
2.5	The workflow of the forward approaches for MSK/NMSK models	23
2.6	The workflow of the inverse approaches for MSK/NMSK models	25
2.7	The workflow of the inverse skeletal-forward neuromuscular approaches	25
2.8	The workflow of the forward skeletal-inverse neuromuscular approaches	28
3.1	Model structure: (a) Toeless (b) Toe-included	36
3.2	Model structure with the 3D ellipsoidal volumetric contact	39
3.3	Resultant joint angles of the vertical jump simulation	46
3.4	Resultant joint torques of the vertical jump simulation	47
3.5	Resultant ground reaction forces of the vertical jump simulation	48
3.6	Comparison of normal force and model weight	49
3.7	The proportion of the reaction tangential force to the reaction normal force when the foot is in contact with the ground	50
3.8	Resultant foot position and orientation in the vertical jump simulation	50
4.1	2D human model with nine bodies and eleven DOFs	55
4.2	Side and top views of the ellipsoidal contact model for the right foot (This figure is only for visualization purpose. The positions, orientations and dimensions of the ellipsoids are not to scale.)	61

4.3	Developed human model with the ellipsoidal foot-ground contact in MapleSim	63
4.4	Phases of right and left leg during one gait cycle starting and ending with the right heel-strike	64
4.5	The planned trajectory for the right metatarsal joint angle	65
4.6	The flowchart of GlobalSearch	68
4.7	The flowchart of direct orthogonal collocation	71
4.8	The lower extremity joint torques from trajectory optimization (first column) and optimal control (second column) (The dotted lines represent the mean experimental torques and the gray areas show ± 1 standard deviations of the mean experimental torques reported by [18])	76
4.9	The tangential and normal ground reaction forces from trajectory optimization (first column) and optimal control (second column) (The dotted lines represent the mean experimental GRFs and the gray areas show ± 1 standard deviations of the mean experimental GRFs reported by [18])	77
4.10	The optimized contact model geometry from trajectory optimization	78
4.11	The optimized contact model geometry from optimal control	78
4.12	The lower extremity joint angles from optimal control (The gray areas in the plots of hip, knee and ankle joint angles represent the mean experimental angle data with the specified standard deviations reported by [18] and the gray lines in the plots of metatarsal angles represent the trajectory we planned and considered as the initial guess for the optimization)	82
4.13	The residual forces and moment acting on the pelvis obtained from trajectory optimization (first column) and optimal control optimization (second column)	83
4.14	The optimized contact model geometry from the new approach	88
4.15	The tangential and normal ground reaction forces from the new approach (The gray areas show ± 1 standard deviations of the mean experimental GRFs reported by [18])	89
5.1	The feasible areas for the demanded torques. (The black curves are the demanded torques and the light gray areas are infeasible. The upper and lower dark gray curves are the fitted active-torque-angle and passive-torque-angle curves, respectively)	100

5.2	The feasible areas for the demanded active torques. (The black curves are the demanded active torques and the light gray areas are infeasible. The upper dark gray curves are the fitted active-torque-angular-velocities) . . .	101
5.3	The workflow of the MSK model	102
5.4	The joint angles simulated by the MSK model (The dotted lines represent the mean experimental data and the gray areas show ± 1 standard deviations of the mean experimental data)	107
5.5	The joint torques simulated by the MSK model (The dotted lines represent the mean experimental data and the gray areas show ± 1 standard deviation of the mean experimental data)	108
5.6	The ground reaction forces simulated by the MSK model (The dotted lines represent the mean experimental data and the gray areas show ± 1 standard deviation of the mean experimental data)	108
5.7	The workflow of the NMSK model	109
5.8	The joint angles simulated by the NMSK model (The dotted lines represent the mean experimental data and the gray areas show ± 1 standard deviations of the mean experimental data)	120
5.9	The joint torques simulated by the NMSK model (The dotted lines represent the mean experimental data and the gray areas show ± 1 standard deviations of the mean experimental data)	121
5.10	The ground reaction forces simulated by the NMSK model (The dotted lines represent the mean experimental data and the gray areas show ± 1 standard deviations of the mean experimental data)	121
5.11	The muscle excitations simulated by the NMSK model (The dotted lines represent the mean processed EMG data and the gray areas show ± 1 standard deviations of the mean processed EMG data)	122
6.1	Root-mean-square errors of the joint angles from the MSK-model and NMSK-model optimizations using the different cost functions	133
6.2	Root-mean-square errors of the ground reaction forces from the MSK-model and NMSK-model optimizations using the different cost functions	134
6.3	Root-mean-square errors of the joint torques from the MSK-model and NMSK-model optimizations using the different cost functions	134

6.4	Root-mean-square errors of the muscle excitations from the NMSK-model optimization using the different cost functions	135
6.5	The joint angles from the NMSK-model fully-predictive simulation (The dotted lines represent the mean experimental data and the gray areas show ± 1 standard deviations of the mean experimental data)	140
6.6	The ground reaction forces from the NMSK-model fully-predictive simulation (The dotted lines represent the mean experimental data and the gray areas show ± 1 standard deviations of the mean experimental data)	140
6.7	The joint torques from the NMSK-model fully-predictive simulation (The dotted lines represent the mean experimental data and the gray areas show ± 1 standard deviations of the mean experimental data)	141
6.8	The muscle excitations from the NMSK-model fully-predictive simulation (The dotted lines represent the mean experimental data and the gray areas show ± 1 standard deviations of the mean experimental data)	141
7.1	Normalized root-mean-square errors of the joint angles from the slow-gait and fast-gait simulations	149
7.2	Normalized root-mean-square errors of the ground reaction forces from the slow-gait and fast-gait simulations	150
7.3	Normalized root-mean-square errors of the joint torques from the slow-gait and fast-gait simulations	150
7.4	Normalized root-mean-square errors of the muscle excitations from the slow-gait and fast-gait simulations	151
7.5	Metabolic cost of transport for different gait speeds	152
7.6	The joint angles from the NMSK-model optimization for different gait speeds (The dotted lines represent the mean experimental data and the gray areas show ± 1 standard deviations of the mean experimental data)	153
7.7	The ground reaction forces from the NMSK-model optimization for different gait speeds (The dotted lines represent the mean experimental data and the gray areas show ± 1 standard deviations of the mean experimental data)	154
7.8	The joint torques from the NMSK-model optimization for different gait speeds (The dotted lines represent the mean experimental data and the gray areas show ± 1 standard deviations of the mean experimental data)	155

7.9	The muscle excitations from the NMSK-model optimization for different gait speeds (The dotted lines represent the mean experimental data and the gray areas show ± 1 standard deviations of the mean experimental data)	156
-----	---	-----

Chapter 1

Introduction

Human gait analysis is very complex because of highly nonlinear human motion equations, muscle dynamics, and foot-ground contact. This analysis gets more complicated if the researchers want to predict human gait for evaluative studies, including the design of wearable robotic systems, athletic training, rehabilitation, orthosis design, and orthosis tuning. Human gait predictive simulation is still challenging researchers to increase the prediction accuracy and computational efficiency for evaluative studies. The majority of recent predictive gait simulations focused on adult and elderly subjects, but pediatric clinician-scientists prefer to rely more on the findings from pediatric gait predictive simulations than from adult gait predictive simulations.

The main goal of this thesis is to develop an accurate and computationally-efficient predictive dynamic simulation for child gait. In the following chapter, we clarified the primary motivations for this thesis and indicated our significant adaptations and contributions to child gait predictive simulation. Finally, we gave a brief outline of our research towards the contributions.

1.1 Motivations

1. Regarding the recent literature, there are few research studies on fully-predictive gait simulations [45, 90, 109, 121], and there is a need to decrease the computational time of the fully-predictive simulations and simultaneously increase the accuracy of the predicted results. Recent fully-predictive studies are limited by numerical programming, which requires a finite difference method to evaluate the gradients and Hessians

in the optimization problem. Finite differencing is an error-prone methodology and may result in unreliable results for higher-order derivatives.

2. In recent predictive gait simulations, a finite number of contact points, moving relative to the foot, have been used to model the foot-ground contact. These foot-ground contact models can be assumed as multiple-point contact models, in which the normal contact force is evaluated by the depth of penetration using the Hunt-Crossley method [67]. Since the Hunt-Crossley method is restricted to contact points (not contact surfaces), an unnatural foot shape is obtained. In a recent study, Brown and McPhee [21] have developed an ellipsoidal foot-ground contact model that may have better accuracy and higher calculation speed than its comparable foot-ground contact models. However, there are some gaps in Brown and McPhee's approach; not only did they not include both feet in the contact parameter identification process, but they did not also consider the dynamics of the lower extremities. Furthermore, when they included friction in their model, the contact parameter identification yielded inaccurate parameters and results.
3. To the best of the author's knowledge, the metatarsal joints have not been included or their angles and torques have not been reported in the recent predictive simulations even though metatarsal joints have an important role in gait analyses [40].
4. The majority of recent predictive gait simulations focused on adult and older people [45, 90, 109]. In contrast, the clinical centers working on child rehabilitation and treatments of child gait disorders prefer to rely more on pediatric gait simulations than adult gait simulations [149]. Children not only are different from adults in body size, but they also have younger muscles, less stiffness and damping in their joints that play an important role in gait simulations.
5. The majority of the recent predictive gait simulations used an anatomically-detailed muscle model (i.e., Hill-type muscle model) to simulate the muscles. However, it is challenging to fit an anatomically-detailed muscle model to specific subjects due to computational and modeling challenges [51]. Muscle torque generators (MTGs) allow researchers to develop simplified but accurate muscle models that fit specific subjects more easily than the anatomically-detailed muscle models [114]. Despite this fact, there are a limited number of child gait predictive simulations developed using MTG models [166]. Furthermore, to the best of the author's knowledge, the current MTG models have not been used to predict muscle excitations comparable with EMG data.

6. The majority of the recent predictive gait simulations used an anatomically-detailed neuromuscular model to calculate metabolic energy consumption [45, 90]. However, an MTG-based neuromuscular model, which is simpler than an anatomically-detailed neuromuscular model, would estimate metabolic energy consumption more easily. To the best of the author’s knowledge, the MTG models have not been employed to estimate metabolic energy consumption.

According to the above-mentioned motivations, to develop a computationally-efficient and accurate predictive gait simulation, a fast optimal control method, symbolic programming, an accurate volumetric foot-ground contact model, and a two-segment foot model may be required. In addition, since there are very few predictive simulations studying pediatric gait [46, 166], developing a child gait high-fidelity predictive simulation is of vital importance to model physiologically-realistic natural, slow and fast gaits.

1.2 Adaptations and Contributions

The above-mentioned motivations inspired us to develop substantial contributions and adaptations to the recent human gait predictive simulations and make some significant adaptations specifically to the recent child gait predictive simulations. To distinguish between the contributions and the adaptations, we itemized adaptations by “A” and contributions by “C” in this section.

- (A) Some recent predictive gait simulations were developed using direct collocation optimal control [45, 90, 109]. The direct collocation method is computationally-efficient compared to the equivalent methods (e.g. direct shooting [130] and trajectory optimization [43]) since this optimal control method considers the dynamic equations as algebraic constraints and solves them implicitly without explicit integrations [42]. In this thesis, we used GPOPS-II, a direct collocation optimal control toolbox in MATLAB [128] to develop the foot-ground contact parameter identification, MTG parameter identification, data-tracking gait simulations, and also predictive gait simulations.
- (A) Motivation #1 inspired us to use symbolic programming (to generate optimized simulation code and exact derivatives) for our gait simulations with the aim of increasing computational efficiency and prediction accuracy. Studies such as [14, 57, 72, 73, 105]

have shown that the use of symbolic equations can enhance the computational efficiency and accuracy of optimal control methods. Thus, we used MapleSim to extract symbolic motion dynamics equations.

- (A) Motivation #2 encouraged us to fill in the gaps of Brown and McPhee’s contact model (i.e., the 3D ellipsoidal volumetric foot-ground contact model [21]). We developed a computationally-efficient symbolic ellipsoidal volumetric foot-ground contact model that better captures the foot geometry and simulates more accurate normal and tangential reaction forces than [21].
- (C) Motivation #3 caused us to include metatarsal joints (in addition to hip, knee, and ankle joints) for the feet of our human model. We believe that the prediction accuracy of predictive gait simulations may be improved by including metatarsal joints. In this thesis, we predicted and showed physiologically-meaningful angles and torques for the metatarsal joints that are in agreement with the literature.
- (C) Motivation #4 inspired us to develop accurate, computationally-efficient, and simplified musculoskeletal (MSK) and neuromusculoskeletal (NMSK) models for children that predict physiologically-realistic torques, motions, ground reaction forces, muscle excitations, and metabolic energy consumption for natural, slow and fast gaits.
- (A) Motivations #5 and #6 prompted us to use MTGs and generate simplified but accurate MSK and NMSK models that best fit child gait. We adapted the MTG model, recently proposed by [114], to our child gait model.
- (C) We used our proposed MTG-based MSK and NMSK models to develop a wide range of child natural-gait simulations ranging from fully-data-tracking to fully-predictive simulations. We evaluated the effect of different cost terms on the realism of the predicted results and compared the MSK-model and NMSK-model optimizations in terms of computational efficiency and prediction accuracy. Our proposed MTG-based NMSK model enabled us to predict muscle excitations comparable with EMG data and estimate the metabolic energy rate consistent with the rates reported in the literature.
- (C) We evaluated whether the proposed MSK-model and NMSK-model optimizations could minimize the reliance of simulations on experiments and predict dynamically-consistent and physically-realistic slow and fast gaits of children, without tracking the experimental data of the corresponding slow and fast gaits. The NMSK-model optimization also enabled us to estimate muscle excitations and cost of transport

(COT: metabolic energy consumed per unit body mass per unit distance traveled) for the slow and fast gaits of children. We plotted the estimated COT values with respect to the gait speeds; the plot follows the expected ‘U’-shaped curve, where the minimum (the most efficient COT) occurs at the natural speed (preferred speed) [82].

1.3 Thesis Outline

To assist researchers in gait simulation, Chapter 2 classifies recent gait simulation methods according to three categories: (1) “*human model*” where we categorized human dynamic models into skeletal, musculoskeletal, and neuromusculoskeletal models; (2) “*problem formulation*” where we showed that the dynamic equations were either integrated or differentiated or implicitly solved to formulate a gait problem; (3) “*simulation solvers*” where we discussed and compared fully-data-tracking, semi-tracking/predictive, and fully-predictive methods. Furthermore, we presented the commonly-used biomechanics approaches to solve the muscle redundancy problem.

Although this thesis aims to develop a predictive gait simulation, first, a simpler task (vertical jump) is studied in Chapter 3 to investigate: (1) What type of foot-ground contact model can properly model ground reaction forces. (2) Whether the toe segments (metatarsal joints) play an important role in lower-extremity tasks.

In Chapter 4, we developed A 2D torque-driven 11-DOF human model considering the findings of the previous two chapters. The multibody dynamic equations and the contact equations were developed symbolically, and the experimental data, used to identify the contact parameters and validate the simulated results, were presented. Two different approaches (i.e., GlobalSearch trajectory optimization and direct collocation optimal control) were taken to identify the contact parameters. Then, as a third approach, the optimal control approach was modified by adding mass-&-joint-property identification and some constraints to estimate more realistic values for the contact parameters. Finally, the three approaches were compared in terms of simulation accuracy and computational efficiency.

Chapter 5 introduced the MTG model used for our child model. The MTG parameters were fitted to the child model considering the experimental child gait motion data. We then developed an MSK model in which the fitted MTG model replaced the musculoskeletal geometry and muscle contraction dynamics. The MSK model was used to investigate whether the fitted MTGs can generate realistic motion, torques, and GRFs. Next, an NMSK model was developed by adding the muscle activation dynamics to the developed MSK model and identifying the remaining muscle parameters for the child model. Our

proposed NMSK model also enabled us to predict muscle excitations and estimate COT with a good approximation.

We used the MTG-based MSK and NMSK child models, proposed in Chapter 5, to predict a child natural-speed (1.26 m/s) gait in Chapter 6. We developed two separate direct collocation optimal controls: MSK-model optimization and NMSK-model optimization. For each model's optimization, we investigated eight multi-objective cost functions composed of a wide range of cost terms, including dynamic-based, stability-based, human-criteria-based, and data-based cost terms. We evaluated the effect of these cost terms on the realism of the predicted results, and compared the MSK-model and NMSK-model optimizations in terms of computational efficiency and prediction accuracy.

Chapter 7 evaluated whether the MSK-model and NMSK-model optimizations, developed in Chapter 6, could minimize the reliance of simulations on experiments and predict dynamically-consistent and physically-realistic slow and fast gaits, without tracking the experimental data of the corresponding slow and fast gaits. We used the MSK-model and NMSK-model optimizations to predict four different-speed gaits, including very slow walking at 0.9 m/s (XS), slow walking at 1.09 m/s (S), fast walking at 1.29 m/s (M), and very fast walking at 1.58 m/s (L). In the slow-gait and fast-gait optimizations, the experimental data of the slow and fast gaits were not tracked at all, and instead, the experimental data of the natural-speed gait (i.e., natural walking at 1.26 m/s) were scaled with respect to the cycle times of the slow and fast gaits, and then the scaled data were used in the initial guess, the data-based cost term and the stability-based cost term of the cost function.

Chapter 8 summarized the main achievements of this research and recommended some possible open areas and directions to advance this research.

Chapter 2

Literature Review

Human motion and joint moment/muscle force prediction/estimation are two of the most challenging research topics in biomechanics. Human motion prediction can be very helpful in different areas such as surgical intervention planning, prosthesis and orthosis design, and athletic training. We will motivate this literature review through the following examples.

Example 1: in total hip replacement surgeries, the prevalence of dislocations following surgery has motivated researchers to implement pre-surgical planning for positioning of the acetabular cup in a safe zone to decrease the likelihood of dislocation [1, 102, 164]. This can be done using available safe zone studies [1, 37, 38], which have been found lacking or implementing computer models and predictive dynamic simulations [2, 102, 147] to predict the hip joint reaction force, and then find the optimal position for the acetabular cup by minimizing this force.

Example 2: an effective design for a prosthesis or orthosis is a human-centered design, which considers human movement [48, 65, 92, 141, 190]. Without human motion prediction, the human-centered device design can only be verified by performing experimental trials on manufactured prototypes. However, the final iterative design will be expensive and inefficient. Therefore, there is a great need for human movement prediction in prosthesis and orthosis design.

Example 3: clinical biomechanists are interested in joint moment and reaction force analyses [54]. Joint reaction forces, which directly affect joint functions, should be minimized for the elderly and injured walkers to reduce pain in their joints [77, 120, 188]. These forces should also be minimized for athletes to improve their performance in doing a specific task optimally [26, 85].

The main goal of this chapter is to shed light on the features of the recent analysis methods of human gait and to compare these methods in terms of control methodologies. To find relevant publications for this chapter, a specific search algorithm has been used. The search algorithm was limited to the recent decade and included the keywords “human motion/gait prediction, predictive simulation method, forward/inverse dynamics of human movement” and excluded certain areas (i.e., balance control and machine learning). 70% of the references in this article were found using this search algorithm. The remaining 30% were published prior to 2010 and are included in this article since they represent seminal contributions to human motion analysis.

In this review, a few of the cited papers do not target human gait specifically; however, their methodologies can be extended to human gait studies. Furthermore, balance control in human motion is not reviewed in this review, the main focus of which is on optimization-based predictive simulation methods. In these methods, stability is usually provided by stabilization constraints and not by balance control techniques. For more information about human balance and posture control during gait, the readers are directed to two review articles: [111, 185]. Moreover, machine learning techniques are not covered in this review since they are mainly used for tracking purposes and not for predictive simulation studies, which are the focus of this thesis. Available machine learning techniques in human gait have been reviewed in [131].

This chapter is organized as follows.¹ In Section 2.1, first, essential terms in human task analyses are defined, followed by an explanation of problem formulation (which use explicit or implicit dynamic formulations), human model types, and simulation solvers (i.e., data-tracking, semi-tracking/predictive, and fully-predictive methods).

Based on the workflow of the biomechanics analysis, human model types are divided into skeletal (SK), musculoskeletal (MSK) and neuromusculoskeletal (NMSK) models. Different problem formulation and simulation solvers developed for SK and MSK/NMSK models are discussed in Sections 2.2 and 2.3, respectively. Furthermore, in the latter section, the muscle redundancy problem and the routines to solve it are presented.

Next, in Section 2.4, recent methods for analyzing human gait models are summarized and various limitations are discussed. Furthermore, future prospects of improving predictive simulation methods are presented.

¹The majority of this chapter has been extracted from [42].

2.1 Basic Concepts

In this section, the main technical terms in human task analyses are briefly discussed in order to categorize reviewed studies. First, some author-defined terminologies are discussed. Next, based on our human task analysis classification, a comprehensive workflow, illustrating all parts of the human task analysis is presented. Finally, the human model types and simulation solvers are introduced.

2.1.1 Terminologies

Approach vs. Method

Approach refers specifically to problem formulation, while method indicates a general framework used to solve the human motion analysis problem.

Routine vs. Formulation

Routine is used for any optimization methodology, while formulation indicates any calculation procedure.

Estimation vs. Prediction

Estimation refers to the condition that the experimental data is available and corresponding simulation data is estimated using a method with data-tracking error evaluation. On the other hand, the prediction is used to find simulation data independent of the data-tracking error.

2.1.2 Problem Formulation

A human body can perform a task by receiving neural commands from the central nervous system (CNS). In biomechanics analyses, a dynamic formulation is developed from the workflow shown in Figure 2.1. This workflow shows the path from the neural commands to a specific posture and vice versa. The dynamic formulation can be represented either explicitly or implicitly. In the explicit dynamic formulation, the system dynamics are directly integrated or differentiated while in the implicit dynamic formulation, the system

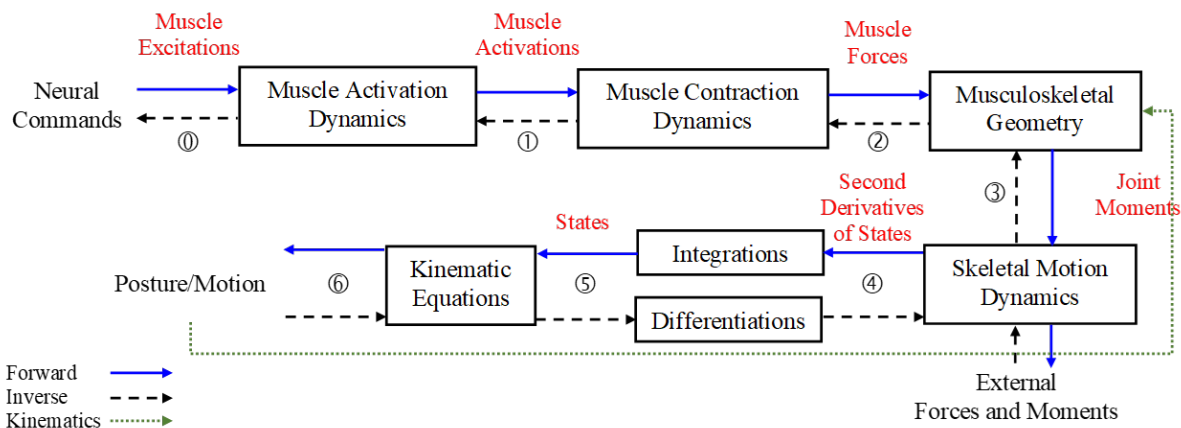


Figure 2.1: Dynamic formulation workflow

dynamics are considered as constraint equations that are implicitly satisfied inside an optimization-based simulation.

An explicit dynamic formulation can be categorized according to forward, inverse and mixed approaches. However, since there is no need to use integration/differentiation methods to solve dynamics equations in implicit approaches, they cannot be categorized like the explicit approaches. We refer to the implicit dynamic formulation as the implicit approach, which is discussed in Section 2.3.6 in more detail.

In explicit dynamic formulation, the solid arrows show the path of the forward (e.g., forward dynamics) approaches and the dashed arrows specify the path of the inverse (e.g., inverse dynamics) approaches.

In forward approaches, neural commands are received to produce muscle excitations, which are the inputs to muscle activation dynamics. Muscle activation dynamics can be modeled by first-order differential equations [139]. Muscle contraction dynamics are often modeled using a Hill-type muscle model to convert muscle activations to muscle forces [140]. Musculoskeletal geometry includes muscle attachment sites, muscle lines of actions, wrapping points and surfaces, and moment arms [6]. This geometry and muscle contraction dynamics are used to calculate joint moments (i.e., the input of skeletal motion dynamics). Note that in this thesis, joint moment and joint torque are used interchangeably. Skeletal motion dynamics are ordinary differential equations, which are solved by numerical integration to determine the motion/posture. Inverse approaches are the reverse of the forward approaches. In other words, posture/motion is used to determine the neural commands. It should be noted that to estimate physiologically-meaningful values for the

neural commands, muscle activation dynamics, and muscle contraction dynamics must be included in the analysis; an example of this is presented in the fully inverse approach of [148].

In addition to forward and inverse approaches, there are other approaches that are called mixed approaches in this review. In explicit dynamic formulations, a mixed approach may exploit the best features of forward and inverse dynamics approaches.

2.1.3 Human Models

Based on Figure 2.1, biomechanics models can fall into three categories: SK, MSK, and NMSK models. NMSK models are the most complex models since they include all the blocks shown in Figure 2.1. In MSK models, muscle activation dynamics is excluded and in SK models, muscle activation dynamics, muscle contraction dynamics and musculoskeletal geometry are excluded. These definitions of human models are introduced to avoid any misconceptions while referring to them throughout this thesis.

2.1.4 Simulation Solvers

Once a dynamic formulation for a human model is selected, a solver is required to simulate the model for a specific task. Simulation solvers use predictive simulation methods including non-optimization- or optimization-based methods. Non-optimization-based methods benefit from straight-line programming and/or non-optimal controllers to solve the simulation problem of a specific task. With experimental motion data and using data-tracking errors, these methods can compute the joint torques or muscle forces. Since experimental data is needed, these methods can be considered as data-tracking or semi-data-tracking methods.

In these methods, a data-tracking error is used. The main feature of these methods is their intrinsic realism because of tracking motion data [174]. However, a comprehensive database of human motions is needed to get meaningful results. Furthermore, we cannot study the effects of changes in the task conditions, since the previously-prescribed data does not contain the new changes (e.g., we cannot determine the outcome of a new surgical procedure for which no measurement data is available).

Optimization-based methods use optimization routines and/or optimal controllers for task analysis. Optimization-based methods predict the optimal motion of human tasks [79] and fall into two different categories: semi-predictive and fully-predictive methods

[127]. In contrast to semi-predictive methods, fully-predictive methods are knowledge-based methods that do not track measured data at all.

Fully-predictive methods do not require a motion database so they can be used to study how the changes in task conditions affect the results. For example, Chung et al. [27] have used only a knowledge-based cost function to predict joint motions and joint torques for both normal human running and slow jogging along curved paths without data-tracking. The multi-objective function of this optimization includes dynamic effort, impulse and upper-body yawing moment. The upper-body yawing moment should be minimized to avoid slipping on the ground [76]. The effects of foot location and orientation on the predicted results of running have been studied as well.

For fully-predictive methods, it is necessary and also challenging to define physiologically-meaningful objective functions [5] to satisfy human criteria. A physiologically meaningful cost function is an objective function that includes all the essential human criteria required for converging to a physiologically meaningful solution [148]. The essential human criteria are different for various human subjects and tasks. For example, the criterion for healthy walkers and walkers with orthoses or prostheses may be to walk with the minimum metabolic energy (i.e., the consumed energy per unit walking distance) [93, 167]. On the other hand, for disabled walkers, a healthy gait pattern might be an additional criterion.

There is a belief that the prediction of human motion would be more realistic if a semi-predictive method is exploited [127]. Pasciuto et al. [127] have developed a constrained nonlinear optimization problem, in which the objective function is a weighted combination of data-based and knowledge-based contributions. To validate their proposed method, they have predicted human motion and joint torques during clutch pedal depression using semi-predictive and fully-predictive methods separately and then compared the results. The comparison confirmed that the semi-predictive method predicts more realistic human motion and joint torques.

2.1.5 Human Task Analysis Classification

Using the technical terms described in this section, a general human task analysis classification is introduced in Figure 2.2. In this classification, all recent methods of human motion analysis can be categorized according to problem formulation and simulation solver.

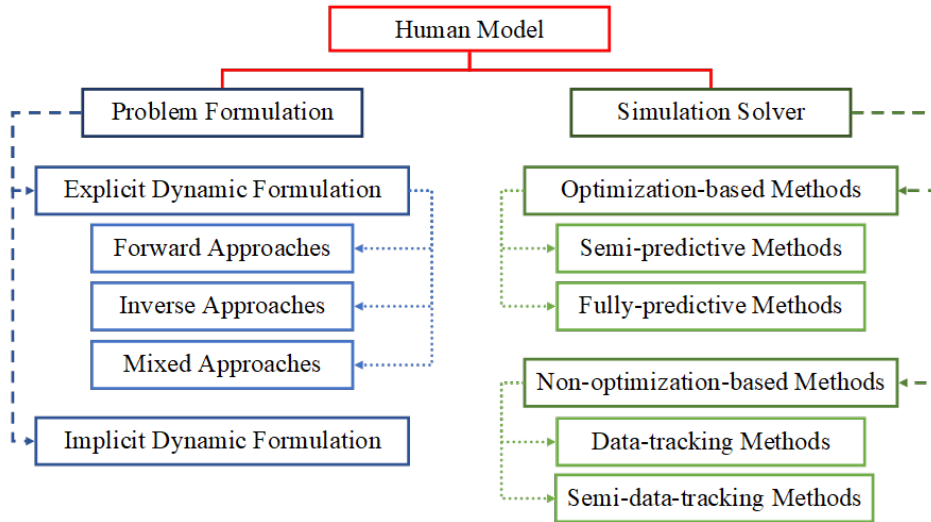


Figure 2.2: The flowchart of human task analysis classification

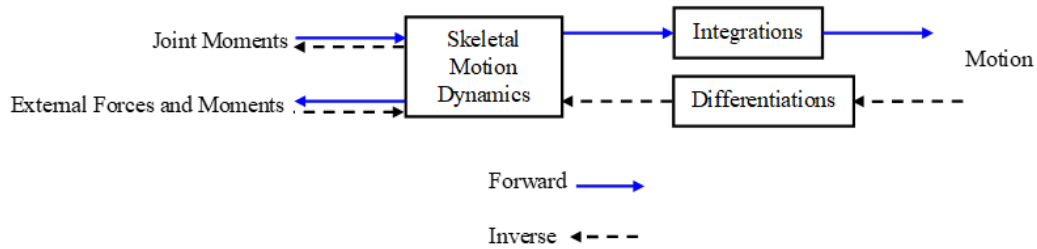


Figure 2.3: The workflow of forward and inverse approaches for SK models

2.2 Skeletal Models

In this section, problem formulations for SK models are presented for different explicit dynamic formulations (Inverse Approaches, Forward Approaches, and Mixed Approaches sections). Figure 2.3 shows the workflow of forward and inverse approaches. Different simulation solvers corresponding to each formulation are discussed within each section. The implicit approach will be discussed in the latter section.

2.2.1 Inverse Approaches

There are different methods to determine human joint moments. An invasive method is an instrumented prosthesis, which is not always practical. Another method is the inverse dynamics method, in which given captured motion data and measured external force and moment data, the inverse SK motion dynamics is solved for the joint torques [49, 137]. This method is a non-optimization-based method, in which motion data and ground-foot contact force data are required to be measured using a motion capture system and a force plate, respectively. Uncertainty in body segment parameters and errors in the experimental measurements and data-processing may result in unrealistic joint torques and inconsistencies between kinematics and ground reaction forces [124, 138, 162].

Although this method is non-invasive and relatively fast, unrealistic joint torques may be predicted due to numerical differentiation errors and inaccurate model parameters. Optimization-based methods may be used to improve the results of the inverse approaches. For example, in [44], inverse dynamics is used within a constrained optimization to reduce the inconsistency in the results of the inverse dynamics. In this paper, the optimization algorithm has applied minor changes to the measured kinematics to make the kinematic mechanically consistent with measured external forces. In other words, Kinematics are adjusted until simulated forces match experiments.

2.2.2 Forward Approaches

The joint torques obtained from the inverse dynamics can be used as the inputs to the forward SK motion dynamics in order to estimate the motion. Ideally, the motion estimated from the forward dynamics should perfectly match captured motion data. However, there may be discrepancies between the estimated motion and the captured motion data depending on the integration algorithm of the forward motion dynamics, the kinematic constraint stabilization algorithm and the differential-algebraic equation solver. Thus, to fulfill stability and robustness in the forward SK motion dynamics for human gait, three different control methodologies have been recently proposed: under-actuated, fully-actuated and kinematically-constrained methodologies.

The first methodology is needed when the human gait is under-actuated and the number of joint actuators is less than the degrees of freedom (DOFs) of the human model that freely moves in the plane/space. Therefore, there is no direct control over the three/six DOFs of the base body with respect to the global coordinate system. Hence, researchers are required to consider a foot-ground contact model to implicitly control those three/six DOFs [90, 130].

In the second methodology, all DOFs are considered to be actuated. Then, a set of non-physical forces and moments, accounting for the inconsistency between calculated and captured motions, are assumed as a residual wrench. This wrench is composed of linear and rotational actuators to control the absolute DOFs of the base body (pelvis or trunk in most cases). This methodology is used to obtain dynamically-consistent equations. The residual reduction algorithm (RRA) has been proposed [34] to reduce the residual wrench in order to closely track the captured motion. For example, Millard et al. [112] considered proportional-derivative (PD) controllers for controlling body joints and a balance controller for externally manipulating the pitch of the head-arms-trunk (HAT) segment.

In the third methodology, a kinematically-constrained foot-ground contact model is imposed to provide a stable gait. During the single-support phase of the gait cycle, one foot is constrained to be fixed to the ground, yielding a fully-actuated open-chain model [175]. During the double-support phase, both feet are fixed to the ground, yielding an over-actuated closed-chain model [95]. To provide stability, kinematic stabilization constraints are applied for each phase separately [12, 75, 148].

2.2.3 Mixed Approaches

Some of the mixed approaches use the forward dynamics model and a controller with/without an inverse dynamics model to update the joint torques based on the data-tracking error obtained from the forward dynamics simulations. Since these approaches have a feedback controller, they are also called feedback-control approaches. The hybrid zero dynamics-based control method (HZD) uses a feedback-control approach. Martin and Schmiechler [100] have used HZD to estimate the gait motion over the full ranges of speeds by tracking experimental walking data. They have compared two planar models of the lower extremities (one of which in contrast to the other one does not have ankle joints) to study the critical role of the ankle joints in the human gait. HZD parameterizes joint angles as functions of a gait variable (i.e., step progression), which is an explicit function of time. HZD has been developed based on prior work suggesting that humans control their gait motion using phase variables [61]. Initially, HZD was used for point-foot robots. Later, Martin and Schmiechler used HZD by considering rigid circular feet, since the center of pressure between the foot and ground tends to trace circular arc patterns during walking [100].

Computed torque control method (CTC) also uses a feedback-control approach to estimate the gait motion in SK models. This method was initially used in robotics. In CTC, the controller contains an inverse dynamics model. Mouzo et al. [118] have developed a 2D human model to analyze human gait using this method. CTC is a control method

that uses motion tracking error to update predicted joint torques, evaluated by an inverse dynamics model, and then solves motion dynamics by the forward integration. To find the best estimation for joint torques, Mouzo et al. [118] have considered different sets of the forward dynamic outputs (i.e., motions of DOFs and ground reaction forces) as control inputs for CTC. Foot-ground contact, which was modeled based on [158], is a volumetric contact model. They have concluded that the weighted trajectories of all the DOFs can be the best control input to get satisfactory results.

Another method is the proportional-integral-derivative control (PID), which is a classical feedback control method for controlling the plant model by feeding back the past error. Proportional-derivative control (PD) is a special case of PID. Pàmies-Vilà et al. [125] have compared the capabilities of PD and CTC in solving the forward dynamics of SK models. A kinematic perturbation was used for tuning the PD gains and pole placement techniques were used to determine control parameters in CTC. First, using experimental motion data, inverse dynamics was solved to determine joint torques. Then the calculated joint torques were used as the input of the forward motion dynamics to estimate the motion and ground reaction forces using PD and CTC separately. They showed that CTC outperforms PD for a balanced forward dynamics analysis.

To deal with the challenges of the inverse approach, one cannot use the aforementioned non-optimization-based feedback controllers for prediction. Thus, some studies have recently applied optimization-based methods so that they can predict/estimate joint torques with motion prediction/estimation.

A practical optimization-based method is the model predictive control (MPC). MPC uses an internal model to estimate/predict the output, compare it with the reference data, and finally predict control inputs of the plant model by minimizing a cost function that can contain a data-tracking error (i.e., semi-predictive). Not only does MPC provide stability for the model but it also has predictive features. MPC is a fast near-optimal controller that seems very well-suited to real-time biomechatronic applications [106].

Sun et al. [170, 171] have simulated the human CNS using MPC in conjunction with PID. To validate their method, human gait has been modeled using the simulated CNS. The plant model is a 2D 9-DOF SK human model and the controller of the plant model is a combination of an MPC and PID. The methodology of the simulated CNS is as follows. First, either single support phase (SSP) or double support phase (DSP) is selected using the ground contact feedback of both feet. Next, joint torques, which are predicted using the MPC and PID, enter the plant model as inputs to predict motions. If SSP is selected, the PID and MPC are used to keep the HAT upward and reach a reference step length, respectively. If DSP is selected, the PID and MPC are used to keep the HAT upward and

reach a reference center of mass velocity at the end of DSP, respectively.

2.3 Musculoskeletal/Neuromusculoskeletal Models

MSK/NMSK modeling is used to study how neural commands are converted to mechanical motion by means of musculotendon units spanning joints [145]. Muscle-driven models are developed to study the role of muscles in human motions because muscles affect the energy flow between body segments. Muscle forces can be predicted using muscle-driven models. Prediction of muscle forces is advantageous since by having muscle forces during healthy and impaired movements, we can improve treatments for walking disorders as well as training programs for athlete performance. Recently, muscle-driven models have also been used to determine muscle synergies and coordination.

To evaluate the muscle forces in an MSK/NMSK model, the muscle force-sharing problem should be solved. This muscle redundancy problem requires an optimization routine with a dynamic formulation. Since the muscle redundancy problem is solved using optimization-based methods, all the dynamic analysis approaches for the MSK/NMSK models are optimization-based methods (i.e., semi-predictive optimization methods or fully-predictive methods).

In this section, the muscle redundancy problem and the routines to solve it are presented. Then, problem formulations for MSK/NMSK models are presented by dividing them into explicit dynamic formulation (Forward Approaches, Inverse Approaches, and Mixed Approaches sections) and implicit dynamic formulation (Implicit Approaches section). Different simulation solvers corresponding to each formulation are discussed within each section.

2.3.1 Muscle Redundancy Problem

In the human body, since the number of muscles is more than the number of actuating joints (i.e., there are many different muscle coordinations to generate a specific human movement), a muscle redundancy problem should be solved for motion analysis. To solve the muscle redundancy problem, it seems a logical interpretation to assume that the CNS adjusts muscle forces in an optimized manner [4, 29]. Zajac et al. [193, 194] have presented a thorough review of concepts and routines, proposed up to 2003, to address this challenge. In general, different variations of two optimization routines are used to calculate muscle forces during human tasks: static optimization and dynamic optimization.

Static Optimization

Static optimization (SO) is an inverse approach (e.g., experimental motion and externally applied forces are considered as the inputs to the MSK model). In SO, muscle forces are optimized and the cost function is calculated using time-marching; in other words, time frames are solved sequentially. On the other hand, some researchers have used the concept of static optimization in combination with either a forward approach [161] or a mixed approach [145, 189]. In these approaches, the inputs are neural controls (i.e., muscle activations or excitations), which are taken as optimization variables to estimate muscle forces through static optimization. In the meantime, the outputs (i.e., torques or kinematics of the model) are calculated through the mixed or forward approaches and compared with the experimental data to adjust the cost function for the static optimization.

In static optimization routine, different expressions can be used as the cost functions which can be found in [28, 177]. Static optimization solves a different optimization at each time instance and then considers coupling between time instances to simulate dynamic equations. The instantaneous cost function results in low computation time and makes SO suitable for real-time simulations. Although SO is appropriate for semi-predictive optimization-based methods, it is not suitable for minimizing a cost function during a whole task (e.g., metabolic energy) because it may lead to sharp fluctuations in control inputs. In addition, since SO does not account for contraction and activation dynamics, it may cause unphysiological results.

Dynamic Optimization

Dynamic optimization (DO) solves a two-point boundary-value problem in the optimal control of the MSK/NMSK models [31]. To solve this problem, there are some studies that have used parameterized optimization to solve the optimal control problem, and they have reported satisfactory results [30, 50, 126, 151].

DO is suitable for the motions affected by the dominant muscle activation dynamics and co-contraction [117]. Since DO, unlike SO, uses the time history of the simulation along with the muscle contraction and activation dynamics, unphysiological results are not obtained, and it is possible to define time-integral cost functions. However, it has high computation time compared to SO.

Other than DO and SO, different variations of them can be utilized to model muscle dynamics by minimizing a cost function that includes a data-tracking term, and muscle activation and contraction dynamics. These variations are discussed in the following paragraphs.

Different Variations of Static Optimization

Modified static optimization (MSO) was proposed to overcome the deficiencies of SO [3, 184]. MSO is similar to SO, with the difference in having modified cost functions and nonlinear constraints, which are related to the contraction and activation dynamics. Wen et al. [184] proposed a novel cost function combining the kinematic and EMG data to estimate the muscle forces that are more coherent with EMG data than the muscle forces estimated by SO.

Another variation of SO has been proposed by Thelen and Anderson [174] to predict muscle activations. This optimization routine is a variant of CTC on the muscle level (not on the joint level), which is why it is called computed muscle control (CMC). CMC is a feedback-control approach and it is a combination of a PID controller, SO and forward dynamics models. It improves the results of the SO model, by simulating the forward dynamics model and feeding back the error to the SO model using the PID controller. CMC is able to track experimental motion data by feeding predicted muscle forces as the inputs to the forward dynamics model of studied movements (e.g., walking [91] and running [64]). Although CMC is more accurate than SO, it has the following drawbacks. First, since foot-ground contact forces are directly applied in CMC, inconsistencies may appear between estimated motion and experimental motion data. Second, because of explicit integration techniques, CMC may have a poor convergence.

For data-tracking using forward simulations, CMC is accurate enough. However, Shourijeh et al. [161] have proposed a type of static optimization that is less complicated and as accurate as CMC, and it is more appropriate for the implementation of the forward approaches. They have solved the muscle redundancy problem using forward static optimization (FSO) and compared it with CMC in terms of computation time and prediction accuracy. The muscle activations have been predicted and motion has been estimated by tracking the movement of an arm model to validate the proposed optimization routine. FSO is similar to MSO, where instead of inverse dynamics, the forward dynamics problem is solved with activations or excitations as inputs. Looking closely, FSO is a special case of nonlinear MPC (NMPC), which optimizes the current time step while considering a single future time step. Another variation of FSO has been utilized in [23, 182]; these studies use different numerical algorithms for the implicit solution of the dynamic equation.

Different Variations of Dynamic Optimization

Typically, in DO, neural excitations are optimization variables that drive the NMSK model through the forward dynamics [117]; this optimization routine is also called forward dy-

dynamic optimization (FDO). FSO is like an FDO in which the objective function is optimized at each time step while satisfying kinematic constraint equations of the forward dynamics integration [161]. Anderson and Pandy [8] have utilized FDO to determine the muscle coordination in human gait. They have reported a CPU time of 10,000 hours to solve the optimization for half a walking cycle. FDO is considerably time-consuming since many numerical integrations are required to be computed for motion dynamics equations.

In another study [9], Anderson and Pandy have also claimed that it is not necessary to model muscle activation and contraction dynamics for walking analysis because they have little effect on the computed muscle forces. By disregarding muscle activation and contraction dynamics in the optimization problem, the consistency with muscle physiology was reduced but the numerical calculation became faster [28]. Although FDO without muscle dynamics is faster, to better assess individual muscle function, muscle activation and contraction dynamic models are essential.

Sometimes in DO, muscle forces can also be the optimization variables to produce desired joint torques obtained from the inverse dynamics problem of an MSK model [107], so-called inverse dynamic optimization (IDO). Some researchers use the concept of dynamic optimization, in a forward/inverse approach and consider different inputs as optimization variables to solve the time-integral cost function [152].

To increase the computation speed, IDO with the inverse dynamics approach is used instead of FDO. In IDO, muscle dynamics can be considered as differential constraints [107]; satisfying muscle dynamics as constraints is faster than directly solving the muscle dynamics. To further increase the computation speed, the muscle constraints can also be neglected in IDO. However, the prediction accuracy may decrease and unphysiological results may be obtained.

To increase the prediction accuracy of IDO (when muscle constraints are not included), IDO can be combined with a forward approach that includes the muscle contraction/activation dynamics (i.e., paths from 0 to 1/2 in Figure 2.1) [122]. This optimization routine, which is called inverse-forward dynamic optimization (IFDO), can also be combined with the forward dynamic model of the MSK model to generate a correction control input to the optimization problem (i.e., feedback-control approach); this gives the so-called inverse-forward dynamic optimization control (IFDOC) [122].

Ackermann [3] has used another variation of IDO, so-called extended inverse dynamics (EID), to solve the muscle redundancy problem by inverse dynamics equations. In EID, the inputs to the optimizer are the muscle forces along the corresponding tendons (path from 6 to 2 in Figure 2.1). Once the optimization problem was solved, the activations and neural excitations are evaluated by inverting contraction (i.e., following the path from

2 to 1 in Figure 2.1) and activation dynamics (i.e., following the path from 1 to 0 in Figure 2.1), respectively. EID is analogous to MSO, but in MSO the optimal problem is solved instantaneously and the results of a time step are only dependent on the results of the previous time step. The computational load of EID is also less than FDO, and in contrast to SO, it considers contraction and activation dynamics together with a time-integral cost function [4]. However, the feasibility of EID is restricted by the size of the optimization problem.

To overcome some limitations of EID, Quental et al. [132] have proposed window moving inverse dynamics optimization (WMIDO). In WMIDO, a window is considered to be moving across a number of instants of time until the muscle redundancy problem is solved. Using this routine, the researchers are able to fully simulate the muscle dynamics.

Another type of dynamic optimization is the neuromusculoskeletal tracking (NMST) which has been developed by Seth and Pandy [152] to predict muscle forces by minimizing the torque-tracking error and muscular effort. NMST has two stages; in stage 1, the inverse SK model (path from 6 to 3) with sliding-mode tracking is used to predict joint torques. In stage 2, the forward neuromuscular dynamics (path from 0 to 2) is used to obtain optimal muscle forces such that the muscular model (path from 2 to 3) gives a torque close to the predicted torque in stage 1.

In addition to the unknown muscle force prediction, if some model parameters should be identified in an IDO problem, single inverse dynamic optimization cannot solve the problem. Rasmussen et al. [136] have proposed an optimization routine called inverse-inverse dynamic optimization (IIDO) that solves this issue by introducing an outer inverse dynamic parameter identification [30]. In this routine, both the inputs and outputs of the inverse dynamics are optimized through an outer optimization loop around the inverse dynamics in order to identify model parameters by maximizing the metabolic efficiency of the human task.

Other Routines

There are some other routines for solving muscle redundancy problem. But, since they cannot be easily classified according to SO or DO, they are discussed in this section.

In another approach, an analytical optimization technique has been used by Challis and Kerwin [24] to predict muscle forces. However, the evaluated forces are not bounded. Hence, this optimization routine may result in negative values for muscle forces, which is unphysiological. Terrier et al. [172] have used the pseudo-inverse to evaluate the inverse of the muscle moment arm matrix, then the muscle force constraints were imposed with

the aid of the null space definition in quadratic programming. This optimization routine required some simplifications such as considering muscles as string elements. There are also other studies that have used specific tools such as stochastic modeling and muscle fatigue criterion to deal with muscle force sharing problem [99, 153].

Researchers have also used a neural strategy, so-called muscle synergy, for simplifying the control of multiple degrees of freedom. Muscle synergy theory (MST) deals with the muscle force sharing problem with a biologically-plausible aspect [176]. Based on MST, during a task, muscles are activated in a group called synergies. Thus, instead of having multiple muscular actuators, each joint will move by a small number of actuators (synergies). Although MST is computationally-efficient [139], mostly it has been used in the inverse dynamics analysis [157, 165, 168, 195]. Yoshikawa et al. [192] have used equilibrium-point-based synergies to translate human movement to a robot. Sharif Razavian et al. [154] have considered muscle synergies based on the task space in the forward dynamic simulations.

Recent studies in the human movement analysis have focused on the optimization-based predictive methods for obtaining novel movements [32, 110, 130]. However, in most of the aforementioned routines, experimental motion data is explicitly tracked; thus, novel movements cannot be predicted. To solve the muscle redundancy problem for novel movements, the optimization problem should be stated in terms of an optimal control problem. In the next section, we will discuss different optimal control methods and the possibility of their use for solving this problem.

2.3.2 Optimal Control Methods

Optimal control methods are divided into two categories: indirect and direct methods (see Figure 2.4) [135]. Indirect methods use the calculus of variations to obtain analytical expressions of optimal control that are adjoint differential equations. Thus, boundary-value problems should be solved to obtain the optimal solution. However, finding an initial guess for adjoint variables is challenging since most of the variables are not physically meaningful. Furthermore, adjoint differential equations are highly nonlinear; hence, backward integration of those differential equations can be numerically unstable.

In direct methods, it is not required to solve boundary-value problems. Instead, the control and/or state are parameterized and the optimal control problem is solved as a nonlinear programming problem (NLP). Systems with large-scale NLP (e.g., optimal control of human movement) can be solved using different software packages such as interior point

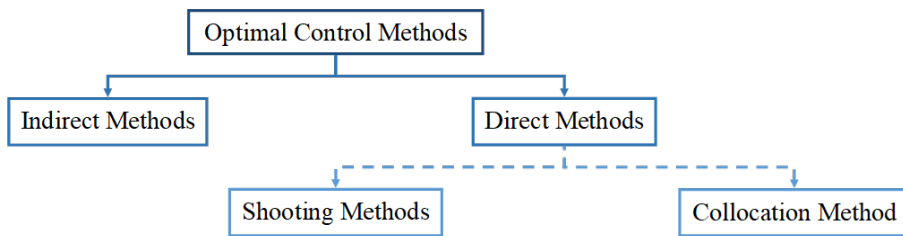


Figure 2.4: Different methods in optimal control theory

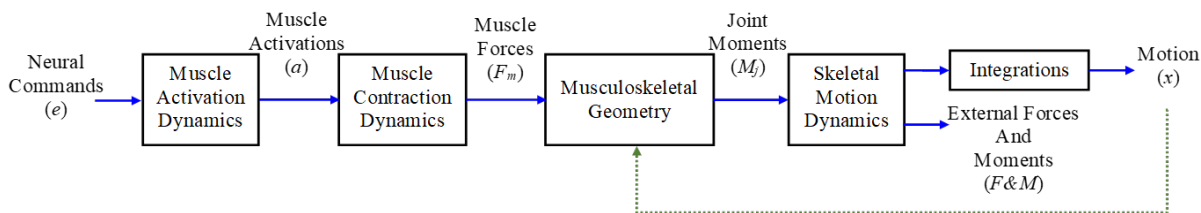


Figure 2.5: The workflow of the forward approaches for MSK/NMSK models

optimizer (IPOPT) and sparse nonlinear optimizer (SNOPT). Direct methods are divided into two methodologies: direct shooting [116] and direct collocation [182].

In the direct shooting method, only the control inputs are parameterized and its computation time is much more than the direct collocation method in which both control inputs and states are parameterized. The direct shooting method computes numerical integration of dynamic differential equations during the optimization process, while the direct collocation method considers the dynamic equations as algebraic constraints, thereby not needing to compute explicit integration. However, convergence in direct collocation method heavily relies on a good initial guess, which can be challenging to define.

2.3.3 Forward Approaches

In forward approaches, all dynamic equations are solved by forward integration and the muscle redundancy problem is addressed using one of the optimization routines with the forward approach discussed in Section 2.3.1. Figure 2.5 illustrates the order of the different stages to generate forward approaches for MSK/NMSK models.

Any simulation solver that uses SO [9, 117], FDO [30, 50, 117, 126, 151], or FSO [23, 156, 182] to solve the muscle redundancy problem in an MSK/NMSK model is an optimization-based predictive method for a forward approach.

Since experimental data are not always available, and also data-tracking or semi-data-tracking optimization-based methods are not good for the prediction of novel motions, some researchers have focused on the forward approaches without data-tracking [115, 130] using either the simulated annealing algorithm or direct shooting method.

Using the simulated annealing algorithm, Miller [115] has developed a 3D NMSK model to fully predict human gait by minimizing metabolic energy expenditure without data-tracking. To determine metabolic energy expenditure, he has considered five methods that differ in their treatment of muscle activity, muscle lengthening, and eccentric work. Then, he has compared the methods in terms of their predictive abilities. In this research, muscle activation and contraction dynamics have been developed based on the Hill-type muscle models. All five models have predicted similar speeds, step lengths, and stance phase duration.

Porsa et al. [130] have compared two direct optimal control methods (i.e., direct shooting and collocation methods) in terms of computation time. Note that direct collocation method is an implicit approach and its corresponding methods are discussed in Section 2.3.6. These two control methods have been implemented on a planar MSK model to predict joint motions and muscle activations for the highest vertical jump without tracking experimental data. The foot-ground contact has been modeled using eight contact spheres per foot. The results showed that both methods converged to the same solution when their initial guesses are the same, but direct collocation converged up to 249 times faster than direct shooting.

2.3.4 Inverse Approaches

In inverse approaches, as shown in Figure 2.6, all dynamic equations are solved inversely to avoid forward integration problems. For inverse approaches, semi-predictive optimization-based [32] or fully-predictive [148] methods can be used to solve the simulation problem. The methods using IDO [107], EID and MSO [3] to solve muscle redundancy problem are types of optimization-based predictive methods for inverse approaches.

Schiehlen [148] has introduced an optimization-based method to simultaneously predict muscle forces and body motion. In this method, generalized coordinates have been considered as parameterized functions (spline polynomials) [3]. Furthermore, since muscle activations and excitations were required for defining an energy cost function and optimization constraints, those have been obtained by feeding muscle forces in inverse muscle contraction and activation dynamics. Finally, muscle forces and motion polynomials for an

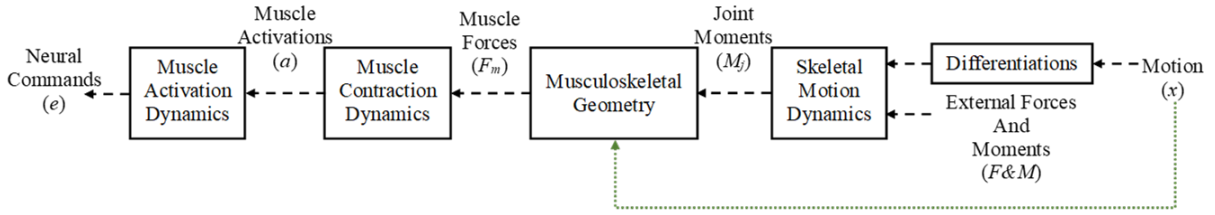


Figure 2.6: The workflow of the inverse approaches for MSK/NMSK models

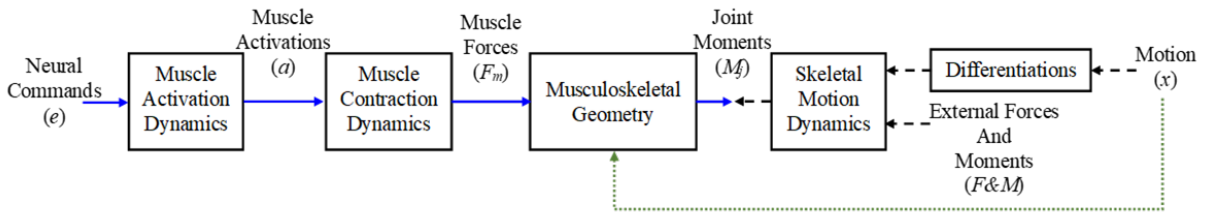


Figure 2.7: The workflow of the inverse skeletal-forward neuromuscular approaches

unsymmetrical walking have been evaluated by minimizing the energy cost and deviation from normal walking.

2.3.5 Mixed Approaches

Inverse Skeletal-Forward Neuromuscular Approaches

For human gait analysis, inverse skeletal-forward muscular models, unlike the forward simulations, do not require two complex and time-consuming elements: the balance controller [129] and foot-ground contact model [159]. As illustrated in Figure 2.7, in such approaches, muscle activation dynamics, muscle contraction dynamics, and musculoskeletal geometry are generated forwardly and only SK motion dynamics is solved inversely. Then, the joint moments, obtained from the forward and inverse parts, are compared or the predicted results may be updated by a feedback controller (i.e., feedback-control approach). For example, NMST uses the feedback-control approach with inverse skeletal and forward neuromuscular models. Semi-predictive optimization-based methods for these approaches are generally used to evaluate joint moments [133] and predict muscle activations [189].

Rajagopal et al. [133] have created an open-source high-fidelity 3D MSK model for human lower extremity to study human gait. The model includes an SK upper body and

an MSK lower body. The musculotendon parameters are obtained from both cadavers and young healthy subjects. First, they have solved forward muscle activation and contraction dynamics to predict muscle activations and joint moments using CMC through tracking experimental motion data. To verify their model, they have compared the predicted muscle activations and joint torques with EMG data and inversely obtained joint torques, respectively. They could generate muscle-driven simulations in less than 10 minutes; hence, their model is computationally fast. The model and experimental data are available on https://simtk.org/projects/full_body/.

Yamasaki et al. [189] have proposed a general semi-predictive optimization-based method for predicting muscle activations with a low computational cost. Their method has been validated for a single-joint NMSK model. First, a forward neuromuscular model and an inverse skeletal model have been developed for a general model with N joints and M musculotendon units. Then, the muscle redundancy problem has been solved using static optimization and compared with experimental joint torques in order to predict muscle activations. The main difference between the proposed method and similar methods is the use of static optimization as a feedback controller (i.e., optimization-based method for feedback-control approach). Furthermore, in addition to the motion data, first to fourth derivatives of the motion data have been applied as the input to the model and they have been used in defining constraints for the static optimization.

Since EMG-driven models are used in inverse skeletal-forward neuromuscular simulations, their results are highly dependent on EMG data. The shortcoming of such simulations is that the EMG data may be adversely affected by cross-talk [47], movement artifacts [33] and preprocessing such as choice of filter type and cut-off frequencies [186]. Furthermore, activities of the deeply located muscles cannot be recorded by surface EMGs. Thus, researchers decided to predict muscle excitations in addition to joint moments to overcome the shortcomings of measured EMG data [146, 160].

Sartori et al. [146] have presented a 3D NMSK model to predict muscle excitations and joint torques using motion data from five healthy subjects during walking and running. Their model could also predict the excitations of some deeply-located muscles, which were missed during EMG data recording by surface EMGs. First, using experimental EMG data and motion data, they have forwardly solved muscle activation dynamics, muscle contraction dynamics and musculoskeletal geometry to determine joint torques. Then, they have compared obtained joint torques with experimental joint torques, determined by inversely solving motion dynamics given the experimental motion data, to obtain joint torque errors. Finally, static optimization has been utilized to predict muscle excitations by tracking experimental joint torques and EMG signals. This is done by minimizing the sum of squared joint torque and EMG errors.

Shourijeh et al. [160] have developed a forward neuromuscular model and inverse skeletal model to predict muscle excitations, muscle forces and joint moments by tracking the joint moments inversely obtained from experimental motion data. They used a genetic algorithm (GA), sequential quadratic programming (SQP) and nonlinear simplex optimizer in the aforementioned sequence to achieve convergence for their optimization problem. The predicted muscle excitations were in a good correlation with the experimental EMG data for human gait.

In another study, Meyer et al. [110] have predicted joint torques using patient-specific musculoskeletal geometry. To reduce the errors stemming from scaled geometry, this study presents a method to automatically adjust the EMG-driven NMSK model based on the patient's musculoskeletal geometry including muscle-tendon lengths, velocities and moment arms. The model parameters are calibrated by comparing the calculated joint moments with the obtained joint moments from the inverse motion dynamics. The results have shown that with geometric adjustment, the predicted joint moments are more accurate than the models without those adjustments. All the data and model of this study are available on <https://simtk.org/projects/emgdrivenmodel>.

Unlike most EMG-driven NMSK models, which predict the joint moments using scaled generic musculoskeletal geometry, subject-specific models can predict joint torques using subject-specific musculoskeletal geometry. In each subject, the neural excitation patterns can be obtained by EMG data. Thus, NMSK models can be developed as subject-specific models. Such models can be used to assist patients with neurological disorders since EMG signals can identify the error in neurological control [63].

Ma et al. [96] have modified the calculation efficiency and prediction accuracy of the current EMG-driven models. They have developed a patient-specific EMG-driven NMSK model including four parts: (1) MSK model that is developed based on patient's motion and external load data to evaluate muscle kinematics (i.e., moment arms and musculotendon lengths). (2) EMG-driven model in which forward dynamics of muscle activation and contraction are solved using the muscle geometry obtained from (1) and raw EMG data to predict joint moments. (3) Inverse motion dynamics that has been applied to determine reference joint moments from patient's motion data. (4) Parameter optimization in which parameters of muscle activation and contraction dynamics are optimized through joint moment error tracking. This method can accurately predict joint moments in real-time simulations.

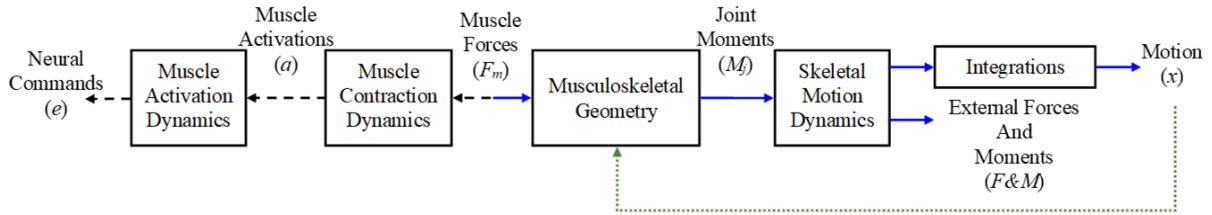


Figure 2.8: The workflow of the forward skeletal-inverse neuromuscular approaches

Forward Skeletal-Inverse Neuromuscular Approaches

Unlike inverse approaches, in the forward skeletal-inverse neuromuscular approach, instead of motion inputs, muscle forces are parameterized [156] as shown in Figure 2.8. Shourijeh and McPhee [156] have developed a 2D NMSK model considering a volumetric foot-ground contact. They have parameterized muscle forces using Fourier series. Human motion and muscle activations have been predicted using global parameterization within an optimal control problem. The predicted results were quite in a good agreement with the experimental data. The method of this paper is somehow similar to the method presented in [148], while in this paper muscle forces are parameterized and motion dynamics are solved forwardly.

Feedback-control Approaches

Any simulation solver that uses CMC [174] or IFDOC [122] to solve the muscle redundancy problem in an MSK/NMSK model is a type of optimization-based method for feedback-control approach.

Ehsani et al. [35] have developed a general MSK model to predict muscle activations and muscle force patterns for an arbitrary human task. To this end, first, motion dynamics of the skeletal model have been developed and then musculoskeletal geometry and muscle contraction dynamics have been added to the skeletal model. Finally, CMC has been exploited to predict muscle activations to drive the MSK model by tracking experimental motion data. To validate the proposed model, a biceps curl has been simulated using this algorithm. The predicted muscle activations were quite close to EMG data captured for a biceps curl.

2.3.6 Implicit Approaches

By parameterizing the control inputs and states, direct collocation methods convert the system dynamics to an algebraic equation. Thus, since these methods do not explicitly use the forward/inverse dynamics approaches, they are types of implicit approaches. As it was discussed in the forward approaches, experimental data are not always available; thus, some biomechanics researchers have focused on the mixed approaches without data-tracking [83, 87, 90, 109, 130] using direct collocation methods to predict novel movements.

Lee and Umberger [83] have created a framework to predict motion and muscle activations for MSK models using the direct collocation method. Motion and muscle activations (which have been considered as states and control inputs of the optimization problem, respectively) have been predicted simultaneously during the optimization process. Muscle activation and motion dynamics have been extracted using the biomechanical modeling software: OpenSim. The authors have used the IPOPT solver in MATLAB to apply direct collocation method for their optimization. Their model and method are available on <http://simtk.org/home/directcolloc>.

Lin and Pandy [87] improved the capabilities of CMC by using the combination of CMC and direct collocation. They have proposed a semi-predictive optimization-based method to predict muscle excitations of walking and running tasks using both CMC and direct collocation methods. CMC has been exploited to determine a feasible initial guess for the state and control variables of direct collocation. Their method consists of three steps; in the first step, CMC used the measured motion and contact forces to calculate muscle excitations (control variables) and reproduce the motion (state variables). In the second step, the calculated state and control variables from the previous step were discretized and a foot-ground contact model, simulated using six contact spheres under each foot, was used to generate an initial guess for the next step by minimizing the defect errors to satisfy the defect constraints. Defect constraints associated with the generalized speeds were generally larger than those corresponding to the other state variables due to inconsistencies between kinematics and ground reaction forces. In the last step, a direct collocation method was used to estimate the motion and predict muscle excitations by minimizing a multi-objective cost function including a data-tracking term and a physiological term.

Recently, Lin et al. [90] have exploited the direct collocation method to propose a fully-predictive method for the prediction of motion, muscle excitations, foot-ground contact forces and also joint contact forces. They have developed an NMSK model to study human gait at different speeds, including a 3D model of articular contact for the knee joint and a foot-ground contact model. First, a data-tracking collocation optimization has been solved to estimate a feasible initial guess. Then, independent of experimental data, a predictive

collocation optimization has been developed to predict novel patterns for human gait.

Meyer et al. [109] have also developed a patient-specific EMG-driven NMSK model that is synergy-controlled and able to predict walking motions for post-stroke individuals. In this method, muscle synergy is used to solve muscle redundancy problem. In this study, the developed method has been compared with muscle activation-controlled and torque-controlled methods in terms of the accuracy of walking motion prediction using the direct collocation method. Since direct collocation method is sensitive to the initial guess, this study has presented a practical procedure to estimate a meaningful initial guess and predict the motion. First, a “calibration optimization” was applied to determine contact parameters by tracking walking at 0.5 m/s. Then, the “tracking optimization” was used to determine the initial guess for the walking speed of 0.5 m/s by tracking walking at the same speed. Finally, the “prediction optimization” was applied for different walking speeds. The accuracy of the method is checked by applying the prediction optimization for the 0.5 m/s walking. Motion prediction is done for the 0.8 m/s speed by tracking walking at 0.5 m/s, and a challenge-based study is done for the speed of 1.1 m/s. All three control methods (i.e., synergy-controlled, muscle activation-controlled and torque-controlled methods) predict the motion well for 0.5 m/s walking by tracking the same speed. Only the synergy-controlled and muscle activation-controlled methods could predict 0.8 m/s (fast) walking by tracking 0.5 m/s (slow) walking. Only the synergy-controlled model has predicted 1.1 m/s (very fast) walking without any data-tracking.

Sometimes experimental data is also used in the direct collocation methods. De Groot et al. [32] have used the direct collocation method to solve the muscle redundancy problem and predict muscle activations given experimental motion data. First, the experimental motion data has been applied to an MSK model in OpenSim to inversely generate joint moments. Muscle geometry has been also obtained from the MSK model in OpenSim. Then, the joint moments and muscle geometry have been used in the optimization process to solve muscle contraction dynamics for predicting muscle activations. Their method has been implemented on both 2D and 3D MSK models. In this research, two different formulations have been considered for muscle contraction dynamics. In the first formulation, tendon force has been considered as a state to describe contraction dynamics as algebraic constraints. In the second formulation, muscle length has been assumed as a state. The results proved that the first formulation, in contrast to the second one, could converge to an optimal solution in all cases for all initial guesses.

2.4 Summary

The main goal of this chapter was to highlight the features of the recent analysis methods of human motion (mainly for gait) and to draw a detailed comparison between these methods in terms of problem formulation and simulation solver. To this end, the recently-developed problem formulations and simulation solvers were classified and separately discussed for SK, MSK, and NMSK models to assist researchers to select an appropriate analysis method depending on their research purpose.

Dynamic formulation approaches are either explicit or implicit. Explicit approaches were divided into forward, inverse and mixed approaches. A mixed approach may exploit the best features of forward and inverse dynamic approaches. In the explicit dynamic formulation, the system dynamics are directly integrated or differentiated while in the implicit dynamic formulation, the system dynamics are considered as constraint equations that are implicitly satisfied inside an optimization-based simulation.

Once a dynamic formulation is selected for a human model, a solver is required to simulate the model for a specific task. Simulation solvers are either non-optimization- or optimization-based. They are categorized according to data-tracking, semi-data-tracking, semi-predictive, and fully-predictive methods, depending on whether a data-tracking term exists in the solver or not. Data-tracking methods are pervasive because of their intrinsic realism. However, they require a comprehensive database of human motion and we cannot study the effects of changes in the task condition since the motion data are previously prescribed for the model. In contrast, predictive methods do not require a motion database so they can be used to study how the changes in task conditions affect the results. The prediction may be more accurate if semi-predictive are exploited.

A brief overview of the most significant methods (since 2014) for human task analysis has been categorized according to SK, MSK, and NMSK models in Tables 2.1, 2.2, and 2.3, respectively. The tables include the problem formulations and simulation solvers recently exploited for human task analysis and since the main focus of this thesis is on gait task, the aim was to primarily cover the references on gait analysis in these tables. A few non-gait applications are included because of the significance of the analysis methods.

Among the problem formulation approaches classified in this chapter, mixed and implicit approaches have been the most popular in the recent literature on predicting human gait. Since SK models are simpler than MSK/NMSK models, they enable researchers to focus on more complex control methods by disregarding muscle dynamics. However, for most biomechanics applications, muscle dynamics should be considered to predict more realistic motions and joint contact forces.

Table 2.1: Recent methods to analyze SK models

Ref.	DOF	Application	Problem Formulation	Simulation Solver
[100]	Lower extremities: 9-DOF model and 7-DOF model (without ankles)	Joint torque prediction and motion estimation over the full range of gait speeds	Feedback-control mixed approach	HZD
[118]	Full-body: 14 DOF	Joint torque prediction and motion estimation for human gait	Feedback-control mixed approach	CTC
[125]	Full-body: 14 DOF	Comparison between PD and CTC in motion estimation for walking	Feedback-control mixed approach	PD, CTC
[127]	Lower extremity: 13 DOF	Clutch pedal depression motion and joint torques prediction	Forward approach	Hybrid predictive method
[27]	Full-body: 55 DOF	Joint torque and motion prediction for running and a slow jog along curved paths	Forward approach	Sequential quadratic programming (SQP)
[170, 171]	Lower extremities: 9 DOF	Joint torque prediction and motion estimation for human gait (to design prosthesis and orthosis before manufacturing)	Feedback-control mixed approach	A combination of MPC and PID
[13]	Full-body: 55 DOF	Joint torque prediction and motion estimation for walking and jumping on a box	Machine learning, training: inverse approach	General regression neural network

Table 2.2: Recent methods to analyze MSK models

Ref.	DOF	Application	Problem Formulation	Simulation Solver
[161]	An arm:1 DOF with 7 muscles and 2 DOF with 6 muscles	Muscle activation prediction and motion estimation for an arm movement	Forward approach	FSO
[130]	Lower extremities: 10 DOF, 48 muscles	Motion prediction/estimation and muscle activation prediction for vertical jump	Forward approach and implicit approach	Direct shooting and collocation methods
[133]	Full-body: 37 DOF, 80 muscles	Muscle forces and joint moments prediction for walking and running	Feedback-control mixed approach	CMC
[35]	General model	Muscle activation/force prediction and motion estimation (tested for biceps curl)	Feedback-control mixed approach	CMC
[83]	1 DOF with 2 muscles	Motion and muscle activation prediction; scaled it for a 2D lower extremity model	Fully-predictive implicit mixed approach	Direct collocation method

Table 2.3: Recent methods to analyze NMSK models

Ref.	DOF	Application	Problem Formulation	Simulation Solver
[115]	Lower extremities: 23 DOF with 40 muscles	Fully-predictive human gait motion by minimizing metabolic energy	Forward approach	Simulated annealing algorithm
[148]	Lower extremities: 16 DOF with 28 muscles	Muscle force prediction and motion estimation for an unsymmetrical walking	Inverse approach	Parameter optimization
[146]	Full-body: 19 DOF with 34 muscles	Muscle excitation and joint moment predictions for human walking and running	Inverse skeletal-forward neuromuscular mixed approach	Static optimization
[160]	Lower extremities: 16 DOF with 46 muscles	Muscle excitation/force and joint moment predictions for human gait	Inverse skeletal-forward neuromuscular mixed approach	Genetic algorithm (GA), SQP, Nonlinear simplex optimizer
[189]	Single joint with a pair of antagonistic muscles	Muscle activation prediction (which is applicable to any NMSK model)	Inverse skeletal-forward neuromuscular mixed approach	Static optimization
[96]	Knee joint with 8 muscles	Joint moment prediction in real time for gait rehabilitation	Inverse skeletal-forward neuromuscular mixed approach	Simulated annealing algorithm
[110]	Lower extremities: 29 DOF with 35 muscles	Patient-specific joint moment prediction for gait rehabilitation	Inverse skeletal-forward neuromuscular mixed approach	SQP
[156]	Lower extremities: 11 DOF, 16 muscles	Muscle activation prediction and motion estimation for human gait	Forward skeletal-inverse neuromuscular mixed approach	Global parameterization
[87]	Full-body: 21 DOF with 66 muscles	Muscle excitation and motion prediction for walking and running	Implicit approach	CMC, Direct collocation method
[90]	Full-body: 25 DOF with 80 muscles	Motion, muscle excitation, foot-ground contact force, and joint contact force prediction for human gait at different speeds	Implicit approach	Direct collocation method
[109]	Full-body: 31 DOF with 70 muscles	Prescribing walking motion for an individual post-stroke using motion prediction in rehabilitation	Implicit approach	Direct collocation method
[32]	Lower extremities: a 9-DOF 2D model with 18 muscles and a 16-DOF 3D model with 86 muscles	Muscle activation prediction for human gait	Implicit approach	Direct collocation method

Regarding the recent literature on MSK/NMSK models, there are very few research studies on fully-predictive simulations of novel gait motions independent of motion data-tracking [90, 109], and there is still a need to decrease the computation time of the fully predictive simulations and increase the accuracy of the predicted results. Promising future avenues to increase the speed of predictive gait simulations include the use of symbolic programming (to generate optimized simulation code and exact derivatives) and the use of fast near-optimal model-predictive controllers.

Recent fully-predictive studies are limited by numerical programming, which requires a finite difference method to evaluate the gradients and Hessians in the optimization problem. However, finite differencing is an error-prone methodology and may result in unreliable results for higher-order derivatives. Studies such as [57, 72, 105, 123] have shown that symbolic dynamic equations can resolve this issue. Furthermore, the use of symbolic equations can enhance the accuracy and speed of optimal control methods [14].

To model the foot-ground contact in these fully-predictive simulations, a finite number of contact points, moving relative to the foot, has been used. Hence, these foot-ground contact models can be assumed as multiple point contact models, in which the normal contact force is evaluated by the depth of penetration using the Hunt-Crossley method [67]. However, since the Hunt-Crossley method is restricted to the contact points (not the contact surfaces), an unnatural foot shape is obtained. In a recent study, Brown and McPhee [21] have developed an ellipsoidal foot-ground contact model that may have better accuracy and higher calculation speed than its comparable foot-ground contact models.

To the best of the author’s knowledge, the metatarsal joints have not been included or their angles and torques have not been reported in the recent predictive simulations even though metatarsal joints have an important role in gait analyses [40]. Thus, the accuracy of predictive gait simulations may be improved by including toe joints, and by replacing multiple point contact foot ground models with volumetric or other distributed methodologies that better capture the foot geometry.

In conclusion, to develop a computationally-efficient and accurate predictive simulation of gait, we believe that symbolic programming, a fast optimal control method, an accurate volumetric foot-ground contact model, and two-segment foot model are required. Although the aim of this thesis is to develop a predictive gait simulation including all of these requirements, first, a simpler task (vertical jump) is studied in the next chapter to investigate the importance of these requirements.

Chapter 3

Human Vertical Jump Simulation

To develop a high-fidelity human gait model, it is necessary to have an accurate foot-ground contact and include all the body segments that play an important role in lower-extremity tasks. Thus, in this chapter, a simpler task (i.e., human vertical jump) was developed to investigate: (1) What type of foot-ground contact model can properly model GRFs. (2) Whether the toe segments (metatarsal joints) play an important role in lower-extremity tasks.

To investigate the importance of the toe segments in lower-extremity tasks, two human models (i.e., one with the toe segments and the other one without the toe segments) were developed to simulate vertical jump and then the simulated results were compared.

To select a proper foot-ground contact model, two different foot-ground contact models were developed for the vertical jump: 2D kinematically-constrained contact model and 3D ellipsoidal volumetric contact model. In the 2D kinematically-constrained contact, the foot is constrained to be fixed to the ground when the foot is in contact with the ground. In the 3D ellipsoidal volumetric contact, the foot is modeled by three ellipsoids and the foot can freely move with respect to the ground even during contact. The simulated results of the contact models were compared for the vertical jump.

In the following chapter, first the model properties and the skeletal motion dynamics are presented. Then the optimization method is fully described, and finally, the results are illustrated and discussed.

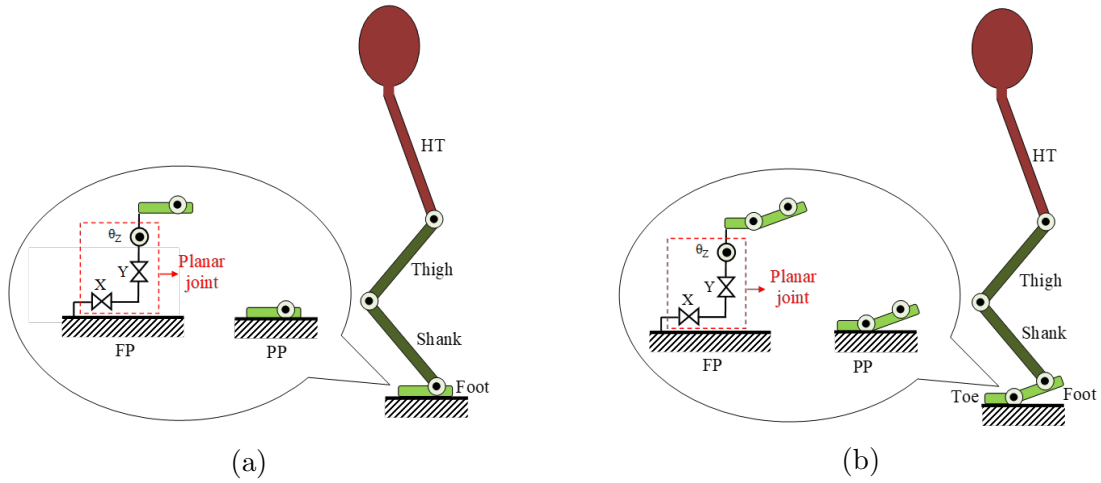


Figure 3.1: Model structure: (a) Toeless (b) Toe-included

3.1 Kinematically-Constrained Contact

The human vertical jump model with kinematically-constrained contact model consists of two phases: the preflight phase (PP) and the flight phase (FP). In PP, the human model first crouches and then thrusts the upper extremities while the foot is constrained to be fixed to the ground. In FP, the human model leaves the ground.

3.1.1 Model Properties

To shed light on the important role of the toe segment in the tasks done by lower extremities, two skeletal models were developed in this section: toeless and toe-included models (Figure 3.1).

The toeless model is composed of four bodies, foot, shank, thigh and head-trunk (HT), and driven by three 1-DOF joints: ankle, knee, and hip. During the jump in the sagittal plane, the DOF of this model is three and six in preflight and flight phases, respectively. The toe-included model has an extra body, which is the toe body, and consequently an extra 1-DOF joint which is the metatarsal joint. The DOF of this model is four and seven in preflight and flight phases, respectively. Table 3.1 shows the anthropometric parameters of the model extracted from [186]. Since the motions of left and right lower extremities are exactly the same during the vertical jump, both toes, feet, shanks and thighs were

Table 3.1: Body segment properties

Body	Mass (kg)	Length (m)	Center of Mass	Moment of Inertia (kg.m ²)
Toe	0.59	0.080	0.040	1.867e-3
Foot	1.78	0.116	0.077	9.626e-3
Shank	7.63	0.503	0.285	1.760e-1
Thigh	16.40	0.440	0.250	3.313e-1
Head-Trunk	47.40	0.660	0.404	3.361

Table 3.2: The variables in the toeless model

Phase	n	\mathbf{q}	m	$\boldsymbol{\tau}$
PP	3	$\{\theta_{ankle}, \theta_{knee}, \theta_{hip}\}$	3	$\{\tau_{ankle}, \tau_{knee}, \tau_{hip}\}$
FP	6	$\{x, y, \theta_z, \theta_{ankle}, \theta_{knee}, \theta_{hip}\}$		

considered in modeling. In other words, the values of masses and moments of inertia indicated for toe, foot, shank and thigh in Table 3.1 have been already doubled.

3.1.2 Dynamic Modeling

The model was developed in MapleSim (2016.2 Maplesoft, Waterloo, ON, Canada) to extract SK motion dynamics using “Multibody Analysis” module. Since the DOF of PP is different from the DOF of FP, these phases were modeled separately for extracting their motion dynamics. “Multibody Analysis” determines the motion dynamics based on the general form of multibody dynamic equations for a time step:

$$M_{n \times n} \ddot{\mathbf{q}}_{n \times 1} = \mathbf{F}(\mathbf{q}_{n \times 1}, \dot{\mathbf{q}}_{n \times 1}, \boldsymbol{\tau}_{m \times 1})_{n \times 1} \quad (3.1)$$

where M is the generalized mass matrix, \mathbf{q} is the vector of the generalized coordinates and \mathbf{F} is a vector which groups the Coriolis, centrifugal, and gravitational effects. The vector $\boldsymbol{\tau}$ represents actuating joint torques. Also, n and m specify the numbers of the generalized coordinates and actuating joints, respectively. Table 3.2 and Table 3.3 show n , \mathbf{q} , m and $\boldsymbol{\tau}$ in toeless and toe-included models, respectively. There is also a damper across each joint. The damper can model viscous friction effects when the joint moves, thereby improving the results of numerical integration [81].

Using the multibody analysis module of MapleSim, matrix M and vector \mathbf{F} were obtained and therefore the second derivative of generalized coordinates were determined using:

Table 3.3: The variables in the toe-included model

Phase	n	\mathbf{q}	m	$\boldsymbol{\tau}$
PP	4	$\{\theta_{metatarsal}, \theta_{ankle}, \theta_{knee}, \theta_{hip}\}$	4	$\{\tau_{metatarsal}, \tau_{ankle}, \tau_{knee}, \tau_{hip}\}$
FP	7	$\{x, y, \theta_z, \theta_{metatarsal}, \theta_{ankle}, \theta_{knee}, \theta_{hip}\}$		

$$\ddot{\mathbf{q}}_{n \times 1} = M_{n \times n}^{-1} \mathbf{F}_{n \times 1} \quad (3.2)$$

where M^{-1} is the inverse of matrix M . The generalized coordinates were obtained by integrating $\ddot{\mathbf{q}}$ two times.

3.2 3D Ellipsoidal Volumetric Foot-Ground Contact

Since the 3D ellipsoidal volumetric contact model is more complex than the kinematically-constrained contact model, the human vertical jump model with this contact model was divided into three phases to more accurately simulate the motion. The phases are called the crouching phase (CP), the thrust phase (TP) and the flight phase (FP). The human model first crouches in CP and then thrusts the lower extremities in TP and finally leaves the ground and vertically jumps in FP. Unlike the kinematically-constrained contact model, the foot can freely move with respect to the ground during all three phases thanks to the compliant contact model, so the DOF of the model in all three phases is identical.

Since the ellipsoidal contact model has been developed based on the volumetric contact model which considers pressure across the whole contact surface, this contact can model conforming geometries e.g. foot-ground contact [16]. Besides, using volumetric contact, rolling resistance, tangential friction and spinning friction can be modeled by some equations in addition to the normal force. These equations result in a contact model which is more accurate than discrete elastic foundation models, and not significantly more complex than point contact models [20]. The practical types of contact models in biomechanics are fully explained in the next chapter in Section 4.1.2.

In this study, the most recent volumetric contact model [21], in which contact surface is modeled by ellipsoids, was used. Ellipsoids can approximate the complex geometry of foot more closely than spheres can. The contact equations for an ellipsoid contacting a plane were extracted from [20].

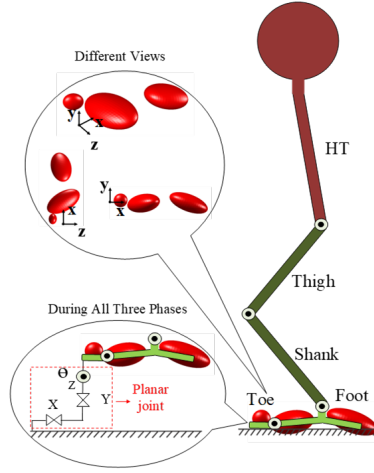


Figure 3.2: Model structure with the 3D ellipsoidal volumetric contact

Table 3.4: Ellipsoidal contact model parameters

Parameter	Description
k_V	Volumetric stiffness
a_V	Volumetric damping coefficient
μ_d	Coefficient of friction
a, b, c	Dimensions
r_x, r_y, r_z	Position
α, β, γ	Body-fixed Euler angles

3.2.1 Model Properties

The 7-DOF toe-included model generated in Section 3.1 was used in this section and the ellipsoidal contact model was applied to the two-segment foot using three ellipsoids contacting the ground. Two ellipsoids, i.e. ball and heel, were used to represent the foot segment and one ellipsoid to represent the toe segment. Figure 3.2 shows the SK model and foot-ground contact geometry.

The parameters of ellipsoidal contact model are listed in Table 3.4. Three dimension parameters determine the ellipsoid radii in the local x-, y- and z-axes, respectively. The position parameters specify the locations of the ellipsoid centroids with respect to the foot or toe frames. The orientation parameters determine the rotations of the ellipsoid frames.

For the gait task, Brown and McPhee [21] identified all the contact parameters except for μ_d . To model the vertical jump, we used the same values for the contact parameters.

However, we manually adjusted a_V and μ_d values for the vertical jump simulation which is explained in Section 3.3.

3.2.2 Dynamic Modeling

Using the contact equations for an ellipsoid contacting a plane, the foot-contact model of an ellipsoid were created as a “Custom Component” with variable contact parameters in MapleSim. Then three duplicates of that custom component were added to the toe-included model to model toe, ball, and heel ellipsoids. The main advantage of using a custom component is that not only we can easily add it to any multibody model generated in MapleSim, but we can also add as many “Custom Components” as we need to the contact model, depending on the accuracy of the analysis.

Since the multibody analysis module does not have access to the equations inside the custom component, this module cannot generate the motion dynamics of the model. Thus, the “C-code Extraction” module of MapleSim was used to obtain the motion dynamics of the model with ellipsoidal contact. Although the C-code extraction module also uses Eq. 3.1 to generate the motion dynamics, matrix M and vector F cannot be extracted separately. In other words, C-code extraction would be a black box and we have only access to its inputs and outputs.

3.3 Predictive Vertical Jump Simulation

To simulate the highest vertical jump, the direct collocation optimal control method was used not only to predict the human motion but also to estimate joint torques and foot-ground contact forces.

To solve the optimization problem, GPOPS-II, a direct collocation optimal control toolbox for MATLAB [128] was used. The dynamic constraints, path constraints, event constraints, boundary conditions and the cost function of the optimization were specified in a way to generate the highest possible vertical jump for human. These constraints and conditions are described in the following section.

States and Control Inputs

In this optimization, the states, \mathbf{x} , were set to the generalized coordinates and their time derivatives. The control inputs, \mathbf{u} , were set to the joint torques:

Table 3.5: Maximum possible ranges of human joint angles, angular velocities and torques

Joint	Angle (degree)		Angular Velocity (degree/s)		Torque (N.m)	
Toe	-45	80	-1200	1500	-4000	2000
Ankle	50	110	-1200	1500	-4000	2000
Knee	-150	0	-1200	1500	-2000	1500
Hip	-30	100	-1200	1500	-2000	1500

$$\begin{aligned}\mathbf{x} &= \{\mathbf{q}, \dot{\mathbf{q}}\} \\ \mathbf{u} &= \boldsymbol{\tau}\end{aligned}\tag{3.3}$$

In GPOPS-II, in each jumping phase, three different ranges must be defined for the states as initial, final and total ranges, while only a single range must be assumed for the control inputs as the total range. However, to define some constraints on initial and final points of phases, the initial and final ranges of control inputs are also required. To resolve this, joint torques were also considered as states to enable ourselves to define initial and final ranges for them:

$$\mathbf{x} = \{\mathbf{q}, \dot{\mathbf{q}}, \boldsymbol{\tau}\}\tag{3.4}$$

Since the new state vector includes joint torques, the derivative of joint torques can be assumed as control inputs (Eq. 3.5). This assumption can also reduce noise in the torque values predicted by the optimization.

$$\mathbf{u} = \dot{\boldsymbol{\tau}}\tag{3.5}$$

Boundary Conditions

In GPOPS-II, the lower and upper boundaries of states (generalized coordinates, their time derivatives and joint torques) and control inputs (time derivatives of joint torques) should be specified. The maximum possible ranges of the states (Table 3.5) were extracted from [25, 104], and the ranges of control inputs were assumed to be considerably greater than joint torque ranges. The initial, final, and total ranges of each jumping phase were defined based on the considered maximum ranges and the posture of the human at each phase.

Table 3.6: Guess points

Model		Phases		
Kinematically- Constrained Contact	Toeless	Preflight		Flight
	Toe-included	Preflight		Flight
Ellipsoidal Volumetric Contact	Toe-included	Crouching	Thrust	Flight

The diagram illustrates human postures at various guess points for three different models. Each posture is represented by a stick figure with an orange head, green torso and legs, and blue feet. The ground is indicated by a horizontal line with small blue rectangles representing contact points.

- Kinematically-Constrained Contact (Toeless):** Shows four preflight postures where the feet are flat on the ground, and three flight postures where the feet are off the ground.
- Kinematically-Constrained Contact (Toe-included):** Shows four preflight postures where the feet are flat on the ground, and three flight postures where the feet are off the ground.
- Ellipsoidal Volumetric Contact (Toe-included):** Shows three crouching postures where the feet are flat on the ground, three thrust postures where the feet are off the ground, and three flight postures where the feet are off the ground.

Guess Points for States and Control Inputs

Guess points were defined for states and control inputs in a way to effectively lead the optimization process towards the optimal solution. To this end, the guess points were defined for joint angles and torques based on the experimental data reported for human jump in [104], and the guess points for angular velocities were obtained by differentiating the guessed joint angles. Table 3.6 shows the posture of a human at each guess point for the three under-study models.

Dynamic Constraints

Since the optimization problem is solved in MATLAB, the motion dynamics, generated in MapleSim, should be exported to MATLAB.

The motion dynamic equations of the models with kinematically-constrained contact,

Table 3.7: Event constraints

Model		Phase	Constraints
Kinematically- Constrained Contact	Toeless	Preflight	$(a_{i,x,y})_{COM} = 0, (F_{f,y})_c = 0$
		Flight	$(v_{f,y})_{COM} = 0$
	Toe-included	Preflight	$(a_{i,x,y})_{COM} = 0, (F_{f,y})_c = 0$
		Flight	$(v_{f,y})_{COM} = 0$
Ellipsoidal Volumtric Contact	Toe-included	Crouching	$(a_{i,x,y})_{COM} = 0$
		Thrust	$(F_{f,y})_c = 0$
		Flight	$(v_{f,y})_{COM} = 0$

generated by the multibody analysis module, were exported to MATLAB using the ‘‘Code Generation’’ command in Maple symbolic computing software (2016.2 Maplesoft, Waterloo, ON, Canada). The motion dynamic equations of the model with compliant contact, generated by C-code extraction module, were exported to MATLAB by compiling the C-code file in MATLAB. The exported equations were directly used in GPOPS-II as dynamic constraints.

Event Constraints

Event constraints are imposed to the model either at the initial or at the final time instants of the phases. The event constraints in different phases of the models are indicated in Table 3.7. The indices i and f denote initial and final points, respectively. The indices COM and c represent the center of mass of the model and foot-ground contact, respectively.

At the beginning of the preflight phase and crouching phase, the acceleration of COM would be zero since the model is in static equilibrium. The normal contact force would be zero just before leaving the ground (at the end of the preflight phase for kinematically-constrained contact and at the end of the thrust phase for compliant contact). The last event constraint was imposed to the end of flight phase to make the vertical velocity of the model equal zero since it would be zero when the model reaches the highest position.

In addition to above-mentioned event constraints, in order to provide continuity between the subsequent phases, it was assumed that the time and states at the end of one phase should be equal to the time and states at the beginning of the subsequent phase.

Table 3.8: Path constraints

Model		Constraint (imposed to each phase separately)
Kinematically-Constrained Contact	Toeless	$\Delta x_{\text{COM}} = 1 \text{ cm}$
	Toe-included	$\Delta x_{\text{COM}} = 6 \text{ cm}$
Ellipsoidal Volumetric Contact	Toe-included	$\Delta x_{\text{COM}} = 0.2 \text{ cm}$

Table 3.9: Cost functions

Model	Cost Function
Kinematically-Constrained Contact	$w_1 \left(\frac{v_{y,max\,desired}}{v_{y,f}} \right)_{\text{COM}}^2 \Big _{\text{PP}} + w_2 \left(\frac{y_{max\,desired}}{y_f} \right)_{\text{COM}}^2 \Big _{\text{FP}}$
Compliant Contact	$w_1 (\theta_{\text{knee}} - \theta_{\text{desired}})^2 + w_2 (\dot{\theta}_{\text{knee}})_{\text{CP}}^2 \Big _{\text{CP}} +$
	$w_3 \left(\frac{v_{y,max\,desired}}{v_{y,f}} \right)_{\text{COM}}^2 \Big _{\text{TP}} + w_4 \left(\frac{y_{max\,desired}}{y_f} \right)_{\text{COM}}^2 \Big _{\text{FP}}$

Path Constraints

Path constraints are the constraints that must be satisfied during the path of phases. Since the task is vertical jump, a path constraint was imposed to restrict the horizontal motion of COM during the jump as much as possible. Table 3.8 shows the least possible variation of COM position in the horizontal direction for each model. These values were obtained by trial and error to lead the optimization to the optimal results.

Cost Function

To achieve the highest vertical jump, a physiologically-meaningful cost function was minimized for each model (Table 3.9). The weights of cost terms, w_i , were tuned manually with the aim of simulating a natural vertical jump. The weight values are indicated in Table 3.10.

To have the highest position for COM at the end of flight phase, the COM vertical velocity at the beginning of the flight phase should be as large as possible. Therefore, the cost function for kinematically-constrained contact aims to not only maximize the height of the COM (y_f) in the end of flight phase but also to maximize the COM vertical

Table 3.10: The values of weights in each model

Model		w_i
Kinematically-Constrained Contact	Toeless	$w_1 = 1, w_2 = 12$
	Toe-included	$w_1 = 1, w_2 = 1$
Ellipsoidal Volumetric Contact	Toe-included	$w_1 = 2, w_2 = 1, w_3 = 1, w_4 = 5$

Table 3.11: Solver properties

Solver	IPOPT	Number of meshes	30
Derivation supplier	SparseCD	Number of iterations	5000
Tolerance	$1e - 6$	Number of collocation points (n)	$4 < n < 20$

velocity ($v_{y,f}$) in the end of the preflight phase. The values $v_{y,max\,desired}$ and $y_{max\,desired}$ have been assumed as 10 (m/s) and 1 (m), respectively. In the cost function for compliant contact, the crouching term [11] was imposed to bend the knee to reach the desired angle (-110 degree) and the two other terms were exactly the same as the cost terms for the kinematically-constrained contact.

Optimization Solver Properties

The properties of the optimization solver are mentioned in Table 3.11.

3.4 Results and Discussion

In this section, the resultant joint angles, torques, GRFs and foot position and orientation, that were predicted for the three models, are shown and discussed.

3.4.1 Joint Angles

Figure 3.3 shows the predicted joint angles using the three models. The first and second columns present the results for the toeless and toe-included models with the kinematically-constrained contact, and the last column shows the results of the toe-included model with the compliant contact.

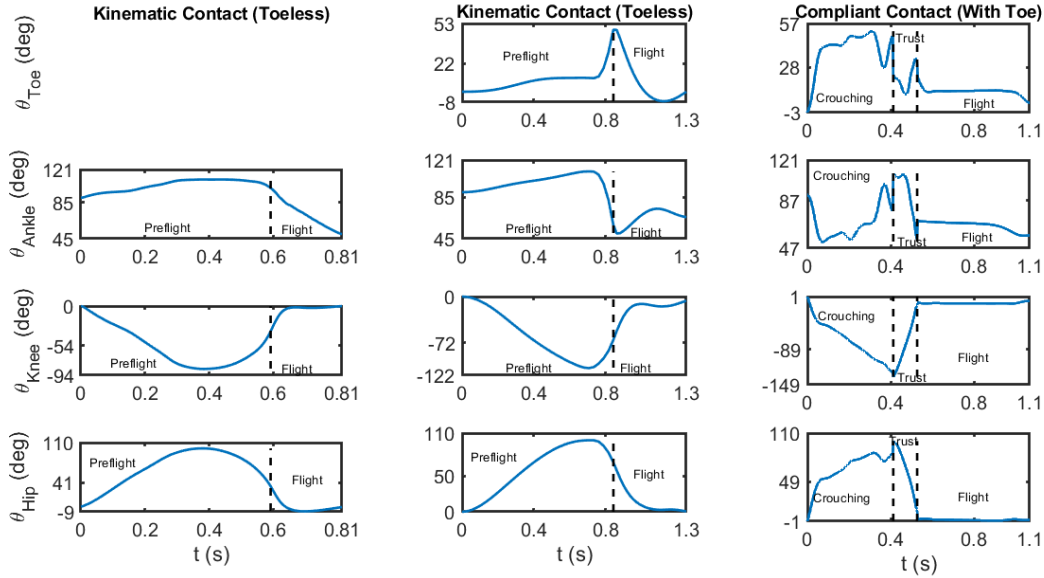


Figure 3.3: Resultant joint angles of the vertical jump simulation

As shown in Figure 3.3, the joint angle ranges of the all three models are approximately equal except for the knee angle; the knee joint in compliant contact model (-150 degree) bent more than those in kinematically-constrained contact models (-94 and -122 degree) due to the extra term defined in the cost function of compliant contact to make knee bend in the crouching phase.

Once the foot is in contact with the ground, the foot was set to be fixed to the ground in kinematically-constrained contact models while in compliant contact model, the foot was not fixed to the ground and there were extra three DOF and also extra stiffness between the foot and ground. That is why time histories of joint angles in the crouching and thrust phases are not as smooth as those in the preflight phases of kinematically-constrained models.

3.4.2 Joint Torques

Figure 3.4 shows the predicted joint torques using the three models. The torque ranges of the toeless model are considerably less than the torque ranges of the two other models. Because the toeless model is not able to produce high torques and cannot jump as high as

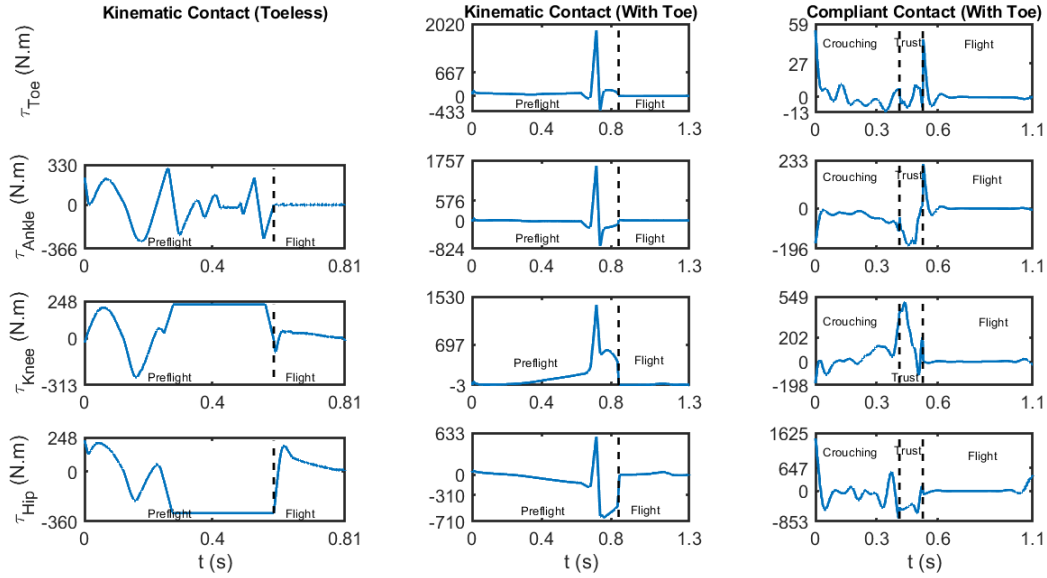


Figure 3.4: Resultant joint torques of the vertical jump simulation

the toe-included models. However, the toeless model is more stable than the toe-included model when the contact is kinematically-constrained.

There is a sharp fluctuation in the torque values of the second model just before the transition to the flight phase since the contact has been modeled kinematically and the toe transits suddenly from a fixed posture to a free posture. Although the contact has also been modeled kinematically in the toeless model, there is not such a fluctuation before the transition to the flight phase. The reason is that in the toeless model, the foot has greater mass and length than the toe. Thus the toeless model is more stable than the toe-included model once the contact is kinematically modeled. On the other hand, since in compliant contact model, the contact has been realistically modeled and the foot can freely move in all phases, there is no sharp fluctuation in torque values.

3.4.3 Foot-Ground Contact Forces

Figure 3.5 shows the predicted ground reaction forces using the three models. Since the task is a vertical jump, it is desirable to reduce the tangential reaction force as much as possible. The range of tangential reaction force in compliant contact model is considerably

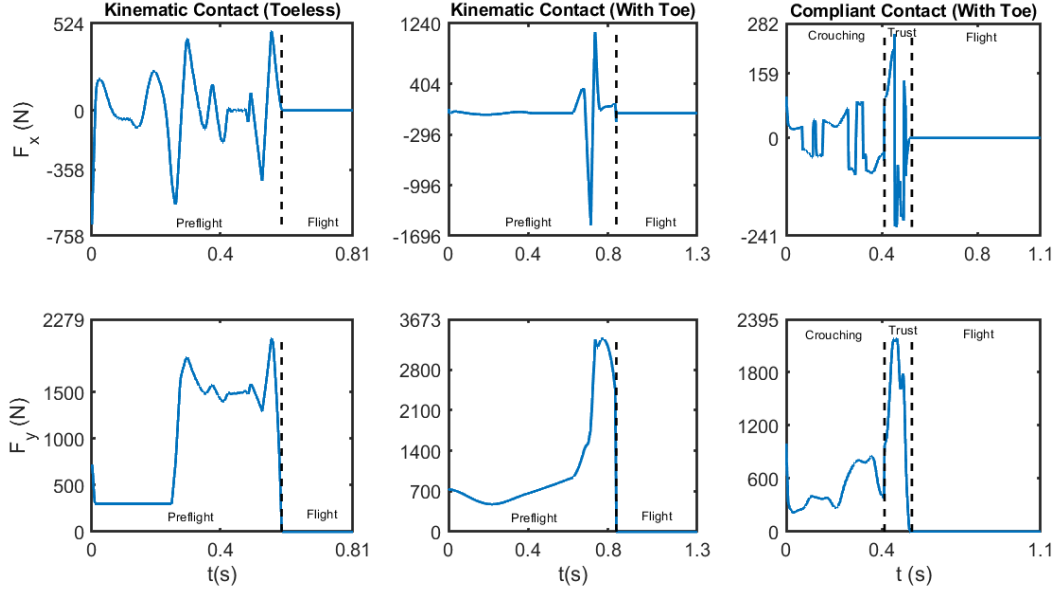


Figure 3.5: Resultant ground reaction forces of the vertical jump simulation

less than those in the kinematically-constrained contact models. Thus, compliant contact can be more realistic than the kinematically-constrained model.

The sharp fluctuation in the tangential reaction force of the second model, just before the transition to the flight phase, can be justified by the same reason mentioned in Section 3.4.2.

Regarding the plots of normal reaction forces, once the model goes downward, the normal force is less than the weight of the model (720 N) and when the model goes upward, the normal reaction force would be more than the model weight (Figure 3.6).

The maximum feasible static friction coefficient for each of the three models can be estimated approximately using the predicted reaction tangential and normal forces:

$$\mu_s \geq \left| \frac{F_x}{F_y} \right| \quad (3.6)$$

where μ_s is the static friction coefficient and it must be always equal to or greater than the proportion of the reaction tangential force to the reaction normal force. Figure 3.7 illustrates that the static frictions should be greater than 1.4, and 1 for the toeless and

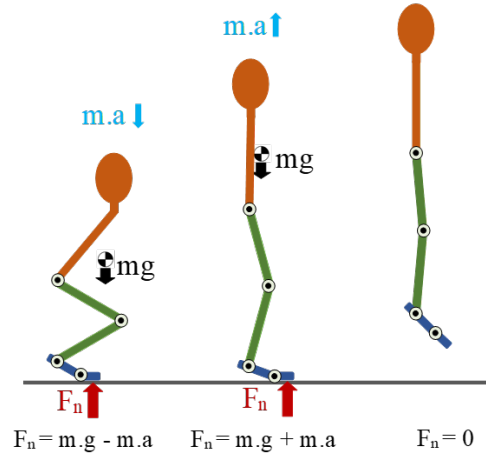


Figure 3.6: Comparison of normal force and model weight

toe-included models with kinematically-constrained contact, respectively while it is only 0.12 for the compliant contact model.

For the kinematically-constrained contact models, since the foot is rigidly fixed to the ground in the preflight phase, 1.4 and 1 are satisfactory values for the static friction. However, for the compliant contact model, 0.12 is much lower than expected. This issue can be considered as a limitation of using a velocity-based friction model since this friction model assumes that sticking occurs at very small relative velocities (0.01 m/s), while the true sticking would have a velocity of zero. Jackson et al. [70] also used a velocity-based friction model and obtained a static coefficient of friction of only 0.1. This is particularly surprising since the subject was wearing sports shoes, which should have a higher coefficient of friction.

3.4.4 Foot Position and Orientation

Since the task is a vertical jump, it is desirable to minimize the COM displacement in the horizontal direction as much as possible to predict a more stable task. This goal is better achieved using compliant contact compared to kinematical contact (Figure 3.8). In addition, the model with compliant contact is able to jump 89 cm which is considerably higher than toeless and toe-included models with kinematically-constrained contact (14 and 66 cm, respectively).

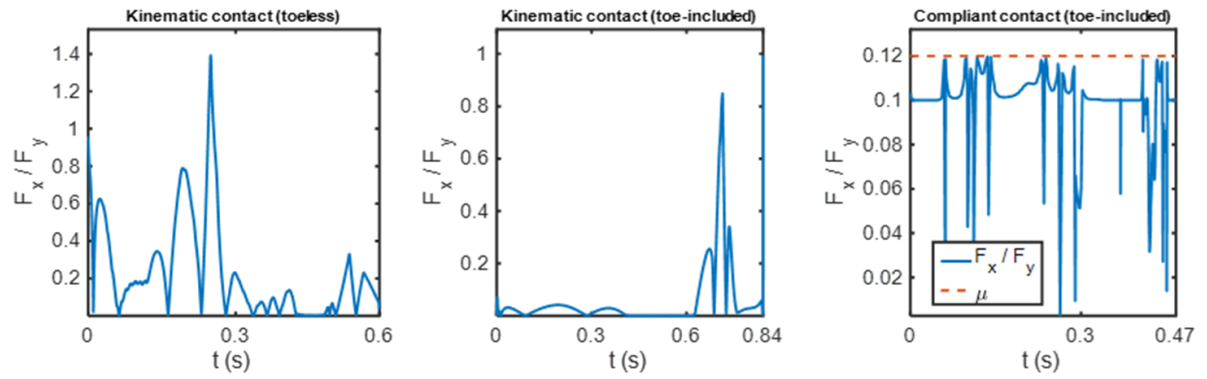


Figure 3.7: The proportion of the reaction tangential force to the reaction normal force when the foot is in contact with the ground

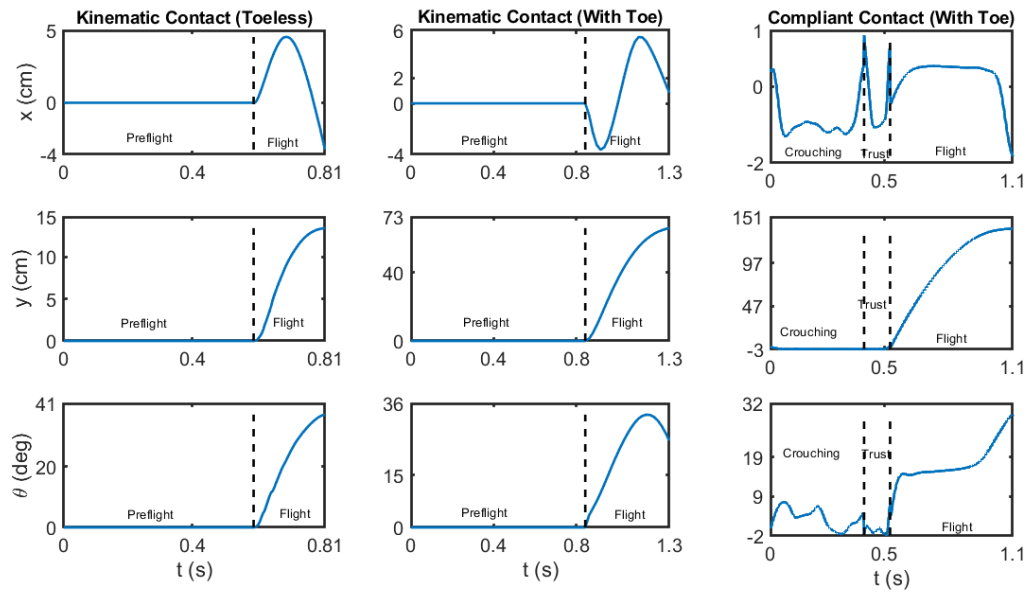


Figure 3.8: Resultant foot position and orientation in the vertical jump simulation

3.5 Conclusion

In this chapter, the time histories of the joint angles, joint torques, foot-ground contact forces and foot position and orientation, predicted for the three models during jumping, were shown and discussed. The general trends and ranges of predicted joint angles and normal reaction forces are in a good agreement with the experimental results reported in [104] since the initial guess for the predictive optimization in this study has been extracted from that paper.

It was concluded that the toeless model is not able to generate high torques and jump as high as the toe-included models. However, the toeless model is more stable than the toe-included model when the contact is kinematically-constrained. In the third case with detailed contact model, there are negligible horizontal deflection and no sharp torque fluctuations when compared to the previous two models. In conclusion, the most natural prediction of human jumping has been obtained using a model that includes the toe and a volumetric model of foot-ground contact. The main features and achievements of this study have been confirmed in [39, 41]. However, there are some weaknesses which should be addressed in the future work.

Firstly, the same contact parameters, estimated in [21] for a subject-specific gait motion, were used in this study for jumping task. This assumption seems reasonable since the height, mass and foot size of the model in this study are roughly close to the subject's in [21]. However, the foot-ground interaction in jumping and gait tasks are intrinsically different and it is required to identify the contact parameters specifically for the jumping task to get more accurate results.

Secondly, according to the recent literature [90, 109], to enable the optimization to converge to a more realistic and optimal solution, not only the number of guess points should be large enough but also they should be generated based on experimental data. However, in this study, only seven and nine guess points have been considered for kinematically-constrained and compliant contact models, respectively.

Thirdly, since the different joint torque ranges and trends have been reported in the literature for human vertical jump [84, 104], to verify the predicted joint torques in this study it is better to solve inverse dynamics using the predicted motion and reaction foot-ground forces and moments and then compare the obtained joint torques with the predicted ones. In addition, an experimental test can be done to verify the predicted results.

Lastly, the free motion of the model with respect to the ground has been determined with three generalized coordinates of the foot with respect to the ground. However, to reduce noise in the results and get more stable motion, it may be better to assign those

three DOF to the HAT, which has a high proportion of the total mass. This results in better conditioning of the mass matrix.

In the next chapter, we will develop a 2D human gait model including metatarsal joints with a 3D ellipsoidal volumetric contact model to identify the contact parameters for children. The next chapter will fill in the gaps of this chapter; we will define the free motion of the model using three DOF of HAT with respect to the ground, consider strong initial guess, and employ experimental-data-tracking cost terms.

Chapter 4

Foot-Ground Contact Model Development For Child Gait

The results of Chapter 3 illustrated that a toe-included human model with 3D ellipsoidal volumetric foot-ground contact would simulate a lower-extremity task more accurately than a toeless human model with a kinematically-constrained foot-ground contact. Moreover, it was shown that the contact model has a significant effect on the simulated results. Consequently, to develop a realistic simulation, contact parameters must be tuned regarding the experimental data of the task which is simulated.

The findings from Chapter 3 led us to develop a 2D human model, including metatarsal joints, with a 3D ellipsoidal volumetric contact model and identify the contact parameters regarding child gait experimental data.

This chapter is organized as follows¹. The human model is described in Section 4.1 and the experimental data, used to identify the contact parameters and validate the simulated results, is presented in Section 4.2. In Section 4.3, two different approaches (i.e., Trajectory Optimization and Optimal Control) were taken to identify the contact parameters. Then, in Section 4.4, the optimal control approach was modified by adding mass-property identification and it was taken as a third approach to estimate values for the contact parameters. Finally, the results are concluded in Section 4.5.

¹The majority of this chapter was extracted from [43].

4.1 Model Description

In this section, first, the human model is described. Then, a thorough review of the major types of contact model is provided and the 3D ellipsoidal volumetric foot-ground contact model is explained and compared with the other contact models. Finally, the method to extract the symbolic dynamic equations of the human model with the 3D ellipsoidal contact is defined.

4.1.1 Human Model

The human model is a 2D torque-driven model that moves in the sagittal plane. It includes 9 bodies and 11 degrees of freedom (DOFs). The bodies are head-arms-trunk (HAT), thighs, shanks, hind-fore-feet, and toes. The DOFs are 3-DOF HAT-to-ground joint, 1-DOF hip joints, 1-DOF knee joints, 1-DOF ankle joints, and 1-DOF metatarsal joints. The schematic of the human model is shown in Figure 4.1. The global coordinate system (GCS) is assumed to be fixed to the ground exactly under the center of mass of HAT at the start of simulation. Axes X , Y and Z are in the longitudinal, vertical, and lateral directions, respectively (as shown in Figure 4.1).

It is a common approach to assume head, arms and trunk as a single body (HAT) in human gait analyses [115, 156, 170, 171], since the effects of suppressing the arm swing on the kinematics, kinetics, and energetics of human gait are less than 10% [180].

The anthropometric data of the HAT, thighs and shanks were extracted from [186] and given in Table 4.1. In this table, BM and BH are the mass and height of the human, respectively. We set BM and BH to 41.4 kg and 1.47 m, respectively. These values represent the average mass and height of 20 healthy child subjects with an age of 10.8 ± 3.2 years. For more information about our subjects and their gait experimental data, the readers are directed to Section 4.2. SM and SL represent the segment mass and segment length, expressed as a fraction of BM and BH, respectively. COM, expressed as a fraction of SL, is the center of mass position of the segment, measured from proximal head of the segment. ROG, expressed as a fraction of SL, is the radius of gyration around the COM, used to calculate the moment of inertia (MOI) of the segment.

At each joint, a rotational spring and a damper were employed. The values of the spring stiffness (K) and damping coefficient (B) of the joints were extracted from [169] and expressed in Table 4.2. The damper models the viscous friction effect and the spring functions like a passive feedback system. Although K cannot exactly model the inherent joint stiffness, it provides numerical stability for the dynamics of human gait which is an

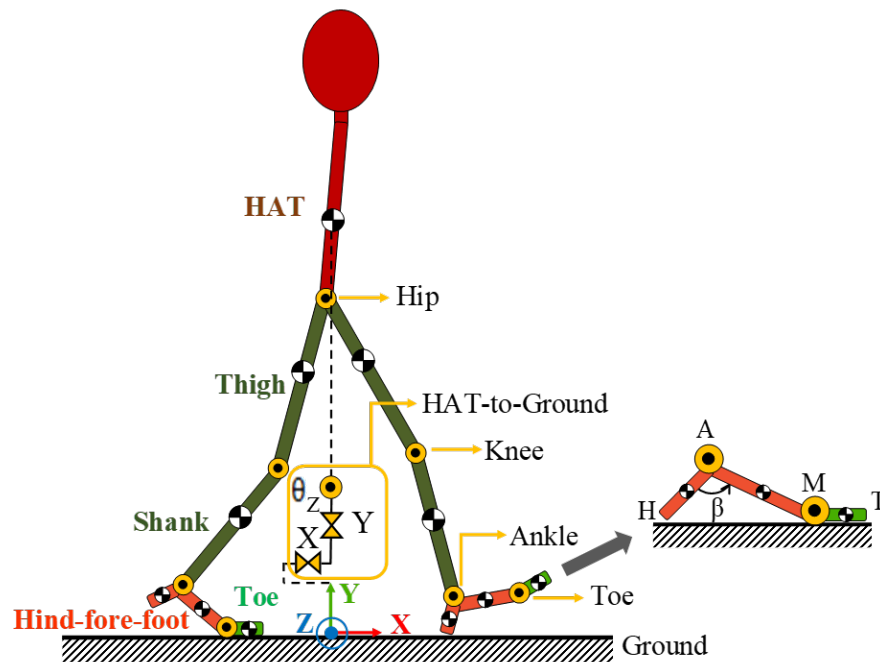


Figure 4.1: 2D human model with nine bodies and eleven DOFs

Table 4.1: Anthropometric data of all segments except for the feet

segment	SM	SL	ROG	COM
HAT	0.678 BM	0.288 BH	0.496 SL	0.626 SL
thigh	0.100 BM	0.245 BH	0.323 SL	0.433 SL
shank	0.047 BM	0.246 BH	0.302 SL	0.433 SL

SM and SL are the segment mass and segment length, respectively. COM is the center of mass position of the segment, measured from proximal head of the segment. ROG is the radius of gyration around the COM. BM and BH are the mass and height of human.

Table 4.2: Joint stiffness and damping coefficient

	hip	knee	ankle
K (Nm/Rad)	2.8762	1.5928	6.0390
B (Nm/Rad/s)	0.0003	2.9794	3.6841

Table 4.3: Anthropometric data of the feet

segment	SM	SL	ROG	COM
MT	2.1e-3 BM	4.3e-2 BH	1.32e-2 SL	0.5 SL
AM	6.2e-3 BM	6.5e-2 BH	2.74e-2 SL	0.5 SL
HA	6.2e-3 BM	4.4e-2 BH	2.74e-2 SL	0.5 SL

The segments are specified in Figure 4.1.

inherently unstable task. In this study, the spring stiffness and damping coefficient of the metatarsal joint were considered to equal the ankle’s values since no values for the metatarsal joint’s stiffness and damping coefficient are reported in the literature to the best of our knowledge.

For the feet, reference [186] has only reported the mass and length of the whole foot which are 0.0145BM and 0.152BH, respectively. There is no conventional anthropometric data for each foot segment in the literature. The weights, COMs, and ROGs of foot segments were estimated, consistent with the foot properties in [36, 143] and the foot segment lengths were calculated based on the optimized foot geometry presented in [155]. The foot segment properties were shown in Table 4.3. Angle β shown in the foot picture of Figure 4.1 is the fixed angle between the fore-foot (AM) and the hind-foot (HA) and it was set to 106 degree similar to the angle employed in [155].

4.1.2 Foot-Ground Contact Model

Among human tasks, gait is one of the most complicated and as a consequence, its predictive simulation is challenging due to its highly nonlinear motion equations, nonlinear muscle dynamics, and nonlinear foot-ground contact model.

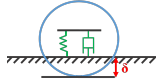
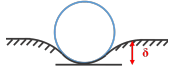
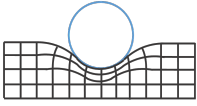
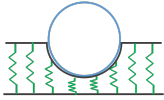
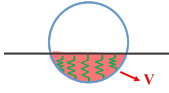
The foot-ground contact can be modeled as kinematic constraints that restrict the motion of discrete points along the bottom of the foot [10, 86, 89]. In these studies, the complex geometry of foot is not required to be explicitly modeled since a number of discrete points can approximately represent the complexity of the foot geometry. However, to achieve a useful predictive human gait simulation, it is important to have an accurate

foot-ground contact model that is consistent with the complex geometry of foot and computationally efficient. The main types of contact models commonly used in biomechanics studies include point contact, finite element contact, elastic foundation contact, surrogate contact, and volumetric contact:

- Point contact models are relatively simple and assume that contact between two surfaces occurs at a point. Two different methods for point contact, Kelvin-Voigt and Hunt-Crossley [67], are illustrated in Table 4.4 (No. 1 and 2). In the first method, the transition between the contact and non-contact conditions is not continuous due to the linear damper. The second method does not suffer from this discontinuity [55]. However, these two point contact models may not be accurate enough for conforming contacts (e.g. foot-ground contact).
- Finite element contact models [196] can provide a more detailed contact model for complex shapes (No. 3 in Table 4.4). However, this is not suitable for biomechanics optimizations or real-time analysis due to the high computational time of finite element analyses.
- In elastic foundation contact models [52], the contact surface is discretized into a finite number of springs. In other words, the bottom of the foot is modeled using a set of discrete viscoelastic elements with Coulomb friction [119, 129]. These contact models can be assumed as multiple point contact models, in which the normal contact force is evaluated by the depth of penetration using the Hunt-Crossley method [67]. No. 4 in Table 4.4 shows the schematic of the elastic foundation contact model.
- Surrogate contact models [88] are computationally efficient in comparison to finite element models and elastic foundation models since they are developed based on lookup tables rather than physical models. Surrogate models are trained to match results from a high-fidelity model. However, they are only appropriate over the conditions for which they have been trained.
- Volumetric contact model [60] is based on the concept of an elastic foundation model, but the contact surface is modeled using a continuous distribution of springs. Thus, it would be more realistic than the elastic foundation model to model complex conforming surfaces (e.g., foot). No. 5 in Table 4.4 shows the schematic of the model and the equation for the normal contact force.

The application of these five contact models to biomechanical modeling has been compared in detail in two review papers [58, 163] to which readers are directed for more information.

Table 4.4: Contact models

No.	method	model	formula
1	Kelvin-Voigt		$F_n = k\delta + d\dot{\delta}$
2	Hunt-Crossley		$F_n = a\delta^n + (b\delta^n)\dot{\delta}$
3	finite element		partial differential equations for each element
4	elastic foundation		discrete force equation at each spring element
5	volumetric contact		$F_n = k_V V(1 + a_V v_{cn})$

F_n is the normal contact force. δ is the penetration of deformation depth. k and d are the spring and damping constants, respectively. a and n are constants dependent on material properties and b is the damping coefficient. k_V and a_V are the volumetric stiffness and damping constants, respectively. Also, V is the volume of penetration and v_{cn} is the relative velocity of the two surfaces at the volumetric centroid.

Some recent gait studies, instead of using volumetric contact equations, modeled the complex geometry of the foot by a large number of spheres or ellipsoids to estimate the penetration depth for Hunt-Crossley equations. This method can be called Hunt-Crossley spherical/ellipsoidal contact model. Lin and Pandy [87], Lin et al. [90], and Porsa et al. [130] utilized this method by modeling the foot-ground contact via six, six and eight spheres, respectively. Lopes et al. [94] have also used six ellipsoids on the sole to model the foot-ground contact. For a conforming surface like a foot, Hunt-Crossley spherical/ellipsoidal contact models are more accurate than the point contact models since the penetration depth is estimated using spheres or ellipsoids. However, the volumetric contact models, in which a volume of penetration is used in the contact equations, can provide a better geometric representation of a conforming surface than Hunt-Crossley spherical contact models. Hunt-Crossley equations are most accurate for point contacts, but there are likely errors when applied to a conforming surface.

Meyer et al. [109] employed the elastic foundation contact using a large number of springs to approximate a continuous load distribution. Thus, the model approaches the accuracy of volumetric contact with the computational efficiency of the elastic foundation method.

In the contact models of [87, 90, 94, 109, 130], a finite number of contact points on the foot have been used. These foot-ground contact models can be assumed as multiple-point contact models, in which the normal contact force is evaluated using the Hunt-Crossley method. Since the Hunt-Crossley method is restricted to the contact points (not the contact surfaces), an unnatural foot shape may be obtained. However, a Hunt-Crossley ellipsoidal contact model [94] is geometrically more natural than the other multiple-point contact models.

Since the volumetric contact model provides a better representation of conforming geometry in comparison to the point contact and elastic foundation models, some human gait studies employed it to simulate the foot-ground contact. The common type of volumetric contact model, generally used for foot-ground contact, is the spherical volumetric contact model. Millard et al. [112] used a 2D two-segment foot model with three volumetric sphere-plane contact pairs. Shourijeh et al. [156, 159] developed that model into a hyper-volumetric model. Mouzo et al. [118] also employed volumetric contact with a polynomial representing the contact surface.

Brown and McPhee [21] have developed an ellipsoidal volumetric foot-ground contact model that takes advantage of the features of ellipsoidal models and volumetric models. In their approach, the foot is modeled by three ellipsoids and the volumetric contact equations for an ellipsoid contacting a plane were employed. Since ellipsoids can match the complex

geometry of the foot surface better than spheres, they used only three ellipsoids to model the foot-ground contact. However, there still exist two gaps in Brown and McPhee’s approach that should be filled before being used in high fidelity human gait analyses.

The first gap is that the contact parameters have been identified by tracking the experimental foot-ground reactions (i.e., the normal force, center of pressure and pressure at the foot surface) measured for one foot during gait. They did not include both feet in the identification process, nor did they consider the dynamics of the lower extremities.

The second gap is that once they included friction in their model, the contact parameter identification yielded inaccurate parameters and results. This gap is due to using a continuous velocity-based friction model in an inverse dynamic identification.

The main contribution of this chapter is to fill in these gaps of the ellipsoidal volumetric contact model, so that it can be used as a computational-efficient and accurate foot-ground contact model in our predictive gait simulation.

In Brown and McPhee’s ellipsoidal volumetric contact model, the contact surface is modeled by ellipsoids and the friction is generated by a continuous velocity-based friction model. In a velocity-based friction model, it is assumed that sticking occurs at a very small transition velocity. In this study [21], the transition velocity was set to 0.1 m/s, which is quite small in comparison to the experimental gait speed (1.26 m/s). Each foot is composed of two bodies: hind-fore-foot and toe. The hind-fore-foot was represented by two ellipsoids (i.e., ball and heel ellipsoids) and the toe was represented by one ellipsoid (i.e., toe ellipsoid). Figure 4.2 shows an approximate schematic for the ellipsoidal contact model of the right foot. Using volumetric contact, the rolling resistance, tangential friction and spinning friction are modeled in addition to the normal force. For further information on the contact equations, readers are directed to [20, 59].

In this study, the global coordinate system is different from that in [21]. To address this, several transformation matrices were employed to locate the ellipsoids in a correct position and orientation with respect to the GCS of this study. Additionally, in reference [21], the ellipsoidal contact model was developed only for the left foot. We reflected the three ellipsoids of the left foot with respect to the sagittal plane to develop the contact model for the right foot. Thus, six ellipsoids (three ellipsoids on each foot) were used to model the contact.

Each ellipsoid contacting a plane has 13 parameters shown in Table 4.5. These parameters were expressed with respect to the segment-fixed local coordinate systems. When the human model is in standing posture, the segment-fixed local coordinate systems have the same position and orientation as the GCS.

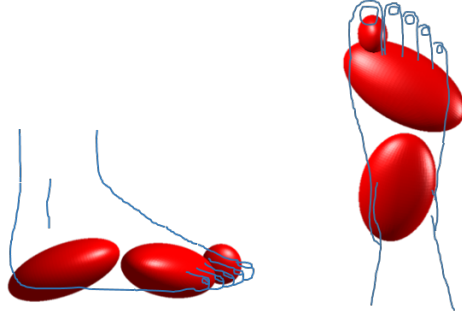


Figure 4.2: Side and top views of the ellipsoidal contact model for the right foot (This figure is only for visualization purpose. The positions, orientations and dimensions of the ellipsoids are not to scale.)

Table 4.5: Volumetric contact model parameters

parameter	description
k_v	volumetric stiffness
a_v	volumetric damping coefficient
μ_s	static friction coefficient
μ_d	dynamic friction coefficient
a, b, c	dimensions
r_x, r_y, r_z	position
γ, β, α	3-2-1 body-fixed Euler angles

Parameters r_x , r_y and r_z specify the locations of the ellipsoid centroids with respect to segment-fixed local coordinate systems; parameters γ , β and α represent 3-2-1 segment-fixed Euler angles with respect to local coordinate systems and parameters a , b and c specify the ellipsoid radii in the local x , y and z axes, respectively.

Since we have three different ellipsoids (ball, heel, and toe), there are 39 parameters in total which will be identified in Section 4.3. It should be noted that the human model is bilaterally symmetric and in gait, the right and left legs perform similar motions but with a time shift. Thus, we only identified the contact parameters of ball, heel and toe ellipsoids on the left foot and then employed the identified parameters for the ellipsoids on the right foot considering the bilateral symmetry of the human model.

4.1.3 Dynamics Modeling

The human with foot-ground contact model was developed in MapleSim (2018. Maplesoft, Waterloo, ON, Canada), as shown in Figure 4.3. An advantage of using MapleSim is that the motion dynamic equations are generated in a symbolic form; also, the velocity and acceleration equations can be directly determined by symbolically differentiating the kinematic expressions with respect to time. The resultant equations are more computationally efficient than a numerical equivalent [103]. If the dynamic equations are evaluated numerically during the optimization, the motion equations have to be differentiated in each iteration of optimization, which leads to a more time-consuming procedure and less accurate results than the optimization in which the symbolic equations are used.

The final symbolic equations, extracted from the MapleSim model, were modified in Maple (2018 Maplesoft, Waterloo, ON, Canada) to reduce the size of the simulation code and get optimal symbolic equations for exporting to MATLAB for use in the optimization process.

4.2 Experimental Data

Experimental gait data is required for parameterizing the contact model and validating the results. To generate an accurate data-tracking optimization for this study, the motion data for all 11 DOF of the model, joint torque data for all 8 joints of the model, and normal and tangential ground reaction forces (GRFs) for both feet are used.

The experimental data processing is categorized into three subsections: (4.2.1) HAT and right leg without metatarsal, (4.2.2) Right metatarsal and (4.2.3) Left leg. In each subsection, it is explained in detail how the data corresponding to those specific segments is extracted, estimated or generated.

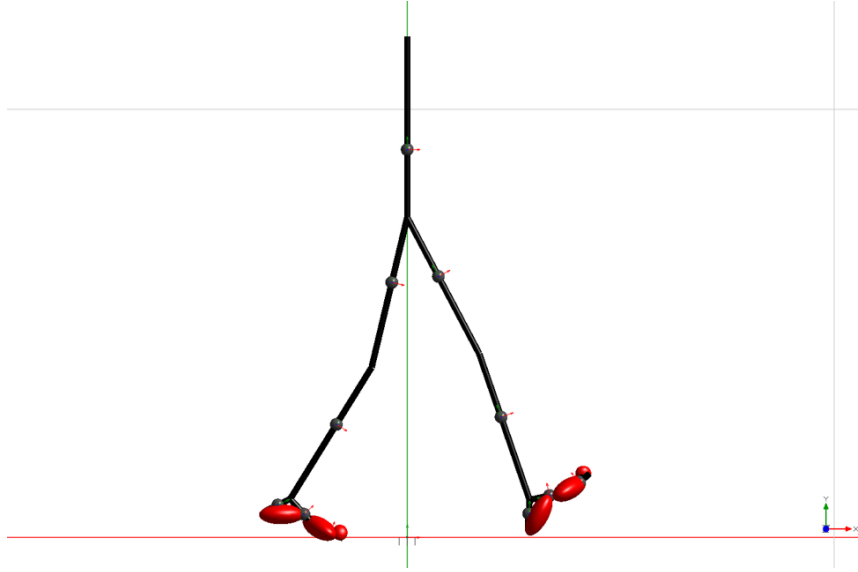


Figure 4.3: Developed human model with the ellipsoidal foot-ground contact in MapleSim

4.2.1 HAT and Right Leg Without Metatarsal Joint

The experimental position of the HAT with respect to the ground, the experimental angles and torques of right hip, knee and ankle joints and the GRFs of the right foot were extracted from [18] for one gait cycle. A gait cycle is composed of two steps and in this study assumed to start and end with the heel-strike of the right foot on the ground.

The orientation of the HAT with respect to the ground was set to zero as the initial guess for the optimization because the variation of this orientation during natural-speed gait is negligible ($-1^\circ \leq \theta_z \leq 1^\circ$ [186]). This angle will be predicted when the other known experimental data are tracked in the optimization.

In reference [18], 20 healthy child subjects (9 males and 11 females with an age of 10.8 ± 3.2 years, a mass of 41.4 ± 15.5 kg and a height of 1.47 ± 0.2 m) have participated. The experimental motions of the HAT, right hip, knee, and ankle have been collected for natural-speed walking using the 9-camera SMART-E motion capture system (BTS, Milano, Italy) and LAMB market set including 29 retroreflective markers. The experimental GRFs of the right foot were measured using two force plates (Kistler, Winterthur, Switzerland). The experimental torques of right hip, knee and ankle were calculated by solving the inverse dynamics problem given the experimental motion and GRFs of the right leg.

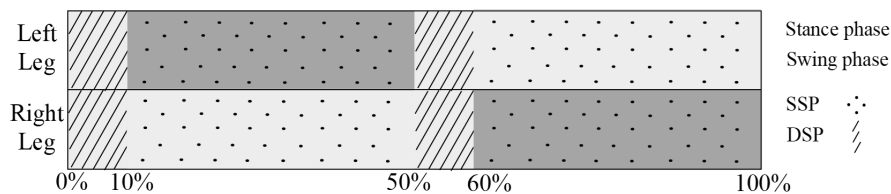


Figure 4.4: Phases of right and left leg during one gait cycle starting and ending with the right heel-strike

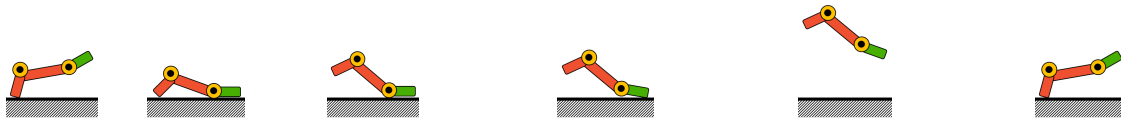
4.2.2 Right Metatarsal Joint

To the best of our knowledge, there is no human gait simulation study using experimentally-measured metatarsal joint data or reporting the resultant metatarsal joint motion and torque from their simulation. There are only a few clinical and laboratory studies measuring motion and pressure data for the different segments of foot (i.e. toe, fore-foot and hind-foot) during the stance phase of gait [78, 80]. However, it would be unreliable to use experimentally-measured toe motion in the gait simulation studies because the rigid body assumption for the foot and marker placement during the measurement makes the toe motion data physiologically impossible for gait simulation studies. Internal movement of the foot causes this inaccuracy in the measurement [21]. Thus, for the angle of right metatarsal, we planned a meaningful trajectory using the method in [40] and considering the measured angle for the metatarsal joint in [80].

The right metatarsal motion during one gait cycle was divided into six known postures: heel-strike, toe-strike, heel-off, toe-off, toe-free and again heel-strike. Between every two subsequent postures, a 5th-order polynomial was fitted given the six known boundary conditions listed in Table 4.6. In this table, $\Delta\theta_a$ is the range for the ankle angle and t_{SSP} and t_{DSP} represent the duration of single-support phase (SSP) and double-support phase (DSP), respectively. During the SSP only one foot is in contact with the ground and in DSP both feet are on the ground. One gait cycle is composed of two SSPs and two DSPs. For our experimental data, each SSP and DSP are 10% and 40% of the gait cycle, respectively [18]. Figure 4.4 shows these phases for both feet which are either in swing or stance phase during the gait cycle. The planned trajectory for the right metatarsal angle is shown in Figure 4.5.

Table 4.6: Known postures for the metatarsal trajectory

heel-strike	toe-strike	heel-off	toe-off	toe-free	heel-strike
$t = 0$	$t = t_{DSP}$	$t = t_{DSP} + t_{SSP}$	$t = 1.9t_{DSP} + t_{SSP}$	$t = 2t_{DSP} + t_{SSP}$	$t = 2t_{DSP} + 2t_{SSP}$
$\theta = \theta_0$	$\theta = \theta_0$	$\theta = 0.12\Delta\theta_a$	$\theta = 0.4\Delta\theta_a$	$\theta = \theta_0$	$\theta = \theta_0$
$\dot{\theta} = 0$	$\dot{\theta} = 0$	$\dot{\theta} = 0$	$\dot{\theta} = 0$	$\dot{\theta} = 0$	$\dot{\theta} = 0$
$\ddot{\theta} = 0$	$\ddot{\theta} = 0$	$\ddot{\theta} = 0$	$\ddot{\theta} = 0$	$\ddot{\theta} = 0$	$\ddot{\theta} = 0$



θ , $\dot{\theta}$ and $\ddot{\theta}$ are the angle, angular velocity and angular acceleration of the right metatarsal, respectively. θ_0 is the metatarsal angle when the toe is free. $\Delta\theta_a$ is the variation of the ankle angle (i.e., the difference between the max and min values of ankle angle). t_{DSP} and t_{SSP} are the duration of DSP and SSP, respectively.

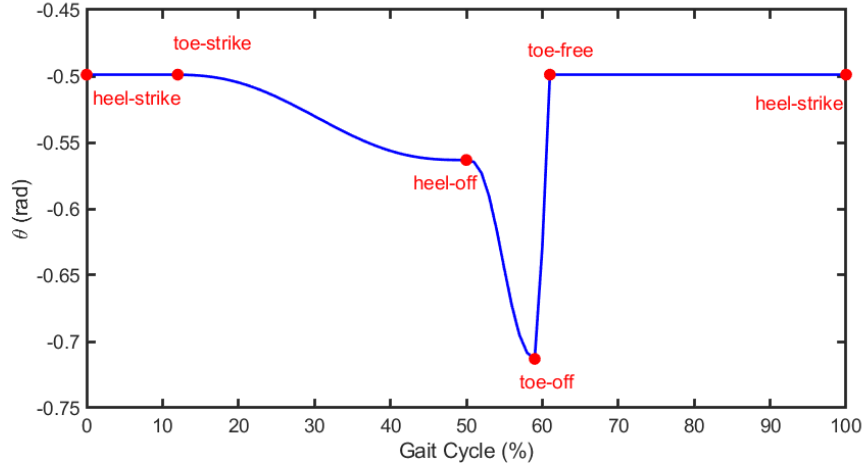


Figure 4.5: The planned trajectory for the right metatarsal joint angle

4.2.3 Left leg

The motions of legs were assumed to be bilaterally symmetric with a time shift during a gait cycle. The time shift (T_{sh}) is equal to $t_{DSP} + t_{SSP}$ based on Figure 4.4. The data of the left leg can be easily generated through the data of the right leg extracted/estimated in Section 4.2.1 and Section 4.2.2.

Since human gait is a periodic task, a Fourier series can be used to generate data for the left leg [101]. A Fourier series was fitted to the data of the right leg, with the Fourier basis signal matrix and the coefficient vector defined as:

$$[x_j]_{r_{n \times 1}} = [1 \quad \cos(i\omega t_j) \quad \sin(i\omega t_j)]_{n \times (1+2m)} \times \begin{bmatrix} a_0 \\ a_i \\ b_i \end{bmatrix}_{(1+2m) \times 1} \quad (4.1)$$

where, n and m are the number of data points and the order of the Fourier series with values of 101 and 5, respectively. Indices i and j are $i = [1, \dots, m]$ and $j = [1, \dots, n]$, respectively. Index r refers to the right leg and x_j is the data (e.g., joint angle, joint torque, and GRF) of right leg at time instant t_j . The Fourier coefficients are a_0 , a_i and b_i . ω equals $2\pi/T_c$ in which T_c is the duration of the gait cycle.

In Eq. 4.1, the data and the signal matrix of the right leg are known. So, the vector of coefficients can be easily obtained. Then, a new Fourier basis signal matrix was created for the left leg:

$$M_l = [1 \quad \cos(i\omega(t_j + T_{sh})) \quad \sin(i\omega(t_j + T_{sh}))]_{n \times (1+2m)} \quad (4.2)$$

where, index l refers to the left leg. Finally, the data of the left leg can be calculated through:

$$[x_j]_{l_{n \times 1}} = M_l \times [1 \quad \cos(i\omega t_j) \quad \sin(i\omega t_j)]_{(1+2m) \times n}^\dagger \times [x_j]_{r_{n \times 1}} \quad (4.3)$$

where $[\]^\dagger$ is pseudoinverse of the matrix. This approach was used to generate joint angles, torques, and GRFs for left leg given the joint angles, torques, and GRFs of the right leg, respectively.

4.3 Foot-Ground Contact Parameter Identification

We used two approaches to identify the contact parameters by tracking not only the experimental foot-ground reactions but also the kinematics and dynamics of the lower extremities: trajectory optimization and optimal control.

Trajectory optimization and optimal control are often confused and used interchangeably [135]. In trajectory optimization, static parameter values are identified to optimize a given performance index. In contrast, in optimal control, time-variant inputs to a system and, optionally, static parameters are estimated to optimize a given performance index.

Since the human model is 2D and the natural walking task is mainly done in the sagittal plane, we could have considered a 2D ellipsis foot-ground contact model to simplify the contact modelling and identification process. However, we considered a 3D ellipsoidal volumetric foot-ground contact model to: (1) Fill in the gaps of Brown and McPhee’s ellipsoidal volumetric contact model [21], and (2) Identify the contact parameters for a general 3D ellipsoidal volumetric contact model during child gait.

In this section, the solvers, methodologies, constraints, cost functions and results of the optimization approaches, developed in MATLAB (R2019b. MathWorks, Natick, MA, USA), are explained and compared.

4.3.1 Trajectory Optimization

Solver

To implement the trajectory optimization, the GlobalSearch algorithm [179], a global optimization toolbox for MATLAB, was used. The GlobalSearch uses a scatter-search mechanism to generate multiple start points for sampling multiple basins of interest. Then, GlobalSearch starts a local solver (i.e., `fmincon`) repeatedly to analyze the start points and remove those points that can not find the global minimum. Finally, the best parameter set that satisfies all constraints and has the lowest cost function value is selected as the global optimization solution. In this approach, the differential equations are solved by explicitly integrating. The flowchart of this optimization method is illustrated in Figure 4.6. This optimization was done on a desktop computer with an Intel[®] Core[™] i7-6700 CPU @ 3.40 GHz with 16.0 GB RAM.

Methodology

In trajectory optimization, the inverse dynamic equations of the model were explicitly solved for the joint torques and ground reaction forces and moments (GRFMs) from the generalized coordinates (i.e., $\mathbf{q}(t)$) and their derivatives (i.e., $\dot{\mathbf{q}}(t)$ and $\ddot{\mathbf{q}}(t)$). Meanwhile, the static parameters were optimized to minimize the cost function and meet the constraints. In this optimization, the generalized coordinates and their derivatives were set to the

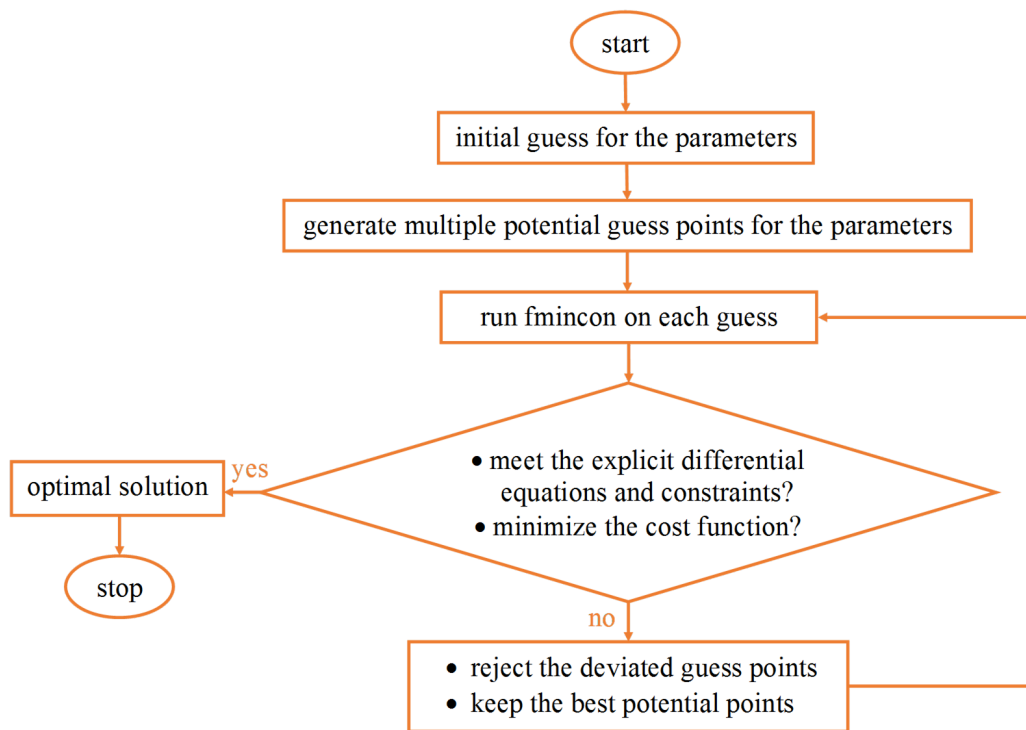


Figure 4.6: The flowchart of GlobalSearch

experimental coordinate positions, velocities, and accelerations. The static parameters, which will be identified, are the 39 contact parameters mentioned in Table 4.5.

Constraints

The dynamic friction coefficient was enforced to be less than the static friction coefficient (Eq. 4.4):

$$\left(\frac{\mu_d}{\mu_s}\right)_{min} \leq \frac{\mu_d}{\mu_s} \leq \left(\frac{\mu_d}{\mu_s}\right)_{max} \quad (4.4)$$

To obtain proper bounds for the μ_d/μ_s of ellipsoids, we tuned the bounds of Eq. 4.4 manually with the aim of avoiding slippage during walking. The best lower and upper bounds, preventing the model from slipping, were 0.55 and 0.99, respectively.

Cost function

Experimental joint torques and GRFs were tracked over time using the following cost function:

$$J = \frac{1}{t_f} \int_{t_0}^{t_f} \left[w_1 \sum_{i=1}^6 \left(\frac{\tau_{sim.} - \tau_{exp.}}{\tau_{max} - \tau_{min}} \right)_i^2 + w_2 \sum_{j=1}^4 \left(\frac{GRF_{sim.} - GRF_{exp.}}{GRF_{max} - GRF_{min}} \right)_j^2 \right] dt \quad (4.5)$$

where t_0 and t_f are the initial time and final time of a gait cycle and equal to 0(s) and 0.98(s), respectively, and w_1 and w_2 are the weighting factors. Indices *sim.* and *exp.* refer to the simulation results and experimental data, respectively. τ is the torque and *GRF* includes the tangential and normal ground reaction forces. i is from 1 to 6 referring to the torques of left and right hip, knee and ankle joints. The metatarsal torques were not tracked since no experimental data for them was available. j is from 1 to 4 referring to tangential and normal forces of the right and left feet. The minimum and maximum values of τ and *GRF* were obtained from the experimental data.

Bounds

We constrained the contact parameters to be within specified bounds shown in Table 4.7. These bounds were physically-meaningful and manually tuned using the reported contact

Table 4.7: Bounds for contact parameters of the ellipsoids on the left leg

ellipsoid	bound	$k_v(N/m^3)$	$a_v(s/m)$	μ_s	μ_d	dimension (mm)			orientation (degree)			position (mm)		
						a	b	c	γ	β	α	r_x	r_y	r_z
toe	lower	1e5	0	0.01	0.01	11.3	10.0	10.0	-50.8	-54.0	143.9	115.4	6.7	21.1
	upper	1e8	3	1.3	1.3	17.7	50.0	16.5	-39.8	-14.5	154.3	153.5	20.0	25.8
ball	lower	1e5	0	0.01	0.01	30.0	14.6	3.0	-75.2	-18.0	-97.5	62.9	4.0	-6.6
	upper	1e8	3	1.3	1.3	140.0	23.0	18.0	-41.1	-3.2	-83.6	99.0	11.4	-5.4
heel	lower	1e5	0	0.01	0.01	23.0	25.0	12.0	-91.8	-28.5	-99.3	-24.2	-3.0	-0.2
	upper	1e8	3	1.3	1.3	40.0	40.0	22.0	-59.7	-16.9	-84.2	-4.4	12.6	0.3

parameters in [21], the friction coefficients reported in [109] for the foot-ground contact, and the shape and dimensions of the human foot segments mentioned in Table 4.3.

After each optimization run, we inspected the cost function value to see whether the manually-tuned bounds bring about a lower value for the cost function than the previously-tuned bounds. From these inspections, we determined that the contact model is more sensitive to the geometrical parameters (i.e., position, orientation, and dimensions of the ellipsoids) than other parameters (i.e., friction, stiffness and damping). Thus, for the geometrical parameters, the bounds were considered large enough to allow the optimization to find the best parameters regarding the optimization constraints.

Initial guess

To help the optimization identify physically-meaningful values for the contact parameters, we used initial guesses for the 39 contact parameters defined in Table 4.5. For the volumetric stiffness, volumetric damping coefficient, the dimensions, positions and orientations of the ellipsoids, the optimal values reported in [21] were used as the initial guess. For the static and dynamic friction coefficients, 0.40 and 0.35 were assumed as the initial guess, respectively, since the required friction coefficient for walking is 0.3 [62].

4.3.2 Optimal Control

Solver

To implement the optimal control algorithm, GPOPS-II [128], a direct orthogonal collocation optimal control toolbox for MATLAB, was used. In this approach, the states and control inputs are parameterized as orthogonal polynomials (in the case of a parameter

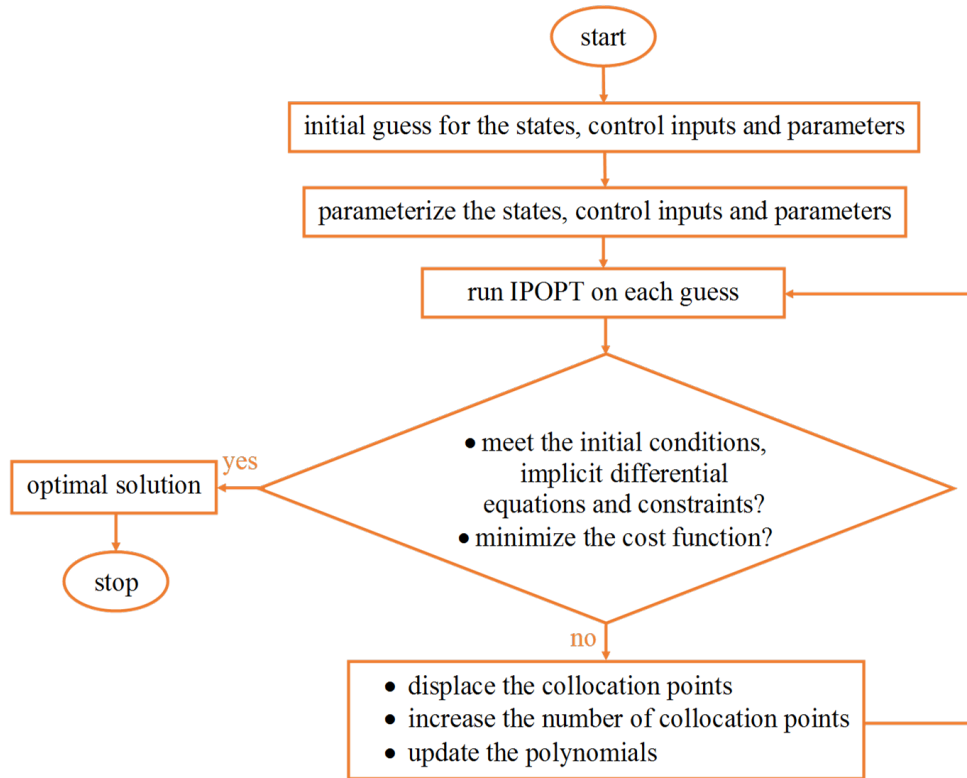


Figure 4.7: The flowchart of direct orthogonal collocation

identification problem, static parameters are added to the set of unknowns). The roots of those polynomials are considered as the collocation points and a local optimizer (i.e., IPOPT) updates the polynomials by increasing the number of the collocation points or displacing the collocation points until the constraints are met and the cost function is minimized regarding a prescribed error threshold. IPOPT is an interior-point optimizer where the constraints are satisfied by a barrier function. In this approach, the differential equations are considered as algebraic constraints that are satisfied during the optimization. The flowchart of this optimization method is illustrated in Figure 4.7. To implement this optimization, we used IPOPT solver in first derivative mode with the tolerance of $1e-5$. Although GPOPS-II contains an adaptive mesh refinement algorithm, we considered a fixed mesh of 100 collocation points, divided into 20 intervals, over the whole gait cycle to reduce the computational time. This optimization was done on a desktop computer with an Intel[®] Core[™] i7-6700 CPU @ 3.40 GHz with 16.0 GB RAM.

Methodology

In our optimal control optimization, the states and control inputs were:

$$\mathbf{x}(t) = [\mathbf{q}(t), \dot{\mathbf{q}}(t), \ddot{\mathbf{q}}(t)] \quad (4.6)$$

$$\mathbf{u}(t) = [\ddot{\mathbf{q}}(t), \boldsymbol{\tau}(t)] \quad (4.7)$$

where the states ($\mathbf{x}(t)$) are the generalized coordinates, velocities, and accelerations. The control inputs ($\mathbf{u}(t)$) are the joint jerks ($\mathbf{u}_1(t) = \ddot{\mathbf{q}}(t)$) and joint torques ($\mathbf{u}_2(t) = \boldsymbol{\tau}(t)$). Considering joint jerks in addition to the joint torques as the control inputs improves convergence and solution smoothness [182]. In this optimization, the states, control inputs, and the 39 contact parameters were parameterized and then optimized to minimize a cost function subject to constraints. The dynamic equations were solved implicitly as algebraic constraints during the optimization. Implicit dynamic modeling is different from explicit forward and inverse dynamics modeling approaches [42].

For a human model with a foot-ground contact model, in the inverse approach, dynamic equations must be explicitly differentiated to estimate the joint torques and GRFMs given the motion and in the forward approach, dynamic equations must be explicitly integrated to predict the motion and GRFMs given the joint torques. Although the inverse approach is relatively fast, unrealistic joint torques may be predicted due to numerical differentiation errors and inaccurate model parameters [42]. On the other hand, the drawback of the forward approach is that explicit integration methods are time-consuming. To avoid the deficiencies of explicit inverse and forward methods, the dynamic equations are implicitly solved as an algebraic constraint; thus, this is neither a forward nor inverse dynamic modeling approach.

Constraints

In addition to the constraint described for the trajectory optimization in Section 4.3.1, three extra constraints were defined for the optimal control optimization:

$$\mathbf{R}_{min} \leq \mathbf{R}_{pelvis} \leq \mathbf{R}_{max} \quad (4.8)$$

$$\dot{\mathbf{x}}(t) = [\dot{\mathbf{q}}(t), \ddot{\mathbf{q}}(t), \mathbf{u}_1(t)] \quad (4.9)$$

$$\mathbf{C}_{min} \leq (\boldsymbol{\tau}_{inv.}(t) - \mathbf{u}_2(t))^2 \leq \mathbf{C}_{max} \quad (4.10)$$

In Eq. 4.8, the residual loads on the pelvis were minimized to ensure dynamic consistency [109]. \mathbf{R} represents the two residual forces and one residual moment acting on the pelvis and the bounds for the residual forces were set to -1 and 1 (N) and for the residual moment was set to -0.1 and 0.1 ($N.m$). Eq. 4.9 is the dynamic constraint which represents the first derivative of states. Eq. 4.10 is the algebraic constraint, in which $\mathbf{u}_2(t)$ is the torque control inputs and $\boldsymbol{\tau}_{inv.}$ is the joint torques inversely obtained by solving the dynamic equations given the states. \mathbf{C}_{min} and \mathbf{C}_{max} were set to 0 and 10^{-12} to implicitly satisfy the motion dynamic equations.

Cost Function

In addition to the torque-tracking and GRF-tracking cost terms, considered for the trajectory optimization in Section 4.3.1, two additional terms were included in the cost function of the optimal control optimization: a motion-tracking term and minimization of the joint jerk. These two terms cannot be used in the trajectory optimization's cost function. The reason is that, in the trajectory optimization, the kinematic inputs are constant and consequently these terms, which are kinematic-based, are always constant and cannot be minimized. The cost function of the optimal control optimization is as follows:

$$J = \frac{1}{t_f} \int_{t_0}^{t_f} \left[w_1 \sum_{i=1}^6 \left(\frac{\tau_{sim.} - \tau_{exp.}}{\tau_{max} - \tau_{min}} \right)_i^2 + w_2 \sum_{i=1}^4 \left(\frac{\text{GRF}_{sim.} - \text{GRF}_{exp.}}{\text{GRF}_{max} - \text{GRF}_{min}} \right)_i^2 + w_3 \sum_{i=1}^{11} \left(\frac{q_{sim.} - q_{exp.}}{q_{max} - q_{min}} \right)_i^2 + w_4 t_f^6 \sum_{i=1}^{11} \left(\frac{u_1}{u_{1max} - u_{1min}} \right)_i^2 \right] dt \quad (4.11)$$

It should be noted that the magnitude of jerk (around $1e5 \text{ Rad/s}^3$) is considerably greater than the other cost terms; the jerk penalty was scaled by t_f^6 [109]. Minimizing the joint jerks results in a feasible solution even with a poor initial guess. The minimum and maximum values of motions and jerks, in the denominators, were obtained from the experimental data.

Bounds

In trajectory optimization, we can only define bounds for the contact parameters. In the optimal control optimization, we can define boundaries not only for the contact parameters

but also for the initial and final times, states at the initial and final times, states and control inputs during the gait cycle time, and also the integrals of the cost terms. The bounds for the initial and final times were considered to be fixed and equal to 0 (s) and 0.98 (s), respectively to match the experimental gait cycle time. The bounds for the generalized coordinates at initial and final times, and the generalized coordinates and torques during the gait cycle time, were determined based on the prescribed standard deviation reported by [18]. The bounds for the contact parameters were set to the bounds used for the trajectory optimization (Table 4.7). The remainder of the bounds (i.e., on the integrals, generalized velocities and accelerations at initial and final times and during the gait cycle time) were tuned regarding the gait experimental data used in this thesis.

Initial guess

The initial guess for time, states, control inputs and the integrals of the cost terms were set to the data described in Section 4.2 and the initial guess for the contact parameters were set to the contact parameters reported in [21].

4.3.3 Results and Discussion

Since the number of constraints, variables and cost terms in the optimal control optimization was higher than those in the trajectory optimization, the computation time of optimal control (11 minutes) was longer than that of the trajectory optimization (6 minutes). However, both of our optimizations, in which symbolic dynamic equations are used, are still more computationally efficient than the equivalent optimizations in which numerical dynamic equations are used [103]. The reason is that in our optimizations, differential equations were symbolically calculated only once and then called in the optimization procedure many times while in the numerical optimization equivalent, differential equations are re-formulated each time they are called, leading to higher computation time.

The values of weighting factors in the cost functions of both optimizations are shown in Table 4.8. The weights of motion, torque and GRF tracking terms were set to 1/4 to have the same effects on the results. The weight of the jerk cost term was set to a lower value ($w_4 = 1/40$) to affect the results less since the jerk term is only for convergence and solution smoothness. It should be noted that in Eq. 4.5 and Eq. 4.11, the tracking terms were divided by the range of each quantity (i.e., maximum value - minimum value) to be dimensionless and comparable.

Table 4.8: Weighting factor values

Optimization	Cost function	Weights
trajectory optimization	Eq. 4.5	$w_1 = 1/4$, $w_2 = 1/4$
optimal control	Eq. 4.11	$w_1 = 1/4$, $w_2 = 1/4$, $w_3 = 1/4$, $w_4 = 1/40$

Table 4.9: Root-mean-square errors for the trajectory optimization and optimal control

Optimization	τ_{hip} (N.m)	τ_{knee} (N.m)	τ_{ankle} (N.m)	GRF _x (N)	GRF _y (N)	R _x (N)	R _y (N)	R _z (N.m)
trajectory optimization	R: 16.46 L: 18.07	R: 11.06 L: 11.18	R: 17.29 L: 17.09	R: 36.42 L: 36.60	R: 234.67 L: 232.46	94.35	349.03	18.12
optimal control	R: 0.42 L: 0.42	R: 0.35 L: 0.35	R: 0.66 L: 0.66	R: 19.81 L: 8.33	R: 26.49 L: 26.38	0	0	0

R_x, R_y and R_z represent the residual forces and torque on the pelvis. R and L refer to right and left legs.

The resultant joint torques and GRFs from the trajectory and optimal control optimizations are shown in Figure 4.8 and Figure 4.9, respectively. The simulated results from the optimal control optimization (second columns in Figure 4.8 and Figure 4.9) were mostly within ± 1 standard deviation of the experimental data. The simulated results from the trajectory optimization (first columns in Figure 4.8 and Figure 4.9) were not as accurate as the results from the optimal control. The root-mean-square errors (RMSEs) of joint torques and GRFs are shown for trajectory optimization and optimal control in Table 4.9.

The geometries of the ellipsoids obtained from the trajectory optimization and optimal control are shown in Figure 4.10 and Figure 4.11, respectively. The geometry information of the left foot, in these two figures, are listed in Tables 4.10 and 4.11, respectively. The ellipsoids of the left and right feet have the same dimensions but are bilaterally symmetric. The optimized ellipsoids from the optimal control matched the geometry of the foot better than those from the trajectory optimization.

Table 4.10: The optimized geometry parameters for the left foot from trajectory optimization

ellipsoid	dimensions (mm)			orientations (degree)			positions (mm)		
	a	b	c	γ	β	α	r_x	r_y	r_z
toe	11.4	46.4	14.8	-46.3	-21.4	151.3	153.5	10.0	23.5
ball	137.7	22.6	3.9	-74.6	-3.9	-89.2	88.2	4.2	-6.0
heel	37.4	35.8	21.3	-79.1	-28.3	-91.7	-4.7	-3.7	0

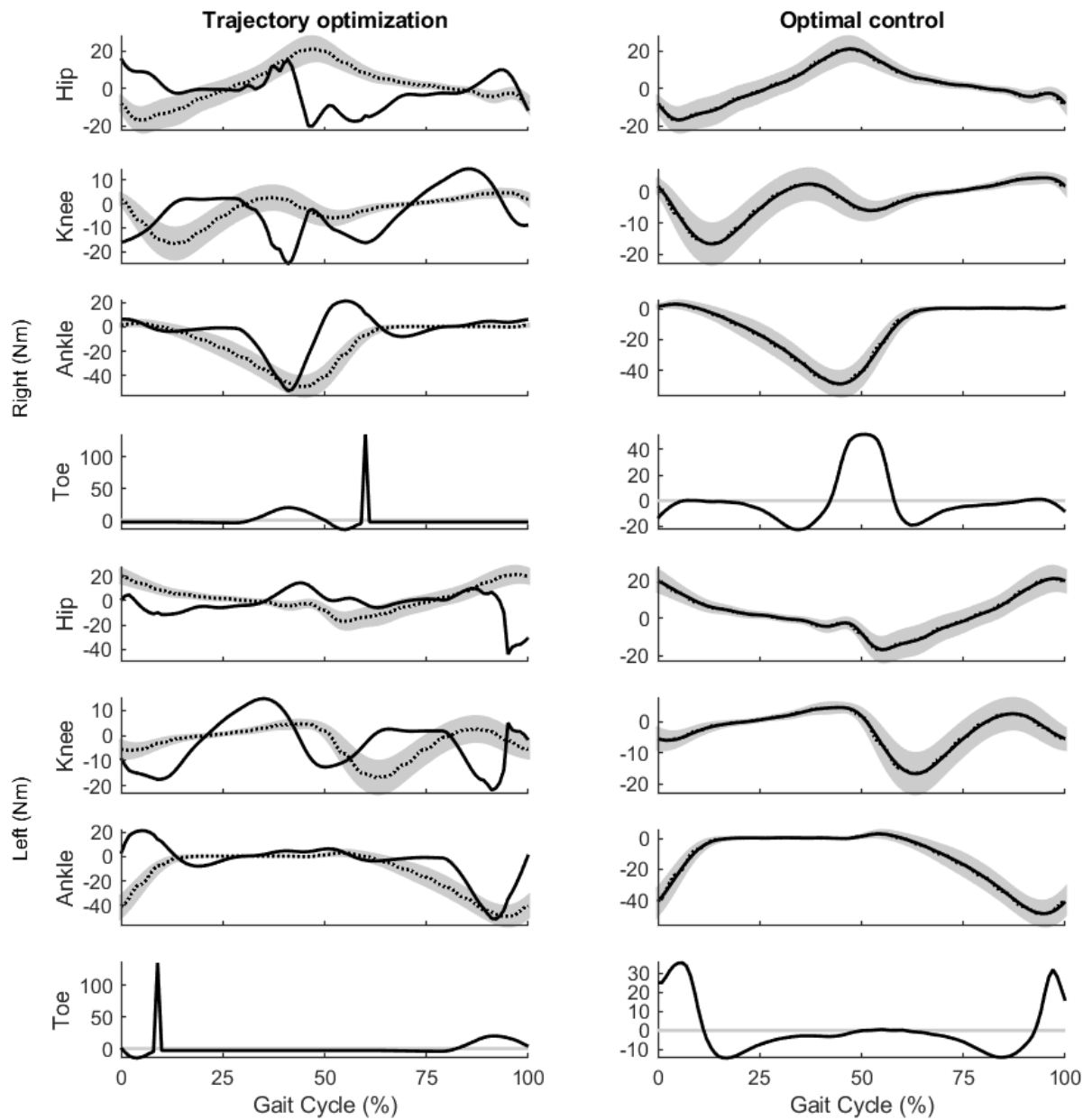


Figure 4.8: The lower extremity joint torques from trajectory optimization (first column) and optimal control (second column) (The dotted lines represent the mean experimental torques and the gray areas show ± 1 standard deviations of the mean experimental torques reported by [18])

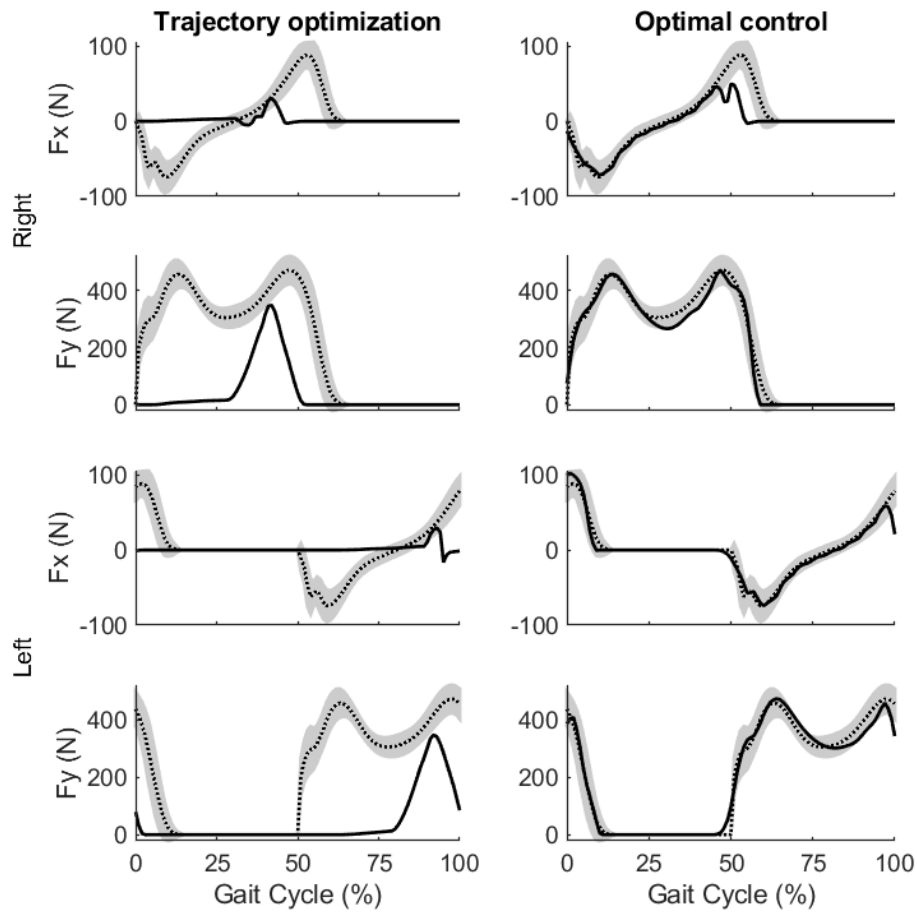


Figure 4.9: The tangential and normal ground reaction forces from trajectory optimization (first column) and optimal control (second column) (The dotted lines represent the mean experimental GRFs and the gray areas show ± 1 standard deviations of the mean experimental GRFs reported by [18])

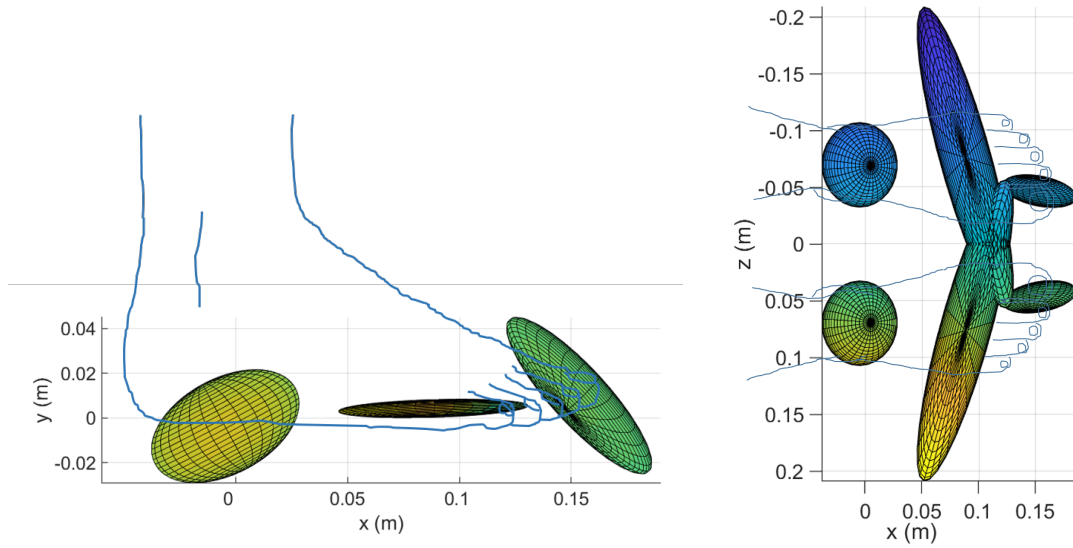


Figure 4.10: The optimized contact model geometry from trajectory optimization

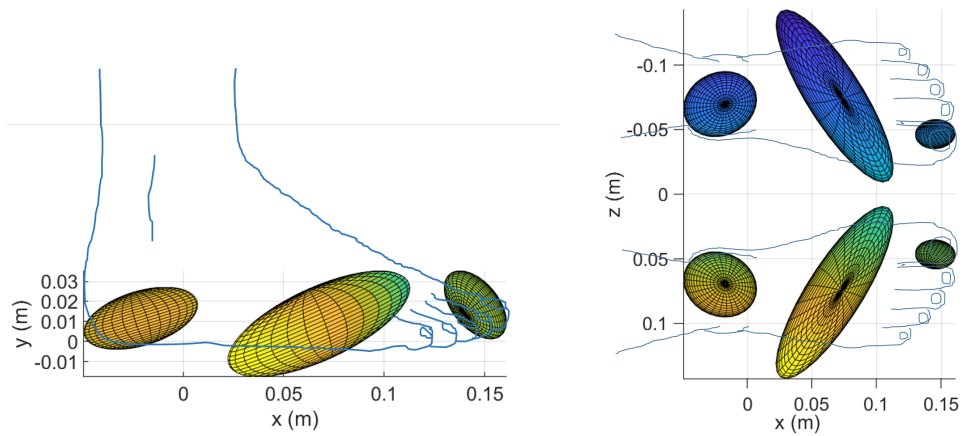


Figure 4.11: The optimized contact model geometry from optimal control

Table 4.11: The optimized geometry parameters for the left foot from optimal control

ellipsoid	dimensions (mm)			orientations (degree)			positions (mm)		
	a	b	c	γ	β	α	r_x	r_y	r_z
toe	11.8	20.0	11.0	-47.3	-29.5	152.5	145.4	18.3	23.5
ball	80.0	21.8	17.9	-57.0	-18.0	-95.5	67.5	8.9	-6.0
heel	24.5	30.0	13.5	-68.9	-17.2	-91.6	-21.2	11.6	0.0

Table 4.12: The optimized contact parameters from trajectory optimization

	toe	ball	heel
k_v (N/m ³)	1.67e7	1.04e7	0.07e7
a_v (s/m)	0.9161	0.6881	1.4732
μ_s	0.0200	0.6256	0.2207
μ_d	0.0139	0.4245	0.1592

The remainder of the contact parameters optimized through the trajectory optimization and the optimal control are in Table 4.12 and Table 4.13, respectively. Each parameter has different values for the three different ellipsoids due to the complex structure of foot. In particular, the human foot consists of 33 joints, 26 bones, 19 muscles and 107 ligaments surrounded by tissue and the different sections of this tissue have different mechanical properties (e.g., roughness and thickness).

Since the center of pressure is much closer to the fore-foot than the toe and heel (i.e., the ball ellipsoid is more in contact with the ground than the heel and toe ellipsoid) during gait, the ball ellipsoids play a more important role in generating the normal GRF, and also avoiding slippage, than the toe and heel ellipsoids. The optimal control optimization identified the largest values for the penetration volume and the dynamic friction coefficient of the ball ellipsoids among the three ellipsoids (see Figure 4.11 and Table 4.13). Furthermore, the optimal control optimization identified the lowest and greatest values for the

Table 4.13: The optimized contact parameters from optimal control

	toe	ball	heel
k_v (N/m ³)	4.60e7	0.12e7	0.95e7
a_v (s/m)	0.0654	3.0000	2.1490
μ_s	0.0102	1.2000	0.1765
μ_d	0.0100	1.1871	0.1121

volumetric stiffness and damping of the ball ellipsoids, respectively, that proves that the ball ellipsoids also have a larger effect on the smoothness of the normal GRFs than the toe and heel ellipsoids.

However, the geometry of the ball ellipsoids, identified in the trajectory optimization, was not as expected. As shown in Figure 4.10, the ball ellipsoids did not have an adequate penetration volume to create the normal GRFs. To compensate, the heel and toe ellipsoids had unnatural geometries and large penetration volumes, which did not succeed in generating accurate GRFs.

Another reason behind the inaccurate tangential GRFs from the trajectory optimization would be the methodology used (explicit inverse dynamics simulation). The friction in our foot-ground contact was generated by a continuous velocity-based friction model. It is difficult for a velocity-based friction model to stay in the sticking regime in an inverse simulation, because any small errors in the experimental velocities (measurement or calculation errors) may lead to large errors in the friction force due to the high sensitivity of friction force to velocity [20]. However, our optimal control optimization, which used implicit dynamics simulation, resulted in a small level of error in the velocity and consequently more accurate tangential GRFs. In the implicit dynamic simulation, the error of the velocity can be controlled better than the explicit inverse dynamics simulation since the joint jerks were considered as a control input and minimized as a cost term and joint torques were also assumed as control inputs driving the model.

Optimal control is more suitable than trajectory optimization to identify a large number of parameters because if some experimental data are not available for being tracked, they can be predicted through the optimal control approach. This optimization provides this possibility for us to track not only the torques, but also the motions for which no experimental data were available.

In the optimal control optimization, the states (i.e., motion and its first and second derivatives) and control inputs (i.e., torques and the third derivative of motion) were parameterized and then estimated through the optimization. Therefore, the absence of the experimental angle and torque for the metatarsal joints and experimental GRMs and center of pressure for the feet were compensated by the predictability feature of the direct collocation method. Figure 4.12 shows the simulated joint angles obtained by the optimal control optimization. Since the simulated joint angles and joint torques, for which the experimental data were available, tracked the corresponding experimental data very well, the optimal control optimization could predict physiologically meaningful values for the angles and torques of the metatarsal joints, for which no experimental data were available.

Predicted metatarsal torques and angles are shown in Figure 4.8 and Figure 4.12,

respectively. Unlike the resultant torques and angles for the hip, knee and ankle joints, the resultant torques and angles for the right and left metatarsals are less symmetric. One reason for this is that the metatarsal torques and angles were fully predicted; we did not have any experimental data of them to track in the optimization. The other reason is that we did not have a strong (i.e., experimental-data-based) initial guess for the metatarsal angles and torques of our subjects.

In the trajectory optimization, the inputs (i.e., motion and its first and second derivatives) were the fixed data measured or calculated from experimental results. Thus, since the third derivatives of motion were always fixed, they could not be minimized unlike the optimal control optimization, in which joint jerks were minimized. Moreover, in the trajectory optimization, unlike the optimal control optimization, no boundaries could be defined for the torques and GRFs to lead them to have meaningful values, and also there was no control on the torques that were constrained to satisfy the inverse dynamics.

Another shortcoming of the trajectory optimization is that no path constraints on the outputs could be applied. Therefore, the residual loads on the pelvis could not be reduced to zero thereby causing inaccurate joint torques to be estimated by the optimization. Figure 4.13 shows the residual forces and moments obtained by the trajectory optimization and the optimal control optimization; The corresponding RMSEs are shown in Table 4.9.

4.4 Contact, Segment, and Joint Parameter Identification Using Optimal Control

The results presented in Section 4.3.3 illustrate that optimal control is more efficient than trajectory optimization in identifying the large number of parameters of the 3D ellipsoidal volumetric contact model. However, in the optimal control approach, there are still a few gaps that should be filled to get more accurate GRF results.

In this section, we fill in the gaps of the optimal control approach by adding some constraints along with identifying some of the segment and joint properties. Using these modifications, we estimate more accurate GRFs and a more natural motion than those estimated by the approaches discussed in Section 4.3.

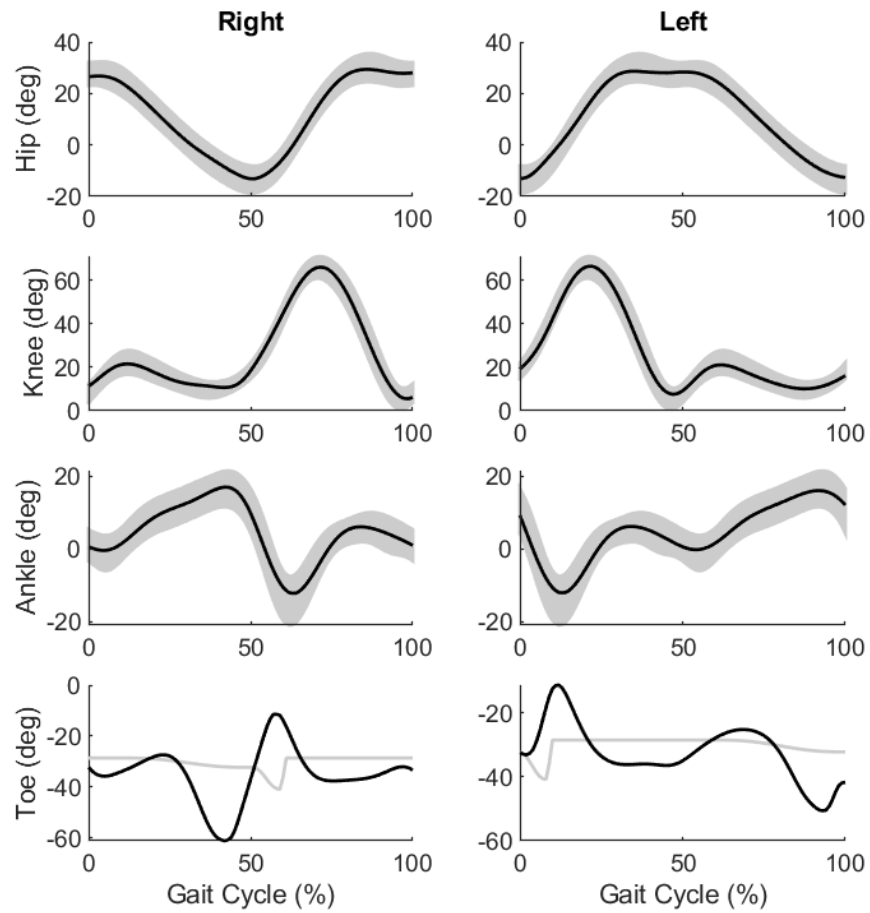


Figure 4.12: The lower extremity joint angles from optimal control (The gray areas in the plots of hip, knee and ankle joint angles represent the mean experimental angle data with the specified standard deviations reported by [18] and the gray lines in the plots of metatarsal angles represent the trajectory we planned and considered as the initial guess for the optimization)

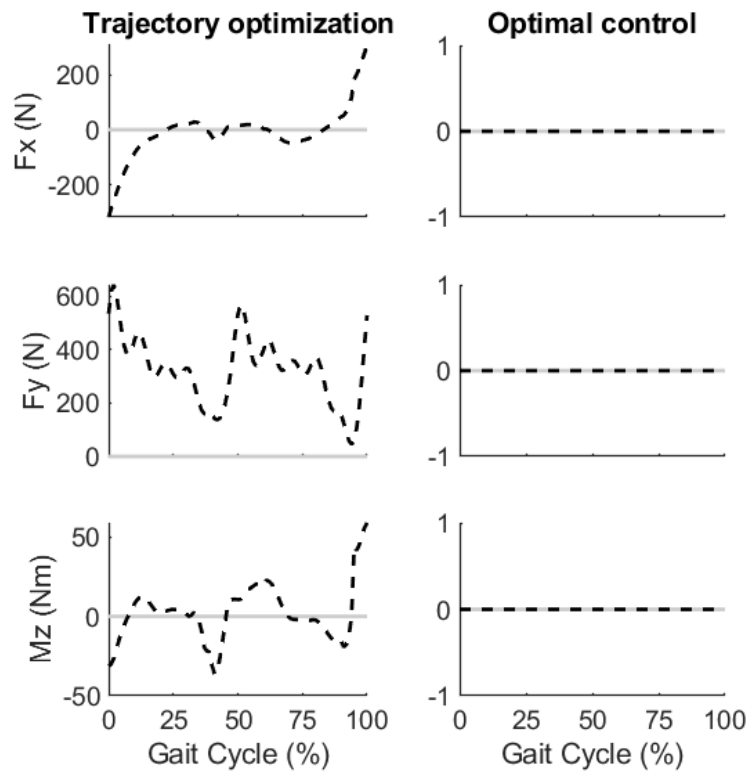


Figure 4.13: The residual forces and moment acting on the pelvis obtained from trajectory optimization (first column) and optimal control optimization (second column)

Table 4.14: Bounds on body and joint parameters

parameter	lower bound	upper bound	parameter	lower bound	upper bound
mass (kg)	$0.5SM_i$	$1.5SM_i$	stiffness (Nm/Rad)	0	$3K_i$
moment of inertia (kgm ²)	$0.5MOI_i$	$1.5MOI_i$	damping (Nm/Rad/s)	0	$3B_i$
center of mass (m)	$0.5COM_i$	$1.5COM_i$			

The index i denotes the initial values that were determined in Section 4.1.1.

4.4.1 Modifications

Body and Joint Property Identification

In the new approach, in addition to 39 contact parameters, 25 more parameters were considered as optimization parameters and identified through the optimal control identification optimization: 12 of these 25 parameters include the masses and moments of inertia of the HAT, thigh, shank, hind-foot, fore-foot and toe segments; 5 of them are the mass centers of the thigh, shank, hind-foot, fore-foot and toe segments; And the 8 remaining parameters are the spring stiffness and damping coefficient of the hip, knee, ankle, and metatarsal joints. To identify these 25 optimization parameters for our child model, we considered relatively large and physically-meaningful bounds. Table 4.14 shows the lower and upper bounds for the segment parameters (mass (SM), moment of inertia (MOI), center of mass (COM)), and joint parameters (spring stiffness (K) and damping coefficient (B)).

The mass properties of the body segments, including mass, moment of inertia, and center of mass, were extracted from [186] and scaled for the model using the average mass and height of the 20 healthy child subjects, as described in Section 4.1.1. Since the mass properties are roughly approximated by scaling, the motion prediction would be more accurate if the mass properties are tuned/identified in addition to the contact parameters through the optimal control identification optimization.

The joint properties, including spring stiffness and damping coefficient, were extracted from [171], as described in Section 4.1.1. The values reported for the spring stiffness and damping coefficient in [171] have been estimated given the experimental gait data for the four healthy adult subjects. However, the focus of our study is on child subjects. Thus, the results would be more natural if joint properties are also identified for the child subjects through the optimal control identification optimization.

Constraint on Normal Reaction Force of Each Ellipsoid

In Section 4.3, no constraint was defined on the simulated GRFs. They were only imposed to track the experimental GRFs through the cost function.

The net normal GRF of a foot is calculated by summing the normal GRFs produced by the three ellipsoids of that foot. Since the contact between the foot and the ground is unilateral (i.e., normal GRF is always positive), the normal GRF of each ellipsoid must be constrained to be positive during the walking in order to have a physically-meaningful contact model. Thus, in the new approach, six additional path constraints were applied to the optimal-control optimization to constrain the six normal GRFs which are produced by the six ellipsoids, to be always positive.

Implicit Dynamics Error Reduction

In the optimal control optimization, implicit dynamic equations are satisfied as the path constraints expressed in Equation 4.10. However, at some iterations of the optimization, this constraint was not satisfied, which violates the predefined bounds (i.e., $[0, 10^{-12}]$). To resolve this issue, we added an extra cost term to the cost function to minimize the implicit dynamics for the 8 DOFs of the legs:

$$J = \frac{1}{t_f} \int_{t_0}^{t_f} \left[w_5 \sum_{i=1}^8 \left(\frac{\tau_{inv.} - u_2}{\tau_{max} - \tau_{min}} \right)_i^2 \right] dt \quad (4.12)$$

Residual Load Reduction

In addition to the violation of the implicit dynamics path constraint, we saw a similar violation in the path constraint on residual forces and torque (Equation 4.8). Thus, in the new approach, another cost term was added to enforce the three residual loads to be minimized:

$$J = \frac{1}{t_f} \int_{t_0}^{t_f} \left[w_6 \sum_{i=1}^3 \left(\frac{R_{pelvis}}{R_{max} - R_{min}} \right)_i^2 \right] dt \quad (4.13)$$

Table 4.15: The body properties tuned through the new approach

		HAT	thigh	shank	toe	forefoot	hindfoot
mass (kg)	initial	28.1	4.14	1.93	0.0858	0.257	0.257
	tuned	26.2	6.21	1.21	0.0429	0.224	0.129
moment of inertia (kgm ²)	initial	1.24	0.0494	0.0230	0.32e-4	4e-4	4e-4
	tuned	1.24	0.0247	0.0184	0.32e-4	4e-4	4e-4
center of mass (mm)	initial	-	155.9	156.6	31.6	47.7	32.0
	tuned	-	133.8	91.6	18.8	66.9	21.7

Although Eq. 4.12 and Eq. 4.13 seem equivalent, we need both to help the optimization solver to find the optimal solution faster and more accurately. Furthermore, our optimization, tracking the mean experimental data of 20 children, may generate higher residual forces and torques than the optimizations tracking subject-specific experimental data. Thus we need Eq. 4.13 to minimize the residual loads.

4.4.2 Results and Discussion

This optimization was done on a desktop computer with an Intel[®] Core[™] i7-6700 CPU @ 3.40 GHz with 16.0 GB RAM. To find the optimal solution subject to the constraints, the new approach took 5 hours, which is considerably longer than the computation time of the previous optimal control approach (11 minutes). The main reason is that the modifications of the new approach made the optimization more constrained than the optimal control approach described in Section 4.3.2. The new approach has six extra path constraints and two extra cost terms. Furthermore, the new approach required the identification of 25 more parameters, for a total of 64 parameters to be identified.

The weighting factors of the two new cost terms were set to 1/4 (i.e., $w_5 = 1/4$ and $w_6 = 1/4$) and the remaining weighting factors were kept unchanged. Table 4.15 and Table 4.16 show the identified values for the 17 body parameters and 8 joint parameters, respectively.

The identified body parameters did not vary significantly compared to the initial values, and the identified values are still within the physiologically-meaningful ranges. For instance, the sum of the identified mass values (41.80 kg) is close to the average mass of the subjects (41.40 kg), and it is within ± 1 standard deviation (i.e., 41.40 ± 15.5 kg) reported for the child subjects by [18].

Regarding the stiffness, the identified values for hip, knee, and ankle did not vary signif-

Table 4.16: The joint properties tuned through the new approach

		hip	knee	ankle	metatarsal
stiffness (Nm/Rad)	initial	2.89	1.59	6.039	6.039
	tuned	2.96	1.77	6.596	9.031
damping (Nm/Rad/s)	initial	3e-4	2.98	3.68	3.68
	tuned	4e-4	0.189	0	5.51

icantly compared to the initial values. The initial values were set to the minimum stiffness values reported for adults in [169]. To provide stability, adults have higher stiffness at joints than children during challenging balance tasks like gait [22]. Thus, it is physiologically-meaningful that the tuned values for our child subjects are close to the minimum stiffness values for adults. On the other hand, for the stiffness of the metatarsal joints, a higher value was identified than its initial value. To the best of our knowledge, there is no stiffness value reported for the metatarsal joint in the literature, and thus no basis to validate the tuned values. However, the high stiffness value can be justified as the metatarsal joint should be stiffer than the other joints to stabilize its motion.

Regarding the damping coefficient, the identified values for hip, knee, and ankle are equal to or less than the initial values. The initial values were set to the minimum damping coefficients reported for adults in [169]. Since adults' joints have higher damping than children [22], the identified values would be physiologically-meaningful. On the other hand, a high value was identified for the damping coefficient of the metatarsal joint, which is necessary for reducing oscillations in response to external perturbations.

The geometries of the ellipsoids, identified through the new approach, are shown in Table 4.17 and Figure 4.14, and the remainder of the identified contact parameters are shown in Table 4.18. The dimensions, positions, and orientations of the ellipsoids did not vary significantly, except for the toe ellipsoid dimensions (i.e., the toe ellipsoid volume). On the other hand, the friction coefficient of the toe ellipsoid, identified through the new approach, has a higher value than the value identified through the optimal control approach. These two modifications on the toe ellipsoid seem necessary for the GRFs to better match the experimental data.

Regarding the friction coefficients in the previous optimal control approach, the friction of the ball ellipsoid was considerably larger than the other ellipsoids to compensate for the low friction values identified for the toe and heel ellipsoids. However, in the new approach, heel and toe ellipsoids even have higher friction coefficients than the ball ellipsoid. When the heel of one foot and the toe of the other foot are in contact with the ground (i.e., at

Table 4.17: The optimized geometry parameters for the left foot from the new approach

ellipsoid	dimensions (m)			orientations (degree)			positions (m)		
	a	b	c	γ	β	α	r_x	r_y	r_z
toe	0.0177	0.0300	0.0165	-33.38	-28.89	155.39	0.1632	0.0041	0.0235
ball	0.0800	0.0206	0.0179	-58.49	-12.45	-89.10	0.0675	0.0089	-0.0060
heel	0.0309	0.0400	0.0135	-83.00	-20.36	-91.08	-0.0256	0.0035	0.0003

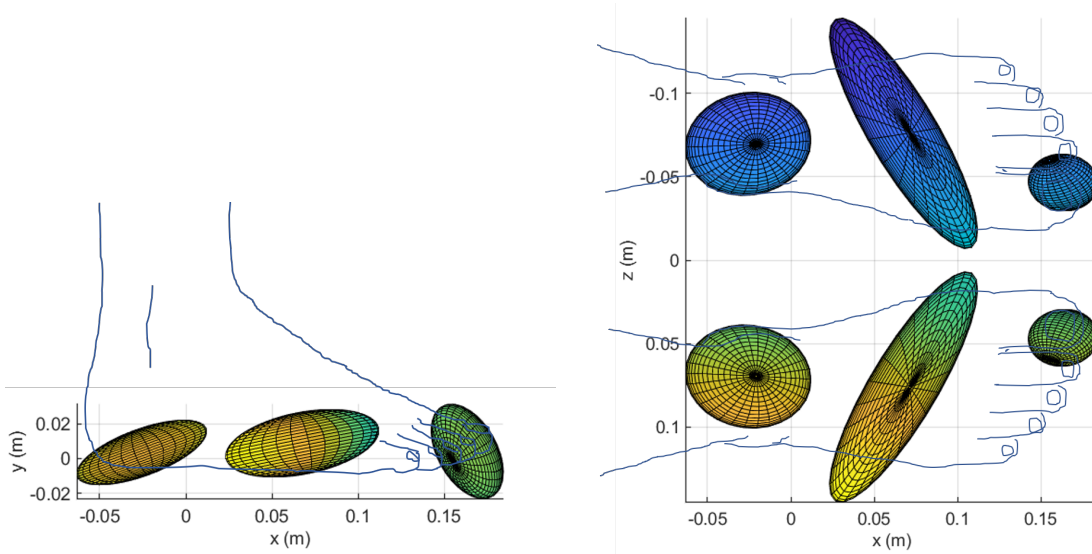


Figure 4.14: The optimized contact model geometry from the new approach

Table 4.18: The optimized contact parameters from the new approach

	toe	ball	heel
k_v (N/m ³)	0.75e7	2.40e7	1.54e7
a_v (s/m)	1.1355	1.89e-5	2.4271
μ_s	0.3404	0.0101	0.1703
μ_d	0.2819	0.0100	0.1686

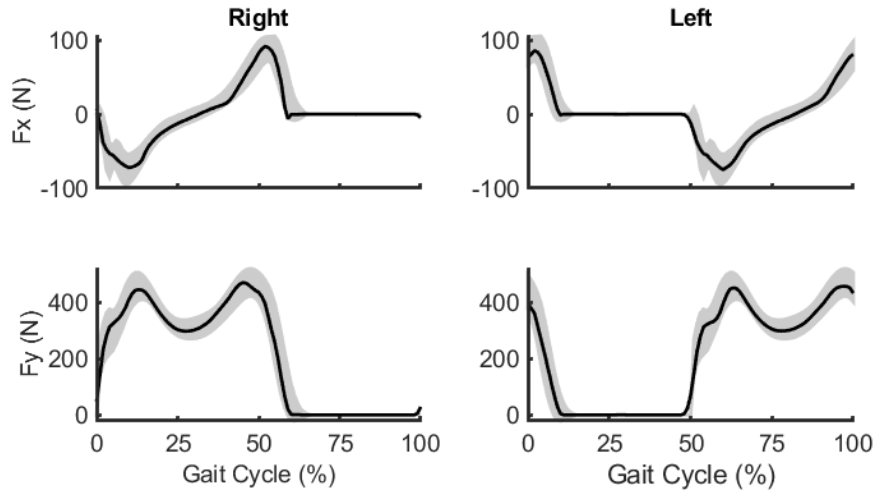


Figure 4.15: The tangential and normal ground reaction forces from the new approach (The gray areas show ± 1 standard deviations of the mean experimental GRFs reported by [18])

the end of the stance phase), more friction is required for toe and heel ellipsoids than the ball ellipsoid to provide a stable motion since the contact area is small at that time.

Figure 4.15 shows the resultant GRFs obtained using the new approach. As previously shown in Figure 4.9, the tangential force of the right foot obtained from the optimal control approach does not match the experimental GRF at the end of the stance phase. However, in the new approach, since the size and friction coefficient of the toe ellipsoid were modified, the obtained tangential force for the right foot is in good agreement with the experimental data. The RMSE for the tangential force of right and left feet are 3.37 N and 2.71 N, respectively, which are about 75% less than the RMSE of the optimal control approach. The RMSE for the normal force of right and left feet are 9.94 N and 10.72 N, respectively, which are 60% less than the RMSE of the previous optimal control approach.

4.5 Conclusion

In this chapter, a 2D human model was developed, and the 3D ellipsoidal volumetric contact was applied on both feet. The dynamic equations of the multibody model and the contact equations were developed symbolically. We employed two different approaches to identify the contact parameters: GlobalSearch trajectory optimization and direct col-

location optimal control. Finally, a third approach was introduced in which the second approach (i.e., optimal control) was modified by adding some constraints and identifying some of the mass and joint properties.

We presented a computationally efficient symbolic ellipsoidal volumetric foot-ground contact model that simulates more accurate normal and tangential reaction forces than previous volumetric models [21]. The results showed that for parameter identification, especially when not all the experimental data are available, optimal control with implicit dynamics is more accurate than the trajectory optimization with inverse dynamics.

We showed that in addition to the contact parameters, the mass and joint properties of the subjects should be identified through the optimization. Since the experimental data of those subjects are tracked in the optimization, the identified values for the mass and joint properties would be more realistic than the initial values estimated from the literature.

For the trajectory optimization, the root-mean-square errors of the resultant tangential and normal ground reaction forces were 36.51 (N) and 234.57 (N). For the optimal control, these errors were 14.07 (N) and 26.44 (N), respectively, and for the third approach, they are 3.04 (N) and 10.33 (N). Although the optimal control approach's errors are considerably lower than those from the trajectory optimization, the errors of the tangential and normal forces from the third approach are 75% and 60% less than the errors from the optimal control approach, respectively. Therefore, the third approach could estimate the most realistic contact parameters among the three approaches. For all child gait simulations in the remainder of the thesis, we will use direct collocation optimal control in which the contact parameters, mass and joint properties are assumed constant and set to the values identified using the third approach in this chapter.

Chapter 5

Muscle-Torque-Generator Model Development For Child Gait

To obtain a physiologically-meaningful prediction for human gait, it is necessary to have a more accurate model than the SK model described in Chapter 4. Although the SK model can be upgraded to a more detailed MSK/NMSK model, some details are not required for this study since joint contact forces (or, muscle forces) do not play an important role. Furthermore, it is challenging to fit a detailed MSK/NMSK to specific subjects. Thus, we upgraded our SK model by adding a reduced muscle model that can more easily fit specific subjects than the detailed muscle models do. In our upgraded model, joints are actuated by groups of agonist and antagonist muscle torque generators (MTGs) [69, 114].

The following chapter is divided into three main sections: (5.1) Muscle-Torque-Generator Model, (5.2) Musculoskeletal Model and (5.3) Neuromusculoskeletal Model. In the Muscle-Torque-Generator Model section, the MTG model used for our child model was introduced. The MTG parameters were fitted to the child model considering the experimental child gait motion data. In the Musculoskeletal Model section, an activation-to-torque model was developed to actuate the joints. The musculoskeletal geometry and muscle contraction dynamics of the MSK model were represented by an MTG model. The MTG parameters were set to the identified values from Section 5.1. The MSK model was used to investigate whether the fitted MTGs can generate motion, torques, and GRFs consistent with the experimental child data. In the Neuromusculoskeletal Model section, an EMG-to-torque model was developed to actuate the joints. The muscle activation dynamics were added to the MSK model of Section 5.2 and the parameters associated with the muscle activation dynamics were identified for the child model. Our proposed NMSK model enabled us to

predict the muscle excitations and estimate the cost of transport (i.e., metabolic energy consumed per unit body mass per unit distance traveled) with a good approximation.

Child gait analyses are required for paediatric rehabilitation and design of wearable robotic systems for children [142] in the future. The main contribution of this chapter is to generate simplified but accurate MSK and NMSK models that best fit children and would support the design of wearable robotic systems for children. The parameters identified in this chapter will be used in the next chapters to predict physiologically-meaningful motion, torque, ground reaction forces (GRFs), and muscle excitations for child gait.

5.1 Muscle-Torque-Generator Model

To generate an anatomically-simplified muscle model, we used the MTG model recently developed by Millard et al. [114]. In their model, each joint is actuated by agonist and antagonist pairs of MTGs that have no co-contractions. A single MTG torque (τ^M) is the sum of active torque (τ_{active}^M) and passive torque ($\tau_{passive}^M$):

$$\tau^M(a, \theta, \dot{\theta}) = \tau_{active}^M(a, \theta, \dot{\theta}) + \tau_{passive}^M(\theta, \dot{\theta}) \quad (5.1)$$

where a , θ and $\dot{\theta}$ are muscle activation, joint angle and angular velocity, respectively. The τ^M obtained from Eq. 5.1 is always positive. Passive torque is produced by muscle tissue, tendons and ligaments when they are stretched. Active torque is produced by groups of agonist and antagonist muscles acting about a specific moment arm [7]. The active and passive torques are modelled as:

$$\tau_{active}^M(a, \theta, \dot{\theta}) = \tau_0^M \left(a \mathbf{t}^A(\theta) \mathbf{t}^V(\dot{\theta}) \right) \quad (5.2)$$

$$\tau_{passive}^M(\theta, \dot{\theta}) = \tau_0^M \left(\mathbf{t}^P(\theta) \left(1 - \beta^P \frac{\dot{\theta}}{\omega_{max}^M} \right) \right) \quad (5.3)$$

where τ_0^M is the maximum isometric torque of the subject. \mathbf{t}^A , \mathbf{t}^V and \mathbf{t}^P are the normalized active-torque-angle, active-torque-angular-velocity and passive-torque-angle curves of the muscle, respectively, that are reported in [7, 71, 114]. These curves are called “*characteristic curves*” since they are dependent on geometric properties of muscles and they vary from muscle to muscle. β^P and ω_{max}^M are the damping term and maximum angular velocity of MTG, respectively. The nonlinear damping term (i.e., $1 - \beta^P \frac{\dot{\theta}}{\omega_{max}^M}$) is included in the passive torque to suppress vibration.

By substituting Eq. 5.2 and Eq. 5.3 for τ_{active}^M and $\tau_{passive}^M$ in Eq. 5.1, $\tau^M(a, \theta, \dot{\theta})$ can be written as:

$$\tau^M(a, \theta, \dot{\theta}) = \tau_0^M \left(a \mathbf{t}^A(\theta) \mathbf{t}^V(\dot{\theta}) + \mathbf{t}^P(\theta) \left(1 - \beta^P \frac{\dot{\theta}}{\omega_{max}^M} \right) \right) \quad (5.4)$$

In this MTG model, characteristic curves are defined as 5th-order Bézier curves that are continuous to the second derivative. Thus, this MTG model can be consistent with gradient-based optimization that is used in our study. The characteristic curves can be fitted to a specific subject by changing the control points of Bézier curves. However, Millard et al. [114] modified the curves' equations with additional parameters that transform the curves. Thus, to fit the MTG model to a specific subject, they have identified the parameters through an optimization rather than directly changing the control points of Bézier curves. The characteristic curves, modified by transformation parameters, are considered as:

$$\mathbf{t}^A(\theta, s^A, \lambda^A) = \lambda^A + (1 - \lambda^A) \mathbf{t}^A\left((\theta - \theta_0)/s^A + \theta_0\right) \quad (5.5)$$

$$\mathbf{t}^V(\dot{\theta}, s^V, \lambda^V) = \lambda^V + (1 - \lambda^V) \mathbf{t}^V(\dot{\theta}/s^V) \quad (5.6)$$

$$\mathbf{t}^P(\theta, \Delta^P, \lambda^P) = (1 - \lambda^P) \mathbf{t}^P(\theta - \Delta^P) \quad (5.7)$$

where $s^A, \lambda^A, s^V, \lambda^V, \Delta^P, \lambda^P$ are the transformation parameters that are called “*fitting parameters*”. By substituting the modified curves in Eq. 5.4,

$$\tau^M(a, \theta, \dot{\theta}, \mathbf{\Gamma}) = s^\tau \tau_0^M \left(a \mathbf{t}^A(\theta, s^A, \lambda^A) \mathbf{t}^V(\dot{\theta}, s^V, \lambda^V) + \mathbf{t}^P(\theta, \Delta^P, \lambda^P) \left(1 - \beta^P \frac{\dot{\theta}}{s^V \omega_{max}^M} \right) \right) \quad (5.8)$$

can be obtained. In addition to the six fitting parameters above-mentioned, an extra fitting parameter (i.e., s^τ) is also used in Eq. 5.8 to scale the maximum isometric torque of the subject. Thus, there exists a total of seven parameters in the MTG model:

$$\mathbf{\Gamma} = \{s^\tau, s^A, \lambda^A, s^V, \lambda^V, \Delta^P, \lambda^P\} \quad (5.9)$$

These parameters are physically-meaningful, and they can be perceived as muscle properties since altering them alters the muscle properties directly. If the value of s^τ increases, the cross-sectional area of the muscle or the moment arm of the joint may increase. Increasing parameters s^A and s^V is equivalent to increasing the optimal fiber length of the muscle, or equivalently, decreasing the moment arm of the muscle. Parameters Δ^P and λ^P

adjust the muscle flexibility. The remaining parameters (i.e., λ^A and λ^V) have been defined to ensure that \mathbf{t}^A and \mathbf{t}^V always have non-zero values and consequently, a will never be omitted from the MTG model.

Millard et al. [114] have verified their approach by fitting these parameters to a 35-year-old male subject stooping to pick up a box. They have extracted the preliminary characteristic curves from [7, 71, 74] including some elite athletes' dynamometry data. They have fitted the curves to the 35-year-old male subject by identifying the fitting parameters through an optimization. In this optimization, $\mathbf{\Pi} = [s^\tau, s^A, s^V, \Delta^P, \lambda^P]$ were included as the optimization variables. Vector $\mathbf{\Pi}_0 = [1, 1, 1, 0, 0]$ was considered as the initial guess for the optimization variables. The optimization variables were enforced to be as close as possible to the initial guess using the cost function:

$$(\mathbf{\Pi} - \mathbf{\Pi}_0)W(\mathbf{\Pi} - \mathbf{\Pi}_0)^T \quad (5.10)$$

where W is the weighting matrix for which the diagonal elements are 1. The remaining fitting parameters (i.e., λ^A and λ^V), were excluded from the identification process and they were set to a constant value (i.e., $\sqrt[4]{\epsilon}$) where $\epsilon = 2.22 \times 10^{-16}$.

Our aim is to modify Millard's MTG model to fit our child model. We found Millard's MTG model well suited for our aim since their MTG model is compatible with gradient-based optimization that is used in our research. Furthermore, Millard's MTG model includes fitting parameters that can be more easily adapted to a child model than the control points of the Bézier curves.

5.1.1 Muscle-Torque-Generator Parameter Identification

To adapt Millard's MTG model to our child model, we developed a direct orthogonal collocation optimal control. We identified all the fitting parameters for the child model regarding the child subjects' experimental gait data. To implement this optimization, we used the IPOPT solver in first derivative mode with the tolerance of 1e-5. Although GPOPS-II contains an adaptive mesh refinement algorithm, we considered a fixed mesh of 100 collocation points, divided into 20 intervals, over the whole gait cycle to reduce the computation time. This optimization was done on a desktop computer with an Intel® Core™ i7-6700 CPU @ 3.40 GHz with 16.0 GB RAM.

For the metatarsal joint, dynamometry data is not easily measurable, and there is no characteristic curve reported for the metatarsal joint in the literature. Thus, in this study, the metatarsal joints were kept torque-driven and MTGs were employed only for the hip,

knee, and ankle joints, and the fitting parameters were identified for them. To decrease the computational time of the identification process, we identified the fitting parameters only for the MTGs of the right leg since our human model is bilaterally symmetric. Then, the same identified parameters for the right leg were used to generate MTGs for the left leg.

Methodology

In this optimal control approach, states and control inputs are set as:

$$\mathbf{x}(t) = [\boldsymbol{\theta}(t), \dot{\boldsymbol{\theta}}(t)] \quad (5.11)$$

$$\mathbf{u}(t) = [\ddot{\boldsymbol{\theta}}(t)] \quad (5.12)$$

where $\mathbf{x}(t)$ includes angles and angular velocities of right hip, knee and ankle joints. $\mathbf{u}(t)$ includes angular accelerations of right hip, knee and ankle joints. There are 6 MTGs in this model. Each joint is activated by a pair of an agonist (i.e., flexor) MTG and an antagonist (i.e., extensor) MTG that have no co-contraction.

Each MTG was modeled using Eq. 5.8, which includes 7 fitting parameters ($\boldsymbol{\Gamma} = \{s^\tau, s^A, \lambda^A, s^V, \lambda^V, \Delta^P, \lambda^P\}$). In total, there are 42 parameters (6 MTGs \times 7 fitting parameters) that we identified for the child model.

The remaining parameters of Eq. 5.8 (i.e., β^P and ω_{max}^M) were set to constant values; Parameter β^P was set to 0.1 for all MTGs [113] and parameter ω_{max}^M was set to the values reported for adults in [114]:

$$\omega_{max}^M = \{9.0234, 9.1804, 19.2161, 16.6330, 11.7646, 17.2746\} \text{ (rad/s}^2\text{)} \quad (5.13)$$

that are for hip extensor, hip flexor, knee extensor, knee flexor, ankle extensor, and ankle flexor, respectively. Although these values are for adults, ω_{max}^M is implicitly tuned for the child model by identifying s^V .

Constraints

Four constraints are required to be satisfied at each time step of this optimization. To constrain the dynamic of the optimization,

$$\dot{\mathbf{x}}(t) = [\dot{\boldsymbol{\theta}}(t), \mathbf{u}(t)] \quad (5.14)$$

was imposed. This constraint generates the first derivatives of the states. To make the MTGs physiologically-meaningful,

$$\tau^M(a_{max}, \theta, \dot{\theta}, \mathbf{\Gamma}) - \tau_{exp.}^M(t) \geq 0 \quad (5.15)$$

$$\tau_{exp.}^M(t) - \tau^M(a_{min}, \theta, \dot{\theta}, \mathbf{\Gamma}) \geq 0 \quad (5.16)$$

$$\mathbf{t}_{max}^P - \mathbf{t}^P(\theta, \Delta^P, \lambda^P) \geq 0 \quad (5.17)$$

were imposed to each MTG, separately. Eq. 5.15 constrains the MTGs generated with the maximum activation to be not less than the experimental torques. Eq. 5.16 constrains the MTGs generated with the minimum activation to be not greater than the experimental torques. Eq. 5.17 constrains the normalized passive-torque-angle curve to be not greater than its feasible upper-bound (i.e., 1.4 [191]).

$\tau_{exp.}^M$ in Eq. 5.15 and Eq. 5.16 is not the $\tau_{exp.}$ but the flexor and extensor components of $\tau_{exp.}$. When the constraint is imposed to a flexor MTG, $\tau_{exp.}^M$ in the constraint is the flexor component of the $\tau_{exp.}$:

$$\tau_{exp.}^M(t) = \tau_{exp.}^{flx.}(t) = \begin{cases} \tau_{exp.}(t) & \tau_{exp.}(t) \geq 0 \\ 0 & \tau_{exp.}(t) < 0 \end{cases} \quad (5.18)$$

and when the constraint is imposed to an extensor MTG, $\tau_{exp.}^M$ in the constraint is the extensor component of the $\tau_{exp.}$:

$$\tau_{exp.}^M(t) = \tau_{exp.}^{ext.}(t) = \begin{cases} -\tau_{exp.}(t) & \tau_{exp.}(t) \leq 0 \\ 0 & \tau_{exp.}(t) > 0 \end{cases} \quad (5.19)$$

In this way, we can split up the experimental torque into a flexor component and an extensor component assuming that there is no co-contraction between them:

$$\tau_{exp.}(t) = \tau_{exp.}^{flx.}(t) + (-\tau_{exp.}^{ext.}(t)) \quad (5.20)$$

It should be noted that Eq. 5.18 and Eq. 5.19 can be used to split up $\tau_{exp.}$ into flexor/extensor components if the joint flexes about the positive axis of the joint coordinate system regarding the right-hand-rule convention. If the joint flexes about the negative axis, Eq. 5.18 will give the extensor components and Eq. 5.19 will give the flexor components.

Table 5.1: Bounds on the fitting parameters

parameter	bound	parameter	bound
s^τ	[1e-4 2]	λ^V	[1e-6 0.99]
s^A	[0.1 10]	Δ^P	[-1 1]
λ^A	[1e-6 0.99]	λ^P	[0 0.99]
s^V	[0.1 10]		

Bounds

The bounds for the states and control inputs were defined considering the experimental data. The bounds for the fitting parameters, shown in Table 5.1, were defined to include all the possible values for the parameters which make Eqs. 5.5-5.7 feasible. The bounds of each MTG were assumed to be identical.

Although s^τ is the coefficient of τ_0^M and its main role is to scale τ_0^M , this parameter also affects scaling the characteristic curves. Considering a large bound for s^τ may cause the optimization to find a value for s^τ that unrealistically scales both τ_0^M and the characteristic curves. To avoid this issue, we scaled τ_0^M of adults given the body mass and body height of our child model and the adult subject:

$$\tau_{0_{ch}}^M = \frac{BM_{ch} BH_{ch}}{BM_a BH_a} \tau_{0_a}^M \quad (5.21)$$

where $\tau_{0_a}^M$, BM_a , and BH_a are the τ_0^M , the body mass, and height of an adult, respectively, extracted from [7]. BM_{ch} and BH_{ch} are the mass and height of our child model. We substituted $\tau_{0_{ch}}^M$ for τ_0^M in the MTG equations of our child model. Using this approach, we can assume a small bound for s^τ scaling only τ_0^M without largely affecting the characteristic curves.

Initial Guess

The initial guess for time, states, and control inputs were defined regarding the child experimental data, and the initial guesses for the fitting parameters were set to

$$\mathbf{\Gamma}_{initial} = \{1, 1, \sqrt[4]{\epsilon}, 1, \sqrt[4]{\epsilon}, 0, 0\} \quad (5.22)$$

that allow Eqs. 5.5-5.7 to give the initial adult curves. In other words, if $\mathbf{\Gamma}_{initial}$ is substituted for the parameters in Eqs. 5.5-5.7, the right-hand-side of the equations will give $\mathbf{t}^A(\theta)$, $\mathbf{t}^V(\theta)$ and $\mathbf{t}^P(\theta)$, respectively.

Table 5.2: The identified MTG fitting parameters

MTG	s^τ (1)*	s^A (1)	λ^A ($\sqrt[4]{\epsilon}$)	s^V (1)	λ^V ($\sqrt[4]{\epsilon}$)	Δ^P (0°)	λ^P (0)
hip ext.	0.9995	0.9801	0.0042	1.0915	0.0078	0	0.0032
hip flx.	1.0067	1.0013	0.0037	1.3149	0.0118	0.2292	0.0032
knee ext.	1.0012	0.9159	0.0045	1.1222	0.0111	0	0.0032
knee flx.	1.0026	0.9765	0.0036	1.0505	0.0049	0	0.0032
ankle ext.	0.9999	1.0032	0.0036	1.0301	0.0034	4.2571	0.0030
ankle flx.	1.0015	1.0127	0.0034	1.0246	0.0044	0	0.0032

* The values inside () are the initial values.

Cost Function

The cost function to identify the fitting parameters for the child model consists of two cost terms:

$$J = w_1 \sum_{i=1}^{42} \left(\frac{\Gamma - \Gamma_{initial}}{\Gamma_{max} - \Gamma_{min}} \right)_i^2 + w_2 \int_{t_0}^{t_f} \sum_{i=1}^6 \left(\frac{x_{sim.} - x_{exp.}}{x_{max} - x_{min}} \right)_i^2 dt \quad (5.23)$$

where Γ_{max} and Γ_{min} were set to the upper and lower values of the feasible bounds assumed for the fitting parameters; $x_{exp.}$, x_{max} and x_{min} were extracted from the experimental motion data. The first cost term enforces the fitting parameters to be as close as possible to the initial guess to avoid underlying changes in the equations of the characteristic curves. The second cost term allows the simulated motion to track the experimental motion and ensure that the identified parameters (and consequently the fitted MTGs) can be used for our child gait simulation. The weights w_1 and w_2 were set to 0.001 and 1, respectively. w_1 was considered to be significantly less than w_2 to let the optimization identify parameters depending more on the child experimental motion than the adults' characteristic curves.

5.1.2 Results and Discussion

The optimization tracked the experimental hip, knee, and ankle angles with very low RMSEs (i.e., 0.46, 0.81, and 0.45 degrees, respectively), and identified the 42 fitting parameters of the right-leg MTGs. The identified values are shown in Table 5.2. To verify the identified values, we did two assessments.

For the first assessment, we plotted $\tau_{exp.}^M$ with respect to θ to ensure that it falls inside the isometric envelope. If $\tau_{exp.}^M(\theta)$ falls inside the isometric envelope, it means that the

demanded torque is within the feasible area, and the fitted MTGs can generate it. The isometric envelope is composed of an upper limit and a lower limit. The upper limit is the fitted active-torque-angle characteristic curve:

$$\tau_A^M = s^\tau \tau_0^M \mathbf{t}^A(\theta, s^A, \lambda^A) \quad (5.24)$$

and the lower limit is the fitted passive-torque-angle characteristic curve:

$$\tau_P^M = s^\tau \tau_0^M \mathbf{t}^P(\theta, \Delta^P, \lambda^P) \left(1 - \beta^P \frac{\dot{\theta}}{s^V \omega_{max}^M}\right) \quad (5.25)$$

Figure 5.1 shows that the torques demanded by the child gait have fallen inside the isometric envelopes.

For the second assessment, we plotted the demanded active torque with respect to $\dot{\theta}$ to examine if it is greater than zero and if it is limited by the fitted active-torque-angular-velocity characteristic curve. The demanded active torque was calculated using:

$$\tau_{Act.}^M = \tau_{exp.}^M - s^\tau \tau_0^M \mathbf{t}^P(\theta, \Delta^P, \lambda^P) \left(1 - \beta^P \frac{\dot{\theta}}{s^V \omega_{max}^M}\right) \quad (5.26)$$

and the fitted active-torque-angular-velocity characteristic curve is:

$$\tau_V^M = s^\tau \tau_0^M \mathbf{t}^V(\dot{\theta}, s^V, \lambda^V) \quad (5.27)$$

Figure 5.2 shows that the active torques demanded by the child gait have been limited by the fitted active-torque-angular-velocity curves. Since the two assessments were satisfied, we can claim that the identified fitting parameters are feasible, and consequently, they can be used in child gait modeling.

5.2 Musculoskeletal Model

An MSK model includes two main parts: a muscular model and an SK model. The muscular model is an activation-to-torque model that can be developed as either an anatomically-detailed or anatomically-simplified model based on the purpose of the research. In the anatomically-detailed muscular model, muscle contraction dynamics and musculoskeletal geometry are developed in detail, and there are many subject-specific parameters that should be identified. In the anatomically-simplified muscular model, muscle torque generators (MTGs) are used to actuate joints. As shown in Figure 5.3, muscle contraction

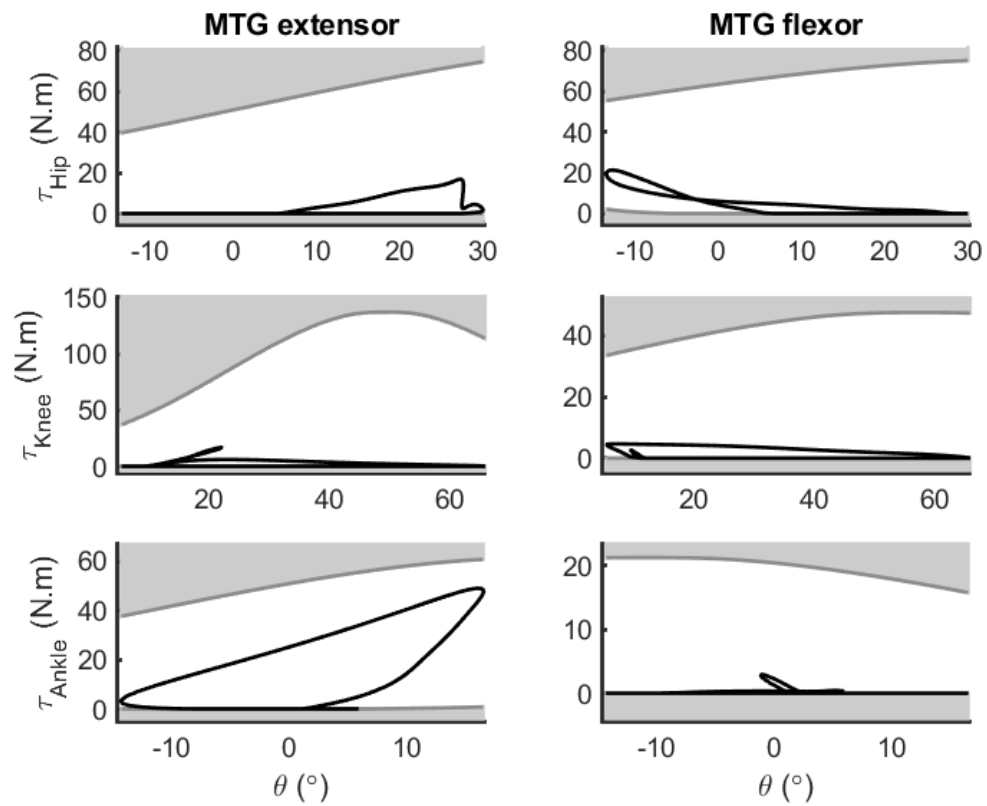


Figure 5.1: The feasible areas for the demanded torques. (The black curves are the demanded torques and the light gray areas are infeasible. The upper and lower dark gray curves are the fitted active-torque-angle and passive-torque-angle curves, respectively)

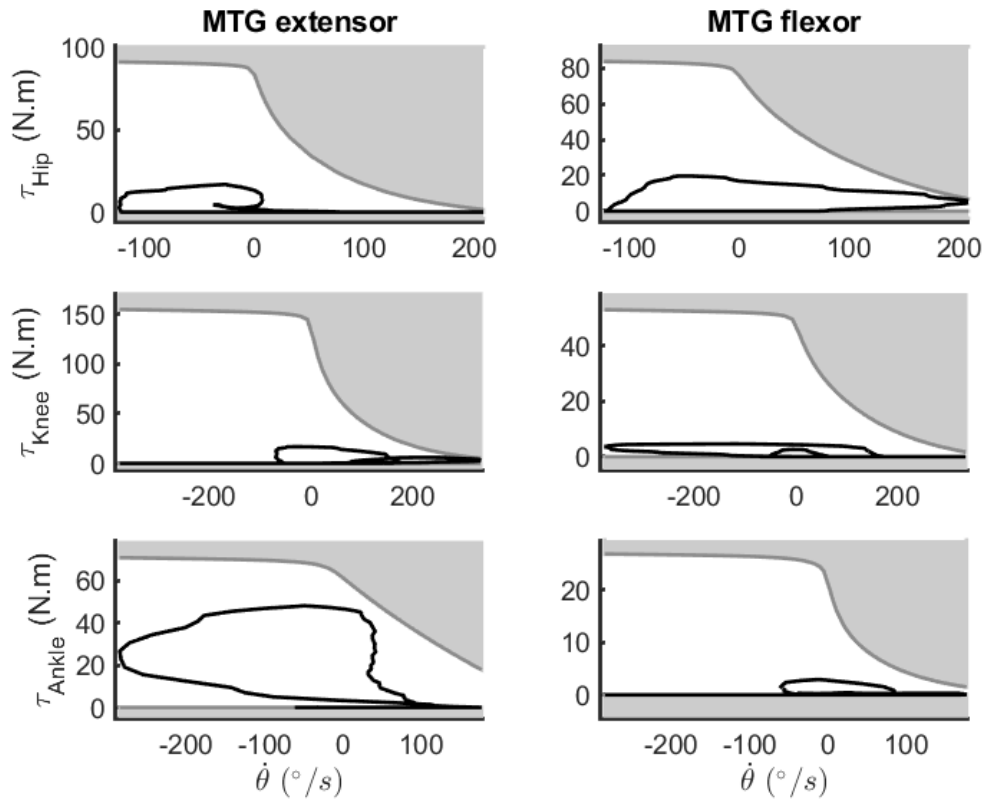


Figure 5.2: The feasible areas for the demanded active torques. (The black curves are the demanded active torques and the light gray areas are infeasible. The upper dark gray curves are the fitted active-torque-angular-velocities)

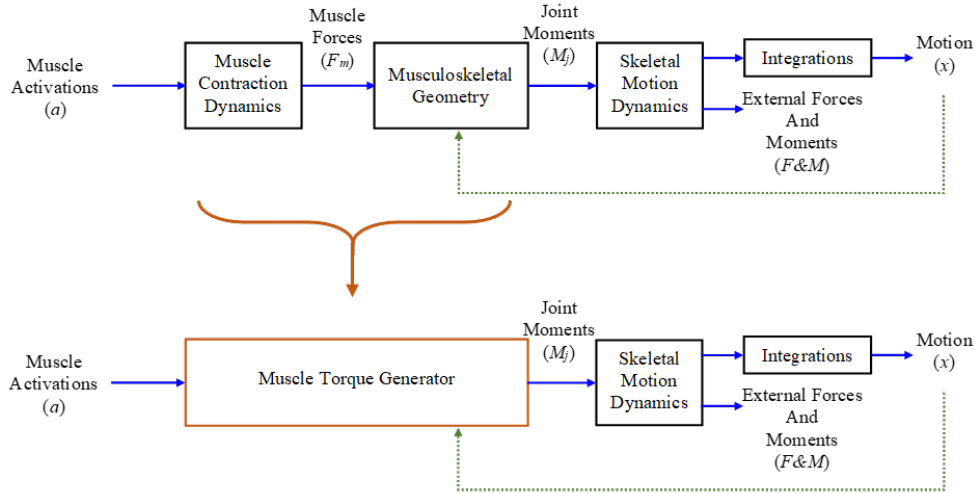


Figure 5.3: The workflow of the MSK model

dynamics and musculoskeletal geometry blocks can be replaced by MTGs. In this way, the MTG parameters, that should be identified subject-specifically, are considerably fewer in number than parameters in the anatomically-detailed muscular model.

In this section, we developed a simplified MSK model in which the MTGs, identified in Section 5.1, were used. Then, through a direct collocation optimal control, we used the MSK model to simulate child gait to investigate whether the fitted MTGs can generate a gait motion consistent with the experimental data.

5.2.1 Natural Child Gait Simulation

For the human model of the MSK model, we considered the same 11-DOF human model and 3D ellipsoidal volumetric foot-ground contact model used for the SK model in Chapter 4. However, in the MSK model, in contrast to the SK model, the hip, knee, and ankle joints are actuated by the MTGs identified in Section 5.1. There are 12 MTGs in the MSK model: each of the hip, knee, and ankle joints of the two legs was assumed to be actuated by a pair of agonist and antagonist MTGs.

We used GPOPS-II to implement the optimal control algorithm. We used the IPOPT solver in first derivative mode with the tolerance of $1e-5$. Although GPOPS-II contains an adaptive mesh refinement algorithm, we considered a fixed mesh of 100 collocation points, divided into 20 intervals, over the whole gait cycle to reduce the computation time. This

simulation was done on a desktop computer with an Intel[®] Core™ i7-6700 CPU @ 3.40 GHz with 16.0 GB RAM.

Methodology

In this optimal control, the states and control inputs are as:

$$\mathbf{x}(t) = [\mathbf{q}(t), \dot{\mathbf{q}}(t), \ddot{\mathbf{q}}(t)] \quad (5.28)$$

$$\mathbf{u}(t) = [\ddot{\mathbf{q}}(t), \mathbf{R}_{pelvis}(t), \boldsymbol{\tau}_{toe}(t), \mathbf{a}(t)] \quad (5.29)$$

where the states include the 11 generalized coordinates, 11 velocities, and 11 accelerations. The control inputs include the 11 joint jerks ($\mathbf{u}_1(t) = \ddot{\mathbf{q}}(t)$), the 3 residual loads on the pelvis ($\mathbf{u}_2(t) = \mathbf{R}_{pelvis}(t)$), the 2 torques of the metatarsal joints ($\mathbf{u}_3(t) = \boldsymbol{\tau}_{toe}(t)$), and the 12 MTG activations ($\mathbf{u}_4(t) = \mathbf{a}(t)$).

In this optimal control, the states and control inputs were parametrized to minimize a cost function including data-tracking cost terms subject to some constraints with the aim of simulating a natural child gait. No parameter was identified in this optimization, and the contact parameters and MTG parameters were set to the values identified in previous sections for the child.

Constraints

The constraints of this optimization are the same as the constraints defined for the contact parameter identification in Chapter 4:

- The dynamic friction was enforced to be less than static friction coefficient (Eq. 4.4).
- The residual loads on the pelvis were imposed to be minimized (Eq. 4.8).
- A dynamic constraint, in which the first derivatives of the states are calculated, was imposed to be satisfied (Eq. 4.9).
- An algebraic constraint, in which the motion dynamics are solved implicitly, was imposed (Eq. 4.10). However, in this optimization, this constraint is slightly different from Eq. 4.10 since MTG activations, instead of the joint torques, are considered as the control inputs. Thus the constraint was modified as:

$$\mathbf{C}_{min} \leq (\boldsymbol{\tau}_{inv.}(t) - \boldsymbol{\tau}_{input}(t))^2 \leq \mathbf{C}_{max} \quad (5.30)$$

where $\boldsymbol{\tau}_{input}(t)$ was defined as:

$$\boldsymbol{\tau}_{input}(t) = [\mathbf{u}_2(t), \boldsymbol{\tau}_j^M(t), \mathbf{u}_3(t)] \quad (5.31)$$

where $\boldsymbol{\tau}_j^M(t)$ includes the 6 joint torques (i.e., torques of hips, knees and ankles) generated by the 12 MTGs (i.e., 6 pairs of agonist and antagonist MTGs). For instance, the right hip torque is generated by the right hip flexor MTG and extensor MTG:

$$\boldsymbol{\tau}_{hip_r}^M(t) = \boldsymbol{\tau}_{flx.hip_r}^M(t) - \boldsymbol{\tau}_{ext.hip_r}^M(t) \quad (5.32)$$

- The normal GRF, created by each ellipsoid, was constrained to be positive during walking.

Bounds

The bounds for the states and the $\mathbf{u}_1(t)$, $\mathbf{u}_2(t)$ and $\mathbf{u}_3(t)$ were set to the same bounds considered for the contact parameter identification in Chapter 4. The bound for the $\mathbf{u}_4(t)$ was set to $[0, 1]$ since we assumed the minimum and maximum values are 0 and 1, respectively.

Initial Guess

The initial guess for the states and the $\mathbf{u}_1(t)$, $\mathbf{u}_2(t)$ and $\mathbf{u}_3(t)$ were set to the initial guess considered for the contact parameter identification in Chapter 4. To determine the initial guess for the $\mathbf{u}_4(t)$, we set $\tau_{exp}^M(t)$ (Eq. 5.18 or Eq. 5.19) equal to the fitted $\tau^M(a, \theta, \dot{\theta}, \boldsymbol{\Gamma})$ (Eq. 5.8) and solved the equation for the $a(t)$ given the experimental motion data. The obtained $a(t)$ was considered as the initial guess for the $\mathbf{u}_4(t)$.

Cost Function

The cost function consists of 7 cost terms:

$$\begin{aligned}
 J = \frac{1}{t_f} \int_{t_0}^{t_f} & \left[w_1 \sum_{i=1}^6 \left(\frac{\tau_{sim.} - \tau_{exp.}}{\tau_{max} - \tau_{min}} \right)_i^2 + w_2 \sum_{i=1}^4 \left(\frac{GRF_{sim.} - GRF_{exp.}}{GRF_{max} - GRF_{min}} \right)_i^2 \right. \\
 + w_3 \sum_{i=1}^{11} & \left(\frac{q_{sim.} - q_{exp.}}{q_{max} - q_{min}} \right)_i^2 + w_4 t_f^6 \sum_{i=1}^{11} \left(\frac{u_1}{u_{1max} - u_{1min}} \right)_i^2 + w_5 \sum_{i=1}^{12} \left(\frac{u_4}{u_{4max} - u_{4min}} \right)_i^2 \\
 + w_6 \sum_{i=1}^3 & \left(\frac{R_{pelvis}}{R_{max} - R_{min}} \right)_i^2 + w_7 \sum_{i=1}^8 \left(\frac{\tau_{inv.} - \tau_{input}}{\tau_{max} - \tau_{min}} \right)_i^2 \left. \right] dt
 \end{aligned} \tag{5.33}$$

where the first three cost terms are the data-tracking terms helping the optimization to simulate a child-like motion. The fourth and fifth cost terms minimize the joint jerk squared and the MTG activation squared. Minimizing the joint jerk squared results in a feasible solution even with a poor initial guess. Minimizing the MTG activation squared is equivalent to minimizing muscle efforts [5]. The last two cost terms help with better dynamic consistency. The maximum and minimum values in the denominators of all cost terms, except for the fourth cost term (i.e., the MTG activation squared), were set to the same values considered for the cost function in Chapter 4. For the fourth cost term, the maximum and minimum values of MTG activations were set to 1 and 0, respectively.

5.2.2 Results and Discussion

Our optimal control methodology simulated the child gait within 2 hours of computation time, which is considerably less than the computation time of the modified approach developed for the contact parameter identification (5 hours). The MSK model including MTGs is more complicated than the torque-driven model used for the contact parameter identification. In the MSK model, each joint torque was modeled by two MTGs, each consisting of three 5th-order Bézier curves. However, the MSK-model simulation is faster than the contact parameter identification since no parameter is identified in the MSK-model simulation. In contrast, in the contact parameter identification, 64 parameters were identified.

The weighting factor values and RMSEs are shown in Tables 5.3 and 5.4, respectively. The cost function's weighting factors were tuned manually to achieve the minimum possible

Table 5.3: Weighting factor values for the gait simulation using the MSK model

Model	Cost Function	Weights
MSK	Eq. 5.33	$w_1 = 1/4$, $w_2 = 1/4$, $w_3 = 1/4$, $w_4 = 1/40$ $w_5 = 1/100$, $w_6 = 1/4$, $w_7 = 1/40$

Table 5.4: Root-mean-square errors for the gait simulation using the MSK model

Model	Leg	Angle (degree)			Torque (N.m)			GRF (N)	
		hip	knee	ankle	hip	knee	ankle	tangential	normal
MSK	Right	0.6	1.1	1.0	3.1	1.8	3.9	7.2	24.2
	Left	0.6	1.2	0.9	2.3	1.1	3.8	4.6	19.7

values of RMSE. The weights of the data-tracking terms were set to larger values than the other cost terms' weights. The reason is that the tracking terms may lead the optimization to simulate a natural gait while the other cost terms only affect convergence, solution smoothness, and dynamic consistency.

Figure 5.4 shows the simulated hip, knee, and ankle angles and the predicted metatarsal angles of the right and left legs. The simulated hip, knee, and ankle angles are within ± 1 standard deviation of the experimental data. The variation range of predicted metatarsal angles is roughly 25 degrees during gait, which is consistent with the angle ranges measured by [70, 97] for the mid-foot joint (10 degrees) and metatarsal joint (30-35 degrees) during child gait.

Jackson et al. [70] measured the right and left metatarsal joint angles for one healthy adult during a gait cycle. Although the metatarsal angles predicted for our child model are in agreement with the metatarsal angles measured for an adult, they do not match exactly for four reasons: (1) Our study is on children and it is not subject-specific; we used the mean experimental data of 20 healthy children for whom metatarsal angles were not measured. (2) We assumed that the time shift between the right and left leg motions equals the sum of the single-support and double-support phase times, which may not be equal to the real time shift. (3) We estimated foot anthropometric data from the literature [36, 143] which may not represent the real foot of the subjects studied in this thesis. (4) We did not have a strong initial guess for the metatarsal joints at the start of the gait cycle.

Figure 5.5 shows the simulated hip, knee, and ankle torques and the predicted metatarsal torques of the right and left legs. The simulated hip, knee, and ankle torques are in good agreement with the experimental torques. According to [97], the maximum total torques (in N.m) of the mid-foot and metatarsal joints are equivalent to 0.9 of the child's mass (in kg). In our simulation, the maximum values predicted for the metatarsal torques (40 N.m

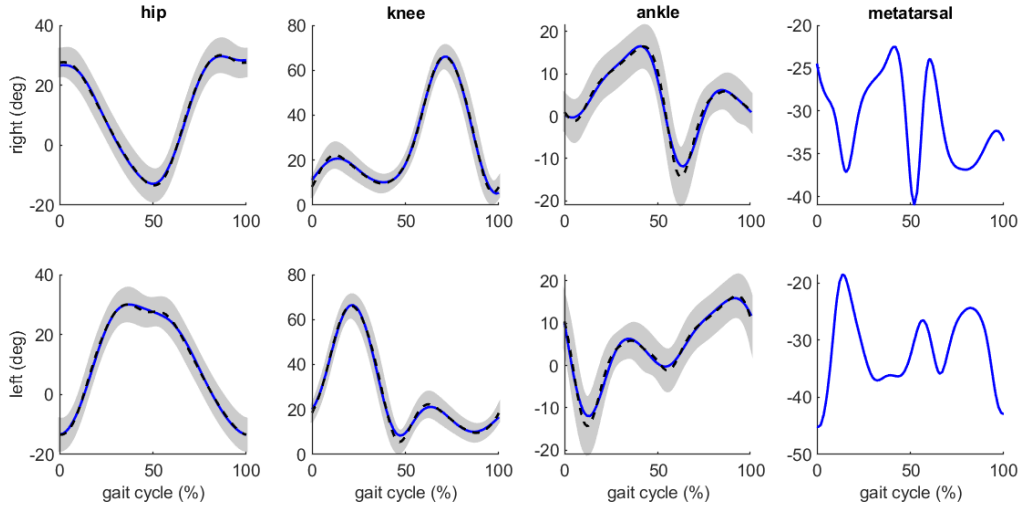


Figure 5.4: The joint angles simulated by the MSK model (The dotted lines represent the mean experimental data and the gray areas show ± 1 standard deviations of the mean experimental data)

for the right joint and 32 N.m for the left joint) are equivalent to 0.97 and 0.77 of our child subjects' average mass (41.4 kg), which is comparable with [97].

The simulated GRFs are also in good agreement with the experimental data, as shown in Figure 5.6. However, the average RMSEs (5.9 N for the tangential force and 22 N for the normal force) are slightly higher than the average RMSEs reported for the torque-driven model in the modified contact parameter identification (3 N for the tangential force and 20.7 N for the normal force). In the modified contact parameter identification section, the body and joint properties, along with the contact parameters, were tuned consistently with the constraints and the cost function during the optimization. However in this section, no parameter is tuned during the optimization in order to reduce the computational time.

5.3 Neuromusculoskeletal Model

In the MSK model, the MTGs were used to generate an activation-to-torque muscular model. To make the MSK model more physiologically-meaningful, we replaced the muscular model with a neuromuscular model and called it the NMSK model. As shown in Figure 5.7, our neuromuscular model is an EMG-to-torque model composed of muscle ac-

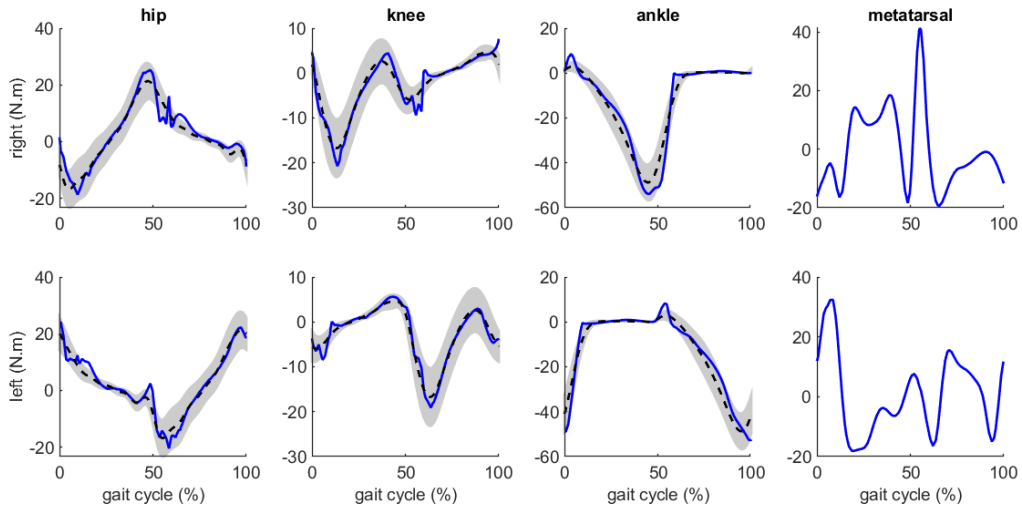


Figure 5.5: The joint torques simulated by the MSK model (The dotted lines represent the mean experimental data and the gray areas show ± 1 standard deviation of the mean experimental data)

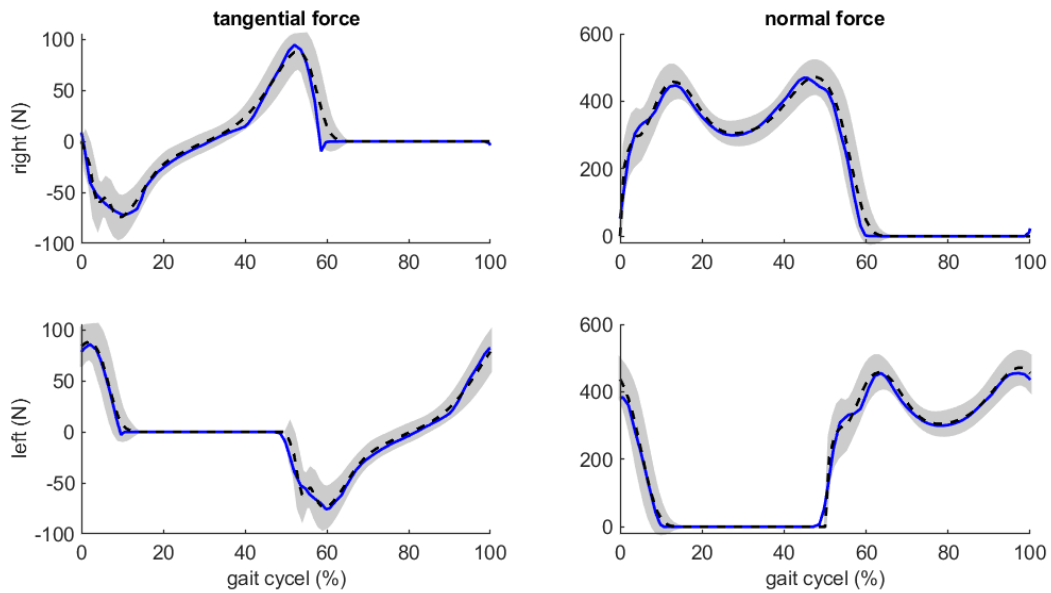


Figure 5.6: The ground reaction forces simulated by the MSK model (The dotted lines represent the mean experimental data and the gray areas show ± 1 standard deviation of the mean experimental data)

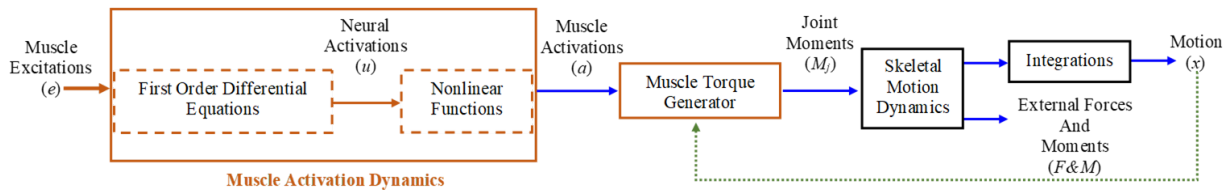


Figure 5.7: The workflow of the NMSK model

tivation dynamics and MTGs. This NMSK model enabled us to predict muscle excitations comparable with EMG data and estimate the metabolic energy rate for the child gait.

In this section, first, we introduced the muscles for which we have the experimental EMG data. Then we modeled the muscle activation dynamics and explained how we calculated the metabolic energy rate using our MTG-based NMSK model. Finally, through a direct collocation optimal control, we used the NMSK model to simulate a child gait and predict the muscle excitations while identifying the remaining parameters corresponding to the muscle activation dynamics.

5.3.1 Experimental EMG Data

Reference [18], from which we extracted experimental motion, torque, and GRF data for our child model, also includes EMG data for eight muscles of the right leg. These muscles are Gluteus Maximus (GM), Rectus Femoris (RF), Vastus Medialis (VM), Bicep Femoris (BF), Soleus (SOL), Peroneus Longus (PL), Gastrocnemius Medialis (GAM), and Tibialis Anterior (TA). Bovi et al. [18] have measured surface EMG signals using an 8-channel wireless electromyograph, ZeroWire (Aurion, Milano, Italy) and 10-*mm*-diameter adhesive electrodes. They have processed the measured EMG signals by rectifying and low-pass filtering (Butterworth 5th order, 3 *Hz* cutoff frequency) and normalizing to the maximum of the root mean square values of 2% intervals across all the subjects' trials.

Considering the assumption that gait is bilaterally symmetric and periodic, we used Fourier series to generate EMG data for the left leg given the EMG data of the right leg. The details of this approach were explained in Section 4.2.3. Thus, we totally considered 16 muscles (i.e., eight muscles per leg) in our NMSK model.

Assuming that the muscles are mono-articular with no co-contraction, we categorized them into agonist-antagonist pairs considering their main functions. In this way, we could compare the EMG data of muscles with the agonist-antagonist pairs of MTGs to investigate

Table 5.5: Agonist-antagonist pairs of muscles actuating joints

muscle type	hip	knee	ankle
extensor	Gluteus Maximus	Vastus Medialis	Soleus, Peroneus Longus, Gastrocnemius Medialis
flexor	Rectus Femoris	Bicep Femoris	Tibialis Anterior

whether MTGs can simulate a physiologically-meaningful gait. Table 5.5 shows the agonist-antagonist pairs of the muscles actuating the hip, knee, and ankle joints.

5.3.2 Muscle Activation Dynamics

As shown in Figure 5.7, we modeled the muscle activation dynamics using a linear first order differential equation and a nonlinear function proposed by [108]. The first order differential equation converts $e(t)$ (i.e., muscle excitations or processed EMG data) to $u(t)$ (i.e., neural activations):

$$\dot{u}(t) = \left(c_1 e(t-d) + c_2 \right) \left(e(t-d) - u(t) \right) \quad (5.34)$$

where d is an electromechanical time delay set to 50 *ms* and c_1 and c_2 are:

$$c_1 = \frac{1}{\tau_{act.}} - \frac{1}{\tau_{deact.}} \quad (5.35)$$

$$c_2 = \frac{1}{\tau_{deact.}} \quad (5.36)$$

where $\tau_{act.}$ and $\tau_{deact.}$ are muscle activation and deactivation time constants, respectively. $\tau_{act.}$ can have a value from 5 to 35 *ms* and we assumed that $\tau_{deact.} = 4\tau_{act.}$. Eq. 5.34 was solved recursively over all time steps, assuming $u(t)$ at the first two time steps equals $e(t-d)$ at these time steps. The nonlinear function transforms $u(t)$ (i.e., neural activations) to $a(t)$ (i.e., muscle activations) using:

$$a(t) = c_3 \sqrt{u(t)} + (1 - c_3)u(t) \quad (5.37)$$

where c_3 is a nonlinearity constant that can have a value from 0 (linear) to 0.75 (highly nonlinear). This muscle activation dynamics model was implemented for all 16 muscles to transform muscle excitations to muscle activations.

5.3.3 Calculation of Metabolic Energy Consumption Rate

Experimental studies have shown that humans prefer to continuously optimize the metabolic energy consumption during walking [150]. In recent predictive gait studies, the metabolic energy consumption was minimized as an energy-based cost term with the aim of simulating a natural motion [45, 90]. To accurately calculate metabolic energy consumption, it is necessary to have an anatomically-detailed neuromuscular model [15, 181], which is computationally-expensive for the predictive simulations in this thesis.

To reduce the computational time for the predictive simulations in which energy-based cost terms are used, we took advantage of our MTG-based neuromuscular model to develop a simpler model for estimating the metabolic energy rate. We used our neuromuscular model features to add some simplifications to the metabolic energy model proposed by Bhargava et al. [15]. To investigate the accuracy of our energy metabolic consumption model, we used it as a cost-term in the child gait simulation in Section 5.3.4.

The total rate of metabolic energy consumption, \dot{E} in W (Watt), is described as the sum of five terms [15]:

$$\dot{E} = \dot{A} + \dot{M} + \dot{S} + \dot{B} + \dot{W} \quad (5.38)$$

where \dot{A} is the activation heat rate, \dot{M} is the maintenance heat rate, \dot{S} is the shortening heat rate, \dot{B} is the basal metabolic rate, and \dot{W} is the work rate.

Activation Heat Rate

The activation heat rate represents the tension-independent heat released by the stimulation of muscles. It is described as the sum of two terms:

$$\dot{A} = \phi m f_{fast} \dot{A}_{fast} e_{fast}(t) + \phi m f_{slow} \dot{A}_{slow} e_{slow}(t) \quad (5.39)$$

where ϕ is a decay function, m is the total mass of the muscle, f_{fast} and f_{slow} are the mass fractions of fast and slow twitch fibers in the muscle, respectively. \dot{A}_{fast} and \dot{A}_{slow} are the activation heat rate constants for fast and slow twitch fibers, respectively, and equal to 133 and 40 W/kg for humans [15]. $e_{fast}(t)$ and $e_{slow}(t)$ are the excitation levels of the fast and slow twitch fibers.

The dimensionless decay function (i.e., ϕ) is represented by:

$$\phi = 0.06 + \exp(-t_{stim}e(t)/\tau_\phi) \quad (5.40)$$

where τ_ϕ is the decay time constant (i.e., 45 ms), $e(t)$ is the muscle excitation, and t_{stim} is the amount of time the muscle has been excited above 10%. For our gait simulation,

Table 5.6: The optimal fiber lengths of the muscles scaled for the child model

Muscle	GM	RF	VM	BF	SOL	PL	GAM	TA
l_{opt} (cm)	12.39	10.32	8.14	12.66	4.16	3.92	5.03	7.99

Table 5.7: The physiological cross-sectional area of the muscles scaled for the child model

Muscle	GM	RF	VM	BF	SOL	PL	GAM	TA
$PCSA$ (cm ²)	9.53	20.68	32.02	8.51	89.28	24.20	11.79	8.09

we constantly estimated t_{stim} during our optimal-control by obtaining the amount of time that $e(t)$ of the muscles have values higher than 10% of the maximum value of $e(t)$.

The total mass of a muscle (i.e., m) can be calculated using [178]:

$$m = \rho \cdot PCSA \cdot l_{opt} \quad (5.41)$$

where ρ is the muscle density of mammals (i.e., 1060 kg/m³), l_{opt} is the optimal fiber length of the muscle, and $PCSA$ is the physiological cross-sectional area of the muscle.

To determine the optimal fiber lengths for the muscles of our child model, we recruited a generic MSK model (i.e., Gait2392) developed in OpenSim [34]. We scaled the generic model using the OpenSim “Scale Model” tool, given the body-segment lengths and BH of our child model. Then, we extracted the scaled l_{opt} values from OpenSim. Table 5.6 shows the optimal fiber lengths of the muscles scaled for the child model.

To estimate $PCSA$ for the child model, we extracted the $PCSA$ values (i.e., $PCSA_a$) reported for a 37-year-old subject (mass: 91 kg and height: 183 cm) in [53] and scaled them for our child model (i.e., $PCSA_{ch}$) using:

$$PCSA_{ch} = \frac{BM_{ch} BH_{ch}}{BM_a BH_a} s^\tau PCSA_a \quad (5.42)$$

As mentioned in Section 5.1, increasing the scaling factor of τ_0^M (i.e., $\frac{BM_{ch} BH_{ch}}{BM_a BH_a} s^\tau$) is equivalent to increasing the $PCSA$ of the muscle. So, we scaled $PCSA_a$ using the same ratio to estimate $PCSA_{ch}$ for the child model. Table 5.7 shows the $PCSA$ values estimated for the child model.

The mass fractions of fast and slow twitch fibers (i.e., f_{fast} and f_{slow}) were reported for human muscles in [181] and for rat muscles in [134]. We extracted the f_{fast} values of all muscles of the child model from [181] except for Peroneus Longus. The f_{fast} value of the Peroneus Longus muscle was extracted from [134]. To make f_{fast} of Peroneus Longus,

Table 5.8: The f_{fast} values considered for the child muscles

Muscle	GM	RF	VM	BF	SOL	PL	GAM	TA
$f_{fast}(\%)$	45	65	50	35	20	50	19	25

extracted from [134], consistent with the rest of the muscles, we scaled it by the ratio of the f_{fast} of Soleus reported in [181] to the f_{fast} of Soleus reported in [134]. Table 5.8 shows the f_{fast} values considered for the child muscles. Subtraction of the f_{fast} value from 1 gives the f_{slow} for each muscle.

The excitation levels of the fast and slow twitch fibers (i.e., $e_{fast}(t)$ and $e_{slow}(t)$) are defined as:

$$e_{fast}(t) = 1 - \cos(\pi/2 e(t)) \quad (5.43)$$

$$e_{slow}(t) = \sin(\pi/2 e(t)) \quad (5.44)$$

To represent the recruitment of both fast and slow twitch fibers, cosine and sine functions were used to convert $e(t)$ into separate levels for $e_{fast}(t)$ and $e_{slow}(t)$.

Maintenance Heat Rate

The maintenance heat rate is the stable heat rate generated during isometric contraction. The maintenance heat rate is dependent on muscle length [15]. However, we ignored this dependence, because it makes the maintenance heat rate function physiologically-infeasible and computationally-expensive. We approximated it as:

$$\dot{M} = m f_{fast} \dot{M}_{fast} e_{fast}(t) + m f_{slow} \dot{M}_{slow} e_{slow}(t) \quad (5.45)$$

where \dot{M}_{fast} and \dot{M}_{slow} are the maintenance heat rate constants for fast and slow twitch fibers, respectively and equal to 111 and 74 W/kg for humans [15].

Shortening Heat Rate

The shortening heat rate is the heat rate produced during a concentric or eccentric contraction. This heat rate was modeled in [15] as:

$$\dot{S} = \begin{cases} -\left(0.16F_0^M + 0.18F^M(t)\right) v_{CE}(t) & v_{CE}(t) \leq 0 \\ -\left(0.157F^M(t)\right) v_{CE}(t) & v_{CE}(t) > 0 \end{cases} \quad (5.46)$$

where $v_{CE}(t)$ is the velocity of the contractile element. For eccentric and concentric contractions, $v_{CE}(t)$ is positive and negative, respectively. F_0^M is the maximum isometric muscle force, and $F^M(t)$ is the muscle force.

Our NMSK model is MTG-based and it is not able to generate $F^M(t)$ and $v_{CE}(t)$, but rather generates $\tau^M(t)$ and $\dot{\theta}(t)$. Thus, we approximated the shortening heat rate using:

$$\dot{S} = \begin{cases} -\left(0.16\tau_0^M + 0.18\tau^M(t)\right) \dot{\theta}(t) & \tau^M(t)\dot{\theta}(t) \geq 0 \\ -\left(0.157\tau^M(t)\right) \dot{\theta}(t) & \tau^M(t)\dot{\theta}(t) < 0 \end{cases} \quad (5.47)$$

where the first case ($\tau^M(t)\dot{\theta}(t) \geq 0$) gives the shortening heat rate of the concentric contraction. This case was assumed to be equivalent to the first case in Eq. 5.46 ($v_{CE}(t) \leq 0$). The reason behind this assumption is that muscle force vector and shortening motion are always in the same direction; consequently, when $v_{CE}(t)$ is negative (i.e., shortening motion), $F^M(t)v_{CE}(t)$ would be positive, which can be estimated by $\tau^M(t)\dot{\theta}(t) \geq 0$ with a good approximation. With the same logic, the second case ($\tau^M(t)\dot{\theta}(t) < 0$) gives the shortening heat rate of the eccentric contraction.

Basal Heat Rate

For our child model, the basal heat rate of each muscle was estimated using the formula in [15]:

$$\dot{B} = 0.0225 m \quad (5.48)$$

where 0.0225 (W/kg) is the basal metabolic rate reported for resting frog skeletal muscle at 0°C.

Work Rate

The work rate is computed in [15] using:

$$\dot{W} = F_{CE}(t) v_{CE}(t) \quad (5.49)$$

where F_{CE} is the force of the contractile element. For our gait simulation, we described the work rate as:

$$\dot{W} = \begin{cases} \tau^M(t) \dot{\theta}(t) & \text{MTG-driven joint} \\ \tau(t) \dot{\theta}(t) & \text{torque-driven joint} \end{cases} \quad (5.50)$$

where we assumed that if the joint is actuated by torque (like metatarsal joints in our model), the work rate of this joint can be estimated as $\tau(t)\dot{\theta}(t)$. Otherwise, if the joint is actuated by a pair of MTGs (like hip, knee, and ankle joints in our model), the work rate of this joint can be estimated as the product of its angular velocity (i.e., $\dot{\theta}(t)$) and the resultant flexor/extensor MTG torques (i.e., $\tau^M(t)$) actuating the joint.

5.3.4 Natural Child Gait Simulation

For the child gait simulation using the NMSK model, we considered the same human model that was used for the MSK model in Section 5.2.1: an 11-DOF human model with 3D ellipsoidal volumetric foot-ground contact model, in which 12 MTGs actuate the hip, knee, and ankle joints.

To implement the optimal control algorithm, GPOPS-II was used. We used the IPOPT solver in first derivative mode with the tolerance of 1e-5. Although GPOPS-II contains an adaptive mesh refinement algorithm, we considered a fixed mesh of 100 collocation points, divided into 20 intervals, over the whole gait cycle to reduce the computational time. This simulation was done on a desktop computer with an Intel[®] Core[™] i7-6700 CPU @ 3.40 GHz with 16.0 GB RAM.

Methodology

In this optimal control approach, the states and control inputs are:

$$\mathbf{x}(t) = [\mathbf{q}(t), \dot{\mathbf{q}}(t), \ddot{\mathbf{q}}(t)] \quad (5.51)$$

$$\mathbf{u}(t) = [\ddot{\mathbf{q}}(t), \mathbf{R}_{pelvis}(t), \boldsymbol{\tau}_{toe}(t), \mathbf{e}(t)] \quad (5.52)$$

all the components of which are the same as those described for the MSK model in Section 5.2.1, except for the fourth component of the control inputs (i.e., $\mathbf{u}_4(t)$). For the MSK model, we considered the 12 MTG activations (i.e., $\mathbf{a}(t)$) as $\mathbf{u}_4(t)$. However, for the NMSK model, we considered the 16 muscle excitations as $\mathbf{u}_4(t)$. In contrast to MTG activations, muscle excitations are physiologically-meaningful and comparable with EMG data. By considering 16 muscle excitations as control inputs, we could use EMG data of the 16 muscles, described in Section 5.3.1, as a strong initial guess for the control inputs, and also validate the predicted muscle excitations by a comparison with the EMG data.

In NMSK-model gait simulation, the states, control inputs, and four parameters were parametrized to minimize a data-tracking cost function subject to some constraints with

the aim of simulating a natural child gait. The contact parameters and MTG parameters were set to the values identified for the child.

The four parameters, identified in this optimization, are:

$$\gamma = \{\tau_{act.}, c_3, s_1, s_2\} \quad (5.53)$$

where $\tau_{act.}$ and c_3 are the muscle activation time constant and nonlinearity constant, used in Eq. 5.35 and Eq. 5.37, respectively. Parameters s_1 and s_2 are the activation weights, defined later.

$\tau_{act.}$ and c_3 were used in the muscle activation dynamics equations. We assumed that $\tau_{act.}$ and c_3 for all 16 muscles are identical [56]. However, to achieve more accurate results, we could have considered separate parameters for the muscles (i.e., 2×16 parameters instead of 2 parameters) to be identified specifically.

Parameters s_1 and s_2 were defined to compose the activations of three muscles (SOL, PL, and GAM), which are the extensor muscles actuating the ankle joint, in order to achieve a single extensor activation for the ankle joint. By defining activation weights, we generated a single extensor activation for the ankle joint and used it in the extensor MTG equation of ankle joint as MTG activation. The idea behind this assumption was taken from the synergy analysis approach [82], where an optimization is applied to decompose the high dimensional set of processed EMG data into a lower dimensional set of time-varying signals. The extensor activation of the ankle was defined as:

$$a_{ext.}^{ankle} = s_1 a_{SOL} + s_2 a_{PL} + (1 - s_1 - s_2) a_{GAM} \quad (5.54)$$

where a_{SOL} , a_{PL} and a_{GAM} are the activations of muscles SOL, PL, and GAM. We substituted $a_{ext.}^{ankle}$ for a in Eq. 5.8 to create an extensor MTG for the ankle joint. This approach was employed only for the ankle extensor, and we assumed that s_1 and s_2 for the right and left ankle extensors are identical.

Among the muscles for which we have EMG data (shown in Table 5.5), only the SOL, PL, and GAM muscles have the same function (i.e., extending ankle joint), and the rest of the muscles have different functions. Thus, there was no need to apply the activation-weight approach for the rest of the muscles. Their activations, generated by muscle activation dynamics, were considered as extensor/flexor MTG activations with a good approximation and substituted for a in Eq. 5.8 to create their equivalent MTGs.

Constraints

The constraints for the NMSK-model gait simulation were held the same as those imposed for the MSK-model gait simulation. The constraints can be found in Section 5.2.1.

Bounds

The bounds for the states and $\mathbf{u}_1(t)$, $\mathbf{u}_2(t)$ and $\mathbf{u}_3(t)$ were set to the same bounds considered for the MSK-model gait simulation in Section 5.2.1. The bound for the $\mathbf{u}_4(t)$ (i.e., muscle excitations) was set to $[0, 0.8]$. Although the bounds for the child processed EMG data are around $[0, 0.4]$, we allowed a larger bound for $\mathbf{u}_4(t)$ to let the optimization find muscle excitation values more focused on the constraints and cost function, than the bounds of experimental EMG data.

The bounds for parameters $\tau_{act.}$ and c_3 were set to $[0.005, 0.035]$ (s) and $[0, 0.75]$, respectively [108]. The bounds for parameters s_1 and s_2 were set to $[0, 0.5]$, based on Eq. 5.54.

Initial Guess

The initial guess for the states and $\mathbf{u}_1(t)$, $\mathbf{u}_2(t)$ and $\mathbf{u}_3(t)$ were set to the same initial guess considered for the MSK-model gait simulation in Section 5.2.1. The processed EMG data was considered as the initial guess for $\mathbf{u}_4(t)$. The initial guess for the parameters $\tau_{act.}$, c_3 , s_1 , and s_2 were set to 0.015, 0.3, 0.33, and 0.33, respectively.

Cost Function

The cost function consists of 8 cost terms:

$$\begin{aligned}
 J = \frac{1}{t_f} \int_{t_0}^{t_f} & \left[w_1 \sum_{i=1}^6 \left(\frac{\tau_{sim.} - \tau_{exp.}}{\tau_{max} - \tau_{min}} \right)_i^2 + w_2 \sum_{i=1}^4 \left(\frac{\text{GRF}_{sim.} - \text{GRF}_{exp.}}{\text{GRF}_{max} - \text{GRF}_{min}} \right)_i^2 \right. \\
 + w_3 \sum_{i=1}^{11} & \left(\frac{q_{sim.} - q_{exp.}}{q_{max} - q_{min}} \right)_i^2 + w_4 t_f^6 \sum_{i=1}^{11} \left(\frac{u_1}{u_{1max} - u_{1min}} \right)_i^2 + w_5 \sum_{i=1}^{16} \left(\frac{a}{a_{max} - a_{min}} \right)_i^2 \\
 + w_6 \sum_{i=1}^3 & \left(\frac{R_{pelvis}}{R_{max} - R_{min}} \right)_i^2 + w_7 \sum_{i=1}^8 \left(\frac{\tau_{inv.} - \tau_{input}}{\tau_{max} - \tau_{min}} \right)_i^2 + w_8 \frac{t_f^6}{\text{BM}^2 d^4} \left(\frac{\dot{E}}{\dot{E}_{max} - \dot{E}_{min}} \right)_i^2 \left. \right] dt
 \end{aligned} \tag{5.55}$$

where the first three cost terms are the data-tracking terms helping the optimization to simulate a child-like motion. The fourth cost term minimizes the joint jerk squared. The fifth term minimizes the muscle activation squared; the 16 muscle activations were obtained by solving the muscle activation dynamics given the 16 muscle excitations as the control

inputs (i.e., u_4). The sixth and seventh cost terms help with better dynamic consistency. The last term was defined to minimize metabolic energy consumption during gait since humans prefer to continuously minimize the metabolic energy consumption while walking.

Except for the fifth and eighth cost terms, all the cost terms have the same denominators considered for the cost function of the MSK-model gait simulation in Section 5.2.1. For the fifth term (i.e., the muscle activation squared), the maximum and minimum muscle activations in the denominators were set to 1 and 0, respectively. For the eighth term (i.e., the rate of metabolic energy consumption), the maximum and minimum \dot{E} values were estimated as:

$$\begin{aligned}\dot{E}_{max} &= (\text{COT}_N \times \text{BM}_{max} \times D) / t_f \\ \dot{E}_{min} &= (\text{COT}_N \times \text{BM}_{min} \times D) / t_f\end{aligned}\tag{5.56}$$

where COT_N (the cost of transport) is equal to $1.6 \text{ (Jkg}^{-1}\text{m}^{-1}\text{)}$ that is reported in [45] for an adult walking at the natural speed; BM_{max} and BM_{min} are 56.9 (kg) and 25.9 (kg) that are the maximum and minimum masses of our child subjects; D is 1.24 (m) that is the distance the child subject travelled. It should be noted that the metabolic energy rate penalty was scaled by $t_f^6 \text{ BM}^{-2}d^{-4}$ since the magnitude of energy rate is considerably greater than the other cost terms. In addition, we did not want the energy cost term to drive other cost terms to become ineffective. To determine the rate of metabolic energy consumption (i.e., \dot{E}), the approach we proposed for MTG-based NMSK models in Section 5.3.3 was used.

5.3.5 Results and Discussion

In comparison to the MSK-model simulation, in the NMSK-model simulation, an additional cost term (i.e., energy term) and muscle activation dynamics of 16 muscles were included. Due to these extra computations, a higher computation time was expected for the NMSK-model simulation. However, the NMSK model simulated the child gait within 2 hours of computation time, which is similar to the MSK-model computation time. It can be explained by two reasons: (1) In the NMSK-model simulation, the control inputs are muscle excitations (not MTG activations), and we had a good initial guess (processed EMG data) for them. (2) The muscle activation dynamics and energy cost term made the NMSK-model simulation more complicated but more physiologically-meaningful. This led the experimental-data-tracking cost terms to be met faster.

The weighting factor values are shown in Table 5.9. For the first seven cost terms, the weighting factors were set to the same weight values considered for the cost function of

Table 5.9: Weighting factor values for the gait simulation using the NMSK model

Model	Cost Function	Weights
NMSK	Eq. 5.55	$w_1 = 1/4, w_2 = 1/4, w_3 = 1/4, w_4 = 1/40$ $w_5 = 1/100, w_6 = 1/4, w_7 = 1/40, w_8 = 1/5$

Table 5.10: The parameters identified by the NMSK model

parameter	$\tau_{act.}$ (s)	c_3	s_1	s_2
initial	0.015	0.3	0.33	0.33
identified	0.006	0.0001	0.25	0.25

the MSK-model gait simulation and for the energy term, w_8 was set to $1/5$, which was obtained by a manual tune to achieve the minimum possible values for the RMSE.

The identified values for the four parameters are shown in Table 5.10. The value identified for $\tau_{act.}$ (activation time constant) is 0.006 (s) and consequently $\tau_{deact.}$ must equal 0.024 (s) due to the constraint (i.e., $\tau_{deact.} = 4\tau_{act.}$) assumed. According to [68], $\tau_{deact.}$ of young women with age of 18-32 years (0.050 s) is 17% less than $\tau_{deact.}$ of old women with age of 64-79 years (0.060 s), respectively. The reason is that the rate of muscle deactivation (i.e., the rate of uptake of calcium ions by the sarcoplasmic reticulum) in young subjects is faster than that in old subjects [68]. In our child model with an age of 10.8 ± 3.2 years, we obtained 0.024 (s) for the $\tau_{deact.}$, which is 50% less than the $\tau_{deact.}$ of young subjects; it would be a logical value since child subjects have younger muscles than young subjects.

The value identified for c_3 (nonlinearity constant) is 0.0001. This low value shows that it is not required to complicate the activation dynamics by considering nonlinearity [173, 187]. The nonlinearity term can be omitted to reduce computation time.

The values identified for s_1 and s_2 (activation weights) are both equal to 0.25. Regarding the identified weights and Eq. 5.54, the coefficient (i.e., weight) of Gastrocnemius Medialis activation must be 0.5, which is greater than the activation weights of the Soleus and Peroneus Longus muscles. The reason is that Gastrocnemius Medialis muscle is the main muscle extending the ankle joint [183]. Furthermore, this muscle is a superficial muscle with a longer moment arm with respect to ankle joint than the moment arms of Soleus and Peroneus Longus, which are deep muscles. Thus, the Gastrocnemius Medialis muscle should contribute a major part of the ankle MTG extensor, and it seems logical that its activation weight has a greater value.

The RMSEs of the NMSK-model simulation are shown in Table 5.11. Comparison of the MSK and NMSK models shows that the simulation accuracy of the NMSK model is very close to the accuracy of the MSK model when all the experimental joint angles,

Table 5.11: Root-mean-square errors for the gait simulation using the NMSK model

Model	Leg	Angle (degree)			Torque (N.m)			GRF (N)	
		hip	knee	ankle	hip	knee	ankle	tangential	normal
NMSK	Right	0.6	1.1	1.0	2.3	1.1	3.8	7.2	24.1
	Left	0.6	1.2	0.9	2.3	1.1	3.8	4.6	19.8

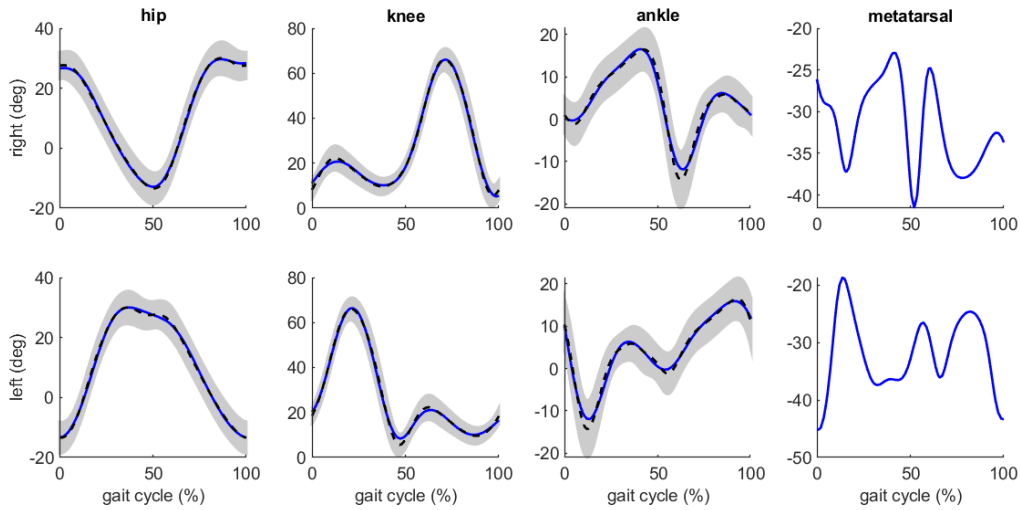


Figure 5.8: The joint angles simulated by the NMSK model (The dotted lines represent the mean experimental data and the gray areas show ± 1 standard deviations of the mean experimental data)

torques, and GRFs are tracked through a cost function. The RMSEs of both models for the joint angles and GRFs are almost the same, but the NMSK model could generate 6 % and 3 % more accurate torques for the right hip and knee joints, respectively.

Figures 5.8 and 5.9 show the joint angles and torques of the right and left legs simulated by the NMSK child model. The simulated hip, knee, and ankle angles and torques are within ± 1 standard deviation of the experimental data. The predicted metatarsal angles and torques are in good agreement with the results predicted by the MSK model. The simulated GRFs are also in good agreement with the experimental data, as shown in Figure 5.10. The mean value of the RMSE of the tangential forces (5.90 N) and normal forces (21.95 N) are identical for the MSK and NMSK models.

Using the metabolic energy consumption rate (\dot{E}) estimated by the NMSK-model simulation, we could calculate the cost of transport (COT) for the natural-speed child gait

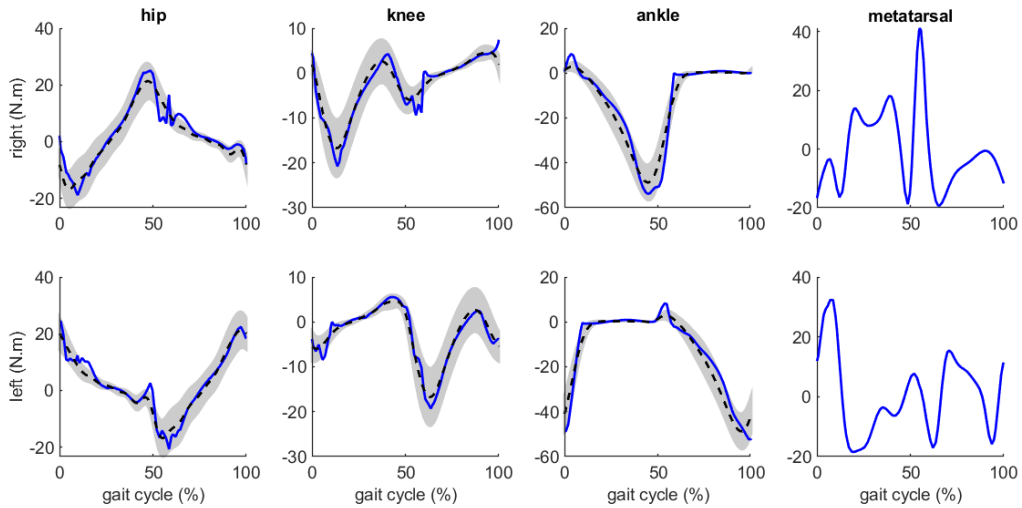


Figure 5.9: The joint torques simulated by the NMSK model (The dotted lines represent the mean experimental data and the gray areas show ± 1 standard deviations of the mean experimental data)

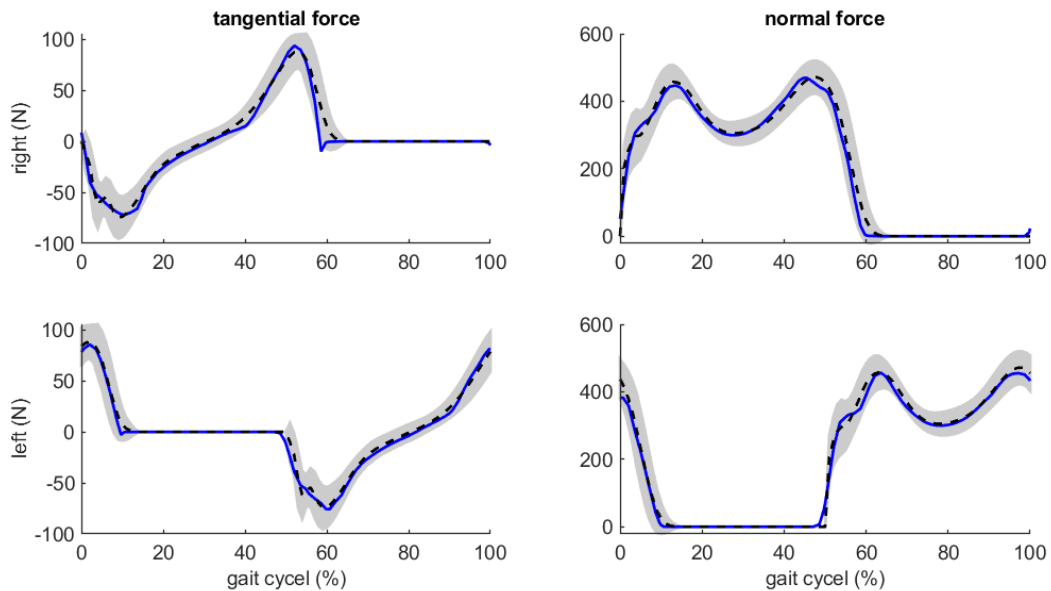


Figure 5.10: The ground reaction forces simulated by the NMSK model (The dotted lines represent the mean experimental data and the gray areas show ± 1 standard deviations of the mean experimental data)

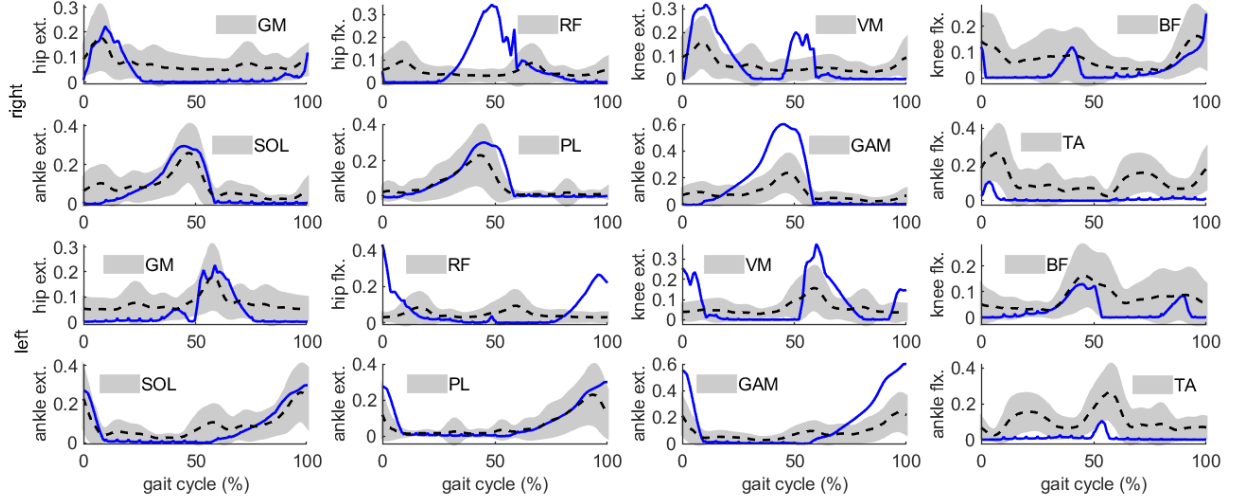


Figure 5.11: The muscle excitations simulated by the NMSK model (The dotted lines represent the mean processed EMG data and the gray areas show ± 1 standard deviations of the mean processed EMG data)

through:

$$COT = \frac{\int_{t_0}^{t_f} \dot{E} dt}{BM \times D} \quad (5.57)$$

and obtain $1.53 \text{ (Jkg}^{-1}\text{m}^{-1}\text{)}$, which is in good agreement with the COT range reported for natural-speed gait in [45].

Our NMSK model also enabled us to define muscle excitations as control inputs and predict them for the child gait. The predicted muscle excitations and their corresponding EMG data are shown in Figure 5.11. The majority of the predicted muscle excitations are in reasonable agreement with the corresponding EMG data. However, the predicted hip flexor, ankle flexor, and the third ankle extensor muscles did not match the corresponding EMG data (i.e., RF, TA, and GAM, respectively) very well.

For the hip flexor muscle, we compared its predicted excitation with the EMG data of Rectus Femoris. It is not a precise comparison since Rectus Femoris is not the main muscle flexing the hip. The main muscles flexing the hip are Psoas Major and Iliacus, which are deeply located, and surface EMGs cannot measure their neural commands. Thus, we did not have appropriate EMG data to compare with our predicted hip flexor. Another reason that Rectus Femoris is not appropriate for validation of hip flexor excitation is that Rectus

Femoris contributes more to extending the knee than to flexing the hip during gait. Rectus Femoris is a weak hip flexor when the knee extends, and the knee is in an extension state during the majority of a gait cycle (55-60% of a gait cycle).

For the ankle flexor muscle, we compared its predicted excitation with the EMG data of Tibialis Anterior. It is not a precise comparison since Tibialis Anterior performs not only ankle flexion but also ankle inversion. The EMG data of Tibialis Anterior represents the neural commands of both flexion and inversion functions. Due to this, its EMG data has a range higher than the values we predicted for the ankle flexor excitation. Another reason behind the inconsistency between the predicted ankle flexor excitation and Tibialis Anterior EMG data is that we assumed that there is no co-contraction between the ankle extensor and flexor muscles. However, appropriate levels of co-contraction are required to stabilize loaded joints, regulate joint stiffness, and handle sudden changes in the direction of joint motions [144]. Consequently, the absence of co-contraction would have an impact on the realism of the predicted muscle excitations. As shown in Figure 5.11, the excitation predicted for the third ankle extensor is larger than its corresponding EMG data (GAM) and the excitation predicted for the ankle flexor is less than its corresponding EMG data (TA). However, if we consider co-contraction between ankle flexor and extensor, we would predict excitations that are more consistent with the EMG data.

For the third ankle extensor muscle, we compared its predicted excitation with the EMG data of Gastrocnemius Medialis. It is not a precise comparison due to the same reason mentioned above about the absence of co-contraction. Another reason behind the inconsistency between Gastrocnemius Medialis EMG data and the third ankle extensor's excitation is that Gastrocnemius Medialis is not a very active muscle in walking. Thus, Gastrocnemius Medialis may not be a proper muscle to be compared with the predicted excitation for the ankle extensor.

5.4 Conclusion

The main contribution of this chapter was to generate simplified but accurate MSK and NMSK models that best fit a child model and simulate gait.

We modified the MTG model proposed by [114] for our child model. We developed a direct collocation optimal control to identify the MTG parameters for a child model considering the experimental child gait data. We verified that the fitted MTGs are feasible and can be used for child gait modeling.

We employed the fitted MTGs to develop a simplified MSK model. Through a direct

collocation optimal control, we used the MSK model to simulate a child gait to investigate whether the fitted MTGs can generate a gait motion consistent with the experimental data. The results showed that although the MTG-based MSK model is simpler than an anatomically-detailed MSK model, it can simulate child gait with reasonable accuracy. The mean RMSEs for the joint angles, torques, tangential GRFs, and normal GRFs are 0.9 degree, 2.7 N.m, 5.9 N, and 21.95 N, respectively. Furthermore, we could predict physiologically-meaningful angles and torques for the metatarsal joints that are in good agreement with the ranges reported in the literature.

To make the MSK model more physiologically-meaningful, we replaced the muscular model with a neuromuscular model called the NMSK model. This MTG-based NMSK model enabled us to predict muscle excitations comparable with EMG data and estimate the metabolic energy rate for the child gait through a direct collocation optimal control. Muscle activations and metabolic energy consumption during walking are the most commonly used indices to evaluate wearable robotic systems [17]. Thus, our proposed MTG-based NMSK model would be practical to develop energy-based predictive simulations for wearable robotic system evaluations in the future.

In comparison to the MSK-model simulation, in the NMSK-model simulation, an additional cost term (i.e., energy term) and muscle activation dynamics were included. The results showed that most of the predicted muscle excitations and the estimated COT are in good agreement with the literature. The simulation accuracy of the NMSK model is very close to the accuracy of the MSK model when all the experimental joint angles, torques, and GRFs are tracked in the cost function. The RMSEs of both models for the joint angles and GRFs are almost the same, but the NMSK model could generate 6 % and 3 % more accurate torques for the right hip and knee joints, respectively.

The MTG-based MSK and NMSK models proposed in this chapter will be used in the next chapters to predict physiologically-meaningful motion, torque, ground reaction forces (GRFs), and muscle excitations for child gait.

Chapter 6

Natural-Speed Gait Prediction Using the Musculoskeletal and Neuromusculoskeletal Child Models: Investigation of Different Cost Functions

In this chapter, we used the MTG-based MSK and NMSK child models, proposed in Chapter 5, to predict a natural-speed gait that matches the experimental data of children. To this aim, we developed two separate direct collocation optimal controls: (1) “*MSK-model optimization*” in which the MSK model was used, and the control inputs are MTG activations; (2) “*NMSK-model optimization*” in which the NMSK model was used, and the muscle excitations are the control inputs, and the metabolic energy consumption is optimized.

For each model’s optimization, we investigated eight multi-objective cost functions composed of a wide range of cost terms, including dynamic-based, stability-based, human-criteria-based, and data-based cost terms. We evaluated the effect of these cost terms on the realism of the predicted results. Defining different cost functions enabled us to compare the MSK and NMSK models in terms of computational efficiency and prediction accuracy.

6.1 Optimization Methodology

To develop the MSK-model optimization, we used the same approach as in Section 5.2.1. The states are 11 generalized coordinates, 11 velocities, and 11 accelerations. The control inputs are the 11 joint jerks, the 3 residual loads on the pelvis, the 2 torques of the metatarsal joints, and the 12 MTG activations. The constraints, bounds on the states, and control inputs were kept unchanged. Since we did not have a good initial guess (i.e., experimental-data-based initial guess) for the HAT-to-ground position and orientation, the metatarsal joint angles and torques, and the 12 MTG activations, we considered the corresponding results predicted in Section 5.2.1 as the initial guess for them. The initial guess of the remaining states and control inputs were kept unchanged.

To develop the NMSK-model optimization, we used the same approach as in Section 5.3.4. The states are 11 generalized coordinates, 11 velocities, and 11 accelerations. The control inputs are the 11 joint jerks, the 3 residual loads on the pelvis, the 2 torques of the metatarsal joints, and the 16 muscle excitations. The constraints, bounds on the states, and control inputs were kept unchanged. The results predicted in Section 5.3.4 were used to define the initial guess for the HAT-to-ground position and orientation, and for the metatarsal joint angles and torques. The initial guess of the remaining states and control inputs were kept unchanged.

No parameter was identified in these two optimizations. The contact parameters, MTG parameters, and muscle-activation-dynamics parameters were set to the values identified for the child model in the previous chapters.

To compose the cost functions for these optimizations, we considered four categories of the cost terms: (1) Dynamic-based cost terms, (2) Stability-based cost terms, (3) Human-criteria-based cost terms, and (4) Data-based cost terms.

We described the dynamic-based cost terms as:

$$\text{Jrk} = \int_{t_0}^{t_f} t_f^6 \sum_{i=1}^{11} \left(\frac{u_1}{u_{1max} - u_{1min}} \right)_i^2 dt \quad (6.1)$$

$$\text{Rsd} = \int_{t_0}^{t_f} \sum_{i=1}^3 \left(\frac{R_{pelvis}}{R_{max} - R_{min}} \right)_i^2 dt \quad (6.2)$$

$$\text{Imp} = \int_{t_0}^{t_f} \sum_{i=1}^8 \left(\frac{\tau_{inv.} - \tau_{input}}{\tau_{max} - \tau_{min}} \right)_i^2 dt \quad (6.3)$$

Eq. 6.1 results in smooth walking by minimizing the joint jerks. Eq. 6.2 provides dynamic consistency for human gait by minimizing the residual loads on the pelvis. Eq. 6.3 implicitly solves the motion dynamics by minimizing the difference between the control-input torques and inverse-dynamics torques for the leg joints. These three dynamic-based cost terms can be employed in our MSK-model and NMSK-model optimizations.

We described the stability-based cost term as:

$$\text{HAT} = \int_{t_0}^{t_f} \sum_{i=1}^3 \left(\frac{q_{sim.} - q_{exp.}}{q_{max} - q_{min}} \right)_i^2 dt \quad (6.4)$$

where $q_{sim.}$ corresponds to HAT-to-ground position and orientation with respect to the ground, and $q_{exp.}$ represents the experimental motion of HAT with respect to the ground. In the previous optimizations, we approximated the experimental position of HAT using the position data of a marker on the pelvis, and we set the experimental orientation of the HAT to zero as its variation during gait is negligible. However, to generate a more accurate simulation in this chapter, we set $q_{exp.}$ of the HAT to the resultant HAT motion obtained from the optimizations in Chapter 5. This cost term does not track actual experimental data. However, it tracks a good approximation of the HAT motion obtained from previous optimizations to provide stability for the gait motion. This stability-based cost term can be employed in our MSK-model and NMSK-model optimizations.

In the literature, predictive gait simulations have used relatively similar methods to provide stability. Nguyen et al. [121] have provided stability using a cost term minimizing the difference between the COM position of the whole body in the x direction and the center of the extended base of support. The extended base of support is defined as the convex area that contains the vertical projections of the two feet on the ground. Meyer et al. [109] provided stability for the predictive gait simulation using a cost term tracking the joint angles of the upper body. Their experimental data was also collected for a subject walking on an instrumented treadmill that keeps the HAT's motion fairly constant with respect to the ground. Lin and Pandey [90] have also provided stability for their predictive gait simulation using path constraints. They imposed the path constraints on the generalized coordinates and velocities to keep them as close as possible to the values of the generalized coordinates and velocities previously obtained from a gait data-tracking optimization.

We described the human-criteria-based cost terms as:

$$\text{Act}_{MSK} = \int_{t_0}^{t_f} \sum_{i=1}^{12} \left(\frac{u_4}{u_{4max} - u_{4min}} \right)_i^2 dt \quad (6.5)$$

$$\text{Act}_{NMSK} = \int_{t_0}^{t_f} \sum_{i=1}^{16} \left(\frac{a}{a_{max} - a_{min}} \right)_i^2 dt \quad (6.6)$$

$$\text{Mtb} = \int_{t_0}^{t_f} \frac{t_f^6}{\text{BM}^2 d^4} \left(\frac{\dot{E}}{\dot{E}_{max} - \dot{E}_{min}} \right)^2 dt \quad (6.7)$$

Eq. 6.5 minimizes 12 MTG activations for the MSK-model optimization; Eq. 6.6 minimizes 16 muscle activations for the NMSK-model optimization. Humans prefer to walk with minimum muscle efforts, and these two cost terms are equivalent to minimizing muscle efforts [5]. Furthermore, previous simulation studies have shown that a cost function including a muscle-activity cost term results in more accurate motion prediction than a cost function without a muscle-activity cost term. Eq. 6.7 minimizes the metabolic energy consumption during walking. Experimental studies have shown that humans prefer to continuously optimize the metabolic energy consumption during walking [150]. This cost term can only be used for the NMSK-model optimization.

We described the data-based cost terms as:

$$\text{Trq} = \int_{t_0}^{t_f} \sum_{i=1}^6 \left(\frac{\tau_{sim.} - \tau_{exp.}}{\tau_{max} - \tau_{min}} \right)_i^2 dt \quad (6.8)$$

$$\text{Ang} = \int_{t_0}^{t_f} \sum_{i=1}^6 \left(\frac{q_{sim.} - q_{exp.}}{q_{max} - q_{min}} \right)_i^2 dt \quad (6.9)$$

$$\text{GRF} = \int_{t_0}^{t_f} \sum_{i=1}^4 \left(\frac{\text{GRF}_{sim.} - \text{GRF}_{exp.}}{\text{GRF}_{max} - \text{GRF}_{min}} \right)_i^2 dt \quad (6.10)$$

In Eq. 6.8 and Eq. 6.9, the hip, knee, and ankle joint torques and angles track the corresponding experimental data. In Eq. 6.10, the differences between the simulated and

experimental GRFs are minimized. The data-based studies have shown that to achieve the most realistic simulation, it is necessary to track an actual motion in similar conditions [127]. These three data-based cost terms can be used in our MSK-model and NMSK-model optimizations.

Using the above-mentioned cost terms, we generated different multi-objective cost functions for each of the MSK-model and NMSK-model optimizations. Table 6.1 shows the configurations of the cost functions. We categorized the cost functions into eight groups according to the cost terms used in them. The cost terms, specified by a checkmark in each row of Table 6.1, were first multiplied by weighting factors (given in Table 6.2) and then summed together to form the cost function named at the beginning of the row.

In all cost functions, dynamic-based, stability-based, and human-criteria-based cost terms were used since these are the vital cost terms for generating a dynamically-consistent, stable, and human-like gait prediction. It should be noted that for the MSK-model optimization, there is one human-criteria-based cost term (i.e., Act_{MSK}), and for the NMSK-model optimization, there are two human-criteria-based cost terms (i.e., Act_{NMSK} and Mtb).

In the data-tracking (DT) cost function, all three data-based cost terms (i.e., Trq, Ang, and GRF) were used. In the semi-data-tracking (SDT) cost functions, two of the data-based cost terms were used; in the SDT1 cost function, Ang and GRF were used, and in the SDT2 cost function, Trq and GRF were used, and in the SDT3 cost function, Trq and Ang were used. In the semi-predictive (SP) cost functions, only one data-tracking cost term was used. The data-tracking cost terms GRF, Ang, and Trq were used in SP1, SP2, and SP3 cost functions, respectively. In the fully-predictive (FP) cost function, no data-tracking cost term was used.

Regarding the defined cost functions, we developed a total of 16 optimizations (i.e., eight optimizations for each of the MSK and NMSK models) using direct collocation optimal control. We used GPOPS-II with the IPOPT solver in first derivative mode to implement these optimizations with the tolerance of $1e-5$. Similar to the optimizations in Chapter 5, we considered a fixed mesh of 100 collocation points, divided into 20 intervals, over the whole gait cycle. These optimizations were done on a desktop computer with an Intel® Core™ i7-6700 CPU @ 3.40 GHz with 16.0 GB RAM.

Table 6.1: The configurations of the multi-objective cost functions for the MSK-model and NMSK-model optimizations

#	cost function	model	cost terms									
			dynamic-based			stability-based	human-criteria-based			data-based		
			Jrk	Rsd	Imp	HAT	Act _{MSK}	Act _{NMSK}	Mtb	Trq	Ang	GRF
(1)	data-tracking (DT)	MSK	✓	✓	✓	✓	✓	-	-	✓	✓	✓
		NMSK	✓	✓	✓	✓	-	✓	✓	✓	✓	✓
(2)	semi-data-tracking (SDT1)	MSK	✓	✓	✓	✓	✓	-	-	-	✓	✓
		NMSK	✓	✓	✓	✓	-	✓	✓	-	✓	✓
(3)	semi-data-tracking (SDT2)	MSK	✓	✓	✓	✓	✓	-	-	✓	-	✓
		NMSK	✓	✓	✓	✓	-	✓	✓	✓	-	✓
(4)	semi-data-tracking (SDT3)	MSK	✓	✓	✓	✓	✓	-	-	✓	✓	-
		NMSK	✓	✓	✓	✓	-	✓	✓	✓	✓	-
(5)	semi-predictive (SP1)	MSK	✓	✓	✓	✓	✓	-	-	-	-	✓
		NMSK	✓	✓	✓	✓	-	✓	✓	-	-	✓
(6)	semi-predictive (SP2)	MSK	✓	✓	✓	✓	✓	-	-	-	✓	-
		NMSK	✓	✓	✓	✓	-	✓	✓	-	✓	-
(7)	semi-predictive (SP3)	MSK	✓	✓	✓	✓	✓	-	-	✓	-	-
		NMSK	✓	✓	✓	✓	-	✓	✓	✓	-	-
(8)	fully-predictive (FP)	MSK	✓	✓	✓	✓	✓	-	-	-	-	-
		NMSK	✓	✓	✓	✓	-	✓	✓	-	-	-

Table 6.2: The weighting factors for the cost terms of the MSK-model and NMSK-model optimizations

#	cost function	model	weghits of cost terms									
			dynamic-based			stability-based	human-criteria-based			data-based		
			Jrk	Rsd	Imp	HAT	Act _{MSK}	Act _{NMSK}	Mtb	Trq	Ang	GRF
(1)	data-tracking (DT)	MSK	1/40	1/4	1/40	1/4	1/100	-	-	1/4	1/4	1/4
		NMSK	1/40	1/4	1/40	1/4	-	1/100	1/5	1/4	1/4	1/4
(2)	semi-data-tracking (SDT1)	MSK	1/40	1/4	1/4	1/4	1/100	-	-	-	1/4	1/4
		NMSK	1/40	1/4	1/10	1/4	-	1/100	1/5	-	1/4	1/4
(3)	semi-data-tracking (SDT2)	MSK	1/40	1/4	1/4	1/4	1/100	-	-	1/4	-	1/4
		NMSK	1/40	1/4	1/10	1/4	-	1/100	1/5	1/4	-	1/4
(4)	semi-data-tracking (SDT3)	MSK	1/40	1/4	1/4	1/4	1/100	-	-	1/4	1/4	-
		NMSK	1/40	1/4	1/20	1/4	-	1/100	1/5	1/4	1/4	-
(5)	semi-predictive (SP1)	MSK	1/40	1/10	1/3	1/2	1/100	-	-	-	-	1/4
		NMSK	1/40	1/10	1/20	1/2	-	1/100	1/5	-	-	1/4
(6)	semi-predictive (SP2)	MSK	1/40	1/4	1/4	1/4	1/100	-	-	-	1/4	-
		NMSK	1/40	1/4	1/10	1/4	-	1/100	1/5	-	1/4	-
(7)	semi-predictive (SP3)	MSK	1/40	1/4	1/4	1/4	1/100	-	-	1/4	-	-
		NMSK	1/40	1/4	1/10	1/4	-	1/100	1/5	1/4	-	-
(8)	fully-predictive (FP)	MSK	1/40	1/4	1/4	1/4	1/100	-	-	-	-	-
		NMSK	1/40	1/10	1/4	1	-	1/100	1/5	-	-	-

6.2 Results and Discussion

In this section, the results of the 16 optimizations are shown and discussed to compare the MSK and NMSK models in terms of prediction accuracy and computational time. Comparison of these optimizations sheds light on the roles of the different cost terms in the realism of the predicted results.

6.2.1 Weighting Factor Examination

The weighting factors of the cost terms used in each optimization are given in Table 6.2. The weights were tuned manually to achieve the minimum possible values of RMSEs for the optimization results. The weights of the data-based, human-criteria-based, and Jrk cost terms are identical for the different cost functions, while the weights of the other cost terms were changed based on the data-based cost terms used in the cost functions.

The stability-based cost term's weight has a high value in the SP1 cost function of both MSK-model and NMSK-model optimizations and in the FP cost function of the NMSK-model optimization, in comparison to its weight values in the remainder of the cost functions. On the other hand, the Rsd cost term got lower weights in the SP1 cost function of both MSK-model and NMSK-model optimizations and in the FP cost function

Table 6.3: Computational times of the MSK-model and NMSK-model optimizations with the different cost functions

model	DT	SDT1	SDT2	SDT3	SP1	SP2	SP3	FP
MSK	2 hrs	10 hrs	8 hrs	3 hrs	14 hrs	3 hrs	15 hrs	10 hrs
NMSK	2 hrs	3 hrs	3 hrs	1 hrs	2 hrs	2 hrs	2 hrs	6 hrs

of the NSMK-model optimization. The high weight of the stability-based cost term (i.e., enforcing more stability) and the low weight of the Rsd cost term (i.e., reducing dynamic consistency) could compensate for the absence of torque-tracking and angle-tracking cost terms in the SP1 and FP cost functions.

The Imp cost term’s weight has the lowest value in the DT cost functions, where all three data-based cost terms were used. It shows that the three data-based cost terms can assist the optimization in solving the implicit dynamic equations of the child gait. Consequently, if the experimental data of either motions, torques, or GRFs are not available, we have to consider a larger weight for the Imp cost term to have a dynamically-consistent gait simulation.

6.2.2 Computational Time Examination

The computational times of the MSK-model and NSMK-model optimizations are shown in Table 6.3. Although we expected high computational times for the NMSK-model optimizations due to the complexity of the equations of the NMSK model, MSK-model optimizations took considerably longer to converge to an optimal solution.

When the DT cost function was used, the MSK-model and NMSK-model optimizations had the same computational time (2 hrs). It demonstrates that when we have a fully-data-tracking cost function, in which all the data of angles, torques, and GRFs are tracked, the MSK and NMSK models behave similarly and converge with the same speed. However, when the remainder of the cost functions, in which not all the data-based cost terms are used, the convergence times of the MSK-model optimizations are considerably longer than those of the NMSK-model optimizations.

The direct collocation optimal control is very sensitive to the initial guess. The poor initial guess increases the convergence time of the optimization [109]. Since, for the MSK-model optimization, we did not have a good initial guess (i.e., experimental-data-based initial guess) for some states and control inputs, including the HAT-to-ground position and orientation, the metatarsal joint angles and torques, and the 12 MTG activations,

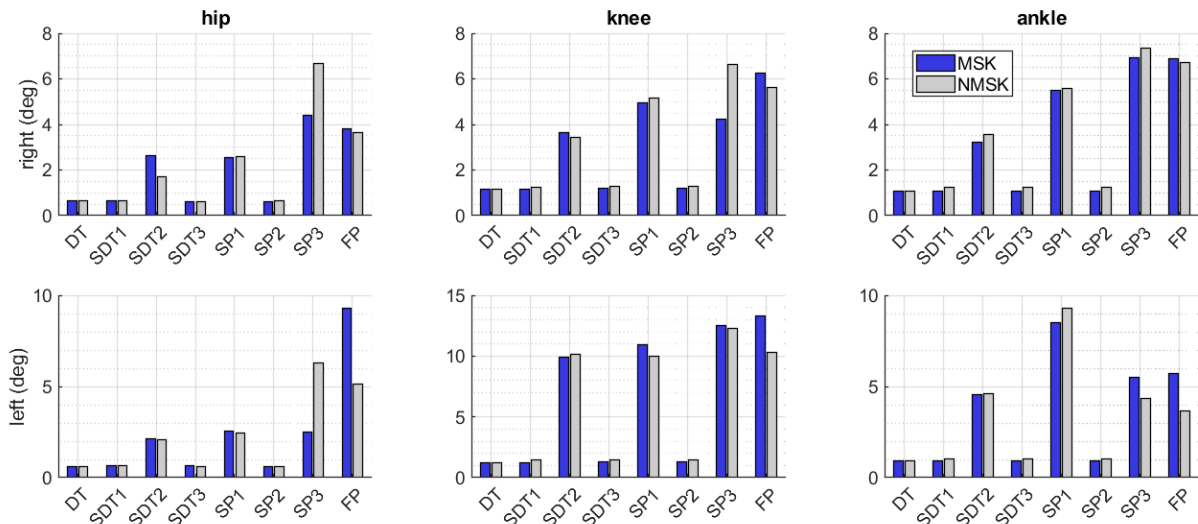


Figure 6.1: Root-mean-square errors of the joint angles from the MSK-model and NMSK-model optimizations using the different cost functions

the convergence times of the MSK-model optimizations increased. On the contrary, the NMSK-model optimizations had shorter computational times (considerably faster convergences) since we had reasonable initial guess for the 16 control inputs of the NMSK-model optimization (i.e., EMG data were used as the initial guess for the muscle excitations).

6.2.3 Prediction Accuracy Examination

The RMSEs of the joint angles, GRFs, and torques from the MSK-model and NMSK-model optimizations with the different cost functions are shown in Figures 6.1, 6.2, and 6.3, respectively. The RMSEs of the muscle excitations from the NMSK-model optimization with the different cost functions are shown in Figure 6.4.

Disregarding the model types and the cost terms used, the simulated angles, GRFs, torques, and muscle excitations of the right and left legs may not have the same RMSEs due to three reasons: (1) Since we only had the experimental data of the right leg, we had to generate data for the left leg from the experimental data of the right leg using a Fourier series. Thus, the experimental data considered for the left leg in this thesis were not accurate (experimentally-measured). (2) We assumed that the time shift between the right and left leg motions equals the sum of the single-support and double-support

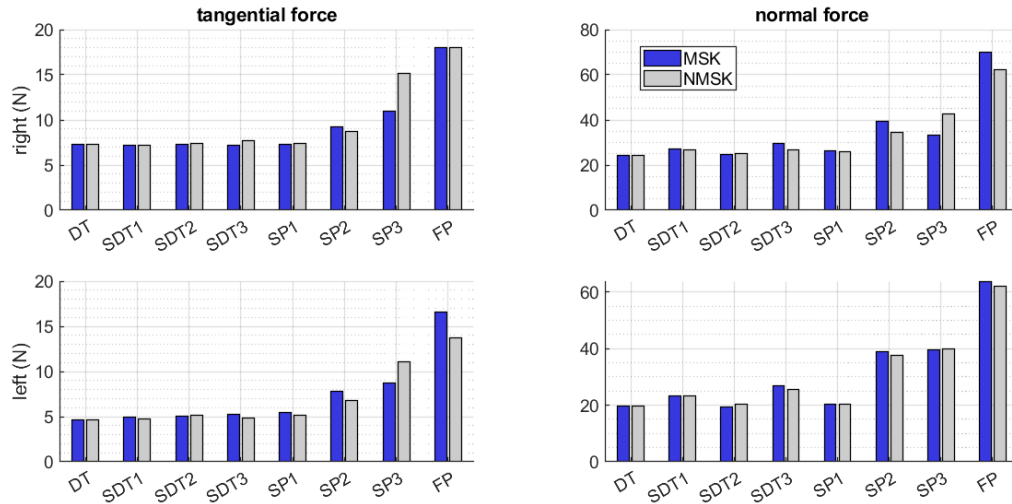


Figure 6.2: Root-mean-square errors of the ground reaction forces from the MSK-model and NMSK-model optimizations using the different cost functions

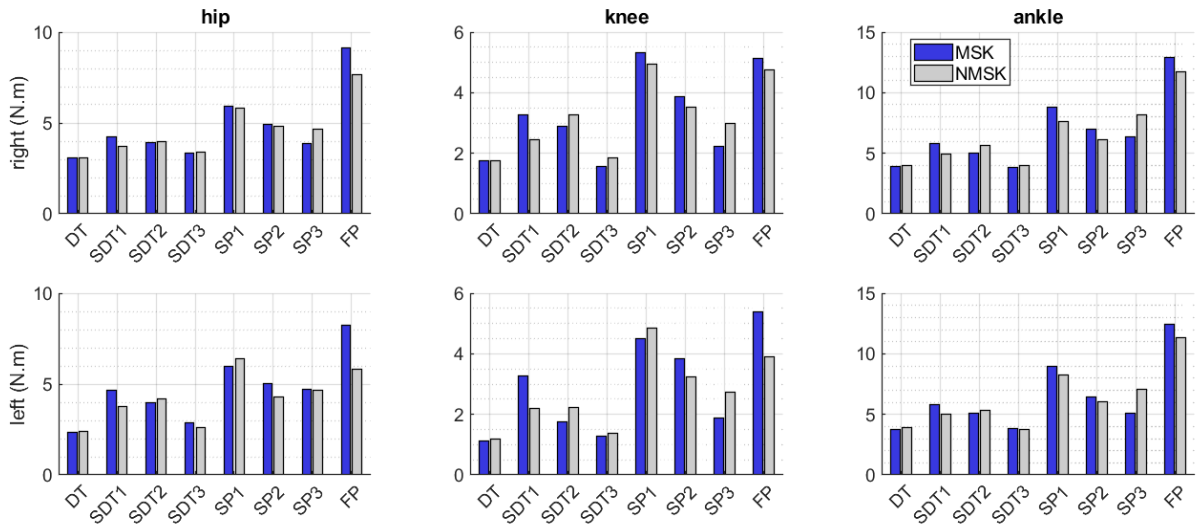


Figure 6.3: Root-mean-square errors of the joint torques from the MSK-model and NMSK-model optimizations using the different cost functions

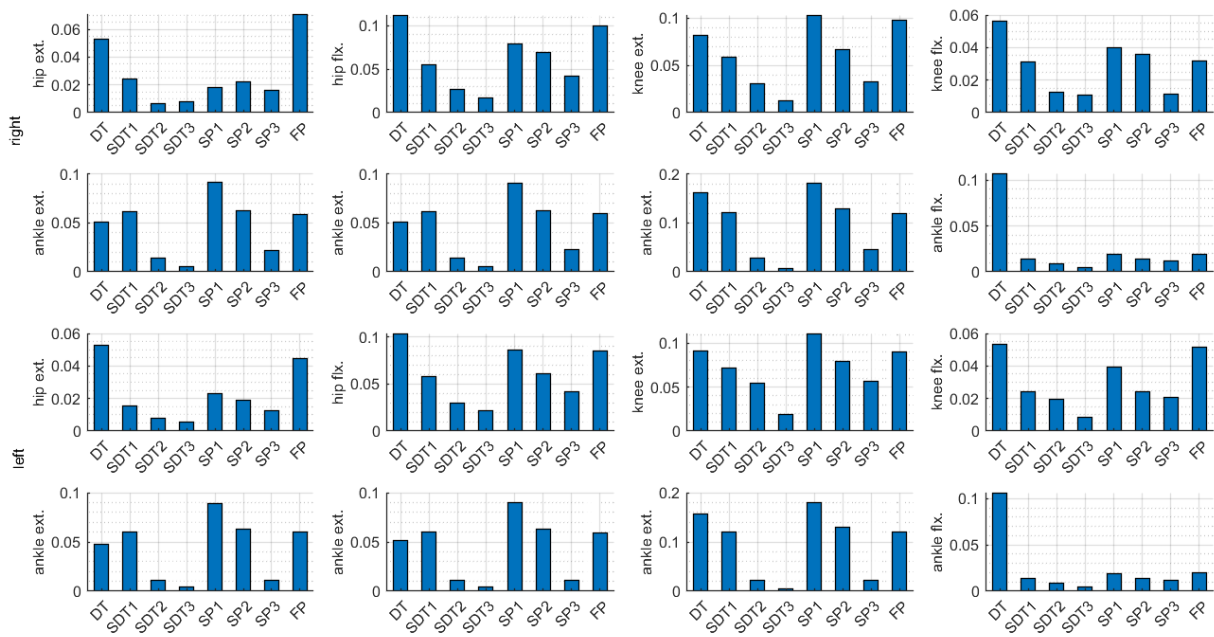


Figure 6.4: Root-mean-square errors of the muscle excitations from the NMSK-model optimization using the different cost functions

phase times which may not be equal to the real time shift. (3) The experimental data, reported for both legs in the literature [109], show that the right and left legs do not have completely symmetric motion during gait. Despite these reasons, we believe that our proposed optimizations can result in very close RMSEs for the right and left legs if experimental data are collected for both legs.

When MSK and NMSK Models Have Similar Performances

According to the RMSE plots, the MSK-model and NMSK-model optimizations had relatively similar prediction accuracy when the cost function used was either DT, SDT3, or SP1.

In the DT cost function, all the data-based cost terms are included. The MSK-model and NMSK-model optimizations converge with the same speed using this cost function and have similar prediction accuracy. The only difference is that the NMSK-model optimization could predict muscle excitations and calculate COT, while the MSK-model optimization could not. Thus, if all the data of motions, torques, and GRFs are available to compose the DT cost function and the muscle excitations and COT are not required to be calculated, it is efficient to use an MSK-model optimization, which has less complex equations than the NMSK-model optimization. It should also be noted that, according to Figure 6.4, the muscle excitations predicted by the NMSK-model optimization with the DT cost function were not very accurate in comparison to those predicted by the other cost functions.

In the SDT3 cost function, only two of the three data-based cost terms (i.e., Ang and Trq cost terms) are included. The MSK-model and NMSK-model optimizations with the SDT3 cost function had very low convergence times (3 hrs and 1 hrs, respectively) and very high prediction accuracy compared to the optimizations with other cost functions. The results of the NMSK-model optimization with the SDT3 cost function show that to develop a computationally-efficient and accurate gait simulation using the NMSK model, it is sufficient to only use two of the three data-based cost terms (i.e., Ang and Trq cost terms).

The Ang and Trq cost terms can provide a good estimation for both states and control inputs of the optimization without the GRF cost term's assistance. In other words, when tracking the data of angles and torques at the same time, we do not need the force-tracking cost term anymore. The reason is that the implicit dynamics equations, including GRF equations, are already met as path constraints, and angle-tracking and torque-tracking cost terms are sufficient to assist the optimization in solving the implicit dynamics. Thus, it is not required to use a redundant cost term (GRF cost term) in the cost function since

a redundant cost term confuses the cost function, increases the computational time, and decreases prediction accuracy. According to Figure 6.4, among all NMSK-model optimizations, the NMSK-model optimization with the SDT3 cost function could predict the most accurate muscle excitations. On the contrary, the NMSK-model optimization with the DT cost function (including the three data-based cost terms) is among the least accurate optimizations in muscle excitation prediction.

In the SP1 cost function, only one of the three data-based cost terms (i.e., GRF cost term) is included. The MSK-model and NMSK-model optimizations with the SP1 cost function have relatively similar low prediction accuracy. The force-tracking cost term can assist the optimization in solving the foot-ground contact equations, and consequently, estimating accurate GRFs. However, this cost term cannot assist the optimization in estimating accurate values for the states and control inputs. Thus, it is required to use at least one of the torque-tracking or angle-tracking cost terms along with the force-tracking cost term to improve the prediction accuracy. According to Figure 6.4, among all NMSK-model optimizations, the NMSK-model optimization with the SP1 cost function predicted the least accurate muscle excitations.

When MSK Model Has Better Performance Than NMSK Model

According to the RMSE plots, when either the cost function SDT2 or SP3 was used, the MSK-model optimization had better prediction accuracy than the NMSK-model optimization. However, the NMSK-model optimization could predict relatively accurate muscle excitations using these two cost functions. In the SDT2 cost function, only two of the three data-based cost terms (i.e., Trq and GRF cost terms) are included, and in the SP3 cost function, only one of the three data-based cost terms (i.e., Trq cost term) exists. The common feature of SDT2 and SP3 cost functions is that both have the torque-tracking cost term but not the angle-tracking cost term.

In the NMSK-model optimizations, there is one further human-criteria-based cost term (i.e., Mtb cost term) compared to the MSK-model optimizations. Most of the equations of the Mtb cost term consist of joint torques. Thus, the torque-tracking cost term is more effective in the NMSK-model optimizations than the MSK-model optimizations that do not have the Mtb cost term. The torque-tracking cost term enforces the NMSK-model optimization to focus more on estimating accurate control inputs (i.e., accurate muscle excitations and joint torques) and less on predicting accurate states and GRFs. In conclusion, to develop an accurate gait simulation using the NMSK model, the torque-tracking cost term should be used along with the angle-tracking cost term.

When NMSK Model Has Better Performance Than MSK Model

According to the RMSE plots, the NMSK-model optimization had better prediction accuracy than MSK-model optimization when either the cost function SDT1, SP2, or FP was used.

In the SDT1 cost function, only two of the three data-based cost terms (i.e., Ang and GRF cost terms) exist, and in the SP2 cost function, only one of the three data-based cost terms (i.e., Ang cost term) exists. The common feature of SDT1 and SP2 cost functions is that both have the motion-tracking cost term assisting the optimization in estimating accurate values for the states.

As explained for the SDT2 and SP3 cost functions, when there is no motion-tracking cost term, the prediction accuracy of the NMSK-model optimizations was less than that of the MSK-model optimizations. However, when either the SDT1 or SP2 cost function, having the motion-tracking cost term, was used, the NMSK-model optimizations had considerably better prediction accuracy than the MSK-model optimizations. It should also be noted that, according to Figure 6.4, the muscle excitations predicted by the NMSK-model optimizations with the SDT1 and SP2 cost functions were not very accurate in comparison to those predicted by the SDT2 and SP3 cost functions having torque-tracking cost term.

The MSK-model and NMSK-model optimizations with the FP cost function had less prediction accuracy than the optimizations with cost functions having at least one data-based cost term. The reason is that there is no data-based cost term in the FP cost function to assist the optimization in estimating accurate values for the states, control inputs, and GRFs.

When the fully-predictive cost function was used, the NMSK-model optimization had considerably better prediction accuracy and shorter convergence time than the MSK-model optimization. The reason is that in the NMSK-model optimization, we had one additional human-criteria-based cost term (i.e., Mtb cost term) and good initial guess for the 16 control inputs (i.e., muscle excitations). Thus, for a fully-predictive gait simulation, the NMSK model performs more efficiently than the MSK model in terms of prediction accuracy and computational time. The RMSEs of the NMSK-model optimizations with the fully-predictive cost function, although being higher than the RMSEs of the NMSK-model optimization with the data-tracking cost functions, are reasonably low compared to the ranges of the experimental angles, torques, GRFs, and muscle excitations. The results of the NMSK-model optimization with the FP cost function are illustrated in detail in the next section.

6.2.4 Fully-Predictive Gait Simulation Using The Neuromusculoskeletal Model

Our NMSK-model optimization with the fully-predictive cost function, done using direct collocation optimal control, can be considered as a fully-predictive child gait simulation since there is no data-based term in the constraints and the cost function. This optimization simulates the child gait using only dynamic-based, stability-based, and human-criteria-based cost terms.

The only two prerequisites for our fully-predictive simulation were as follows: (1) We identified the contact parameters, MTG parameters, and the muscle-activation-dynamics parameters through fully-data-tracking optimizations and then used the identified values for the fully-predictive simulation; (2) Since the direct collocation optimal control is very sensitive to the initial guess, we used either a data-based or data-consistent initial guess for states and control inputs. The initial guess for hip, knee, and ankle angles and muscle excitations were data-based (i.e., experimental angle and EMG data were used as initial guess). The initial guess for the angles and torques of the metatarsals, and the position and orientation of the whole-body COM were data-consistent (i.e., the corresponding results from the fully-data-tracking cost terms were used as initial guess).

As shown in Table 6.2, for the NMSK-model optimization with the FP cost function, we considered a relatively high weight for the stability-based cost term to increase stability, and we considered a low weight for the Rsd cost term to reduce the dynamic consistency. These modifications on the weights compensated for the absence of the data-based cost terms and helped predict stable and human-like gait. As given in Table 6.3, the computational time of the NMSK-model optimization with the FP cost function is 6 hours. This duration is 40% less than the computational time of the MSK-model optimization with the FP cost function (i.e., 10 hours) since the NMSK-model optimization with the FP cost function had reasonable initial guess for the control inputs, and this is important in increasing the convergence speed.

To demonstrate the prediction accuracy of our fully-predictive child gait simulation, we have included the predicted results in this section. Figures 6.5, 6.6, 6.7, and 6.8 show the predicted angles, GRFs, torques, and muscle excitations, respectively.

The RMSEs of the hip, knee, and ankle angles, predicted by the NMSK-model fully-predictive optimization, are 25%, 16%, and 19% less than those predicted by the MSK-model fully-predictive optimization, respectively. The RMSEs of the hip, knee, and ankle torques, predicted by the NMSK-model fully-predictive optimization, are 23%, 17%, and 9% less, and the RMSEs of the tangential and normal ground reaction forces are 9% and 7%

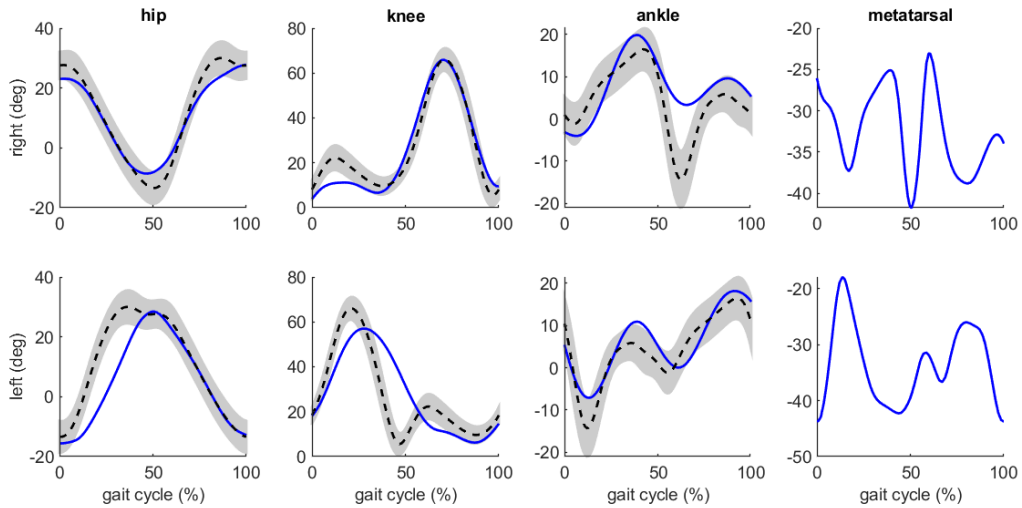


Figure 6.5: The joint angles from the NMSK-model fully-predictive simulation (The dotted lines represent the mean experimental data and the gray areas show ± 1 standard deviations of the mean experimental data)

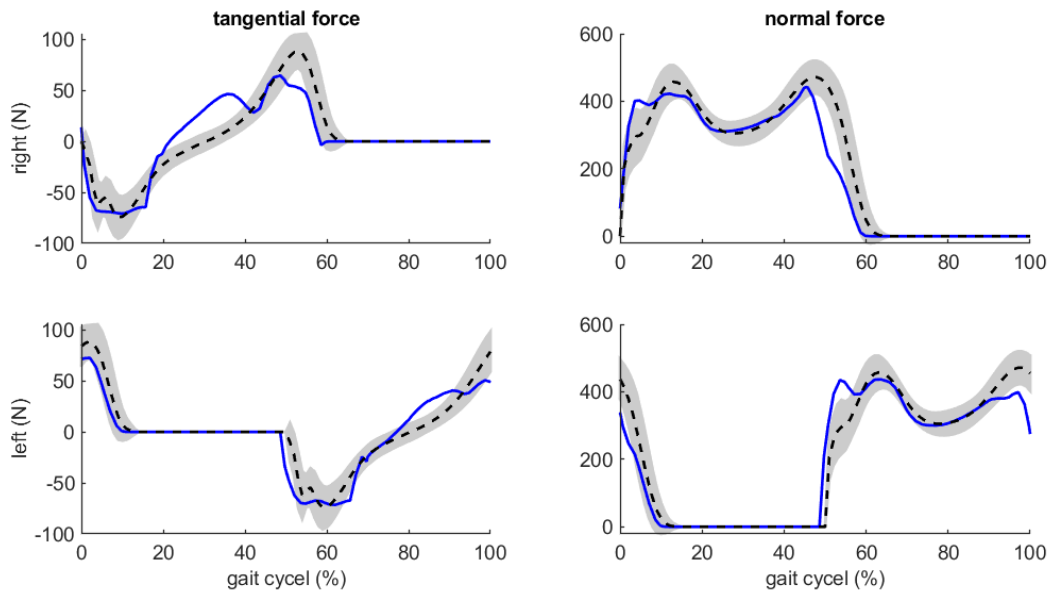


Figure 6.6: The ground reaction forces from the NMSK-model fully-predictive simulation (The dotted lines represent the mean experimental data and the gray areas show ± 1 standard deviations of the mean experimental data)

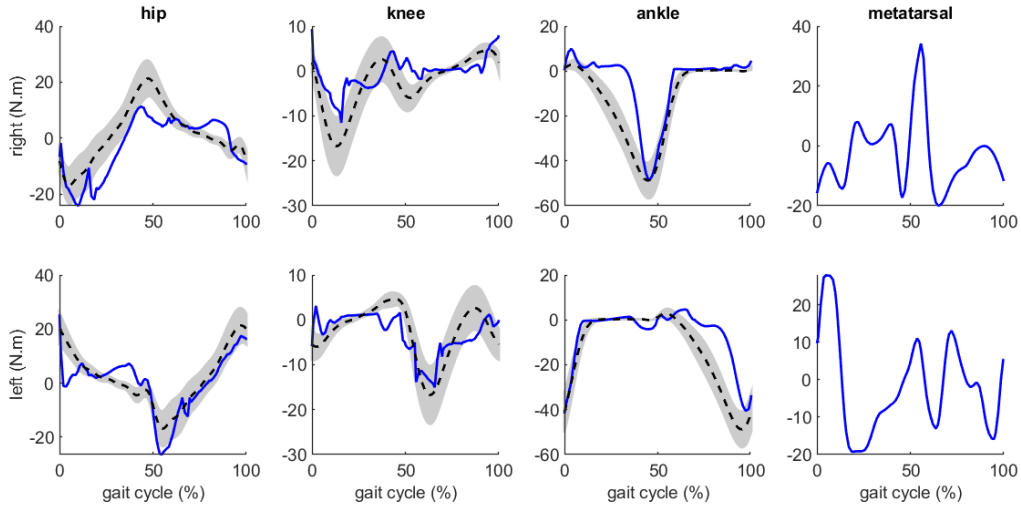


Figure 6.7: The joint torques from the NMSK-model fully-predictive simulation (The dotted lines represent the mean experimental data and the gray areas show ± 1 standard deviations of the mean experimental data)

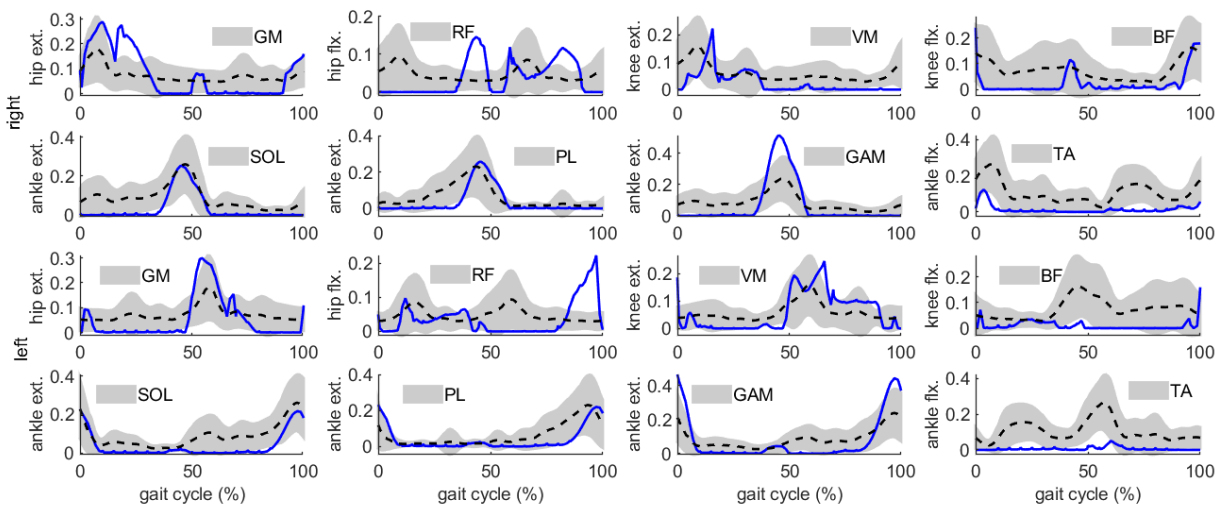


Figure 6.8: The muscle excitations from the NMSK-model fully-predictive simulation (The dotted lines represent the mean experimental data and the gray areas show ± 1 standard deviations of the mean experimental data)

less than those predicted by the MSK-model fully-predictive optimization. The metatarsal angles and torques predicted by the NMSK-model fully-predictive optimization are also in good agreement with the results simulated by the fully-data-tracking optimizations of Chapter 5.

The majority of the muscle excitations predicted by the NMSK-model fully-predictive optimization are in good agreement with the corresponding EMG data. The comparison between the muscle excitations shown in Figure 5.11 and Figure 6.8 concludes that the muscle excitations predicted by the NMSK model with the fully-predictive cost function are more consistent with the EMG data than the muscle excitations predicted by the fully-data-tracking cost function. It shows that an optimization, that is over-constrained with data-tracking cost terms, can not predict very natural muscle excitations. The RMSE mean value of the muscle excitations from the fully-predictive cost function is 12% less than that of the fully-data-tracking cost function.

6.3 Conclusion

In this chapter, we used the MTG-based MSK and NMSK models to simulate a natural-speed child gait. We developed a total of 16 optimizations (8 optimizations for each model), ranging from fully-data-tracking to fully-predictive optimizations, to compare the MSK and NMSK models in terms of prediction accuracy and computational time. We investigated the roles of a wide range of cost terms in achieving a realistic simulation. These cost terms included dynamic-based, stability-based, human-criteria-based, and data-based cost terms.

From the manually-tuned weighting factors, we concluded that a relatively high weight for the stability-based cost term and a low weight for the residual-load-squared cost term are required when there is no data-tracking cost term in the cost function. Besides, when the cost function includes all the data-tracking cost terms (i.e., torque-tracking, angle-tracking, and GRF-tracking cost terms), implicit dynamic equations are solved faster, and consequently, the implicit-dynamic-squared cost term does not need a large weight. However, the absence of either of these data-tracking cost terms causes us to increase the weight of the implicit-dynamic-squared cost term to ensure dynamic consistency.

From the computational times of the optimizations, we determined that the NMSK-model optimizations are more computationally-efficient than MSK-model optimizations since the control inputs of the NMSK-model optimizations are muscle excitations with a reasonable initial guess (i.e., EMG data were used as the initial guess for the muscle excitations).

From the prediction accuracy investigation, we noted that if all the data of motions, torques, and GRFs are available to compose the DT cost function and the muscle excitations and COT are not required to be calculated, it is efficient to use an MSK-model optimization, which has less complex equations than the NMSK-model optimization. Furthermore, we showed that to develop a computationally-efficient and accurate gait simulation using the NMSK model, it is sufficient to only use two of the data-tracking cost terms: angle-tracking and torque-tracking. This optimization could predict the most accurate muscle excitations as well. On the other hand, when the GRF-tracking cost term was used in the absence of the angle-tracking and torque-tracking cost terms, the MSK-model optimization predicted absolutely inaccurate angles and torques, and the NMSK-model optimization predicted not only inaccurate angles, torques but also the least accurate muscle excitations.

The other interesting outcome of the prediction accuracy investigation is that when the torque-tracking cost term was used in the absence of the angle-tracking cost term, the NMSK-model optimization had worse prediction accuracy than the MSK-model optimization. However, the NMSK-model optimization could predict relatively accurate muscle excitations. On the other hand, when the angle-tracking cost term was used in the absence of the torque-tracking cost term, the NMSK-model optimization had better prediction accuracy than the MSK-model optimization.

The main achievement of this chapter is that when the fully-predictive cost function was used, the NMSK-model optimization could predict angles, torques, and GRFs 20%, 16%, and 8% more accurately than the MSK-model optimization. The computational time of the NMSK-model optimization was also 40% less than the time of the MSK-model optimization. Besides, the muscle excitations predicted by the NMSK-model fully-predictive optimization were 12% more accurate than those predicted by the data-tracking optimization.

There are two prerequisites for our proposed NMSK-model fully-predictive optimization: (1) The contact parameters, MTG parameters, and the muscle-activation-dynamics parameters should be identified through fully-data-tracking optimizations, and then the identified values can be used for the fully-predictive simulation; (2) The initial guess for the hip, knee, and ankle angles, muscle excitations, angles and torques of the metatarsals, and also the position and orientation of the HAT should be experimental-data-consistent.

In the next chapter, we will use the MSK-model and NMSK-model optimizations to predict dynamically-consistent slow and fast gaits for children without tracking the slow and fast gait experimental data in the optimizations.

Chapter 7

Slow-Speed and Fast-Speed Gait Prediction Using the Musculoskeletal and Neuromusculoskeletal Child Models: A Semi-Predictive Approach

This chapter evaluated whether the MSK-model and NMSK-model optimizations, developed in Chapter 6, could minimize the reliance of simulations on experiments and predict dynamically-consistent and physically-realistic slow and fast gaits, without tracking the experimental data of the corresponding slow and fast gaits.

We considered four different-speed gaits, including very slow walking at 0.9 m/s (XS), slow walking at 1.09 m/s (S), fast walking at 1.29 m/s (M), and very fast walking at 1.58 m/s (L), to generate the slow-gait and fast-gait simulations¹. To predict gaits at these four speeds, we used the MSK-model and NMSK-model optimizations with the data-tracking (DT) cost function developed for the natural-speed gait simulation in Chapter 6; however, three modifications were applied: (1) The experimental data of the natural-speed gait (i.e., natural walking at 1.26 m/s (N)) were scaled with respect to the cycle times of the slow and fast gaits, and then the scaled data were used as initial guess in the slow-gait and fast-gait simulations; it should be noted that we scaled (stretched/shrank) the natural gait experimental data only in time and kept the magnitude of them unchanged. (2) In the slow-gait and fast-gait simulations, the final times (i.e., gait cycle times) and the bounds

¹We selected the names of XS, S, M, and L for compatibility with [18] from which we extracted the experimental data of the child different-speed gaits.

on the states and control inputs were determined based on the experimental data of the corresponding slow and fast gaits. (3) The scaled natural gait data were used to compose the data-based and stability-based cost terms of the cost function.

Our slow-gait and fast-gait simulations can be considered “*semi-predictive simulations*” since the experimental data of the corresponding slow and fast gaits were not tracked in them.

7.1 Semi-Predictive Optimization Methodology

We simulated each of the XS, S, M, and L gaits using the MSK-model and NMSK-model optimizations with the DT cost function. Thus, we developed a total of eight optimizations to generate the slow-gait and fast-gait simulations. The details of each MSK-model and NMSK-model optimization were explained in Section 6.1. The cost terms used in the DT cost function of each model’s optimization were mentioned in Table 6.1. For the slow-gait and fast-gait simulations, the states, control inputs, and constraints were kept unchanged, and the only modifications are as follows:

- For the natural-speed gait simulation in Chapter 6, the lower and upper bounds on the final time were considered to be equal (i.e., the final time was enforced to be fixed), and the upper and lower bounds were set to 0.98 s, which was the experimental gait cycle time of child natural-speed gait. For the slow-gait and fast-gait simulations, we set the lower and upper bounds on the final time equal to the experimental gait cycle times of child’s XS, S, M, and L gaits that were equal to 1.30 s, 1.12 s, 0.95 s, and 0.83 s, respectively. The bounds on the states and control inputs were also determined based on the prescribed standard deviations of the experimental data for child’s XS, S, M, and L gaits. We extracted the experimental data of the child different-speed gaits from [18]; this paper is the same reference from which we extracted the child natural-speed gait experimental data used in the previous chapters. For the HAT-to-ground position and orientation, the metatarsal joint angles and torques, and the 12 MTG activations, the bounds were kept equal to the ones defined for the natural-speed gait simulation.
- For the natural-speed gait simulation in Chapter 6, most of the initial guesses were set to the natural-speed gait experimental data and the initial guess of the HAT-to-ground position and orientation, the metatarsal joint angles and torques, and the 12 MTG activations were set to the corresponding results obtained from a fully-data-tracking gait simulation. However, we wanted to minimize the reliance of our

slow-gait and fast-gait simulations on experiments. To do so, first, we scaled the initial guess used in the natural-speed gait simulation with respect to the XS, S, M, and L gait cycle times, while keeping the magnitudes of them unchanged. Then, we used the scaled values as the initial guess for all slow and fast gait simulations.

- The cost functions used for the slow-gait and fast-gait simulations are the same as the DT cost functions used for the natural-speed gait simulation in Chapter 6. Row number 1 in Table 6.1 shows the cost terms of the DT cost functions for the MSK-model and NMSK-model optimizations. The only difference between the cost functions of natural-speed gait and different-speed gait simulations is in their stability-based and data-based cost terms. In the stability-based and data-based cost terms of the natural-speed gait simulation, the natural gait experimental data were used. However, in the stability-based and data-based cost terms of the slow-gait and fast-gait simulations, we used the natural gait experimental data that were already scaled with respect to the XS, S, M, and L gait cycle times. The DT cost functions of the slow-gait and fast-gait simulations were defined as:

$$\begin{aligned}
J_{MSK} = \frac{1}{t_f} \int_{t_0}^{t_f} & \left[w_1 t_f^6 \sum_{i=1}^{11} \left(\frac{u_1}{u_{1Nmax} - u_{1Nmin}} \right)_i^2 + w_2 \sum_{i=1}^3 \left(\frac{R_{pelvis}}{R_{Nmax} - R_{Nmin}} \right)_i^2 + \right. \\
& w_3 \sum_{i=1}^8 \left(\frac{\tau_{inv.} - \tau_{input}}{\tau_{Nmax} - \tau_{Nmin}} \right)_i^2 + w_4 \sum_{i=1}^3 \left(\frac{q_{sim.} - q_N}{q_{Nmax} - q_{Nmin}} \right)_i^2 + w_5 \sum_{i=1}^{12} \left(\frac{u_4}{u_{4Nmax} - u_{4Nmin}} \right)_i^2 + \\
& \left. w_6 \sum_{i=1}^6 \left(\frac{\tau_{sim.} - \tau_N}{\tau_{Nmax} - \tau_{Nmin}} \right)_i^2 + w_7 \sum_{i=1}^6 \left(\frac{q_{sim.} - q_N}{q_{Nmax} - q_{Nmin}} \right)_i^2 + w_8 \sum_{i=1}^4 \left(\frac{GRF_{sim.} - GRF_N}{GRF_{Nmax} - GRF_{Nmin}} \right)_i^2 \right] dt
\end{aligned} \tag{7.1}$$

$$\begin{aligned}
J_{NMSK} = & \frac{1}{t_f} \int_{t_0}^{t_f} \left[w_1 t_f^6 \sum_{i=1}^{11} \left(\frac{u_1}{u_{1Nmax} - u_{1Nmin}} \right)_i^2 + w_2 \sum_{i=1}^3 \left(\frac{R_{pelvis}}{R_{Nmax} - R_{Nmin}} \right)_i^2 + \right. \\
& w_3 \sum_{i=1}^8 \left(\frac{\tau_{inv.} - \tau_{input}}{\tau_{Nmax} - \tau_{Nmin}} \right)_i^2 + w_4 \sum_{i=1}^3 \left(\frac{q_{sim.} - q_N}{q_{Nmax} - q_{Nmin}} \right)_i^2 + w_5 \sum_{i=1}^{12} \left(\frac{u_4}{u_{4Nmax} - u_{4Nmin}} \right)_i^2 + \\
& w_6 \frac{t_f^6}{BM^2 d^4} \left(\frac{\dot{E}}{\dot{E}_{max} - \dot{E}_{min}} \right)^2 + w_7 \sum_{i=1}^6 \left(\frac{\tau_{sim.} - \tau_N}{\tau_{Nmax} - \tau_{Nmin}} \right)_i^2 + w_8 \sum_{i=1}^6 \left(\frac{q_{sim.} - q_N}{q_{Nmax} - q_{Nmin}} \right)_i^2 + \\
& \left. w_9 \sum_{i=1}^4 \left(\frac{GRF_{sim.} - GRF_N}{GRF_{Nmax} - GRF_{Nmin}} \right)_i^2 \right] dt
\end{aligned} \tag{7.2}$$

where J_{MSK} and J_{NMSK} are the cost functions of the MSK-model and NMSK-model optimizations, respectively. The index N denotes the natural gait experimental data scaled in time with unchanged magnitudes.

We developed the eight different-speed gait simulations using direct collocation optimal control. We used GPOPS-II with the IPOPT solver in first derivative mode to implement these optimizations with the tolerance of 1e-5. Similar to the previous optimizations, we considered a fixed mesh of 100 collocation points, divided into 20 intervals, over the whole gait cycle. These optimizations were done on a desktop computer with an Intel[®] Core[™] i7-6700 CPU @ 3.40 GHz with 16.0 GB RAM.

7.2 Results and Discussion

In this section, the results of the slow-gait and fast-gait simulations are shown and discussed. We also compared the MSK and NMSK models in terms of prediction accuracy and computational time to evaluate whether they are effective for predicting slow and fast gaits, without tracking the experimental data of the corresponding slow and fast gaits.

For the weighting factors of the cost functions, J_{MSK} and J_{NMSK} (Eq. 7.1 and Eq. 7.2, respectively), we initially considered the same weight values used for the DT cost functions in the natural-speed gait simulation in Chapter 6. We then tried to manually tune them for each of the XS, S, M, and L gait simulations. After a great number of manual tunes,

Table 7.1: Weighting factors for the slow-gait and fast-gait simulations

simulation	model	cost function	weights
XS, S, M, L	MSK	J_{MSK} (Eq. 7.1)	$w_1 = 1/40$, $w_2 = 1/4$, $w_3 = 1/40$, $w_4 = 1/4$ $w_5 = 1/100$, $w_6 = 1/4$, $w_7 = 1/4$, $w_8 = 1/4$
XS, S, M, L	NMSK	J_{NMSK} (Eq. 7.2)	$w_1 = 1/40$, $w_2 = 1/4$, $w_3 = 1/40$, $w_4 = 1/4$ $w_5 = 1/100$, $w_6 = 1/5$, $w_7 = 1/4$, $w_8 = 1/4$, $w_9 = 1/4$

Table 7.2: Computational times of the slow-gait and fast-gait simulations

model	XS	S	M	L
MSK	18 hrs	12 hrs	10 hrs	12 hrs
NMSK	8 hrs	6 hrs	4 hrs	5 hrs

we concluded that the weight values of the DT cost functions in the natural-speed gait simulation give the minimum RMSEs for the slow-gait and fast-gait stimulations as well. Thus, we finally set the weights of cost functions J_{MSK} and J_{NMSK} equal to the weights of the DT cost functions used for the natural-speed gait simulation. Table 7.1 shows the weights of cost terms of J_{MSK} and J_{NMSK} .

The computational times of the slow-gait and fast-gait simulations are given in Table 7.2. The slow-gait and fast-gait simulations are not as computationally-efficient as the natural-speed gait simulation with the DT cost function that took only 2 hours for either MSK-model and NMSK-model optimizations. In the slow-gait and fast-gait simulations, we did not use the corresponding slow and fast gait data, and instead, we used the scaled natural gait data that were not very strong initial guess for the slow-gait and fast-gait simulations.

In the natural-speed gait simulations, we observed that when the corresponding experimental data were not tracked, the MSK-model optimizations took longer than the NMSK-model optimization to converge to an optimal solution. The reasons were explained in Section 6.2.2. Due to the same reasons, for the slow-gait and fast-gait simulations, the MSK-model optimizations took twice as long as the NMSK-model optimizations to converge to an optimal solution as shown in Table 7.2.

According to the computational times in Table 7.2, XS and L gait simulations took longer to converge than S and M gait simulations, respectively. Since the S and M gaits' speeds are close to the natural gait's speed, the ranges of joint angles, torques, GRFs, and muscle excitations of the S and M gaits are similar to those of the natural gait. In contrast, the XS and L gaits have ranges significantly different from the natural gait's ranges. The use of the scaled natural gait data as the initial guess and in the data-based

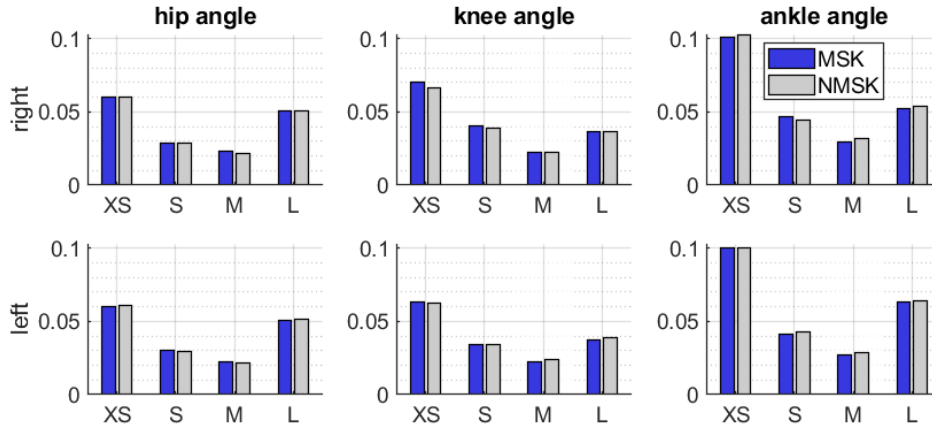


Figure 7.1: Normalized root-mean-square errors of the joint angles from the slow-gait and fast-gait simulations

cost terms led the S and M gait simulations to converge faster than the XS and L gait simulations. In conclusion, the larger the gap there exists between the speed of slow or fast gaits and the speed of natural gait, the longer the computational time for slow-gait or fast-gait simulations.

In Chapter 6, we calculated the RMSEs to compare the different cost functions' prediction accuracy in simulating natural-speed gait. However, in this chapter, since the ranges for the experimental data of the slow and fast gaits are not identical, the prediction accuracies of the slow-gait and fast-gait simulations cannot be compared fairly by comparing the RMSEs. Thus, we calculated the normalized root-mean-square errors (NRMSEs) by dividing RMSEs by the range of experimental data to make them dimensionless and consequently comparable [66]. The range of experimental data is defined as the maximum value minus the minimum value. The NRMSEs of the joint angles, GRFs, and torques from the MSK-model and NMSK-model optimizations for slow-gait and fast-gait simulations are shown in Figures 7.1, 7.2, and 7.3, respectively.

According to the NRMSE plots, the accuracies of the MSK-model and NMSK-model optimizations were similar in predicting joint angles and ground reaction forces for the slow-gait and fast-gait simulations. However, the NMSK-model optimization's accuracy is higher than the MSK-model optimization's accuracy in predicting joint torques for the different-speed gait simulations. The NMSK-model optimization could predict the joint torques of the XS, S, M, and L gaits more accurately than the MSK-model optimization by approximately 17%, 12%, 10%, and 2%, respectively. The good accuracy of the NMSK-

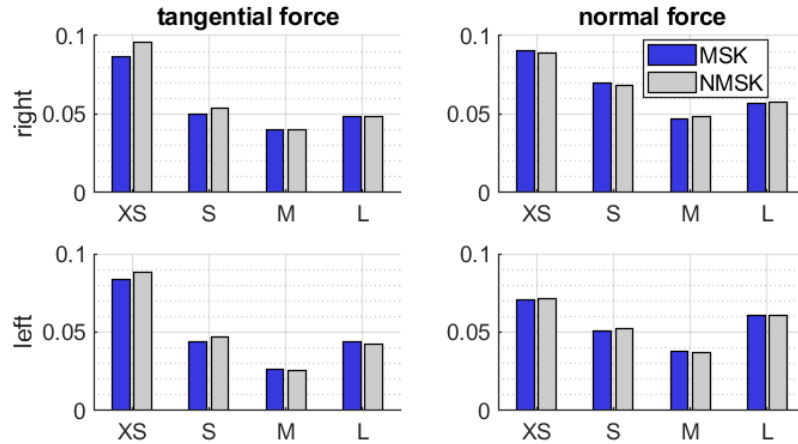


Figure 7.2: Normalized root-mean-square errors of the ground reaction forces from the slow-gait and fast-gait simulations

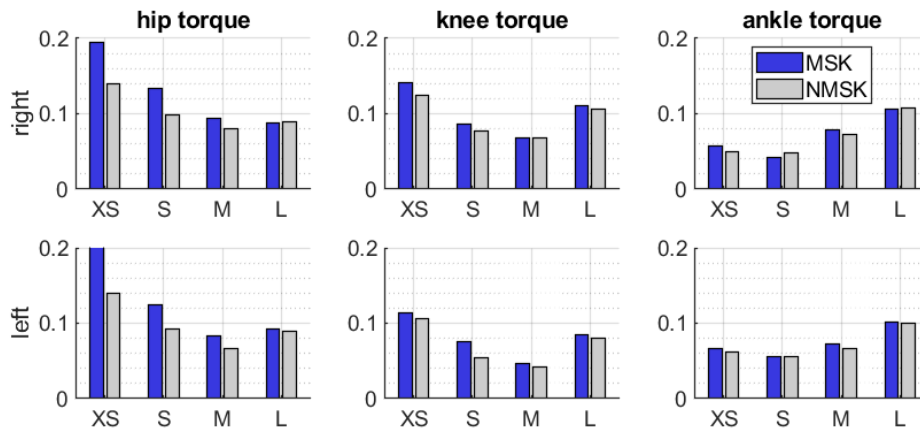


Figure 7.3: Normalized root-mean-square errors of the joint torques from the slow-gait and fast-gait simulations

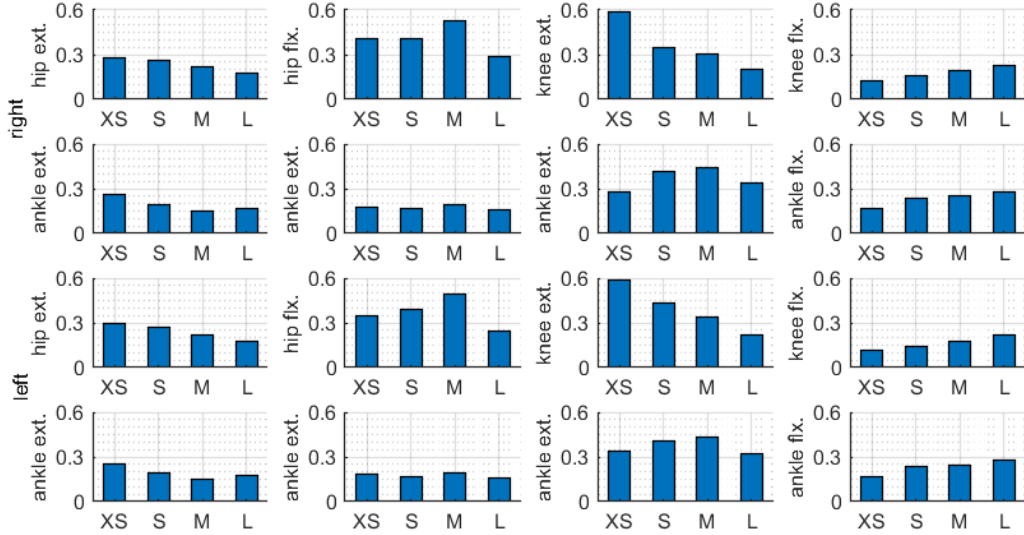


Figure 7.4: Normalized root-mean-square errors of the muscle excitations from the slow-gait and fast-gait simulations

model optimization is a result of having one additional human-criteria-based cost term (i.e., metabolic energy consumption). Besides, we had good initial guess for the 16 control inputs (i.e., we used scaled EMG data of natural gait data as the initial guess for the muscle excitations) that yield accurate joint torques.

Due to the same reason mentioned for the computational times, the use of the scaled natural gait data as initial guess and in the data-based cost terms led the S and M gait simulations to predict more accurate joint angles, torques, and ground reaction forces than the XS and L gait simulations, respectively.

The NRMSEs of the muscle excitations from the NMSK-model optimization for slow-gait and fast-gait simulations are shown in Figure 7.4. Although there is no EMG-data-tracking cost term in the cost function, the NRMSE values of the muscle excitation are relatively low compared to EMG data ranges. The slow-gait and fast-gait simulations had almost similar accuracy in predicting muscle excitations since, similar NRMSEs were obtained for most muscle excitations.

Using the NMSK-model optimization, we could estimate COT for the child natural gait in Chapter 5 ($1.53 \text{ Jkg}^{-1}\text{m}^{-1}$). In this chapter, we calculated the COT for the child slow and fast gaits, which are 2.18, 1.99, 1.96, and 1.99 $\text{Jkg}^{-1}\text{m}^{-1}$ for the XS, S, M, and L

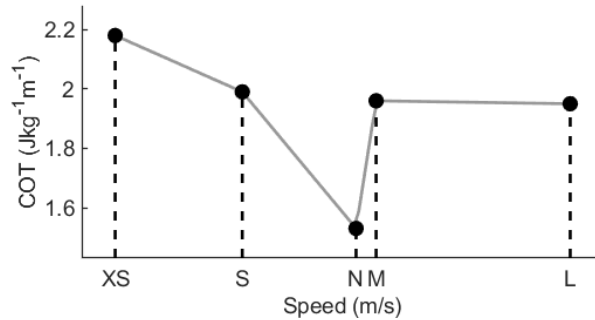


Figure 7.5: Metabolic cost of transport for different gait speeds

gaits, respectively. Figure 7.5 shows the metabolic costs of transport with respect to the gait speeds, which is in good agreement with the plots reported in the literature [19, 45]. According to the literature [19], the COT of human walking as a function of walking speed is a ‘U’-shaped curve, and the minimum value of this curve (the most efficient COT) occurs at the natural speed (preferred speed).

To demonstrate the accuracy of the NMSK-model optimization in predicting slow and fast gaits, we showed the resultant joint angles, GRFs, torques, and muscle excitations in Figures 7.6, 7.7, 7.8, and 7.9, respectively. The results show that the predicted hip, knee, and ankle angles and torques, and the predicted GRFs are all within ± 1 standard deviation of the corresponding slow-gait and fast-gait experimental data.

The resultant metatarsal angles and torques are within the reported ranges for the metatarsal joint angles and torques of the child gait, respectively [97]. According to our results, when the walking speed increases from XS (0.9 m/s) to L (1.58 m/s), the range of metatarsal angles decreases from 40 degrees to 20 degrees, and the range of metatarsal torques increases from 55 N.m to 65 N.m. Mager et al. [98] have also reported similar changes in the metatarsal angle and torque ranges when they studied the role of foot biomechanics in walking and jogging.

According to Figure 7.9, the XS gait muscle excitations fluctuate more (i.e., approximately have 1 decibel less signal-to-noise ratio) than the muscle excitations of the other gaits. Consequently, the torques of the XS gait, generated from the muscle excitations, fluctuate more (i.e., approximately have 3 decibels less signal-to-noise ratio) than the torques of the other gaits, as shown in Figure 7.8. We set the initial guess of the XS-gait muscle excitations to the scaled natural gait EMG data, which have larger values than the bounds prescribed for the XS-gait muscle excitation based on the XS gait experimental EMG data. This inconsistency between the initial guess and bounds of the muscle excitations increases

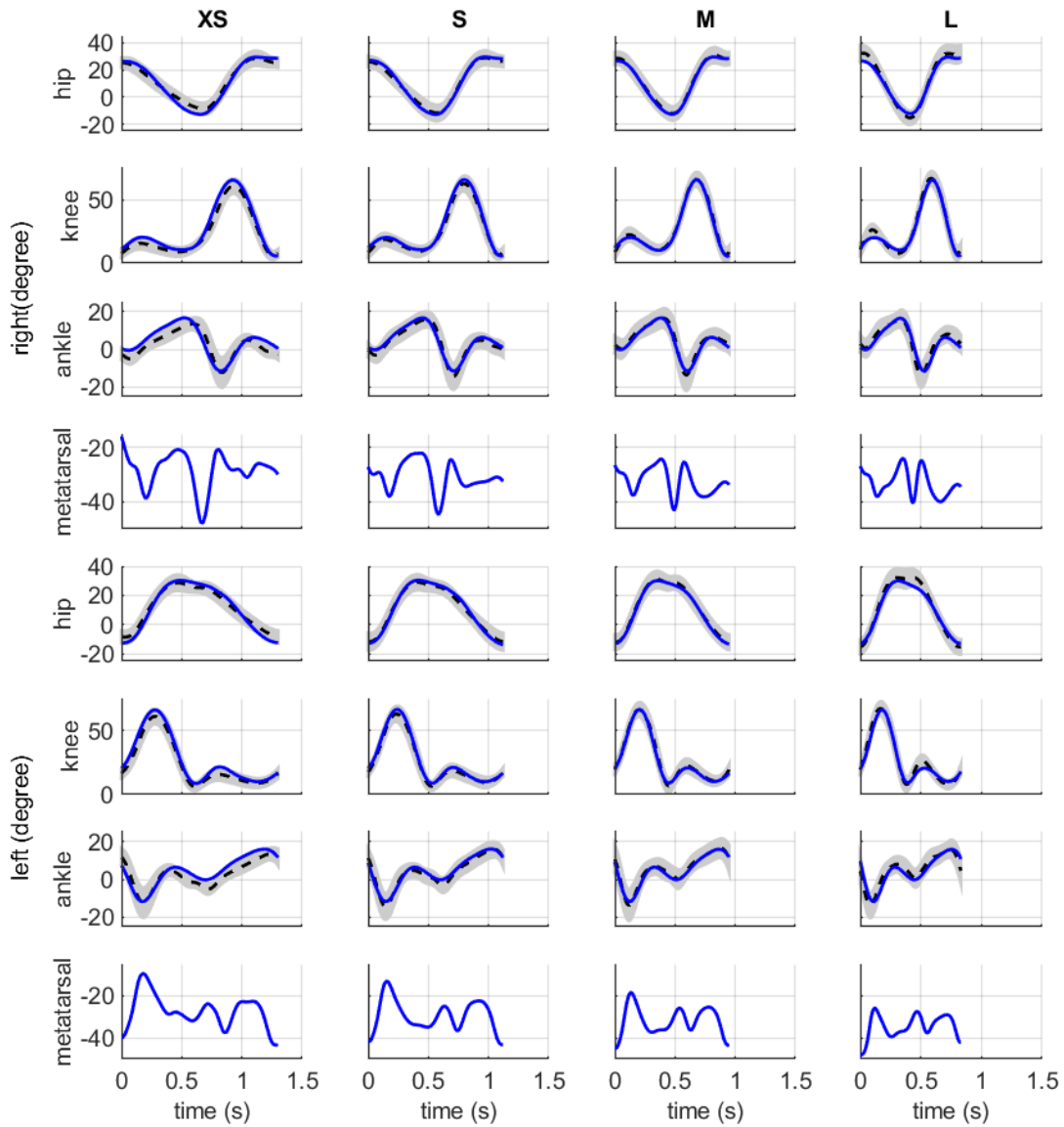


Figure 7.6: The joint angles from the NMSK-model optimization for different gait speeds (The dotted lines represent the mean experimental data and the gray areas show ± 1 standard deviations of the mean experimental data)

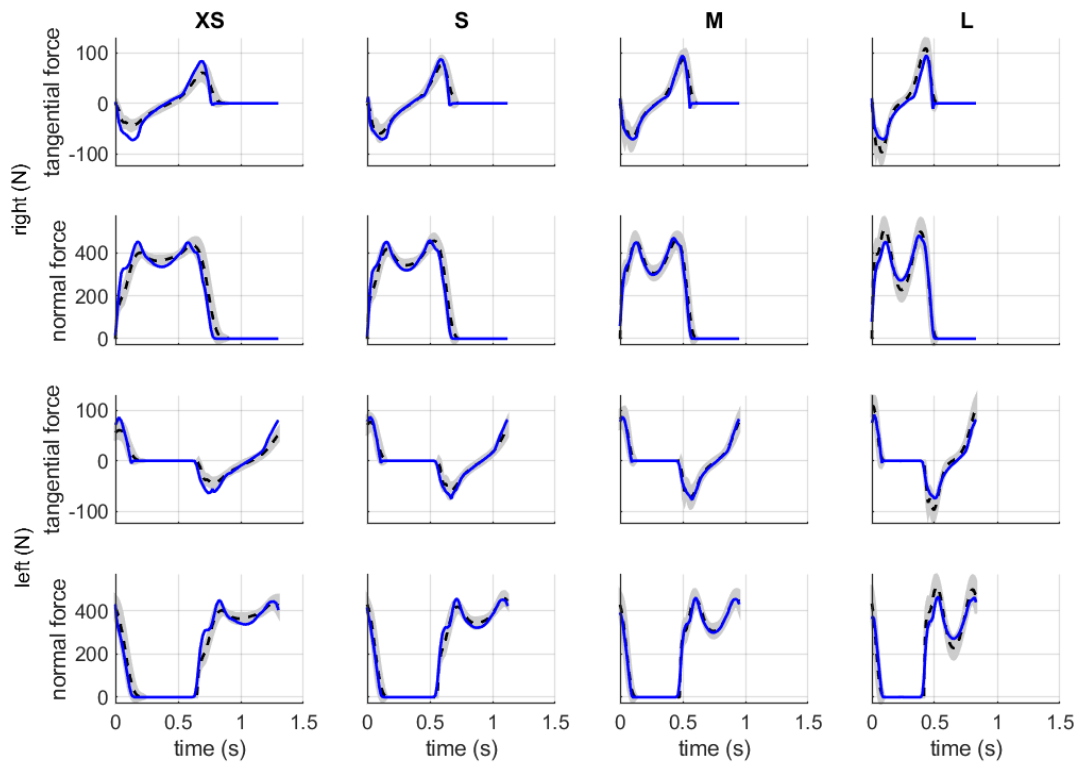


Figure 7.7: The ground reaction forces from the NMSK-model optimization for different gait speeds (The dotted lines represent the mean experimental data and the gray areas show ± 1 standard deviations of the mean experimental data)

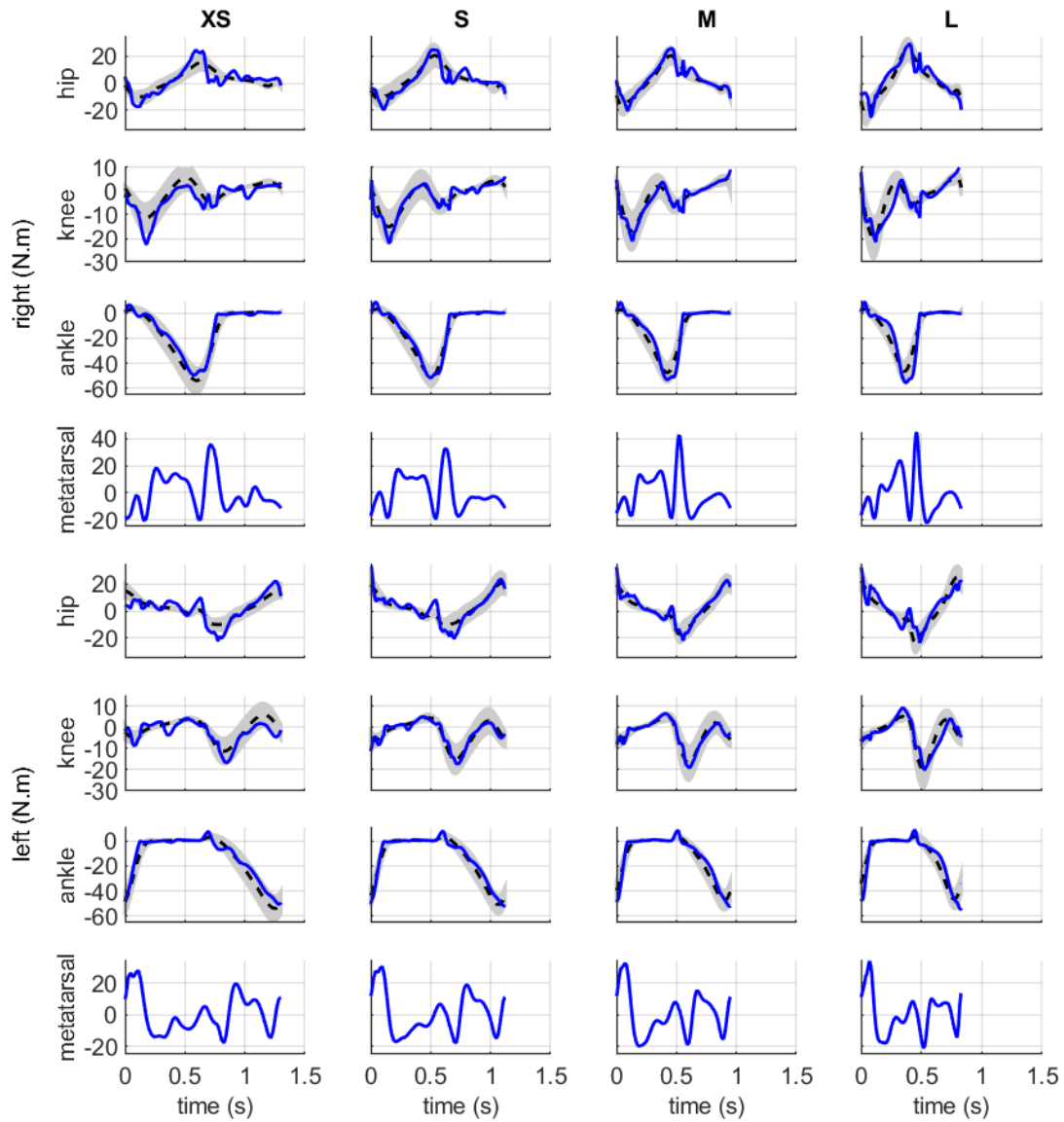


Figure 7.8: The joint torques from the NMSK-model optimization for different gait speeds (The dotted lines represent the mean experimental data and the gray areas show ± 1 standard deviations of the mean experimental data)

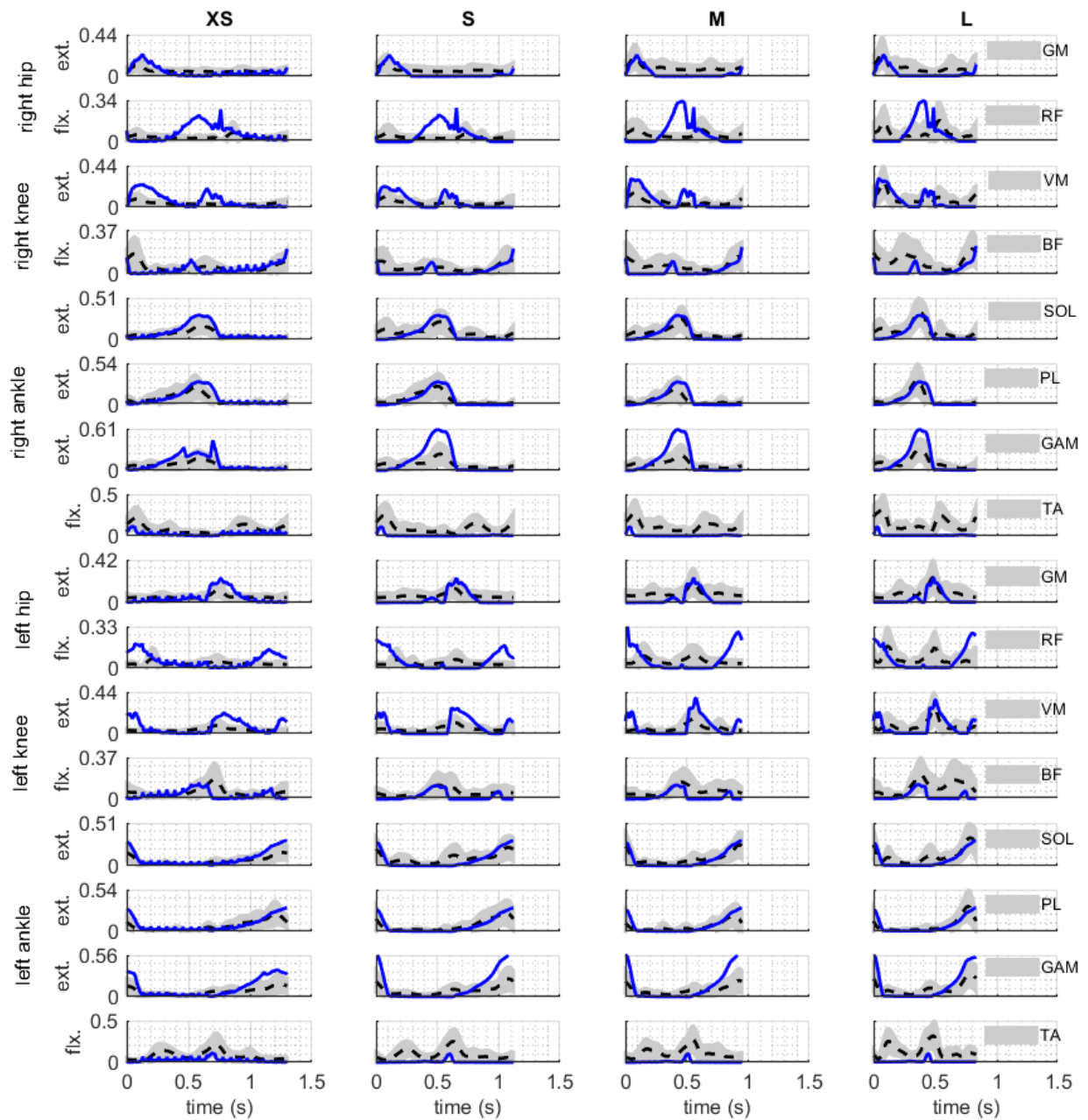


Figure 7.9: The muscle excitations from the NMSK-model optimization for different gait speeds (The dotted lines represent the mean experimental data and the gray areas show ± 1 standard deviations of the mean experimental data)

the XS-gait simulation’s computational time and makes the resultant muscle excitations noisy.

7.3 Conclusion

In this chapter, we used our proposed MSK-model and NMSK-model optimizations to generate semi-predictive simulations and predict four different-speed gaits: very slow walking at 0.9 m/s (XS), slow walking at 1.09 m/s (S), fast walking at 1.29 m/s (M), and very fast walking at 1.58 m/s (L). In the different-speed gait simulations, we did not use the experimental data of the slow or fast gaits since we wanted to evaluate whether our proposed MSK-model and NMSK-model optimizations are able to predict dynamically-consistent and physically-realistic slow and fast gaits when no experimental data are available for them. To determine the initial guess, the stability-based, and data-based cost terms of the different-speed gait simulations, we used the experimental natural gait data that were scaled with respect to the different-speed gaits’ cycle times.

The results of the different-speed gait simulations showed that the NMSK-model optimization is more computationally-efficient and accurate than the MSK-model optimization in simulating slow and fast gaits without tracking the experimental data of the corresponding slow and fast gaits. The MSK-model optimization took twice as long as the NMSK-model optimization to converge to an optimal solution. The NMSK-model optimization predicted the joint torques of the XS, S, M, and L gaits more accurately than the MSK-model optimization by approximately 17%, 12%, 10%, and 2%, respectively. We also concluded that the larger the gap there exists between the speed of slow or fast gaits and the speed of natural gait, the longer the computational time and the less accurate the results for slow-gait or fast-gait simulations.

The NMSK-model optimization also enabled us to estimate muscle excitations and COT for the different-speed gaits. The resultant muscle excitations and COT values were in agreement with our experimental EMG data and the COT values reported in the literature, respectively. We also plotted the COT values with respect to the gait speeds and confirmed a ‘U’-shaped curve, where the minimum (the most efficient COT) occurs at the natural speed (preferred speed).

Chapter 8

Conclusion

This thesis developed a 2D 11-DOF child model actuated by muscle torque generators and in contact with the ground through a 3D ellipsoidal volumetric foot-ground contact model. We took advantage of muscle torque generators to obtain simplified but accurate and computationally-efficient musculoskeletal and neuromusculoskeletal models for children to predict physiologically-realistic torques, motions, ground reaction forces, muscle excitations, and metabolic energy consumption for natural, slow, and fast gaits using direct collocation optimal control.

In this chapter, we summarized the main achievements and suggested some possible open areas of research.

8.1 Summary

In Chapter 2, the main goal was to highlight the features of recent analysis methods of human gait. The recently-developed problem formulations and simulation solvers were classified and separately discussed for SK, MSK, and NMSK models to help researchers select an appropriate analysis method depending on their research purpose. We concluded that to develop a computationally-efficient and accurate predictive simulation of gait, symbolic programming, a fast optimal control method, an accurate volumetric foot-ground contact model, and a two-segment foot model are required.

To investigate the importance of these requirements, a simpler task (vertical jump) was studied in Chapter 3. To develop a fully-predictive vertical jump simulation, we generated two human models (i.e., one with the toe segments and the other one without the toe

segments) and compared two different foot-ground contact models (i.e., 2D kinematically-constrained contact model and 3D ellipsoidal volumetric contact model). We concluded that: (1) A toe-included human model with 3D ellipsoidal volumetric foot-ground contact would simulate a lower-extremity task more accurately than a toeless human model with a kinematically-constrained foot-ground contact; (2) Contact parameters must be tuned using a strong initial guess and experimental-data-tracking cost terms to develop a more realistic simulation.

Using the findings from Chapter 3, we developed a 2D human model including metatarsal joints with a 3D ellipsoidal volumetric contact model in Chapter 4, and identified the contact parameters for child gait using three approaches: (1) GlobalSearch trajectory optimization, (2) direct collocation optimal control, and (3) direct collocation optimal control along with mass-&-joint-property identification. Although the second approach's errors were considerably lower than those from the first approach, the errors of the tangential and normal forces from the third approach were 75% and 60% less than the errors from the optimal control approach, respectively. We concluded that the mass and joint properties should be identified along with the contact parameters to have a more realistic simulation. For all child gait simulations in the remainder of the thesis, we used direct collocation optimal control in which the contact parameters, mass and joint properties were set to the identified values.

In Chapter 5, we used MTGs to develop simplified but accurate MSK and NMSK models that best fit child gait. We adapted the MTG model proposed by [114] to our child model and identified the MTG parameters considering the child gait experimental data. We employed the fitted MTGs to develop a simplified MSK model and simulate a child gait. Although the MTG-based MSK model is simpler than an anatomically-detailed MSK model, it could simulate child gait with reasonable accuracy. To make the MSK model more physiologically-meaningful, we replaced the muscular model with a neuromuscular model, NMSK model, which had an additional cost term (i.e., energy term) and muscle activation dynamics. This NMSK model enabled us to predict muscle excitations comparable with EMG data and estimate the metabolic energy rate consistent with the literature. Using the proposed MSK and NMSK models, we could predict physiologically-meaningful angles and torques for the metatarsal joints in good agreement with the literature.

We used the MTG-based MSK and NMSK child models, proposed in Chapter 5, to simulate a child natural-speed gait in Chapter 6. We developed 16 optimizations (8 optimizations for each model), ranging from fully-data-tracking to fully-predictive optimizations, to compare the MSK and NMSK models in terms of prediction accuracy and computational time. We investigated the roles of a wide range of cost terms, including dynamic-based, stability-based, human-criteria-based, and data-based cost terms, in

achieving a realistic simulation. We concluded that the NMSK-model optimizations were more computationally-efficient than MSK-model optimizations since the control inputs of the NMSK-model optimizations are muscle excitations with a reasonable initial guess (i.e., EMG data were used as the initial guess for the muscle excitations). We also showed that a relatively high weight for the stability-based cost term and a low weight for the residual-load-squared cost term are required when there is no data-tracking cost term in the cost function. The absence of either of the data-tracking cost terms (i.e., torque-tracking, angle-tracking, or GRF-tracking cost term) causes us to increase the weight of the implicit-dynamic-squared cost term to ensure dynamic consistency.

According to the findings of Chapter 6, it is sufficient to only use two of the data-tracking cost terms (i.e., angle-tracking and torque-tracking cost terms) to develop a computationally-efficient and accurate NMSK gait model. This optimization could predict the most accurate muscle excitations as well. On the other hand, when the GRF-tracking cost term was used in the absence of the angle-tracking and torque-tracking cost terms, the NMSK-model optimization predicted inaccurate angles, torques, and the least accurate muscle excitations. The main achievement of this chapter was that when the fully-predictive cost function was used, the NMSK-model optimization could predict more accurate results with less computational time than the MSK-model optimization. Furthermore, the muscle excitations predicted by the fully-predictive NMSK-model optimization were more accurate than those predicted by the data-tracking optimization.

In Chapter 7, we used our proposed MSK-model and NMSK-model optimizations to generate semi-predictive simulations and predict four different-speed gaits for children: very slow walking at 0.9 m/s (XS), slow walking at 1.09 m/s (S), fast walking at 1.29 m/s (M), and very fast walking at 1.58 m/s (L). In the different-speed gait simulations, we did not track the experimental data of the slow or fast gaits since we wanted to evaluate whether our proposed MSK-model and NMSK-model optimizations are able to minimize the reliance of simulations on experiments and predict dynamically-consistent and physically-realistic slow and fast gaits, without tracking the experimental data of the corresponding slow and fast gaits. To determine the initial guess, the stability-based and data-based cost terms of the different-speed gait simulations, we used the experimental natural gait data that were scaled with respect to the different-speed gaits' cycle times. We showed that the NMSK-model optimization was more computationally-efficient and accurate than the MSK-model optimization in simulating slow and fast gaits. We also plotted the COT values with respect to the gait speeds. The plot follows the expected 'U'-shaped curve, where the minimum (the most efficient COT) occurs at the natural speed (preferred speed).

8.2 Recommendations for Future Work

We suggest the following directions to advance this research and overcome its limitations:

- A more feasible and accurate gait model may be generated if experimental foot-ground reaction moments and experimental center of pressure location are used for contact parameter identification.
- If contact parameters, mass and joint properties, MTG parameters, and parameters corresponding to the muscle activation dynamics are identified simultaneously using an experimental-data-tracking optimization, more realistic parameters may be obtained that can lead to a more accurate predictive simulation.
- It may be possible to estimate muscle forces using the proposed MTG-based NMSK gait model. Our NMSK gait model could predict physiologically-realistic muscle excitations using the synergy analysis approach [154]. We may be able to take a similar approach to decompose the MTGs into torque components corresponding to muscles. In this way, the muscle forces can be estimated, given the moment arms.
- More accurate muscle excitations may be predicted if EMG data of more muscles are available. To do so, we may need to take the synergy analysis approach to find a physiologically-meaningful relation between the muscle activations and MTG activations.
- A more accurate predictive simulation may be achieved if co-contractions between the agonist and antagonist MTGs are taken into account. To do so, we may need a more elaborate scheme to define physiologically-meaningful co-contractions between the agonist and antagonist MTGs and tune them using an experimental-data-tracking parameter identification optimization.
- The jerk penalty may be reduced by adding arms to our human model, and consequently, a more stable gait may be predicted.

We believe that these directions would open the door for predicting new walking motions in the future.

References

- [1] M. P. Abdel, P. von Roth, M. T. Jennings, A. D. Hanssen, and M. W. Pagnano. What safe zone? The vast majority of dislocated THAs are within the Lewinnek safe zone for acetabular component position. *Clinical Orthopaedics and Related Research*[®], 474(2):386–391, 2016. doi: 10.1007/s11999-015-4432-5.
- [2] S. B. Abujaber, A. R. Marmon, F. Pozzi, J. J. Rubano, J. A. Zeni, and Jr. Sit-to-stand biomechanics before and after total hip arthroplasty. *The Journal of arthroplasty*, 30(11):2027–33, 2015. doi: 10.1016/j.arth.2015.05.024.
- [3] M. Ackermann. *Dynamics and energetics of walking with prostheses*. Phd thesis, University of Stuttgart, Stuttgart, Germany, 2007.
- [4] M. Ackermann and W. Schiehlen. Physiological methods to solve the force-sharing problem in biomechanics. *Computational Methods in Applied Sciences*, 12:1–23, 2008.
- [5] M. Ackermann and A. J. van den Bogert. Optimality principles for model-based prediction of human gait. *Journal of Biomechanics*, 43(6):1055–1060, 2010. ISSN 00219290. doi: 10.1016/j.jbiomech.2009.12.012.
- [6] A. A. Amis, D. Dowson, and V. Wright. Muscle strengths and musculoskeletal geometry of the upper limb. *Engineering in Medicine*, 8(1):41–48, 1979. doi: 10.1243/EMED_JOUR_1979_008_010_02.
- [7] D. E. Anderson, M. L. Madigan, and M. A. Nussbaum. Maximum voluntary joint torque as a function of joint angle and angular velocity: Model development and application to the lower limb. *Journal of Biomechanics*, 40(14):3105–3113, 2007. ISSN 00219290. doi: 10.1016/j.jbiomech.2007.03.022.
- [8] F. C. Anderson and M. G. Pandy. Dynamic optimization of human walking. *Journal of Biomechanical Engineering*, 123(5):381, 2001. ISSN 01480731. doi: 10.1115/1.1392310.

- [9] F. C. Anderson and M. G. Pandy. Static and dynamic optimization solutions for gait are practically equivalent. *Journal of biomechanics*, 34(2):153–61, 2001. ISSN 0021-9290. doi: 10.1016/S0021-9290(00)00155-X.
- [10] F. C. Anderson and M. G. Pandy. Individual muscle contributions to support in normal walking. *Gait and Posture*, 17(2):159–169, 2003. ISSN 09666362. doi: 10.1016/S0966-6362(02)00073-5.
- [11] Y. Aoustin and A. M. Formal'skii. Modeling, control and simulation of upward jump of a biped. *Multibody System Dynamics*, 29(4):425–445, 2013. ISSN 1384-5640. doi: 10.1007/s11044-012-9319-6.
- [12] F. Asano. Stability analysis of underactuated compass gait based on linearization of motion. *Multibody System Dynamics*, 33(1):93–111, 2015. ISSN 1384-5640. doi: 10.1007/s11044-014-9416-9.
- [13] M. Bataineh, T. Marler, K. Abdel-Malek, and J. Arora. Neural network for dynamic human motion prediction. *Expert Systems with Applications*, 48:26–34, 2016. ISSN 0957-4174. doi: 10.1016/J.ESWA.2015.11.020.
- [14] E. Bertolazzi, F. Biral, and M. Da Lio. Symbolic-numeric efficient solution of optimal control problems for multibody systems. *Journal of Computational and Applied Mathematics*, 185(2):404–421, 2006. ISSN 0377-0427. doi: 10.1016/J.CAM.2005.03.019.
- [15] L. J. Bhargava, M. G. Pandy, and F. C. Anderson. A phenomenological model for estimating metabolic energy consumption in muscle contraction. *Journal of Biomechanics*, 37(1):81–88, 2004. ISSN 00219290. doi: 10.1016/S0021-9290(03)00239-2.
- [16] M. Boos and J. McPhee. Volumetric modeling and experimental validation of normal contact dynamic forces. *Journal of Computational and Nonlinear Dynamics*, 8(2):021006, 2012. ISSN 1555-1415. doi: 10.1115/1.4006836.
- [17] Y. Bougrinat, S. Achiche, and M. Raison. Design and development of a lightweight ankle exoskeleton for human walking augmentation. *Mechatronics*, 64:102297, 2019. ISSN 09574158. doi: 10.1016/j.mechatronics.2019.102297.
- [18] G. Bovi, M. Rabuffetti, P. Mazzoleni, and M. Ferrarin. A multiple-task gait analysis approach: Kinematic, kinetic and EMG reference data for healthy young and adult subjects. *Gait & Posture*, 33(1):6–13, 2011. ISSN 09666362. doi: 10.1016/j.gaitpost.2010.08.009.

- [19] D. M. Bramble and D. E. Lieberman. Endurance running and the evolution of Homo, 2004. ISSN 00280836.
- [20] P. Brown. *Contact modelling for forward dynamics of human motion*. Masters thesis, University of Waterloo, 2017.
- [21] P. Brown and J. McPhee. A 3D ellipsoidal volumetric foot–ground contact model for forward dynamics. *Multibody System Dynamics*, 42(4):447–467, 2018. ISSN 1384-5640. doi: 10.1007/s11044-017-9605-4.
- [22] M. Cenciarini, P. J. Loughlin, P. J. Sparto, and M. S. Redfern. Stiffness and damping in postural control increase with age. *IEEE Transactions on Biomedical Engineering*, 57(2):267–275, 2010. ISSN 15582531. doi: 10.1109/TBME.2009.2031874.
- [23] E. K. Chadwick, D. Blana, R. F. Kirsch, and A. J. van den Bogert. Real-time simulation of three-dimensional shoulder girdle and arm dynamics. *IEEE Transactions on Biomedical Engineering*, 61(7):1947–56, 2014. ISSN 1558-2531. doi: 10.1109/TBME.2014.2309727.
- [24] J. H. Challis and D. G. Kerwin. An analytical examination of muscle force estimations using optimization techniques. *Proceedings of the Institution of Mechanical Engineers. Part H, Journal of Engineering in Medicine*, 207:139–148, 1993. ISSN 0954-4119. doi: 10.1243/PIME_PROC_1993_207_286_02.
- [25] K. B. Cheng, C.-H. Wang, H.-C. Chen, C.-D. Wu, and H.-T. Chiu. The mechanisms that enable arm motion to enhance vertical jump performance—A simulation study. *Journal of Biomechanics*, 41(9):1847–1854, 2008. ISSN 00219290. doi: 10.1016/j.jbiomech.2008.04.004.
- [26] Z. Chuanjie and F. Zhengwei. Biomechanical analysis of knee joint mechanism of the national women’s epee fencing lunge movement. *Biomedical Research*, 0(0):104–110, 2017. ISSN ISSN: 0970-938X (Print) — 0976-1683 (Electronic).
- [27] H.-J. Chung, Y. Xiang, J. S. Arora, and K. Abdel-Malek. Optimization-based dynamic 3D human running prediction: effects of foot location and orientation. *Robotica*, 33(02):413–435, 2015. ISSN 0263-5747. doi: 10.1017/S0263574714000253.
- [28] R. D. Crowninshield and R. A. Brand. A physiologically based criterion of muscle force prediction in locomotion. *Journal of Biomechanics*, 14(11):793–801, 1981. ISSN 0021-9290. doi: 10.1016/0021-9290(81)90035-X.

- [29] R. D. Crowninshield, R. C. Johnston, J. G. Andrews, and R. A. Brand. A biomechanical investigation of the human hip. *Journal of Biomechanics*, 11:75–85, 1978. ISSN 00219290. doi: 10.1016/0021-9290(78)90045-3.
- [30] S. Davoudabadi Farahani, M. Svinin, M. S. Andersen, M. de Zee, and J. Rasmussen. Prediction of closed-chain human arm dynamics in a crank-rotation task. *Journal of Biomechanics*, 49(13):2684–2693, 2016. ISSN 00219290. doi: 10.1016/j.jbiomech.2016.05.034.
- [31] D. T. Davy and M. L. Audu. A dynamic optimization technique for predicting muscle forces in the swing phase of gait. *Journal of Biomechanics*, 20:187–201, 1987. ISSN 00219290. doi: 10.1016/0021-9290(87)90310-1.
- [32] F. De Groot, A. L. Kinney, A. V. Rao, and B. J. Fregly. Evaluation of direct collocation optimal control problem formulations for solving the muscle redundancy problem. *Annals of Biomedical Engineering*, 44(10):2922–2936, 2016. ISSN 0090-6964. doi: 10.1007/s10439-016-1591-9.
- [33] C. J. De Luca, L. Donald Gilmore, M. Kuznetsov, and S. H. Roy. Filtering the surface EMG signal: Movement artifact and baseline noise contamination. *Journal of Biomechanics*, 43(8):1573–1579, 2010. ISSN 0021-9290. doi: 10.1016/J.JBIOMECH.2010.01.027.
- [34] S. L. Delp, F. C. Anderson, A. S. Arnold, P. Loan, A. Habib, C. T. John, E. Guendelman, and D. G. Thelen. OpenSim: Open-source software to create and analyze dynamic simulations of movement. *IEEE Transactions on Biomedical Engineering*, 54(11):1940–1950, 2007. ISSN 0018-9294. doi: 10.1109/TBME.2007.901024.
- [35] H. Ehsani, M. Rostami, and M. Gudarzi. A general-purpose framework to simulate musculoskeletal system of human body: using a motion tracking approach. *Computer Methods in Biomechanics and Biomedical Engineering*, 19(3):306–319, 2016. ISSN 1025-5842. doi: 10.1080/10255842.2015.1017722.
- [36] A. Erdemir and S. J. Piazza. Changes in foot loading following plantar fasciotomy: A computer modeling study. *Journal of Biomechanical Engineering*, 126(2):237, 2004. ISSN 01480731. doi: 10.1115/1.1691447.
- [37] C. I. Esposito, B. P. Gladnick, Y.-y. Lee, S. Lyman, T. M. Wright, D. J. Mayman, and D. E. Padgett. Cup position alone does not predict risk of dislocation after hip arthroplasty. *The Journal of Arthroplasty*, 30(1):109–113, 2015. doi: 10.1016/j.arth.2014.07.009.

- [38] C. I. Esposito, K. M. Carroll, P. K. Sculco, D. E. Padgett, S. A. Jerabek, and D. J. Mayman. Total hip arthroplasty patients with fixed spinopelvic alignment are at higher risk of hip dislocation. *The Journal of arthroplasty*, 2017. ISSN 1532-8406. doi: 10.1016/j.arth.2017.12.005.
- [39] M. Ezati, B. Ghannadi, N. Mehrabi, and J. McPhee. Optimal vertical jump of a human. In *4th International Conference On Control Dynamic Systems, And Robotics (CDSR)*, volume 233, pages 1–8, Toronto, Ontario, Canada, 2017. doi: 10.11159/cdsr17.103.
- [40] M. Ezati, M. Khadiv, and S. Moosavian. An investigation on the usefulness of employing a two-segment foot for traversing stairs. *International Journal of Humanoid Robotics*, 14(4), 2017. ISSN 02198436. doi: 10.1142/S021984361750027X.
- [41] M. Ezati, P. Brown, and J. McPhee. Forward dynamic simulation of the human vertical jump including an ellipsoidal volumetric foot-ground contact model. In *World Congress of Biomechanics*, 2018.
- [42] M. Ezati, B. Ghannadi, and J. McPhee. A review of simulation methods for human movement dynamics with emphasis on gait. *Multibody System Dynamics*, 47(3):1–28, 2019. ISSN 1384-5640. doi: 10.1007/s11044-019-09685-1.
- [43] M. Ezati, P. Brown, B. Ghannadi, and J. McPhee. Comparison of direct collocation optimal control to trajectory optimization for parameter identification of an ellipsoidal foot-ground contact model. *Multibody System Dynamics*, pages 1–23, 2020. ISSN 1384-5640. doi: 10.1007/s11044-020-09731-3.
- [44] H. Faber, A. J. van Soest, and D. A. Kistemaker. Inverse dynamics of mechanical multibody systems: An improved algorithm that ensures consistency between kinematics and external forces. *PLOS ONE*, 13(9):e0204575, 2018. ISSN 1932-6203. doi: 10.1371/journal.pone.0204575.
- [45] A. Falisse, G. Serrancolí, C. L. Dembia, J. Gillis, I. Jonkers, and F. De Groote. Rapid predictive simulations with complex musculoskeletal models suggest that diverse healthy and pathological human gaits can emerge from similar control strategies. *Journal of The Royal Society Interface*, 16(157):20190402, 2019. ISSN 1742-5689. doi: 10.1098/rsif.2019.0402.
- [46] A. Falisse, L. Pitto, H. Kainz, H. Hoang, M. Wesseling, S. Van Rossom, E. Papageorgiou, L. Bar-On, A. Hallemans, K. Desloovere, G. Molenaers, A. Van Campenhout,

- F. De Groote, and I. Jonkers. Physics-Based Simulations to Predict the Differential Effects of Motor Control and Musculoskeletal Deficits on Gait Dysfunction in Cerebral Palsy: A Retrospective Case Study. *Frontiers in Human Neuroscience*, 14:40, 2020. ISSN 1662-5161. doi: 10.3389/fnhum.2020.00040.
- [47] D. Farina, R. Merletti, and R. M. Enoka. The extraction of neural strategies from the surface EMG. *Journal of Applied Physiology*, 96(4):1486–1495, 2004. ISSN 8750-7587. doi: 10.1152/jappphysiol.01070.2003.
- [48] J. M. Font-Llagunes, R. Pàmies-Vilà, J. Alonso, and U. Lúgrís. Simulation and design of an active orthosis for an incomplete spinal cord injured subject. *Procedia IUTAM*, 2:68–81, 2011. ISSN 22109838. doi: 10.1016/j.piutam.2011.04.007.
- [49] A. Forner-Cordero, H. Koopman, and F. van der Helm. Inverse dynamics calculations during gait with restricted ground reaction force information from pressure insoles. *Gait & Posture*, 23(2):189–199, 2006. ISSN 0966-6362. doi: 10.1016/J.GAITPOST.2005.02.002.
- [50] A. Frank C., M. G. Pandy, F. C. ANDERSON, M. G. Pandy, A. Frank C., and M. G. Pandy. A dynamic optimization solution for vertical jumping in three dimensions. *Computer Methods in Biomechanics and Biomedical Engineering*, 2(3):201–231, 1999. ISSN 1025-5842. doi: 10.1080/10255849908907988.
- [51] B. J. Fregly. A conceptual blueprint for making neuromusculoskeletal models clinically useful. *Applied Sciences*, 11(5):2037, 2021. ISSN 2076-3417. doi: 10.3390/app11052037.
- [52] B. J. Fregly, Y. Bei, and M. E. Sylvester. Experimental evaluation of an elastic foundation model to predict contact pressures in knee replacements. *Journal of biomechanics*, 36(11):1659–68, 2003. ISSN 0021-9290. doi: 10.1016/S0021-9290(03)00176-3.
- [53] J. A. Friederich and R. A. Brand. Muscle fiber architecture in the human lower limb. *Journal of Biomechanics*, 23(1):91–95, 1990. ISSN 00219290. doi: 10.1016/0021-9290(90)90373-B.
- [54] B. Gervais, A. Vadean, M. Brochu, and M. Raison. Influence of the load modelling during gait on the stress distribution in a femoral implant. *Multibody System Dynamics*, 44(1):93–105, 2018. ISSN 1573272X. doi: 10.1007/s11044-018-9621-z.

- [55] H. Geyer and H. Herr. A Muscle-reflex model that encodes principles of legged mechanics produces human walking dynamics and muscle activities. *IEEE Transactions on Neural Systems and Rehabilitation Engineering*, 18(3):263–273, 2010. ISSN 15344320. doi: 10.1109/TNSRE.2010.2047592.
- [56] B. Ghannadi. *Model-based Control of Upper Extremity Human-Robot Rehabilitation Systems*. PhD thesis, University of Waterloo, 2017.
- [57] B. Ghannadi, N. Mehrabi, R. Sharif Razavian, and J. McPhee. Nonlinear model predictive control of an upper extremity rehabilitation robot using a two-dimensional human-robot interaction model. In *IEEE/RSJ International Conference on Intelligent Robots and Systems (IROS)*, pages 502–507, Vancouver, British Columbia, Canada, 2017. IEEE. ISBN 978-1-5386-2682-5. doi: 10.1109/IROS.2017.8202200.
- [58] G. Gilardi and I. Sharf. Literature survey of contact dynamics modelling. *Mechanism and Machine Theory*, 37(10):1213–1239, oct 2002. ISSN 0094114X. doi: 10.1016/S0094-114X(02)00045-9.
- [59] Y. Gonthier. *Contact Dynamics Modelling for Robotic Task Simulation*. Phd thesis, University of Waterloo, 2007.
- [60] Y. Gonthier, J. McPhee, C. Lange, and J.-C. Piedbœuf. A Contact Modeling Method Based on Volumetric Properties. In *Volume 6: 5th International Conference on Multi-body Systems, Nonlinear Dynamics, and Control, Parts A, B, and C*, volume 2005, pages 477–486. ASME, 2005. ISBN 0-7918-4743-8. doi: 10.1115/DETC2005-84610.
- [61] R. D. Gregg, E. J. Rouse, L. J. Hargrove, and J. W. Sensinger. Evidence for a time-invariant phase variable in human ankle control. *PLoS ONE*, 9(2):e89163, 2014. ISSN 1932-6203. doi: 10.1371/journal.pone.0089163.
- [62] R. Grönqvist, J. Abeysekera, G. Gard, S. M. Hsiang, T. B. Leamon, D. J. Newman, K. Gielo-Perczak, T. E. Lockhart, and C. Y. Pai. Human-centred approaches in slipperiness measurement. In *Ergonomics*, volume 44, pages 1167–1199. Taylor & Francis Group, 2001. doi: 10.1080/00140130110085556.
- [63] R. Hainisch, M. Gfoehler, M. Zubayer-Ul-Karim, and M. G. Pandy. Method for determining musculotendon parameters in subject-specific musculoskeletal models of children developed from MRI data. *Multibody System Dynamics*, 28(1-2):143–156, 2012. ISSN 1384-5640. doi: 10.1007/s11044-011-9289-0.

- [64] S. R. Hamner, A. Seth, and S. L. Delp. Muscle contributions to propulsion and support during running. *Journal of biomechanics*, 43(14):2709–16, 2010. ISSN 1873-2380. doi: 10.1016/j.jbiomech.2010.06.025.
- [65] M. L. Handford and M. Srinivasan. Robotic lower limb prosthesis design through simultaneous computer optimizations of human and prosthesis costs. *Scientific Reports*, 6(1):19983, 2016. ISSN 2045-2322. doi: 10.1038/srep19983.
- [66] <https://cirpwiki.info/wiki/Statistics#Normalization>. Coastal Inlets Research Program (CIRP) Wiki - Statistics.
- [67] K. H. Hunt and F. R. E. Crossley. Coefficient of restitution interpreted as damping in vibroimpact. *Journal of Applied Mechanics*, 42(2):440, 1975. ISSN 00218936. doi: 10.1115/1.3423596.
- [68] S. K. Hunter, M. W. Thompson, P. A. Ruell, A. R. Harmer, J. M. Thom, T. H. Gwinn, and R. D. Adams. Human skeletal sarcoplasmic reticulum Ca²⁺ uptake and muscle function with aging and strength training. *Journal of Applied Physiology*, 86(6):1858–1865, 1999. ISSN 87507587. doi: 10.1152/jappl.1999.86.6.1858.
- [69] K. A. Inkol, C. Brown, W. McNally, C. Jansen, and J. McPhee. Muscle torque generators in multibody dynamic simulations of optimal sports performance. *Multibody System Dynamics*, 50(4):435–452, 2020. ISSN 1573272X. doi: 10.1007/s11044-020-09747-9.
- [70] J. N. Jackson, C. J. Hass, and B. J. Fregly. Development of a Subject-Specific Foot-Ground Contact Model for Walking. *Journal of Biomechanical Engineering*, 138(9):091002, 2016. ISSN 0148-0731. doi: 10.1115/1.4034060.
- [71] M. I. Jackson. *The mechanics of the table contact phase of gymnastics vaulting*. Phd thesis, 2010.
- [72] C. Jansen and J. McPhee. Predictive dynamic simulation of seated start-up cycling using olympic cyclist and bicycle models. In *Proceedings of International Sports Engineering Association*, volume 2, page 220, Brisbane, Australia, 2018. doi: 10.3390/proceedings2060220.
- [73] C. Jin, A. Maitland, and J. McPhee. Hierarchical nonlinear moving horizon estimation of vehicle lateral speed and road friction coefficient. *ASME Letters in Dynamic Systems and Control*, 1(1), 2021. ISSN 2689-6117. doi: 10.1115/1.4046395.

- [74] B. B. Kentel, M. A. King, and S. R. Mitchell. Evaluation of a subject-specific, torque-driven computer simulation model of one-handed tennis backhand ground strokes. *Journal of Applied Biomechanics*, 27(4):345–354, 2011. ISSN 15432688. doi: 10.1123/jab.27.4.345.
- [75] M. Khadiv, M. Ezati, and S. A. A. Moosavian. A computationally efficient inverse dynamics solution based on virtual work principle for biped robots. *Iranian Journal of Science and Technology, Transactions of Mechanical Engineering*, 2017. ISSN 2228-6187. doi: 10.1007/s40997-017-0138-5.
- [76] Y. Kim, B. Lee, J. Yoo, S. Choi, and J. Kim. Humanoid robot HanSaRam: Yawing moment cancellation and ZMP compensation. In *Proceedings of AUS International Symposium on Mechatronics*, Sharjah, 2005.
- [77] R. N. Kirkwood, H. d. A. Gomes, R. F. Sampaio, E. Culham, and P. Costigan. Análise biomecânica das articulações do quadril e joelho durante a marcha em participantes idosos. *Acta Ortopédica Brasileira*, 15(5):267–271, 2007. ISSN 1413-7852. doi: 10.1590/S1413-78522007000500007.
- [78] K. L. Koenraadt, N. M. Stolwijk, D. van den Wildenberg, J. Duysens, and N. L. Keijsers. Effect of a metatarsal pad on the forefoot during gait. *Journal of the American Podiatric Medical Association*, 102(1):18–24, 2012. ISSN 87507315. doi: 10.7547/1020018.
- [79] P. A. Lasota and J. A. Shah. A multiple-predictor approach to human motion prediction. In *2017 IEEE International Conference on Robotics and Automation (ICRA)*, pages 2300–2307. IEEE, 2017. ISBN 978-1-5090-4633-1. doi: 10.1109/ICRA.2017.7989265.
- [80] A. Leardini, M. G. Benedetti, L. Berti, D. Bettinelli, R. Nativio, and S. Giannini. Rear-foot, mid-foot and fore-foot motion during the stance phase of gait. *Gait and Posture*, 25(3):453–462, 2007. ISSN 09666362. doi: 10.1016/j.gaitpost.2006.05.017.
- [81] M. Lebedowska. Dynamic properties of human limb segments. In *International Encyclopedia of Ergonomics and Human Factors, Second Edition - 3 Volume Set*. CRC Press, mar 2006. doi: 10.1201/9780849375477.ch71.
- [82] D. D. Lee and H. S. Seung. Learning the parts of objects by non-negative matrix factorization. *Nature*, 401:788–791, 1999.

- [83] L.-F. Lee and B. R. Umberger. Generating optimal control simulations of musculoskeletal movement using OpenSim and MATLAB. *PeerJ*, 4:e1638, 2016. ISSN 2167-8359. doi: 10.7717/peerj.1638.
- [84] A. Lees, J. Vanrenterghem, and D. D. Clercq. Understanding how an arm swing enhances performance in the vertical jump. *Journal of Biomechanics*, 37(12):1929–1940, 2004. ISSN 0021-9290. doi: 10.1016/J.JBIOMECH.2004.02.021.
- [85] R. L. Lenhart, D. G. Thelen, C. M. Wille, E. S. Chumanov, and B. C. Heiderscheit. Increasing running step rate reduces patellofemoral joint forces. *Medicine and science in sports and exercise*, 46(3):557–64, 2014. doi: 10.1249/MSS.0b013e3182a78c3a.
- [86] Y. P. Lim, Y. C. Lin, and M. G. Pandy. Effects of step length and step frequency on lower-limb muscle function in human gait. *Journal of Biomechanics*, 57:1–7, 2017. ISSN 18732380. doi: 10.1016/j.jbiomech.2017.03.004.
- [87] Y.-C. Lin and M. G. Pandy. Three-dimensional data-tracking dynamic optimization simulations of human locomotion generated by direct collocation. *Journal of biomechanics*, 59:1–8, 2017. ISSN 1873-2380. doi: 10.1016/j.jbiomech.2017.04.038.
- [88] Y.-C. Lin, R. T. Haftka, N. V. Queipo, and B. J. Fregly. Surrogate articular contact models for computationally efficient multibody dynamic simulations. *Medical engineering & physics*, 32(6):584–94, 2010. ISSN 1873-4030. doi: 10.1016/j.medengphy.2010.02.008.
- [89] Y.-C. Lin, H. J. Kim, and M. G. Pandy. A computationally efficient method for assessing muscle function during human locomotion. *International Journal for Numerical Methods in Biomedical Engineering*, 27(3):436–449, 2011. ISSN 20407939. doi: 10.1002/cnm.1396.
- [90] Y.-C. Lin, J. P. Walter, and M. G. Pandy. Predictive simulations of neuromuscular coordination and joint-contact loading in human gait. *Annals of Biomedical Engineering*, 46(8):1216–1227, 2018. ISSN 0090-6964. doi: 10.1007/s10439-018-2026-6.
- [91] M. Q. Liu, F. C. Anderson, M. H. Schwartz, and S. L. Delp. Muscle contributions to support and progression over a range of walking speeds. *Journal of Biomechanics*, 41(15):3243–3252, 2008. ISSN 00219290. doi: 10.1016/j.jbiomech.2008.07.031.
- [92] S. J. Lochner, J. P. Huissoon, and S. S. Bedi. Simulation methods in the foot orthosis development process. *Computer-Aided Design and Applications*, 11(6):608–616, 2014. doi: 10.1080/16864360.2014.914375.

- [93] L. L. Long and M. Srinivasan. Walking, running, and resting under time, distance, and average speed constraints: optimality of walk-run-rest mixtures. *Journal of the Royal Society, Interface*, 10(81):20120980, 2013. ISSN 1742-5662. doi: 10.1098/rsif.2012.0980.
- [94] D. S. Lopes, R. R. Neptune, J. A. Ambrósio, and M. T. Silva. A superellipsoid-plane model for simulating foot-ground contact during human gait. *Computer Methods in Biomechanics and Biomedical Engineering*, 19(9):954–963, 2016. ISSN 1025-5842. doi: 10.1080/10255842.2015.1081181.
- [95] U. Ligrís, J. Carlín, R. Pàmies-Vilà, J. M. Font-Llagunes, and J. Cuadrado. Solution methods for the double-support indeterminacy in human gait. *Multibody System Dynamics*, 30(3):247–263, 2013. ISSN 1384-5640. doi: 10.1007/s11044-013-9363-x.
- [96] Y. Ma, S. Xie, and Y. Zhang. A patient-specific EMG-driven neuromuscular model for the potential use of human-inspired gait rehabilitation robots. *Computers in Biology and Medicine*, 70:88–98, 2016. ISSN 00104825. doi: 10.1016/j.compbiomed.2016.01.001.
- [97] B. A. MacWilliams, M. Cowley, and D. E. Nicholson. Foot kinematics and kinetics during adolescent gait. *Gait and Posture*, 17(3):214–224, 2003. ISSN 09666362. doi: 10.1016/S0966-6362(02)00103-0.
- [98] F. Mager, J. Richards, M. Hennies, E. Dötzel, A. Chohan, A. Mbuli, and F. Capanni. Determination of ankle and metatarsophalangeal stiffness during walking and jogging. *Journal of Applied Biomechanics*, 34(6):448–453, 2018. ISSN 15432688. doi: 10.1123/jab.2017-0265.
- [99] S. Martelli, D. Calvetti, E. Somersalo, and M. Viceconti. Stochastic modelling of muscle recruitment during activity. *Interface Focus*, 5(2):20140094, 2015. ISSN 2042-8898. doi: 10.1098/rsfs.2014.0094.
- [100] A. E. Martin and J. P. Schmiedeler. Predicting human walking gaits with a simple planar model. *Journal of Biomechanics*, 47(6):1416–1421, 2014. ISSN 0021-9290. doi: 10.1016/J.JBIOMECH.2014.01.035.
- [101] T. Mclaughlin and T. Zourntos. *Using Fourier analysis to generate believable gait patterns for virtual quadrupeds*. Masters thesis, Texas A&M University, 2013.
- [102] A. S. McLawhorn, P. K. Sculco, K. D. Weeks, D. Nam, and D. J. Mayman. Targeting a new safe zone: A step in the development of patient-specific component positioning

- in hip arthroplasty. *Orthopaedic Proceedings*, 96-B(SUPP_16):43, 2014. ISSN 1358-992X. doi: 10.1302/1358-992X.96BSUPP_16.CAOS2014-043.
- [103] J. McPhee and C. Wells. Automated symbolic analysis of mechanical system dynamics. *MapleTech*, 3:48–56, 1996.
- [104] A. Meghdari and M. Aryanpour. Dynamic modeling and analysis of the human jumping process. *Journal of Intelligent and Robotic Systems*, 37(1):97–115, 2003. ISSN 09210296. doi: 10.1023/A:1023911408496.
- [105] N. Mehrabi and J. McPhee. Model-based control of biomechatronic systems. In J. Segil, editor, *Handbook of Biomechatronics*, pages 95–126. Academic Press, 1st edition, 2019. ISBN 978-0-12-812539-7. doi: 10.1016/B978-0-12-812539-7.00004-0.
- [106] N. Mehrabi, R. Sharif Razavian, B. Ghannadi, and J. McPhee. Predictive simulation of reaching moving targets using nonlinear model predictive control. *Frontiers in Computational Neuroscience*, 10((submitted)):143, 2017. ISSN 1662-5188. doi: 10.3389/fncom.2016.00143.
- [107] L. L. Menegaldo, A. d. T. Fleury, and H. I. Weber. A ‘cheap’ optimal control approach to estimate muscle forces in musculoskeletal systems. *Journal of Biomechanics*, 39:1787–1795, 2006. ISSN 00219290. doi: 10.1016/j.jbiomech.2005.05.029.
- [108] A. J. Meyer. *Prediction of optimal rehabilitation outcomes post-stroke*. PhD thesis, University of Florida, 2016.
- [109] A. J. Meyer, I. Eskinazi, J. N. Jackson, A. V. Rao, C. Patten, and B. J. Fregly. Muscle synergies facilitate computational prediction of subject-specific walking motions. *Frontiers in Bioengineering and Biotechnology*, 4:77, 2016. ISSN 2296-4185. doi: 10.3389/fbioe.2016.00077.
- [110] A. J. Meyer, C. Patten, and B. J. Fregly. Lower extremity EMG-driven modeling of walking with automated adjustment of musculoskeletal geometry. *PLOS ONE*, 12(7):e0179698, 2017. ISSN 1932-6203. doi: 10.1371/journal.pone.0179698.
- [111] G. Meyer and M. Ayalon. Biomechanical aspects of dynamic stability. *European Review of Aging and Physical Activity*, 3(1):29–33, 2006. ISSN 1813-7253. doi: 10.1007/s11556-006-0006-6.
- [112] M. Millard, J. McPhee, and E. Kubica. Multi-step forward dynamic gait simulation. In C. L. Bottasso, editor, *Multibody Dynamics*, pages 25–43. Springer Netherlands, Dordrecht, 2009. doi: 10.1007/978-1-4020-8829-2_2.

- [113] M. Millard, M. Sreenivasa, and K. Mombaur. Predicting the motions and forces of wearable robotic systems using optimal control. *Frontiers in Robotics and AI*, 4 (AUG):41, 2017. ISSN 2296-9144. doi: 10.3389/frobt.2017.00041.
- [114] M. Millard, A. L. Emonds, M. Harant, and K. Mombaur. A reduced muscle model and planar musculoskeletal model fit for the simulation of whole-body movements. *Journal of Biomechanics*, 89:11–20, 2019. ISSN 18732380. doi: 10.1016/j.jbiomech.2019.04.004.
- [115] R. H. Miller. A comparison of muscle energy models for simulating human walking in three dimensions. *Journal of biomechanics*, 47(6):1373–81, 2014. ISSN 1873-2380. doi: 10.1016/j.jbiomech.2014.01.049.
- [116] R. H. Miller, S. C. E. Brandon, and K. J. Deluzio. Predicting sagittal plane biomechanics that minimize the axial knee joint contact force during walking. *Journal of Biomechanical Engineering*, 135(1):011007, 2012. ISSN 0148-0731. doi: 10.1115/1.4023151.
- [117] M. M. Morrow, J. W. Rankin, R. R. Neptune, and K. R. Kaufman. A comparison of static and dynamic optimization muscle force predictions during wheelchair propulsion. *Journal of Biomechanics*, 47(14):3459–3465, 2014. ISSN 1873-2380. doi: 10.1016/j.jbiomech.2014.09.013.
- [118] F. Mouzo, U. Lugris, R. Pamies Vila, J. M. Font Llagunes, and J. Cuadrado Aranda. Underactuated approach for the control-based forward dynamic analysis of acquired gait motions. In *Proceedings of the ECCOMAS Thematic Conference on Multibody Dynamics*, pages 1092–1100, 2015.
- [119] R. R. Neptune, I. C. Wright, and A. J. van den Bogert. A method for numerical simulation of single limb ground contact events: Application to heel-toe running. *Computer Methods in Biomechanics and Biomedical Engineering*, 3(4):321–334, 2000. ISSN 10255842. doi: 10.1080/10255840008915275.
- [120] D. A. Neumann. Biomechanical analysis of selected principles of hip joint protection. *Arthritis care and research : the official journal of the Arthritis Health Professions Association*, 2(4):146–55, 1989.
- [121] V. Q. Nguyen, R. T. Johnson, F. C. Sup, and B. R. Umberger. Bilevel optimization for cost function determination in dynamic simulation of human gait. *IEEE Transactions on Neural Systems and Rehabilitation Engineering*, 27(7):1426–1435, 2019. ISSN 15580210. doi: 10.1109/TNSRE.2019.2922942.

- [122] A. A. Nikooyan, H. E. J. Veeger, E. K. J. Chadwick, M. Praagman, and F. C. T. van der Helm. Development of a comprehensive musculoskeletal model of the shoulder and elbow. *Medical & biological engineering & computing*, 49(12):1425–35, 2011. ISSN 1741-0444. doi: 10.1007/s11517-011-0839-7.
- [123] V. Norman-Gerum and J. McPhee. Constrained dynamic optimization of sit-to-stand motion driven by Bézier curves. *Journal of Biomechanical Engineering*, 140(12):121011, 2018. doi: 10.1115/1.4041527.
- [124] R. Pàmies-Vilà, J. M. Font-Llagunes, J. Cuadrado, and F. J. Alonso. Analysis of different uncertainties in the inverse dynamic analysis of human gait. *Mechanism and Machine Theory*, 58:153–164, 2012. ISSN 0094-114X. doi: 10.1016/J.MECHMACHTHEORY.2012.07.010.
- [125] R. Pàmies-Vilà, O. Pätkau, A. Dòria-Cerezo, and J. M. Font-Llagunes. Influence of the controller design on the accuracy of a forward dynamic simulation of human gait. *Mechanism and Machine Theory*, 107:123–138, 2017. ISSN 0094-114X. doi: 10.1016/J.MECHMACHTHEORY.2016.09.002.
- [126] M. G. Pandy, F. C. Anderson, and D. G. Hull. A parameter optimization approach for the optimal control of large-scale musculoskeletal systems. *Journal of Biomechanical Engineering*, 114:450–460, 1992. ISSN 01480731. doi: 10.1115/1.2894094.
- [127] I. Pasciuto, S. Ausejo, J. T. Celigüeta, Á. Suescun, and A. Cazón. A comparison between optimization-based human motion prediction methods: data-based, knowledge-based and hybrid approaches. *Structural and Multidisciplinary Optimization*, 49(1):169–183, 2014. ISSN 1615-147X. doi: 10.1007/s00158-013-0960-3.
- [128] M. A. Patterson and A. V. Rao. GPOPS-II. *ACM Transactions on Mathematical Software*, 41(1):1–37, 2014. ISSN 00983500. doi: 10.1145/2558904.
- [129] M. Peasgood, E. Kubica, and J. McPhee. Stabilization of a dynamic walking gait simulation. *Journal of Computational and Nonlinear Dynamics*, 2(1):65, 2007. ISSN 15551423. doi: 10.1115/1.2389230.
- [130] S. Porsa, Y.-C. Lin, and M. G. Pandy. Direct methods for predicting movement biomechanics based upon optimal control theory with implementation in OpenSim. *Annals of Biomedical Engineering*, 44(8):2542–2557, 2016. ISSN 0090-6964. doi: 10.1007/s10439-015-1538-6.

- [131] C. Prakash, R. Kumar, and N. Mittal. Recent developments in human gait research: parameters, approaches, applications, machine learning techniques, datasets and challenges. *Artificial Intelligence Review*, 49(1):1–40, 2018. ISSN 0269-2821. doi: 10.1007/s10462-016-9514-6.
- [132] C. Quental, J. Folgado, and J. Ambrósio. A window moving inverse dynamics optimization for biomechanics of motion. *Multibody System Dynamics*, 38(2):157–171, 2016. ISSN 1384-5640. doi: 10.1007/s11044-016-9529-4.
- [133] A. Rajagopal, C. L. Dembia, M. S. DeMers, D. D. Delp, J. L. Hicks, and S. L. Delp. Full-body musculoskeletal model for muscle-driven simulation of human gait. *IEEE Transactions on Biomedical Engineering*, 63(10):2068–2079, 2016. ISSN 0018-9294. doi: 10.1109/TBME.2016.2586891.
- [134] K. W. Ranatunga and P. E. Thomas. Contraction characteristics of peroneus longus muscle in the anaesthetized rat. In *Proceedings of Physiological Society Meeting*, 1989.
- [135] A. V. Rao. A survey of numerical methods for optimal control. *Advances in the Astronautical Sciences*, 135(1):497–528, 2009. ISSN 1569-3953. doi: 10.1515/jnum-2014-0003.
- [136] J. Rasmussen, M. Damsgaard, and S. T. Christensen. Inverse-inverse dynamics simulation of musculo-skeletal systems. In *Proceedings of the 12th Conference of the European Society of Biomechanics Royal Academy of Medicine in Ireland*. Royal Academy of Medicine in Ireland, 2000.
- [137] L. Ren, R. K. Jones, and D. Howard. Whole body inverse dynamics over a complete gait cycle based only on measured kinematics. *Journal of Biomechanics*, 41(12):2750–2759, 2008. ISSN 0021-9290. doi: 10.1016/J.JBIOMECH.2008.06.001.
- [138] R. Riemer, E. T. Hsiao-Weckslar, and X. Zhang. Uncertainties in inverse dynamics solutions: A comprehensive analysis and an application to gait. *Gait & Posture*, 27(4):578–588, 2008. ISSN 0966-6362. doi: 10.1016/J.GAITPOST.2007.07.012.
- [139] R. Rockenfeller, M. Günther, S. Schmitt, and T. Götz. Comparative sensitivity analysis of muscle activation dynamics. *Computational and Mathematical Methods in Medicine*, 2015:1–16, 2015. ISSN 17486718. doi: 10.1155/2015/585409.

- [140] F. Romero and F. J. Alonso. A comparison among different Hill-type contraction dynamics formulations for muscle force estimation. *Mechanical Sciences*, 7(1):19–29, 2016. ISSN 2191-916X. doi: 10.5194/ms-7-19-2016.
- [141] M. Rosenberg and K. M. Steele. Simulated impacts of ankle foot orthoses on muscle demand and recruitment in typically-developing children and children with cerebral palsy and crouch gait. *PLOS ONE*, 12(7):e0180219, 2017. ISSN 1932-6203. doi: 10.1371/journal.pone.0180219.
- [142] B. Samadi, S. Achiche, A. Parent, L. Ballaz, U. Chouinard, and M. Raison. Custom sizing of lower limb exoskeleton actuators using gait dynamic modelling of children with cerebral palsy. *Computer Methods in Biomechanics and Biomedical Engineering*, 19(14):1519–1524, 2016. ISSN 14768259. doi: 10.1080/10255842.2016.1159678.
- [143] S. S. Sandhu and J. McPhee. A two-dimensional nonlinear volumetric foot contact model. In *Volume 2: Biomedical and Biotechnology Engineering*, pages 703–710. ASME, 2010. ISBN 978-0-7918-4426-7. doi: 10.1115/IMECE2010-39464.
- [144] A. Sarcher, M. Raison, F. Leboeuf, B. Perrouin-Verbe, S. Brochard, and R. Gross. Pathological and physiological muscle co-activation during active elbow extension in children with unilateral cerebral palsy. *Clinical Neurophysiology*, 128(1):4–13, 2017. ISSN 18728952. doi: 10.1016/j.clinph.2016.10.086.
- [145] M. Sartori, M. Reggiani, D. Farina, and D. G. Lloyd. EMG-driven forward-dynamic estimation of muscle force and joint moment about multiple degrees of freedom in the human lower extremity. *PLoS ONE*, 7(12):e52618, 2012. ISSN 1932-6203. doi: 10.1371/journal.pone.0052618.
- [146] M. Sartori, D. Farina, and D. G. Lloyd. Hybrid neuromusculoskeletal modeling to best track joint moments using a balance between muscle excitations derived from electromyograms and optimization. *Journal of Biomechanics*, 47(15):3613–3621, 2014. ISSN 00219290. doi: 10.1016/j.jbiomech.2014.10.009.
- [147] K. Sasaki, M. Hongo, N. Miyakoshi, T. Matsunaga, S. Yamada, H. Kijima, and Y. Shimada. Evaluation of sagittal spine-pelvis-lower limb alignment in elderly women with pelvic retroversion while standing and walking using a three-dimensional musculoskeletal model. *Asian spine journal*, 11(4):562–569, 2017. doi: 10.4184/asj.2017.11.4.562.

- [148] W. Schiehlen. On the historical development of human walking dynamics. In E. Stein, editor, *The History of Theoretical, Material and Computational Mechanics - Mathematics Meets Mechanics and Engineering*, pages 101–116. Springer, Berlin, Heidelberg, 2014. doi: 10.1007/978-3-642-39905-3_7.
- [149] M. H. Schwartz, A. Rozumalski, and J. P. Trost. The effect of walking speed on the gait of typically developing children. *Journal of Biomechanics*, 41(8):1639–1650, 2008. ISSN 00219290. doi: 10.1016/j.jbiomech.2008.03.015.
- [150] J. C. Selinger, S. M. O’Connor, J. D. Wong, and J. M. Donelan. Humans can continuously optimize energetic cost during walking. *Current Biology*, 25(18):2452–2456, 2015. ISSN 09609822. doi: 10.1016/j.cub.2015.08.016.
- [151] G. Serrancofí, J. Font-Llagunes, and A. Barjau. A weighted cost function to deal with the muscle force sharing problem in injured subjects: A single case study. *Proceedings of the Institution of Mechanical Engineers, Part K: Journal of Multi-body Dynamics*, 228(3):241–251, 2014. ISSN 20413068 14644193. doi: 10.1177/1464419314530110.
- [152] A. Seth and M. G. Pandy. A neuromusculoskeletal tracking method for estimating individual muscle forces in human movement. *Journal of biomechanics*, 40(2):356–66, 2007. ISSN 0021-9290. doi: 10.1016/j.jbiomech.2005.12.017.
- [153] R. Sharif Razavian and J. McPhee. Minimization of muscle fatigue as the criterion to solve muscle forces-sharing problem. In *ASME 2015 Dynamic Systems and Control Conference*, number 57243, page V001T15A001. ASME, 2015. ISBN 978-0-7918-5724-3. doi: 10.1115/DSCC2015-9678.
- [154] R. Sharif Razavian, N. Mehrabi, and J. McPhee. A model-based approach to predict muscle synergies using optimization: Application to feedback control. *Frontiers in Computational Neuroscience*, 9:121, 2015. ISSN 1662-5188. doi: 10.3389/fncom.2015.00121.
- [155] M. Sharif Shourijeh. *Optimal Control and Multibody Dynamic Modelling of Human Musculoskeletal Systems*. 2013.
- [156] M. Sharif Shourijeh and J. McPhee. Forward dynamic optimization of human gait simulations: a global parameterization approach. *Journal of Computational and Nonlinear Dynamics*, 9(3):031018, 2014. ISSN 1555-1415. doi: 10.1115/1.4026266.

- [157] M. Sharif Shourijeh, T. E. Flaxman, and D. L. Benoit. An approach for improving repeatability and reliability of non-negative matrix factorization for muscle synergy analysis. *Journal of Electromyography and Kinesiology*, 26:36–43, 2016. ISSN 18735711. doi: 10.1016/j.jelekin.2015.12.001.
- [158] M. S. Shourijeh and J. McPhee. Efficient hyper-volumetric contact dynamic modelling of the foot within human gait simulations. In *Volume 7A: 9th International Conference on Multibody Systems, Nonlinear Dynamics, and Control*, page V07AT10A012. ASME, 2013. ISBN 978-0-7918-5596-6. doi: 10.1115/DETC2013-13446.
- [159] M. S. Shourijeh and J. McPhee. Foot–ground contact modeling within human gait simulations: from Kelvin–Voigt to hyper-volumetric models. *Multibody System Dynamics*, 35(4):393–407, 2015. ISSN 1384-5640. doi: 10.1007/s11044-015-9467-6.
- [160] M. S. Shourijeh, K. B. Smale, B. M. Potvin, D. L. Benoit, M. S. Shourijeh, K. B. Smale, B. M. Potvin, D. L. Benoit, M. S. Shourijeh, K. B. Smale, B. M. Potvin, and D. L. Benoit. A forward-muscular inverse-skeletal dynamics framework for human musculoskeletal simulations. *Journal of Biomechanics*, 49(9):1718–1723, 2016. ISSN 18732380. doi: 10.1016/j.jbiomech.2016.04.007.
- [161] M. S. Shourijeh, N. Mehrabi, and J. McPhee. Forward static optimization in dynamic simulation of human musculoskeletal systems: a proof-of-concept study. *Journal of Computational and Nonlinear Dynamics*, 12(5):051005, 2017. ISSN 1555-1415. doi: 10.1115/1.4036195.
- [162] M. Silva and J. Ambrósio. Kinematic data consistency in the inverse dynamic analysis of biomechanical systems. *Multibody System Dynamics*, 8(2):219–239, 2002. ISSN 13845640. doi: 10.1023/A:1019545530737.
- [163] M. Silva, B. Freitas, R. Andrade, Ó. Carvalho, D. Renjewski, P. Flores, and J. Espregueira-Mendes. Current perspectives on the biomechanical modelling of the human lower limb: a systematic review. *Archives of Computational Methods in Engineering*, 2020. ISSN 18861784. doi: 10.1007/s11831-019-09393-1.
- [164] J. A. Singh. Epidemiology of knee and hip arthroplasty: A systematic review. *The open orthopaedics journal*, 5:80–5, 2011. ISSN 1874-3250. doi: 10.2174/1874325001105010080.
- [165] K. B. Smale, M. Sharif Shourijeh, and D. L. Benoit. Use of muscle synergies and wavelet transforms to identify fatigue during squatting. *Journal of Electromyography*

- and Kinesiology*, 28:158–166, 2016. ISSN 18735711. doi: 10.1016/j.jelekin.2016.04.008.
- [166] M. Sreenivasa, M. Millard, M. Felis, K. Mombaur, and S. I. Wolf. Optimal control based stiffness identification of an ankle-foot orthosis using a predictive walking model. *Frontiers in Computational Neuroscience*, 11:23, 2017. ISSN 1662-5188. doi: 10.3389/fncom.2017.00023.
- [167] M. Srinivasan. Optimal speeds for walking and running, and walking on a moving walkway. *Chaos: An Interdisciplinary Journal of Nonlinear Science*, 19(2):026112, 2009. ISSN 1054-1500. doi: 10.1063/1.3141428.
- [168] K. M. Steele, A. Rozumalski, and M. H. Schwartz. Muscle synergies and complexity of neuromuscular control during gait in cerebral palsy. *Developmental Medicine and Child Neurology*, 57(12):1176–1182, 2015. ISSN 14698749. doi: 10.1111/dmcn.12826.
- [169] J. Sun. *Dynamic modeling of human gait using a model predictive control approach*. PhD thesis, Marquette University, 2015.
- [170] J. Sun and P. A. Voglewede. Dynamic simulation of human gait using a combination of model predictive and PID control. In *Volume 6: 10th International Conference on Multibody Systems, Nonlinear Dynamics, and Control*, page V006T10A008. ASME, 2014. ISBN 978-0-7918-4639-1. doi: 10.1115/DETC2014-35582.
- [171] J. Sun, S. Wu, and P. A. Voglewede. Dynamic simulation of human gait model with predictive capability. *Journal of Biomechanical Engineering*, 140(3):031008, 2018. ISSN 0148-0731. doi: 10.1115/1.4038739.
- [172] A. Terrier, M. Aeberhard, Y. Michellod, P. Mullhaupt, D. Gillet, A. Farron, and D. P. Pioletti. A musculoskeletal shoulder model based on pseudo-inverse and null-space optimization. *Medical Engineering and Physics*, 32(9):1050–6, 2010. ISSN 1873-4030. doi: 10.1016/j.medengphy.2010.07.006.
- [173] D. G. Thelen. Adjustment of muscle mechanics model parameters to simulate dynamic contractions in older adults. *Journal of Biomechanical Engineering*, 125(1):70–7, 2003. ISSN 0148-0731. doi: 10.1115/1.1531112.
- [174] D. G. Thelen and F. C. Anderson. Using computed muscle control to generate forward dynamic simulations of human walking from experimental data. *Journal of Biomechanics*, 39(6):1107–1115, 2006. ISSN 00219290. doi: 10.1016/j.jbiomech.2005.02.010.

- [175] D. Tlalolini, Y. Aoustin, and C. Chevallereau. Design of a walking cyclic gait with single support phases and impacts for the locomotor system of a thirteen-link 3D biped using the parametric optimization. *Multibody System Dynamics*, 23(1):33–56, 2010. ISSN 1384-5640. doi: 10.1007/s11044-009-9175-1.
- [176] M. C. Tresch. Matrix factorization algorithms for the identification of muscle synergies: Evaluation on simulated and experimental data sets. *Journal of Neurophysiology*, 95(4):2199–2212, 2005. ISSN 0022-3077. doi: 10.1152/jn.00222.2005.
- [177] D. Tsirakos, V. Baltzopoulos, and R. Bartlett. Inverse optimization: Functional and physiological considerations related to the force-sharing problem. *Critical reviews in biomedical engineering in Biomedical Engineering*, 25(4-5):371–407, 1997. ISSN 0278-940X. doi: 10.1615/CritRevBiomedEng.v25.i4-5.20.
- [178] T. K. Uchida, J. L. Hicks, C. L. Dembia, and S. L. Delp. Stretching Your Energetic Budget: How Tendon Compliance Affects the Metabolic Cost of Running. *PLOS ONE*, 11(3):e0150378, 2016. ISSN 1932-6203. doi: 10.1371/journal.pone.0150378.
- [179] Z. Ugray, L. Lasdon, J. Plummer, F. Glover, J. Kelly, and R. Martí. Scatter search and local NLP solvers: A multistart framework for global optimization. *INFORMS Journal on Computing*, 19(3):328–340, 2007. ISSN 1091-9856. doi: 10.1287/ijoc.1060.0175.
- [180] B. R. Umberger. Effects of suppressing arm swing on kinematics, kinetics, and energetics of human walking. *Journal of Biomechanics*, 41(11):2575–2580, 2008. ISSN 00219290. doi: 10.1016/j.jbiomech.2008.05.024.
- [181] B. R. Umberger, K. G. Gerritsen, and P. E. Martin. A model of human muscle energy expenditure. *Computer methods in biomechanics and biomedical engineering*, 6(2): 99–111, 2003. ISSN 10255842. doi: 10.1080/1025584031000091678.
- [182] A. J. van den Bogert, D. Blana, and D. Heinrich. Implicit methods for efficient musculoskeletal simulation and optimal control. *Procedia IUTAM*, 2:297–316, 2011. ISSN 2210-9838. doi: 10.1016/J.PIUTAM.2011.04.027.
- [183] S. Watson. Plantar Flexion: Muscles, Function, and More, 2018.
- [184] J. Wen, M. Raison, and S. Achiche. Using a cost function based on kinematics and electromyographic data to quantify muscle forces. *Journal of Biomechanics*, 80: 151–158, 2018. ISSN 18732380. doi: 10.1016/j.jbiomech.2018.09.002.

- [185] D. Winter. Human balance and posture control during standing and walking. *Gait & Posture*, 3(4):193–214, 1995. ISSN 0966-6362. doi: 10.1016/0966-6362(96)82849-9.
- [186] D. A. Winter. *Biomechanics and motor control of human movement*. Wiley, 2009. ISBN 9780470398180.
- [187] J. M. Winters. An improved muscle-reflex actuator for use in large-scale neuromusculoskeletal models. *Annals of Biomedical Engineering*, 23(4):359–374, 1995. ISSN 00906964. doi: 10.1007/BF02584437.
- [188] U. P. Wyss, I. McBride, L. Murphy, T. D. Cooke, and S. J. Olney. Joint reaction forces at the first MTP joint in a normal elderly population. *Journal of biomechanics*, 23(10):977–84, 1990.
- [189] T. Yamasaki, K. Idehara, and X. Xin. Estimation of muscle activity using higher-order derivatives, static optimization, and forward-inverse dynamics. *Journal of Biomechanics*, 49(10):2015–2022, 2016. ISSN 00219290. doi: 10.1016/j.jbiomech.2016.04.024.
- [190] Yanli Geng, Peng Yang, Xiaoyun Xu, and Lingling Chen. Design and simulation of active transfemoral prosthesis. In *2012 24th Chinese Control and Decision Conference (CCDC)*, pages 3724–3728. IEEE, 2012. ISBN 978-1-4577-2074-1. doi: 10.1109/CCDC.2012.6243095.
- [191] M. R. Yeadon, M. A. King, and C. Wilson. Modelling the maximum voluntary joint torque/angular velocity relationship in human movement. *Journal of Biomechanics*, 39(3):476–482, 2006. ISSN 00219290. doi: 10.1016/j.jbiomech.2004.12.012.
- [192] F. Yoshikawa, H. Hirai, E. Watanabe, Y. Nagakawa, A. Kuroiwa, E. Grabke, M. Uemura, F. Miyazaki, and H. I. Krebs. Equilibrium-point-based synergies that encode coordinates in task space: A practical method for translating functional synergies from human to musculoskeletal robot arm. In *2016 IEEE-RAS 16th International Conference on Humanoid Robots (Humanoids)*, pages 1135–1140. IEEE, 2016. ISBN 978-1-5090-4718-5. doi: 10.1109/HUMANOIDS.2016.7803413.
- [193] F. E. Zajac, R. R. Neptune, and S. A. Kautz. Biomechanics and muscle coordination of human walking. Part I: introduction to concepts, power transfer, dynamics and simulations. *Gait & posture*, 16(3):215–32, 2002. ISSN 0966-6362. doi: 10.1016/S0966-6362(02)00068-1.

- [194] F. E. Zajac, R. R. Neptune, and S. A. Kautz. Biomechanics and muscle coordination of human walking: part II: lessons from dynamical simulations and clinical implications. *Gait & posture*, 17(1):1–17, 2003. ISSN 0966-6362. doi: 10.1016/S0966-6362(02)00069-3.
- [195] J. Zariffa, J. Steeves, and D. K. Pai. Changes in hand muscle synergies in subjects with spinal cord injury: Characterization and functional implications. *The Journal of Spinal Cord Medicine*, 35(5):310–8, 2012. ISSN 1079-0268. doi: 10.1179/2045772312Y.0000000037.
- [196] A. Zmitrowicz. Contact stresses: a short survey of models and methods of computations. *Archive of Applied Mechanics*, 80(12):1407–1428, 2010. ISSN 0939-1533. doi: 10.1007/s00419-009-0390-2.